Investigating the effect of microstructural gradient generated during patenting wires on their final mechanical properties

Lais Avila de Oliveira Silva

CENTRALE LILLE

THESE

Présentée en vue
d'obtenir le grade de

DOCTEUR

En

Science des Matériaux

Par

Laís AVILA DE OLIVEIRA SILVA

Ingénieure diplômée de l'Universidade Federal de Minas Gerais (UFMG), Brésil

DOCTORAT DELIVRE PAR CENTRALE LILLE

Titre de la thèse:

Investigation de l'effet du gradient microstructural généré pendant le patentage sur les propriétés mécaniques finales des fils d'acier perlitiques

Soutenue publiquement le 4 mars 2022 devant le jury d'examen :

Président:	Alexandre Legris	Professeur, Université de Lille
Rapporteure:	Cristelle Pareige	Professeure, Université de Rouen
Rapporteur:	Roumen Petrov	Professeur, UGhent University, Belgique
Examinatrice:	Delphine Retraint	Professeure, Université de technologie de Troyes
Examinateur:	Eric Hug	Professeur, Université de Caen
Partenaire industriel:	Christophe Mesplont	Docteur, Expert R&D, Bekaert
Co-encadrant:	Jérémie Bouquerel	Maître de conférence, Centrale Lille Institut
Directeur de thèse:	Jean-Bernard Vogt	Professeur, Centrale Lille Institut

Thèse préparée dans le Laboratoire UMET en partenariat Bekaert

Ecole Doctorale SMRE 104

Acknowledgements

A three-year project has, for sure, counted with a lot of contributions. I would like to first of all thank Bekaert for the support for this research. It was a real pleasure to develop this work. My supervisor, Christophe Mesplont, for all the discussions, patience, and learning.

Still from Bekaert, I would like to thank Pascal Antoine for the opportunity and the constructive exchanges. A special and huge thanks to Wesley, who has been an essential person for this work, and whose kindness has made the way easier. And to all the people of the lab and the offices which whom I had the pleasure to share some time with.

Most of the time I spent at the university and, therefore, most of the acknowledgments would be here too. I will never be able to thank enough Jean-Bernard Vogt for all his help, kindness, teachings, patience... He has been an example of a professor and a person, which I had the great pleasure to have as my supervisor.

I would also like to acknowledge the help of Damien, Ahmed, Alex, Joscelyn, and Jérémie during the development of the thesis. Also, Manon Roland has arrived at the end and has greatly contributed.

I will always have great memories and I'm very thankful for all of my exchanges with the other PhD's students, both from the metallurgy group (too many over the yeas, love them all), the geology group (Jeff, Tommaso and Konstantinos), my brazilian support (Mahira and Isadora) and my office mate, Arthur.

Mahira deserves a whole paragraph because, together with Jean-Bernard, they kept me alive. With their friendship and support, I was capable to overcome all the hard times of the last three years. I am very very thankfull for her friendship and help. It would definetly not be possible without her.

Finally, I would like to acknowledge my family, Alexis, and his family. Thank you for all the love and support!

I hope to have shortly express my gratitude.

Résumé en Français

Les aciers perlitiques, alliages de fer avec 0,8% massique de carbone, sont connus pour leur très grande résistance mécanique en particulier lorsqu'ils sont fortement déformés par procédé de tréfilage. Ce procédé permet la fabrication de fils qui sont dès lors employés à juste titre dans le domaine de la construction, comme par exemple, les câbles de pont. La perlite est une microstructure hiérarchisée c'est-à-dire qu'elle doit être décrite à plusieurs échelles. Le mélange Fe- 0,8%C conduit à générer des lamelles de ferrite (phase α) et de cémentite (phase Fe_3C). La formation de ces lamelles se produit par une croissance coopérative des deux phases dans laquelle le carbone est réparti à l'interface de transformation. L'ensemble des lamelles parallèles forme une organisation appelée colonie, et toutes les colonies présentant la même orientation cristallographique forment un nodule. L'espacement entre les lamelles de ferrite et cémentite est considéré comme le principal paramètre contrôlant les propriétés mécaniques de ces aciers. Il est ainsi classique de se référer à cet espacement inter-lamellaire pour distinguer la perlite en deux groupes : la perlite grossière et la perlite fine. Plus l'espacement inter-lamellaire est petit, plus dure sera la perlite.

Près de 150 ans après la découverte de la microstructure perlitique par Sorby, après de très nombreux travaux de recherche sur la perlite, est-il encore possible d'améliorer les performances d'un tel matériau classique? Comment peut-on innover tant sur le plan scientifique que sur le plan technologique à partir de ce matériau ?

Ces questions, qui ont été le fil directeur de mon projet de thèse, m'ont été adressées par l'entreprise NV Bekaert SA (Bekaert) et le laboratoire UMET.

Un moyen innovant d'améliorer les propriétés mécaniques des matériaux est de générer un gradient de microstructure. Au cours des deux dernières décennies, pour les matériaux de structure tels que les aciers, la production de gradients a été réalisée dans les aciers ferritiques et austénitiques de microstructure «simple», c'est-à-dire monophasés. Ce gradient résulte d'un traitement thermo-mécanique visant à contrôler et produire une forte déformation plastique conduisant à la formation de nanograins à la surface et une microstructure grossière à cœur. L'idée de ce type de traitement

est de conduire à un matériau «gradé» ayant des propriétés mécaniques supérieures à la somme de celles obtenues par chaque type de microstructure prise individuellement. Cet effet de synergie est cependant obtenu si l'épaisseur optimisée de la couche externe est atteinte.

A côte de cette question fondamentalement d'ordre métallurgique, le projet de thèse a pris également en compte un aspect environnemental. En effet, l'une des étapes dans la fabrication des fils comprend le patentage (patenting, en anglais). Ce traitement consiste à immerger les fils dans un bain de plomb chaud pour produire la perlite, ce qui soulève des inquiétudes. En effet, l'agence européenne des produits chimiques (ECHA) a annoncé, le 2 février 2022, le lancement d'une consultation de 3 mois, qui pourrait voir le plomb entrer dans la liste des « substances extrêmement préoccupantes » suite à de nombreux débats à ce sujet lancés en 2018. La plupart des fils d'acier perlitique produits dans le monde étant obtenus par patentage au plomb, il est donc tout à fait pertinent de s'intéresser à sa substitution par d'autres technologies de refroidissement.

Ce travail de thèse s'est donc déroulé dans le cadre d'un contrat de recherche entre l'UMET (Unité Matériaux Et Transformations) de l'Institut Centrale Lille & Université de Lille et l'entreprise NV Bekaert SA (Bekaert), dont le centre technologique est situé à Deerlijk, en Belgique. Bekaert, leader mondial des technologies de transformation et de revêtement des fils d'acier, a obtenu le soutien financier de l'Agence pour l'innovation et l'entrepreneuriat – VLAIO, une organisation gouvernementale flamande qui encourage et soutient la recherche stratégique et industrielle. Bekaert a sollicité l'UMET pour ses compétences reconnues en métallurgie physique et métallurgie mécanique. Ce travail doctoral fait partie d'un projet de plus grande ampleur sur le traitement thermique de haute technologie des fils dans lequel Bekaert analyse la pertinence des gradients de microstructure produits sur les fils de gros diamètre pendant l'étape de patentage utilisant un fluide autre que le plomb liquide. Cela permettrait de mettre sur le marché des matériaux de technicité avancée tout en répondant aux futures lois et contraintes environnementales.

Dans ce projet doctoral, nous avons choisi comme ligne directrice de transposer le concept de gradient microstructural démontré sur les aciers de microstructure simple aux aciers perlitiques, de microstructure beaucoup plus complexe, afin d'améliorer ses propriétés déjà remarquables, en particulier le comportement à la fatigue. Cela permettrait de prolonger la durée d'utilisation de composants en acier perlitique gradé réduisant ainsi leurs remplacements et leur entretien ou encore de réduire le volume de matériau pour la fabrication du composant. Ce défi ou cette tentative est tout à fait raisonnable puisque des gradients dans des aciers perlitiques ont déjà été observés dans le passé de manière involontaire, en particulier pour les fils de grand diamètre, comme

une conséquence indésirable du procédé de production. Comprendre la formation de ces gradients pendant le traitement thermique, leur comportement sous sollicitation mécanique et étudier si ces gradients peuvent être optimisés constituent quelques points clés de la stratégie de ce projet de recherche.

Si l'on veut profiter du procédé industriel de fabrication du fil pour réaliser les gradients de microstructure, il est possible d'agir sur l'une de ces trois étapes: lors de l'austénitisation, lors du refroidissement utilisant habituellement du plomb liquide « le patentage » ou lors du tréfilage, comme indiqué dans la Figure 1. Ainsi, pour la production des gradients, d'autres modes de refroidissement ont également été étudiés et considérés pour résoudre ce problème.

Ainsi, l'objectif principal de ce travail de thèse a été d'expliquer comment peuvent être produits les gradients de microstructure dans les fils de grand diamètre et quels sont leurs effets sur les propriétés mécaniques finales. Cet objectif a nécessité de décliner d'autres objectifs spécifiques en lien avec les différentes étapes du projet. Tout d'abord, il a fallu étudier et reconnaître les paramètres du traitement thermique pouvant affecter la microstructure finale et les propriétés mécaniques finales du fil. En plus de l'effet de ces paramètres de procédé, le rôle de la composition chimique a également été pris en compte. A partir de ces informations obtenues sur ces matériaux monolithiques, les efforts se sont concentrés sur l'obtention de gradients microstructuraux, leurs mécanismes de formation par des moyens thermiques, mécaniques et thermomécaniques. Une fois les matériaux à gradient obtenus, leurs performances mécaniques ont été évaluées notamment en fatigue.

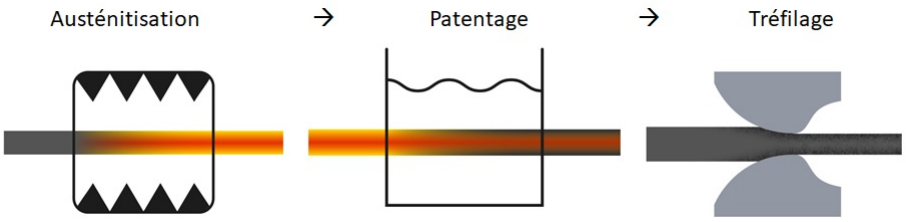

Figure 1: Formation d'un gradient lors de la production des fils d'acier perlitiques.

Compte tenu du fait que la recherche était menée dans un contexte industriel, les moyens techniques pour contrôler la microstructure devaient être aussi proches que possible de ceux existant sur les lignes industrielles, en particulier le patentage. Par conséquent, les traitements thermiques et mécaniques sur lignes de production ont guidé les expériences de laboratoire. Il est d'abord nécessaire d'étudier et de comprendre en profondeur la formation d'une microstructure perlitique basée sur les mécanismes de transformation de phase des aciers perlitiques. Une étude de l'austénitisation et du refroidissement a été dans un premier temps réalisée au laboratoire sur des échantillons

de petite taille, 4 mm de diamètre. Pour cela, le dilatomètre de pointe de l'entreprise Bekaert a été utilisé pour simuler les cycles thermiques industriels. Les diagrammes de transformations de phase pendant le chauffage (Temps-Température-Austénitisation et Chauffage-Continu Transformation) et pendant le refroidissement (Diagramme Temps-Température-Transformation et Refroidissement- Continu Transformation) ont été tracés pour comprendre la décomposition et la formation de la perlite dans les aciers non seulement de composition eutectoïde mais également de composition hypo et hyper eutectoïde. Nous nous sommes également intéressés à identifier les paramètres métallurgiques qui affectent la stabilité de la perlite, et par suite d'apporter une contribution aux mécanismes de la transformation perlitique. L'obtention de ces diagrammes et la connaissance des températures de transformation ont permis d'établir une base pour la caractérisation des gradients, qui ont été ensuite produits par des voies thermique, mécanique et thermomécanique sur des fils d'un diamètre de 6,5 et 12 mm. Outre la distance interlamellaire, la question de la morphologie de la perlite a aussi été étudiée de près. Ensuite, les propriétés en fatigue oligocyclique des éprouvettes monolithiques et à gradients, représentatives de fils de diamètre 6 mm, ont été étudiées sous des sollicitations mécaniques faibles et élevées. Ces essais apporteront un éclairage sur les mécanismes de plasticité cyclique des aciers perlitiques. Enfin, la production des gradients par les différentes technologies de refroidissement a été évaluée et les propriétés mécaniques obtenues après le tréfilage sur le fil final de 2,25 mm ont été analysées.

Enfin, ce travail se termine par l'évaluation de la possibilité d'obtenir de la perlite par des technologies de refroidissement alternatives, de générer un gradient microstructural et de confirmer si ces gradients sont conservés après le tréfilage.

Les principales questions auxquelles ce travail vise à répondre sont résumées ci-après :

- Est-il possible de produire un gradient perlitique ?
- La présence d'un gradient de microstructure produit-elle un avantage par rapport aux fils homogènes ?
- L'épaisseur de gradient peut-elle être contrôlée ? Y a-t-il une épaisseur optimale ?
- Le tréfilage aide-t-il à renforcer le gradient ?
- Quelles sont les limites de la production par gradient ?

- Est-il possible de reproduire une microstructure de gradient par tempcore en carbone élevé avec des fils de plus petit diamètre ? Et de contrôler l'épaisseur de la couche de martensite externe ?
- Peut-il être produit industriellement par patentage au plomb ? Et en utilisant les technologies de refroidissement alternatives ?
- Quels sont les paramètres caractéristiques autres que l'espacement interlamellaire qui contrôlent les propriétés mécaniques des aciers perlitiques ?

Le manuscrit qui comprend l'ensemble de ces questions et de leurs réponses comprend les différents chapitres suivants :

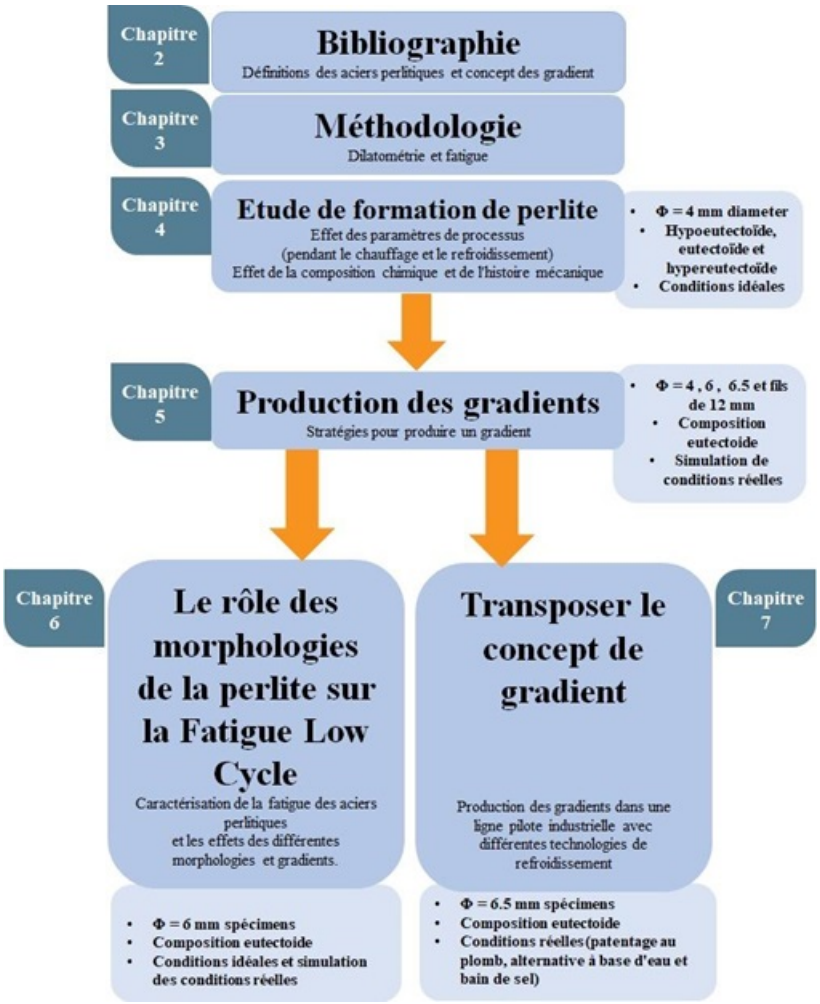

Une variété de fils doit être utilisée pour s'adapter aux différents objectifs et pour caractériser les diverses conditions d'essai. Par conséquent, ils sont divisés en quatre chapitres d'investigation : la formation de la perlite (chapitre 4), les gradients (chapitre

5), les essais mécaniques (chapitre 6) et les essais pilotes (chapitre 7), dans lesquels sont envisagées différentes compositions, l'historique mécanique et les diamètres.

Les principaux résultats de la thèse ainsi que les conclusions sont résumé ci-dessous :

Étape de chauffage et austénitisation

La vitesse de chauffage, depuis la température ambiante jusqu'à la température d'austénitisation n'a pas eu d'impact sur la microstructure finale, ni sur la taille de grain austénitique primaire, ni sur l'homogénéité chimique. Austénitiser à plus haute température et durant des temps plus longs ont conduit à accroitre la taille du grain austénitique.

L'étude de transformation de phases nous a montré que l'austénitisation peut avoir un grand impact sur la formation des phases pendant le refroidissement ultérieur, comme la formation de bainite sensible à une répartition hétérogène dans l'austénite et la formation de martensite observée pour des vitesses de refroidissement critiques. Elle peut aussi affecter la morphologie de la perlite puisque les échantillons formés après le cycle standard de l'ASTM (cycle de stabilisation + 797 °C pendant 5 minutes) présentaient une microstructure lamellaire beaucoup plus espacée, tandis que ceux obtenus par refroidissement continu à la même vitesse de refroidissement présentaient une structure lamellaire interconnectée. De plus, une grande taille de grain est apparue comme la cause de la transformation « anormale » pendant le refroidissement isotherme, affectant ainsi également la cinétique de la transformation $\gamma \rightarrow \alpha + \theta$.

Étape de refroidissement

La morphologie de la perlite est très sensible au mode de refroidissement, étant principalement lamellaire pendant le refroidissement continu et divorcée pendant le refroidissement isotherme, comme indiqué dans la Figure 2 . Nous avons expliqué cette différence de morphologie par les différences de mécanisme de transformation et de cinétique, une croissance de diffusion contrôlée dans le cas de la perlite divorcée, et le contrôle de l'interface pour la perlite lamellaire. En outre, la construction des diagrammes a révélé que la transformation est un peu retardée lorsqu'une taille de grain austénitique est grande mais sans incidence puisque la transformation commence en moins d'une seconde. Il est important de s'intéresser aux caractéristiques de la perlite puisque la dureté varie non seulement avec l'espacement interlamellaire mais aussi avec la morphologie, la dureté la plus faible étant mesurée pour la perlite sphéroïdisée.

L'écart de la teneur en carbone avec la composition eutectoïde a entraîné la formation de phases proeutectoïdes, mais cela n'a eu aucune incidence sur la morphologie de la perlite mais a produit une perlite divorcée pendant le refroidissement isotherme et une perlite lamellaire pendant le refroidissement isochrone. La cinétique

a également été étudiée et, bien qu'un comportement anormal ait été mis en évidence, les deux pics observés au cours de la transformation ont été attribués à la formation de ferrite proeutectoïde ou de cémentite et le deuxième pic est lié à la transformation perlitique. De plus, nous avons constaté que l'acier hypereutectoïde présentait des comportement plus proches de l'acier eutectoïde que de l'acier hypoeutectoïde, comme l'effet de la taille de grain austénitique sur le retard à la transformation. Cependant, l'augmentation de la teneur en carbone n'a pas augmenté la vitesse de refroidissement critique, « dont la martensite est la signature», comme on aurait pu s'y attendre, à cause de la formation de la cémentite proeutectoïde.

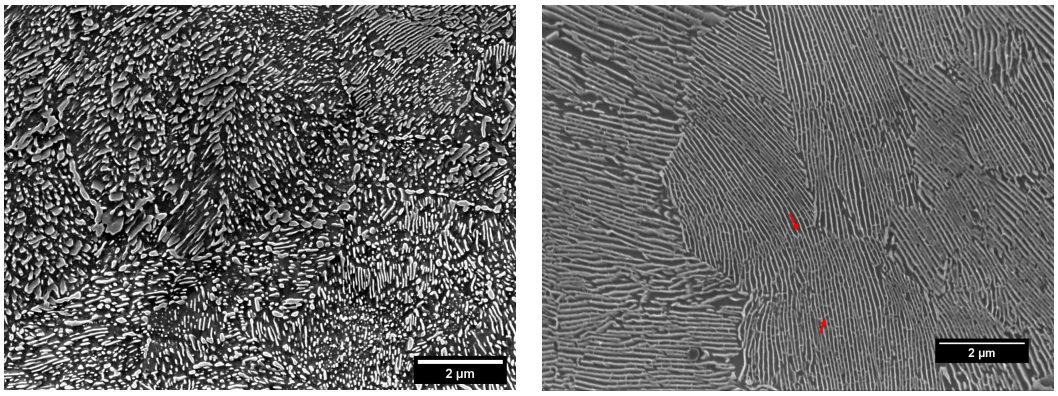

(a) (b)

Figure 2: Micrographies representatives de la microstructure perlitique (a) divorce et (b) lamellaire avec des connections.

Effet de l'histoire mécanique

L'effet de l'influence de l'histoire mécanique a également été étudié mais s'est révélé peu sensible pour produire un effet sur la microstructure finale après l'austénitisation. Des analyses métallurgiques après un chauffage interrompu à 700 °C à des vitesses de chauffage différentes ont été réalisées. Il est apparu que la restauration se produit d'abord dans la cémentite qui se globularise ensuite et que la ferrite forme des parois cellulaires pendant le processus de restauration. Une très petite fraction de recristallisation a été observée, quelques grains nanométriques, ont été observés à l'intérieur des lamelles ferritiques. Cela permet d'expliquer l'absence de l'effet de l'histoire mécanique sur la taille de grain austénitique ou la transformation perlitique ultérieure. Cela se produit parce que les phénomènes connexes se produisent à une échelle lamellaire, tandis que l'austénitisation pourrait être affectée à une échelle de la colonie ou de nodule. Ainsi, lorsque la transformation en austénite commence, elle continue à se nucléer aux joints triples des colonies et consomme les lamelles indépendamment si elles sont recristallisées ou non. La sphéroïdisation n'est pas un obstacle puisque les sphères formées sont petites et rapidement dissoutes.

Formation du gradient

Une fois que tous les paramètres contrôlant la transformation de phase ont été identifiés et compris, la faisabilité d'obtention des gradients a été effectuée avec succès dans le dilatomètre sur les fils de 6 mm et de 12 mm de diamètre. Il a été démontré que les gradients formés pendant l'austénitisation n'entraînaient aucune différence dans le gradient final, du moins pas dans les conditions d'essai.

Par des moyens thermiques, nous avons réussi à produire un gradient de microstructure avec une perlite de faible espacement interlamellaire (perlite fine) à la surface et d'espacement plus important (perlite grossière) à cœur. L'inverse, perlite grossière à la surface et perlite fine à cœur, n'a pas été possible parce que le gradient de température formé n'est pas assez net pour favoriser une transformation sélective à la surface et éviter la transformation du cœur.

Par des moyens mécaniques en modifiant l'angle d'entrée de la filière, il a été possible de réaliser un gradient de microstructure conduisant à une dureté plus élevée en surface qu'à cœur. Toutefois, ces expériences réalisées sur des fils de diamètre 6 mm présentent un intérêt limité car ces fils devront être tréfilés jusqu'à un diamètre de 2,25 mm. La transformation perlitique n'a pas été favorisée et les mêmes cycles de gradients cibles réalisés sur la production de gradient thermique se sont transformés en martensite. Cela permet de conclure que les gradients mécaniques n'améliorent pas les gradients thermiques. La raison pour laquelle la transformation perlitique a été entravée n'est pas encore comprise.

Etude du comportement en fatigue

Ensuite, l'effet des gradients formés et des morphologies perlitiques sur le comportement de fatigue oligocyclique a été étudié. Sur les échantillons monolithiques, la morphologie de la perlite et la distance interlamellaire ont produit des effets significatifs. Pour ces essais de fatigue conduits en déformation imposée, réduire la distance interlamellaire conduit à des niveaux de contrainte cyclique plus élevés mais des durées de vie plus courtes. Le plus intéressant a été l'effet marquant de la morphologie de la perlite, à espacement interlamellaire identique, obtenue par différentes voies thermiques sur le comportement de plasticité cyclique. Cela a conduit à une discussion sur les interactions des dislocations avec les atomes de carbone, dont la distribution varie avec le traitement thermique, et à une explication des phénomènes d'adoucissement - durcissement cyclique. Les analyses des faciès de rupture laissent à penser que la ténacité des aciers perlitiques, lamellaire parfaite ou lamellaire interconnectée, pourrait être intéressante.

Les résultats sur les matériaux avec gradient ont montré une très bonne aptitude à la plasticité cyclique et à la résistance à la fissuration de surface. Cependant, ils n'ont pas présenté de résultats convaincants pour justifier leur production, les valeurs

de contrainte obtenues étaient plus proches de la perlite grossière et la résistance à la fatigue était comparable à la perlite fine, prenant ainsi la caractéristique la moins intéressante de chaque microstructure. Par conséquent, nous avons recommandé de s'attacher davantage à la morphologie de la perlite plutôt qu'au gradient de microstructure pour l'amélioration du comportement à la fatigue des aciers perlitiques.

Du gradient obtenu en laboratoire au gradient obtenu sur ligne pilote

Enfin, la production d'un acier perlitique avec gradient de microstructure été évaluée par le traitement de deux bobines et d'un fil machine, qui présentaient une couche décarburée d'une épaisseur de 20 micromètres, à l'aide de trois technologies de refroidissement différentes et du tréfilage de ces fils à un diamètre final de 2,25 mm. Cette étude a montré que le gradient décarburé est maintenu après tréfilage et qu'il a doublé la durée de fatigue des fils, démontrant ainsi son intérêt. La microstructure obtenue par les trois différentes technologies de refroidissement n'a présenté aucune différence significative ni sur la microstructure ni sur les propriétés mécaniques.

Aux questions initialement posées pour cette thèse, les réponses apportées sont les suivantes :

1. **Est-il possible de produire un gradient perlitique?**

   Oui, il est possible de produire un gradient de microstructure par des moyens thermiques, perlite fine à la surface et perlite grossière à cœur ou décarbure en surface dans de fils 6,5 mm de diamètre.

2. **La structure de gradient représente-t-elle un avantage par rapport aux fils homogènes?**

   Bien que les aciers perlitiques ave gradient ont montré une bonne aptitude à l'accommodation de la plasticité et à contenir les fissures courtes, leurs performances en terme de durée de vie et de niveaux de contrainte cyclique ne justifient pas leur développement mais ne sont pas une gêne. Aucun apport est nettement observé.

   L'acier avec une couche décarburée présente les mêmes propriétés mécaniques que les fils sans gradient, mais présente une résistance à la fatigue accrue, ce qui est avantageux.

3. **L'épaisseur du gradient peut-elle être contrôlée ? Y a-t-il une épaisseur optimale ?**

   Dans le cas du gradient perlitique, il était très compliqué, voire impossible de contrôler son épaisseur sur des fils de 6,5 mm de diamètre parce que le gradient thermique produit n'est pas assez marqué.

Dans le cas du gradient décarburé, il doit être possible de contrôler son épaisseur mais la couche de 20 micromètres formée sur le fil de 6,5 mmm semble être optimale.

4. **Le tréfilage aide-t-il à renforcer le gradient ?**

   La production de gradients thermomécaniques tend à restreindre la formation du gradient microstructural.

5. **Quelles sont les limites de la production par gradient?**

   La principale limite est le diamètre, qui définit l'étendue du gradient thermique et, par conséquent, la différence marquée entre la transformation formée au cœur et à la surface.

6. **Est-il possible de reproduire une microstructure de gradient par coeur de température en carbone élevé avec des fils de plus petit diamètre? Et contrôler l'épaisseur de la couche de martensite externe?**

   Non, ce n'est pas possible parce que la variation de température entre le début de la transformation martensitique et la température la plus basse à laquelle la perlite peut former sont est trop grade et il ne serait pas possible d'éviter la transformation à cœur. Une version bainitique du tempcore a été tentée, cependant, il n'a pas été possible de garder la transformation seulement près de la surface, et la bainite s'est formée à cœur pour les deux diamètres de 6 et 12 mm.

7. **Peut-il être produit industriellement par le patentage au plomb ? Et en utilisant les technologies de refroidissement alternatives ?**

   La production des gradients est tout à fait possible par des moyens réels de production industrielle, mais cela implique d'ajuster la température au début et à la fin du bain. Les autres technologies de refroidissement ont produit la même microstructure et les mêmes propriétés mécaniques finales que le patentage au plomb, ce qui donne des perspectives positives pour la production de gradients par des technologies de refroidissement alternatives. Et, ce qui concerne les gradients décarburés, il est certainement possible de produire à la fois par le patentage au plomb et par le refroidissement alternatif.

Contents

List of Figures

List of Tables

Nomenclature

α	Ferrite
ΔG	Gibbs free energy
$\Delta\epsilon_e$	Elastic strain
$\Delta\epsilon_p$	Plastic strain
$\Delta\epsilon_t$	Total strain
ϵ	Strain
ϵ_d	Drawing strain
γ	Austenite
$\overline{S}$	Average interlamellar spacing
σ	Stress
$\sigma*$	Effective stress
σ_y	Yield stress
θ	Cementite
Fe_3C	cementite
T_e	Eutectoid temperature
Ac_1	Temperature of the start of the transformation to austenite
Ac_3	Temperature of the end of the austenite transformation
Ac_c	Carbide dissolution temperature
Ae_1	Equilibrium temperature of the ferrite to austenite transformation

Ar_1	Ending transformation temperature during cooling
Ar_3	Temperature of start of the transformation during cooling
Bs	Bainite start temperature
Ms	Martensite start temperature
n	Strain hardening exponent
UTS	Ultimate tensile strength

Acronyms

CHT Continous-Heating-Transformation

PAGS Prior Austenite grain size

STD Standard Transformation Diagram

TTA Time-Temperature-Austenitization

WTD Wire Transformation Diagram

Chapter 1

Introduction

Pearlitic steels are known for their very high tensile strength when highly deformed by drawing, as seen in the steel cords, and also for their widely structural application in construction as reinforcement, as springs, and as bridge cables. They present a hierarchical microstructure composed of ferrite and cementite lamellae. The formation of these lamellae happens by a cooperative growth of both the ferrite and cementite in which the carbon is partitioned between the phases at the transformation interface. The parallel lamellae form the organization called a colony, and all the colonies presenting the same crystallography orientation form a nodule. The space between the ferrite and cementite lamella is considered in practice as the main parameter controlling the mechanical properties of these steels, which even divides the pearlite into two groups: coarse and fine pearlite. The smaller the interlamellar spacing, the harder the pearlite.

Almost 150 years after the discovery of the pearlitic microstructure by Sorby [23], is there still a place to innovate using such a classical material?

An innovative way of improving the mechanical properties of steels is the production of a gradient. Also known for quite a while, but receiving especial attention in the last two decades, the gradients are done usually for simple microstructures, ferritic and austenitic steels, by the introduction of plastic deformation at the surface which creates nanograins at the surface and coarse microstructure in the core. The interesting feature of this type of microstructure is that the mechanical properties obtained are higher than the core or the surface separately, it appears to have a synergy effect when reached the optimized thickness of the external layer.

It is proposed in this Ph.D. work to transpose the microstructural gradient concept

to pearlitic steels intending to improve its already remarkable properties, especially the fatigue behavior, so it can prolong its application time and thus diminish its replacements and maintenance. The gradients in pearlitic steels have already been reported [24] as undesired consequences of the production process, especially for large diameter wires. Understanding how these gradients are formed during the heat treatment and how they behave during the deformation and asking if these gradients can be optimized are some of the strategies of this research project.

Following an industrial production line of pearlitic steels, there are three stages under which the microstructure gradients can be formed: the austenitization, the cooling under a technology called lead patenting, and then the drawing, in this respective order and as shown in Figure 1.1. The patenting is a heat treatment for the production of pearlite done by submerging the wires in a hot lead bath. Since 2018, the European Chemicals Agency has added lead to the REACH Candidate List for authorization as a substance of very high concern. Most of the pearlitic steel wires produced around the world are produced using lead patenting and it is, therefore, of most interest to substitute this heat treatment with other cooling technologies. For the production of the gradients, other cooling modes are considered as an attempt of addressing this issue.

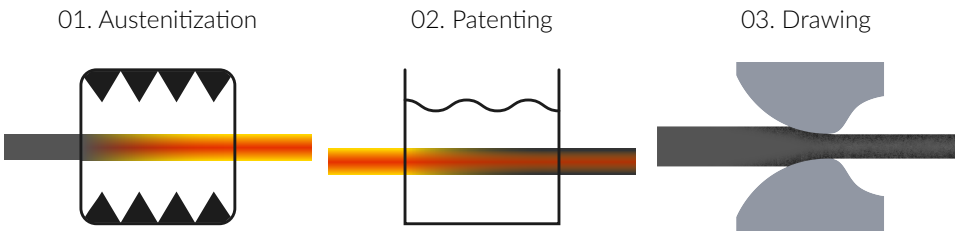

Figure 1.1: Possible steps during the wire production where a gradient can be formed

By the use of an advanced dilatometer to simulate the thermal cycles in lab samples, the phase transformations diagrams of the heating (Time-Temperature-Austenitizing and Continuous-Heating-Transformation diagram) and the cooling (Time-Temperature-Transformation and Continuous-Cooling-Transformation diagram) were assessed to understand the phase transformations of the eutectoid steels and the parameters that affect it. This knowledge builds a background for the characterization of the gradients, which is then assessed by thermal, mechanical, and thermomechanical on wires of a diameter of 6.5 and 12 mm. Then, low cycle fatigue properties of the monolithic and the produced gradients are investigated under low and high strain. Finally, the production of the gradients by the different cooling

technologies is assessed and the obtained mechanical properties after drawing to the 2.25 mm final wire are analyzed.

In short, the basis of this thesis addresses the results concerning the phase transformation during heating and cooling in the 4 mm wires for the eutectoid composition, although the effect of carbon is also investigated, and then the possibilities are enlarged to 6.5 and 12 mm diameter wires. Finally, the response of the 6 mm diameter specimens to cyclic loadings with and without the gradient is investigated.

This thesis was done at UMET (Unité Matériaux Et Transformations) of Centrale Lille Institut & University of Lille in partnership with NV Bekaert SA (Bekaert), which is a world market and technology leader in steel wire transformation and coating technologies, whose Technology Center is located in Deerlijk, Belgium. Proposed by Bekaert, this study was financed by the company and by the Agency for Innovation and Entrepreneurship – VLAIO, a Flemish governmental organization that encourages and supports strategic and industrial research. As a part of a broader project on advanced heat treatment for wire, it attempts to provide solutions to study the effect of the microstructure gradients into big diameter wires during the patenting process to investigate alternatives to the lead-patenting process to be able to fulfill the future environmental legislation and constraints. On this basis, the present research focuses on the understanding of the pearlitic transformation and the parameters that affect it while evaluating its impact on the mechanical properties of pearlitic steels.

1.1 Scope of research

The main objective of this work is to explain how are produced the microstructure gradients in large diameter wires and what are their effects on the final mechanical properties.

This main objective can be split into other specific objectives that address individually each limitation of the process and/or the material. Therefore, a preliminary aim is to investigate and recognize the parameters of the process during the heat treatment that can affect the final microstructure and the final mechanical properties of the wire. Along with the effect of these parameters, it is also intended to explain how chemical composition plays a role.

Next, concentrating on the gradients, it is expected to define the formation

mechanisms of the microstructural gradients produced by thermal, mechanical, and thermomechanical means.

Then, it is expected to have a comprehension of the low cycle fatigue behavior of the gradients and the monolithic specimens considering the stress attained, the fatigue resistance, and plasticity.

The final objective is to assess if the pearlite can be produced by the alternative coolings, evaluate if it is possible to produce a gradient on it, confirm if the gradients are kept after the drawing, and have the effect of the tested heat treatments on the final mechanical properties of the wire.

The main questions that this work intends to answer are listed here below:

1. Is it possible to produce a pearlitic gradient?
2. Does the gradient structure represent an advantage compared to the homogeneous wires?
3. Can the thickness of gradient be controlled? Is there an optimal thickness?
4. Does drawing help to strengthen the gradient?
5. What are the limitations for gradient production?
6. Is it possible to reproduce a gradient microstructure by tempcore in high carbon with smaller diameter wires? And control the thickness of the external martensite layer?
7. Can it be industrially produced by lead patenting? And using the alternative cooling technologies?

1.2 Thesis outline

A variety of wires has to be used to fit with the different purposes and to characterize the various tests conditions. Ergo, they are divided into the four investigation chapters: the phase transformation (4), gradients (5), mechanical tests (6), and pilot tests (7), in which are contemplated different compositions, initial strains, and diameters.

The summary of the thesis organization is as follows:

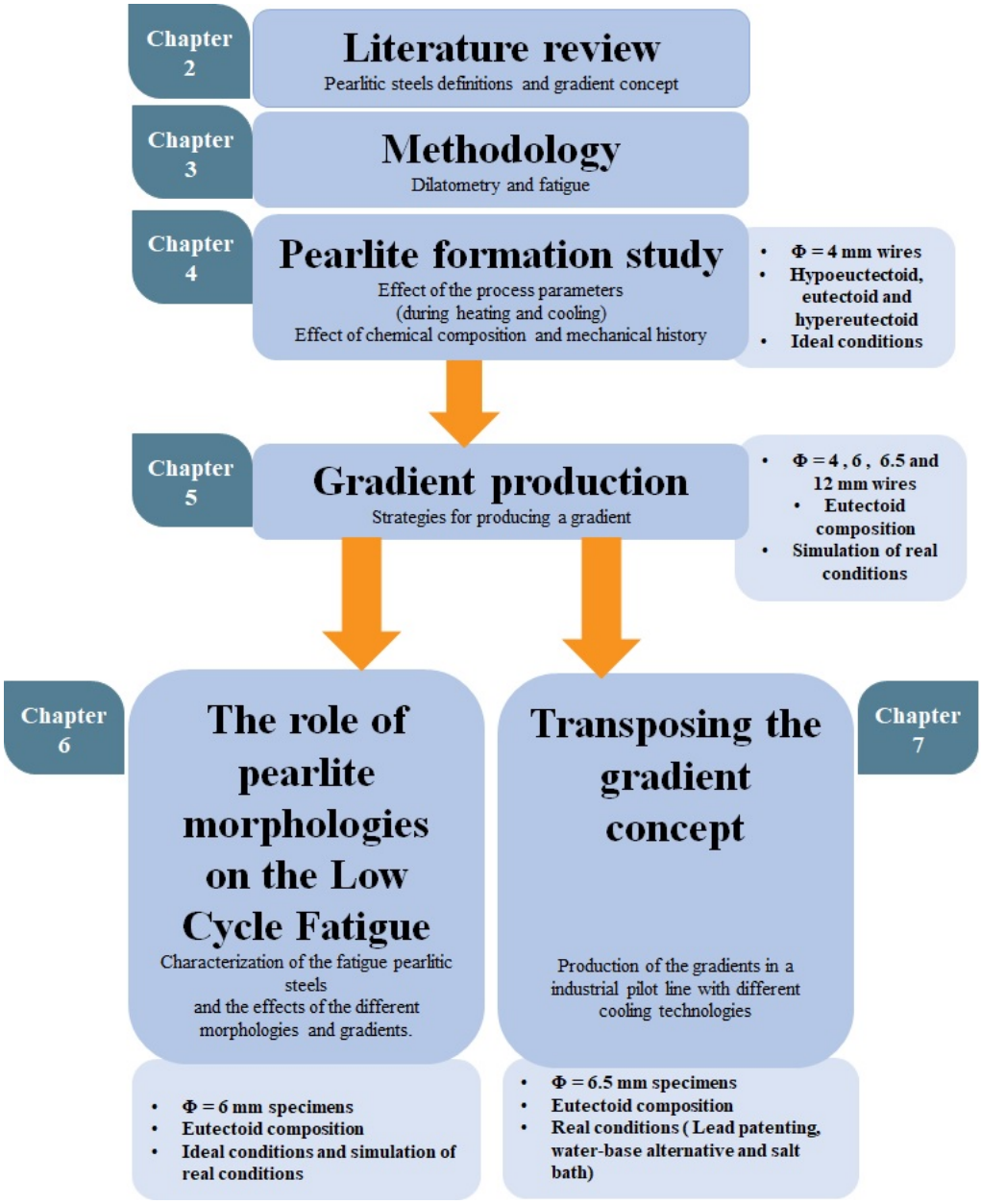
Chapter 2
Literature review
Pearlitic steels definitions and gradient concept
Chapter 3
Methodology
Dilatometry and fatigue
Chapter 4
Pearlite formation study
Effect of the process parameters (during heating and cooling)
Effect of chemical composition and mechanical history
Φ = 4 mm wires
Hypoeuctectoid, eutectoid and hypereutectoid
Ideal conditions
Chapter 5
Gradient production
Strategies for producing a gradient
Φ = 4 , 6 , 6.5 and 12 mm wires
Eutectoid composition
Simulation of real conditions
Chapter 6
The role of pearlite morphologies on the Low Cycle Fatigue
Characterization of the fatigue pearlitic steels and the effects of the different morphologies and gradients.
Φ = 6 mm specimens
Eutectoid composition
Ideal conditions and simulation of real conditions
Transposing the gradient concept
Production of the gradients in a industrial pilot line with different cooling technologies
Φ = 6.5 mm specimens
Eutectoid composition
Real conditions (Lead patenting, water-base alternative and salt bath)
Chapter 7

Chapter 2

Literature review

This chapter will generally review the eutectoid steels, their applications, and the main issues related to their industrial production. Then are revised the basic concepts of pearlitic formation, pearlite morphologies, and their relation with the mechanical properties and fatigue behavior. Finally, the later development of the gradients concepts in steels is highlighted.

2.1 Pearlitic steels

The pearlitic microstructure consists of parallel lamellae of ferrite and cementite that grow by a reconstructive process at temperatures below the austenitic domain. This is a general definition of pearlitic steels, which was first discovered by Sorby, in 1873 [23]. Pearlite is not of a phase but a constituent made of a mixture of two phases.

The pearlite is a product of an eutectoid reaction that, by definition, is a three-phase reaction by which, on cooling, a solid single phase (γ) transforms into two other solid phases at the same time (α and Fe_3C)[1, 10]. Following the $Fe - Fe_3C$ equilibrium diagram, Figure 2.1, this reaction happens at 727 °C at the specific chemical composition of 0.77 wt.%C, called eutectoid temperature (T_e) and eutectoid composition. The formed α phase presents almost no carbon in solid solution while the Fe_3C is very rich in carbon (6.67%C) in the form of carbide, and it gives a proportion of 88% of α to 12 % of Fe_3C. Therefore, it is worth noting that the pearlite is not of a phase, but a bi-phased constituent.

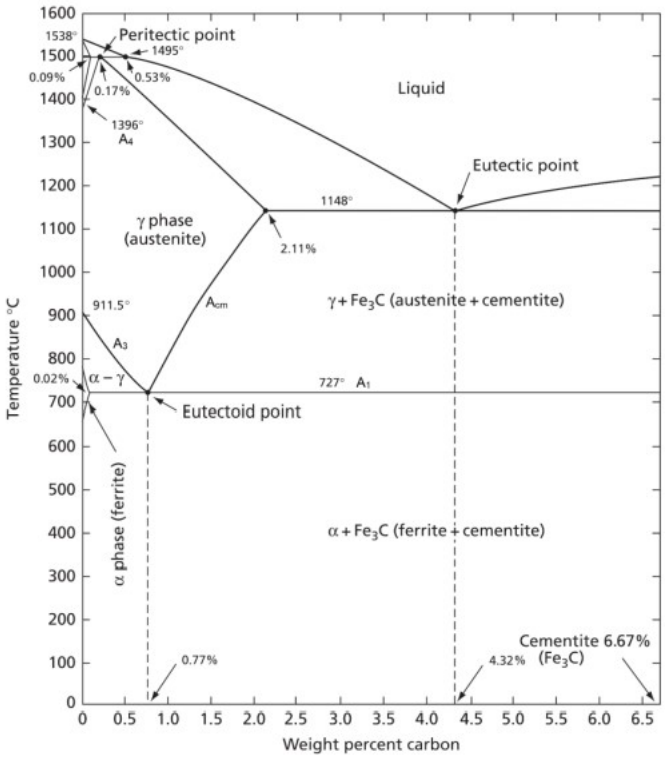

Figure 2.1: The $Fe - Fe_3C$ equilibrium phase diagram [1]

A lower and a higher carbon contents than the eutectoid composition give rise to two other microstructures called hypoeutectoid and hypereutectoid, which are characterized by a mix of pearlite and proeutectoid ferrite and proeutectoid cementite, respectively. The amount of the proeutectoid phases is calculated by a lever rule between the given steel composition ($\overline{C}$), the %C of ferrite, and the eutectoid composition.

The formation of the proeutectoid phases occurs before the pearlitic reaction, as seen in the $Fe - Fe_3C$ diagram, and it takes place at the austenite grain boundaries. The fully pearlitic microstructure and pearlite + proeutectoid ferrite are shown in Figure 2.2a and 2.2b, respectively.

The space between the ferrite and cementite lamellae defines an important parameter of the pearlitic microstructure called interlamellar spacing. When the transformation occurs at very high temperatures, close to the eutectoid temperature (T_e), the obtained interlamellar spacing is large and coarse pearlite is formed. Contrarily, when transformed at lower temperatures, the space is reduced and it is obtained fine pearlite [25, 26, 27].

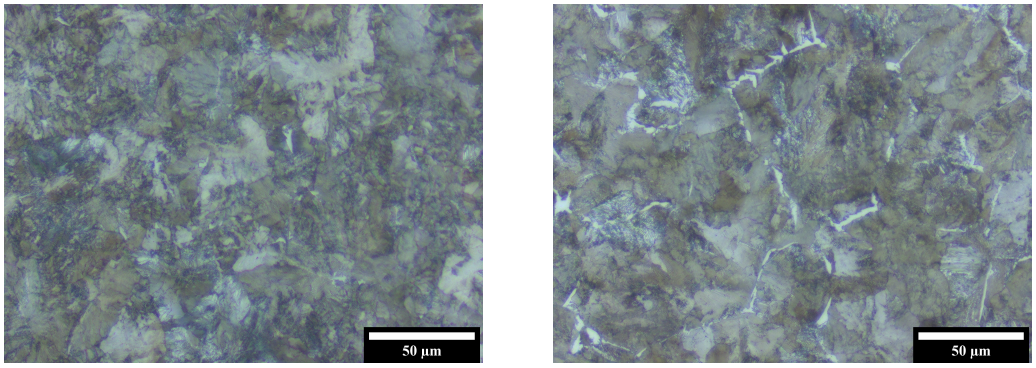

(a) (b)

Figure 2.2: Example of (a) an eutectoid fully pearlitic microstructure and (b) an hypoeuctetoid microstructure with the proeutectoid ferrite at the grain boundaries.

The mechanical properties of the pearlite change greatly from coarse to fine pearlite. It happens because the interlamellar spacing controls the strength of pearlitic steels, which is generally accepted to be used on the calculation of the Hall-Petch relationship [28]. It is thus calculated as follows:

$$\sigma = \sigma_0 + K.\overline{S}^{-\frac{1}{2}} \tag{2.1}$$

where σ is the stress, σ_0 is the friction stress, K is the Hall-Petch constant and $\overline{S}$ is the interlamellar spacing of pearlite. Besides the interlamellar spacing, the carbon content also plays an important role since its increase entails the increase of tensile strength and hardening of the formed pearlitic microstructure [28].

Although the interlamellar spacing is an important feature, the pearlitic microstructure is a complex hierarchical microstructure that presents other organizations at different scales. The interlamellar spacing is at a nanometric scale, ranging from 70 nm to 300 nm. Then all the lamellae that are formed parallel to each other give rise to a next hierarchical level called a colony, which can have from a few microns to a few dozens of microns. And lastly are the nodules that contain several colonies, and by definition it contains all the ferrite and cementite with the same crystallographic orientation [23, 29]. Nodules are the grain-equivalent.

A scheme of the hierarchical distribution of pearlite is shown in Figure 2.3.

The nodule size is known to vary linearly with the prior austenite grain size (PAGS) while the colonies, as the interlamellar spacing, are only dependent on the temperature

of transformation [30, 9, 31]. It is admitted that the nodule does not have a strong effect on the overall mechanical properties, and the colonies control the toughness of pearlitic steels.

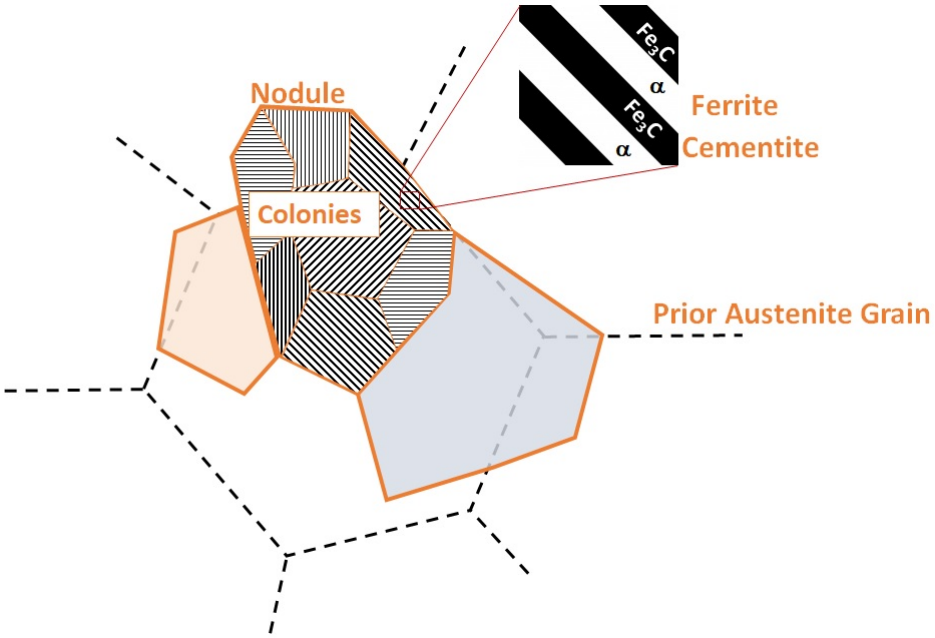

Figure 2.3: Schematic image showing the hierarchical microstructure of a pearlite grain.

The pearlite nucleates at the grain boundaries of the austenite and then it tends to grow towards the adjacent grain that presents an incoherent interface [10]. It is observed in Figure 2.3, in which a nodule is related to two different grains. After it is fully transformed, there is no way to know the original austenitic grain that the pearlite comes from, because it does not have a crystallographic relation with the parent phase such as the martensitic steels. As shown in Figure 2.3, a nodule can be related to several former austenite grains.

These are the main general characteristics of the pearlite and in the next subsections are shown the applications of these microstructures and how they can be obtained by industrial production.

2.1.1 Applications

Pearlitic steels find its main applications relying on its high strength. As a matter of fact, it happens due to the exponential hardening with true strain produced by the drawing [24] observed for the pearlitic microstructure, while the other materials present

a linear hardening. Pearlitic steels actually are the strongest metallic bulk materials, reaching an ultimate tensile strength of 7 GPa when undergoing very high drawing strains (ϵ_d=6.52) in a wire of diameter smaller than 100 µm. [32, 33, 34] This is the case of steel cord that is used for rubber reinforcement.

Pearlitic steels are also used in thicker diameter for structural applications such as concrete reinforcement, springs, bridge cables, and steel ropes. All the mentioned applications require high strength and a certain ductility and certain damage tolerance, which implies that the deformed fine pearlite is mostly implicated. One example is shown in Figure 2.4 which shows a pearlitic cable stayed bridge.

Figure 2.4: Photograph of the Queensferry Crossing a road bridge, in Scotland. With a length of 2.7 km, it incorporates about 37 km of pearlitic cabling, and it is the longest three-tower, cable stayed bridge in the world.

Other applications can be found for less strength demanding applications, such as Champagne cork or Bookbinding wire. These types of consumer goods commercial applications are important and give place to low carbon and coarse pearlite steel wires.

All the above mentioned productions are produced by Bekaert, but the pearlitic microstructure can be used in other markets besides wire applications. The next and one of the most recognized applications is as rails [35, 36], which relies on the high wear resistance of pearlitic steels.

The last one to be mentioned is not related to lamellar pearlite, it is actually related to another morphology of the pearlite that produces spheroids of cementite in a ferritic matrix by a process called spheroidization. Differently from the lamellar pearlite, they are very soft eutectoid steels. This microstructure is mainly used for the production of bearings, in which the soft microstructure is need to allow the machinery, and the

before its final application it is quenched to martensite. [37]

2.1.2 Industrial production

Patenting

In the context of this thesis, the production of pearlitic steel wires for bridge cables is of interest. An example of the manufacturing process is shown in Figure 2.5. It starts from a wire rod, which is subjected to a surface treatment, then the wire passes through a first drawing, it passes by a heat treatment called patenting to restore the deformed pearlite and finally it is drawn again to the final product diameter.

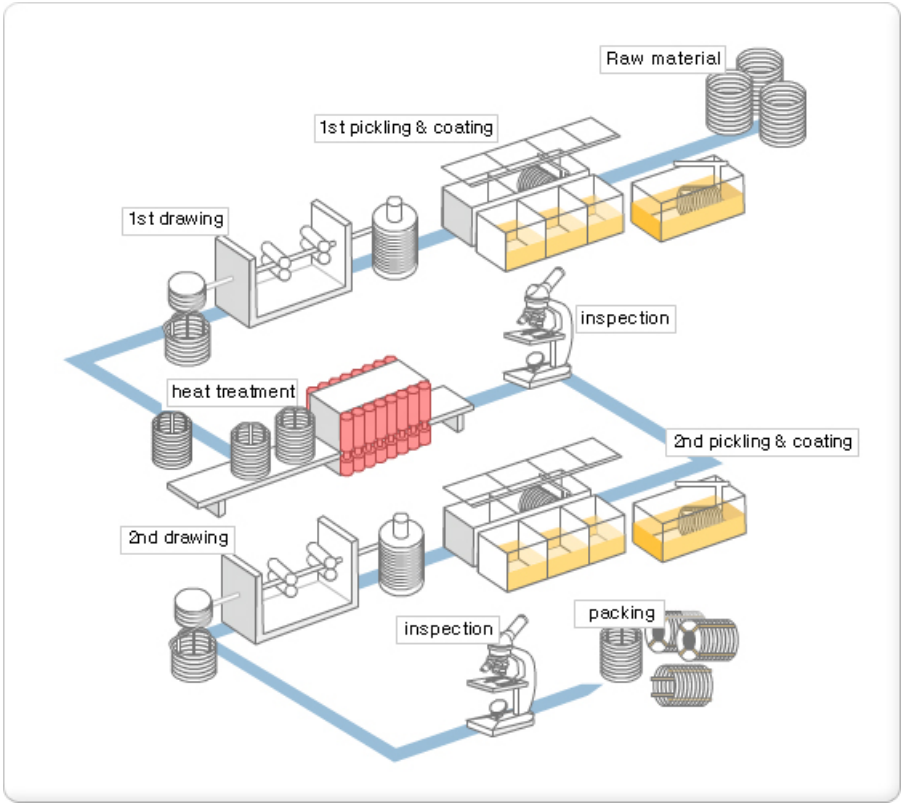

Figure 2.5: Scheme of the typical wire manufacturing processes of pearlitic steel wires.[2]

The step known as patenting, consists in heating the wire to the austenitic domain over a temperature which the austenite is homogeneous, then it is submerged in a hot molten lead bath for the transformation to pearlite to occur and after it, the wire is

cooled to room temperature. This type cooling is assumed to be isotherm and the lead temperature defines the temperature of the transformation, which thus defines whether coarse or fine pearlite will be formed.

The lead patenting is the main cooling technology used worldwide for the production of pearlitic steel wires [38, 39]. However, since 2018, the European Chemicals Agency has added lead to the REACH Candidate List for authorization as a substance of very high concern, besides the already known and documented environmental and health issues related to the lead patenting [40]. As said in reference [40]: " Exposure to environmental lead is clearly a major public health hazard of global dimensions".

Other known submerging technology for producing pearlite is molten salt, [41, 42] which uses nitrate-based and chloride-based salts. Although this technology presents also a high heat extraction as the lead patenting and it is a submerging isotherm cooling, the down side is that it appears to be extremely difficult to use on a industrial scale [43].

Some other alternatives have been developed over the last decades, such as continuous cooling using high-velocity airflow or polymer solution baths [44, 45, 38]. These technologies are able to produce pearlite by continuous cooling, which is a different cooling mode than the lead patenting, and some further investigation on its effects on the final pearlitic microstructure and mechanical properties are still missing.

Drawing

Next step is the drawing, which is a continuous metal forming process under which the wire is pulled through a single or a series of conical dies. As the volume is kept, the decrease in the cross-section has a corresponding increase in the length of the material.

As the wire coils usually come from a hot-rolling process, they present some rust at the surface that is removed by pickling in an acid solution, sulfuric or hydrochloric acid, which is usually followed by a coating of lime, borax, and/or phosphates that apparently works as a lubricant film during drawing [46]. Then the drawing itself is done at room temperature, and that why it is sometimes called cold drawing.

Drawing dies are typically made of diamond or tungsten carbide in the form of inserts or nibs supported in a steel casting piece. The die is constituted of four regions: the entrance zone, a bell-shaped part to funnel the lubricant into the die-wire interfaces;

the deformation zone, a cone-shaped area where the actual reduction in wire diameter occurs; the bearing or land zone, which determines the final size of the drawn wire; and the exit zone, a back relief region. In the process called dry drawing, powdered soaps are introduced in a container before the die entry and coat the die-wire interface when the wire rod passes through it so diminishes the friction forces. In Figure 2.6 is represented one drawing pass.

The critical parameters are die geometry, cross-sectional area reduction, number of passes, drawing speed, and lubricant selection, which are decisive for reaching high quality drawn products with dimensional accuracy and satisfactory surface finish. [47].

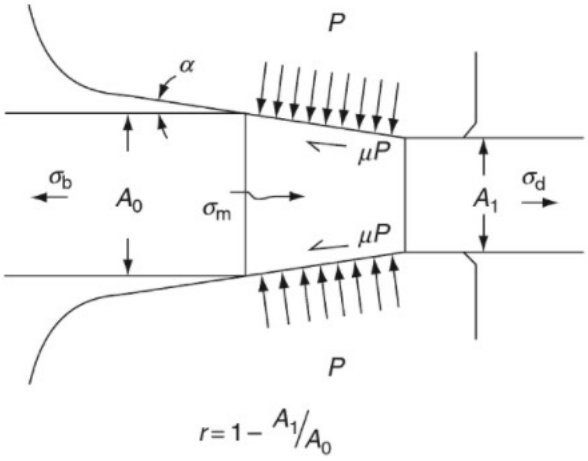

Figure 2.6: Schematic illustration of a drawing pass[3].

The r shown in Figure 2.6 represents the area reduction. The true drawing strain (ϵ_d) can also be calculated during drawing as follows:

$$\epsilon_d = ln(\frac{A_0}{A_1}) = ln(\frac{1}{1-r}) \tag{2.2}$$

During the drawing process, the wire is pulled through the die by a pulling force. The plastic flow of the metal is possible thanks to the combined action of the axial tension force and radial compression imposed by the die. At the die-wire interface, a lateral pressure is imposed by the die due to friction forces. The necessary force to draw the wire is the sum of the necessary force to plastically deform the wire and the force to overcome the friction force. The total work consumed at a draw stand can be partitioned into three components, being the (a) uniform (homogeneous) work required to reduce the cross section without considering the interaction with the die, (b) work

required to overcome frictional resistance, which is the interaction with the die, and (c) redundant (inhomogeneous) that is work required to change the flow direction. These forces are shown in Figure 2.7

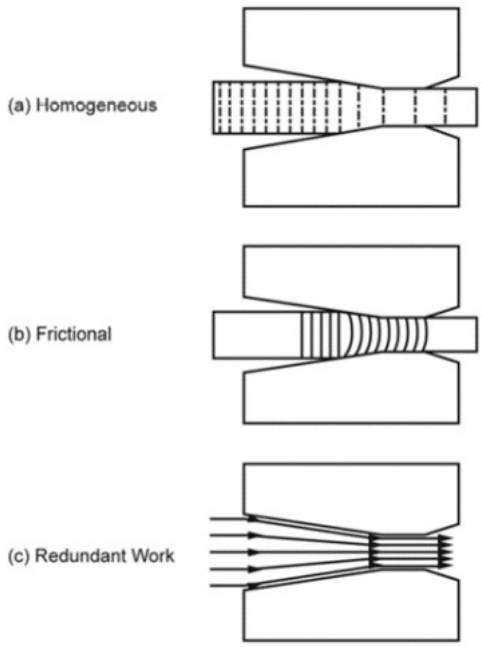

Figure 2.7: Working forces during wire drawing. [3].

Redundant work increases with the increase of the die angle, while the frictional work dominates at low die angles where surface drag is increased as a result of higher contact length in the approach zone for a given reduction, which, in both cases, increases the wire drawing force. Therefore, the optimization of the drawing relays on the optimization of all these forces, which is accomplished by many reduction passes of smaller forces.

The redundant work is responsible of the higher amount of deformation at the surface than in core, which produces a radial strain gradient in the sample. There is a mathematical relation between the area reduction, the die angle α and the semi-die angle (Δ_d) that is defined as the deformation zone. It can be calculated as:

$$\Delta_d \approx (\alpha/r)[1 + (1-r)^{\frac{1}{2}}]^2 \approx 4tan\alpha ln[\frac{1}{(1-r)}] \tag{2.3}$$

From the equation, it is seen that the higher the angle, the higher the deformed zone. This gradient of deformation can, apparently, strengthen the wire in way that is rather noticeable under bending, torsion, threading and annealing operations. [3]

Among the microstructural responses to drawing, the colonies are the ones that rotate to align with the tensile axis and giving the deformation texture, even though the nodules are the gran-equivalent to pearlitic steels [34]. A schematic representation of the lattice rotation is shown in Figure 2.8, in which case the colonies rotate to align the [110] plans with the drawing direction and thus forming the drawing texture [48, 34, 49].

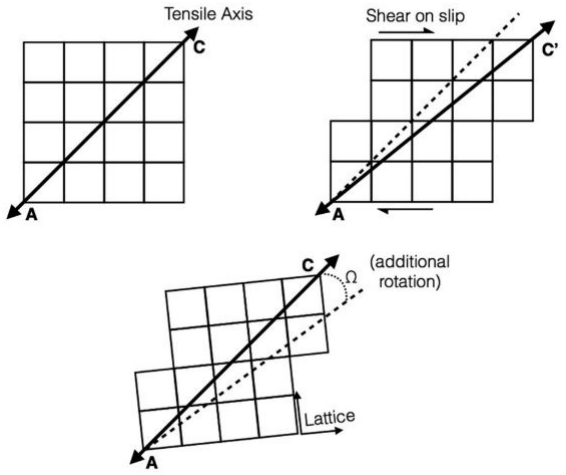

Figure 2.8: Scheme of the formation of the deformation texture in which the grains, the colonies in the case of the pearlite, align with the tensile axis. Extracted from [4]

The drawn wires present some exceptional mechanical properties after drawing [21, 34, 50, 5]. It is been widely investigated why the pearlitic steels present such high tensile properties when severely deformed and it was discovered that the cementite decomposes under high strain and it supersaturates the ferritic lamella in carbon. The distribution of the carbon in the ferritic lamella is shown in Figure 2.9.

The atomic-scale mechanism of deformation-induced cementite decomposition in pearlite says that carbon does not stay in solid solution in ferrite but, instead, it occupies the dislocations walls. It is proven by the fact that the amount of carbon stops decreasing in cementite when the carbon and dislocations starts saturating (at a deformation of about $\epsilon_d = 3.47$ in their study [5]).

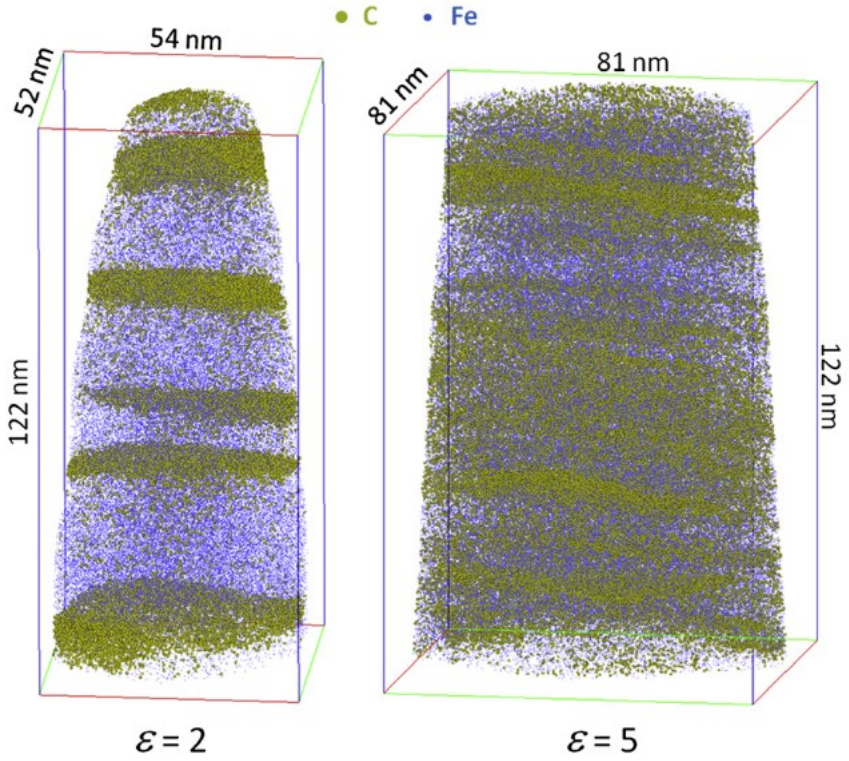

Figure 2.9: 3D atom maps of cold-drawn wires for $\Delta\epsilon_d$= 2 (left) containing roughly 6.8 10^6 atoms within a volume of 54x52x122 nm^3 and $\Delta\epsilon_d = 5$ (right) containing 16.2 106atoms within a volume of 81x81x122 nm^3. For clarity only 2% of the iron (blue) and 20% of the carbon (yellow) atoms are displayed. Extracted from [5].

2.2 Pearlite formation

As shown in the previous sections, the production of the wires comes from an initial pearlitic wire rod that is drawn, subsequently austenitized and then transformed again to pearlite before the final drawing. To have a better understanding of what is happening at microstructural levels, the phase transformation from pearlite to austenite and then from austenite to pearlite are reviewed.

But first, some general consideration about phase transformations are defined. The pearlitic transformation is a reconstructive first order type of transformation, which means that both the parent and the product phase coexist at the transformation temperature and there is flux of atoms across the transformation interface that separate the phases.

The transformation rate will depend on the atomic mobility and the ease of partitioning the atoms ahead of the transformation interface. For the transformation

to happen it must have a gain energy, so both of these processes necessarily dissipate energy. If most of the energy is dissipated while transferring atoms across the interface, it is said to be interface controlled. If most of it is dissipated by diffusing atoms towards/away from the transformation interface, it is said to be diffusion controlled. The concentration profiles between the product and the parent phase will define the kinetics control.[6, 10]

An example of it is shown in Figure 2.10, in which the β phase is growing from the α phase, and $c^{\alpha\beta}$, $c^{\beta\alpha}$ and $\overline{c}$ are the equilibrium concentration α with relation to β, β with relation to α and the average concentration away from the transformation interface, respectively.

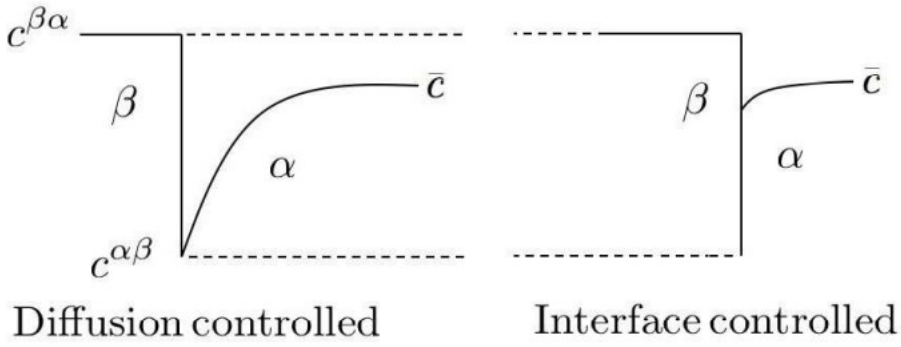

Figure 2.10: Schematic concentration profiles that will define the modes of growth [6]

It is seen that the average concentration in the case of the interface controlled growth is basically the same close of far from the interface, whereas for the diffusion controlled there is a large difference which will oblige some diffusion for the transformation to continue.

Now that these definitions are given, the phase transformation can be discussed.

2.2.1 Pearlite to austenite conversion

The austenitization process is the base of almost all the heat treatments done by the industry. It consists in heating the sample to a temperature completely at the austenitic domain and then transforming to the desired microstructure during cooling. The time, temperature and heating rate can significantly affect the austenitization since it will define grain size and the presence or not of the carbides. Besides, the initial microstructure and its initial state will also influence on these parameters.

There is an agreement in the literature that the transformation from the initial microstructure to austenite happens in three stages: 1) Fast advance of the austenite over the pearlite, which means that the ferrite and cementite are simultaneously consumed, 2) consumption of the proeutectoid ferrite or dissolution of carbides and 3) homogenization of austenite by means of carbon and alloys redistribution. [51, 52, 8]

These stages are dependent on the chemical composition since the transformation to pearlite is interface controlled and for the proeutectoid phases it is diffusion controlled. The dissolution of carbides will also depend on the presence of substitution alloying atoms that will present a lower mobility to diffuse.

Based on these stages it is possible to define the critical transformation temperatures, which some authors change for hypoeutectoid and hypereutectoid steels [8]. For hypoeutectoid, three temperatures can be identified during the heating: Ac_1, A_f, Ac_3, which are the start transformation of pearlite into austenite, the end of the pearlite and then the start the ferrite until complete conversion, respectively. While for hypereutectoid, there are also three temperatures, Ac_1, Ac_3, which are the same the start of the pearlite and end of the pearlitic conversion into austenite, then is the A*cc* temperature, which is carbides dissolution temperature. Ac_1 and Ac_3 temperatures are dependent on the heating rates and if the equilibrium is maintained, the temperatures are then called Ae_1 and Ae_3.

Ac_1 is the temperature that the pearlite starts transforming to austenite. When the initial microstructure has pearlite, the lamellae will transform very fast in the first stage of the transformation, which is the faster one. The dissolution of ferrite and cementite happens simultaneously and cooperatively maintaining the carbon equilibrium on austenite interface. The features that can affect the dissolution rate of pearlite are the colony size and the interlamellar spacing (ILS) [53].

The nucleation of austenite in the pearlite happens on the triple joints of the pearlitic colonies. It has already been shown by some authors that the fourth or triple joints present a higher energy and so, to compensate the creation of a new interface, these nucleation sites are the first ones to be taken [54, 55, 56]. It is shown in Figure 2.11 the main nucleation sites of austenite in pearlite.

The ILS might interferes on the carbon diffusion distance because this distance is dependent on the thickness of the lamellas and it will control the pearlite dissolution rate inside the colonies. The finer the pearlite, the shorter are the diffusion distances for

the carbon, which will entail the uninterrupted equilibrium on the austenite interface so the transformation front can continue to progress quickly.

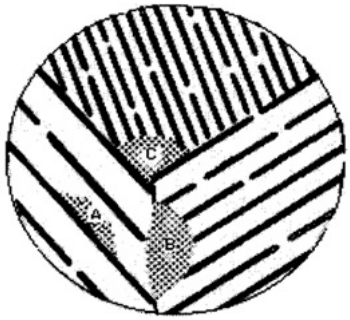

Figure 2.11: Nucleation sites for the austenite in the pearlite. [7]

In the case of spheroidized pearlite, the ferritic matrix is consumed during the first stage and the diffusion of carbon from the carbides to the austenite transformation interface will control the kinetics of the second part of the transformation. The dissolution rate is dependent of the size of the spherical carbides, which are going to provide the carbon to the austenite and allow the transformation to continue.[57]

When the initial microstructure is martensite or bainite, the mechanisms of the transformation and dissolution of carbon are different from the pearlite. There is more carbon trapped in solid solution instead in precipitate form. The laths that compose both structures have very high surface energy, which favours the transformation to austenite, thus also being very fast [8]. For the tempered martensite, it will depend mostly of the carbide size [58].

The Ac_1 can vary with the heating rates [59, 60, 61]. Different authors have shown that with a slow heating there are some changes in the ferrite and cementite during heating before the transformation that lowers Ac_1. It is also known that the fast heating rates, over 100 °C/s, retard the begging of the transformation. This way, the driving force for the transformation is increased and so the nucleation is favoured. As the nucleation is favoured but there is not enough time to the growth, it is expected to have smaller grains.

The Ac_3 temperature defines the end of the transformation, in which the austenite has completely formed but the carbides may have not yet completely dissolved and distribution of solutes is still inhomogeneous. The Ac_3 marks the end of the first stage, which is when all the lamellar pearlite or all the ferrite is transformed to austenite and the slower dissolution will start depending on the equilibrium at the interface of the phase to be dissolved with the austenite.

The last one is the Ac_c temperature, which is the temperature that the carbides have reached the complete dissolution.[8]. It is slower also because there is the diffusion of the alloying elements from the carbides to the austenite; it takes longer to dissolve and to diffuse in the austenitic matrix. It is complicated to define exactly Ac_c and there is no reliable method in the literature to measure it from the dilatometry curve, as it is usually done for Ac_1 and Ac_3. The indirect form to measure it is from the analysis of the martensite or the hardness since both of them vary with the amount of carbon in solid solution and it could help assessing the carbide dissolution during austenitization.

There are many ways to investigate the austenitization process. One method, already enunciated, is by the study of the dilatometry curves where it is possible to track the variations in length with high precision and observe the transformation, so as extracting the information about the Ac_1 and Ac_3 temperatures. It is a very important characterization and it has been widely used [8]. Regarding the microstructure, it is possible to see the effects of a given austenitization cycle on the prior austenite grain size (PAGS), on the grain size distribution and by the presence of undissolved carbides in the cooled microstructure. To make these analysis, it is imperative to do quenching after the austenitization cycle to austenite state.

The diagrams gather the most important information about the heating and the austenitization and it can serve as guide for process parameters. There are two types of diagrams that represent the transformation to austenite and its features, such as carbides dissolution and the regions where it is homogeneous where it is not. They are Time-Temperature-Austenitizing (TTA) and Continuous-Heating Transformation (CHT).

The CHT is a diagram conceived for the continuous heating transformation and it highlights the variations caused by the heating rates. The different times to reach the austenitizing temperatures are reported. It is a guide for continuous heating treatments, especially interesting for industrial cycles that have a short or no holding time. An example of this diagram is shown in Figure 2.12.

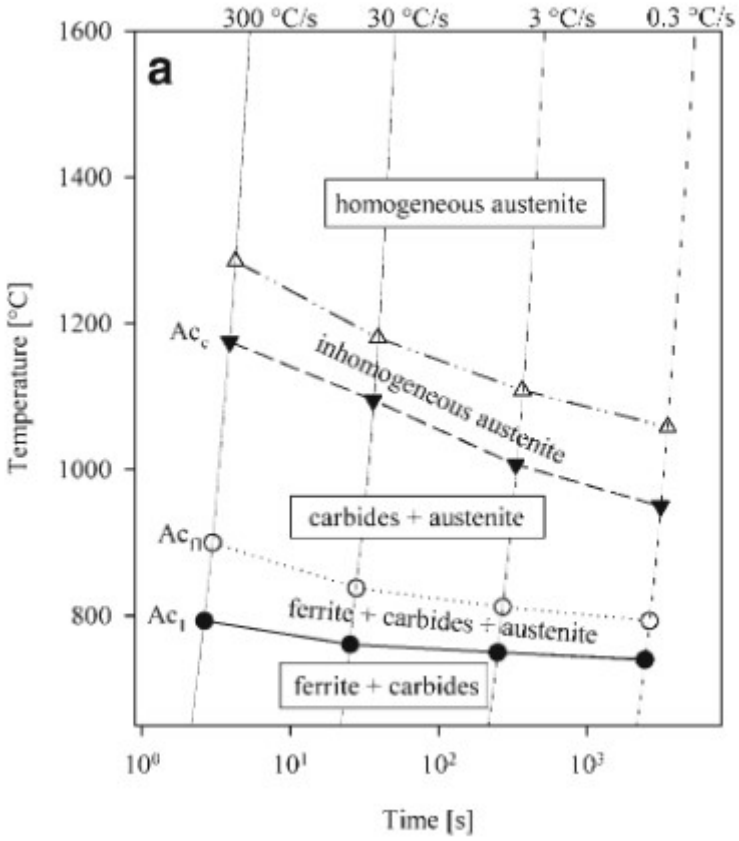

Figure 2.12: Continuous-Heating-Transformation diagram. Extracted from [8]

The TTA diagram emphasizes the effects of time and temperature.

Both diagrams can display the information about the prior austenite grain size (PAGS) and the regions where it is chemically homogeneous or not. The difference is that for the TTA the considered time is a holding time at the austenitizing temperature and it is always the same heating rate, so the time for reaching the austenitizing temperature is not considered [25, 62]. The example of a TTA diagram is shown in Figure 2.13.

Comparing with the cooling diagrams, which are more commonly used in the literature, the CHT diagram would be equivalent to the Continuous-Cooling-Transformation (CCT) one and the TTA follows the same principle as the Time-Temperature-Transformation (TTT) diagram.

Considering the industrial context of this thesis, the knowledge of the short times of austenitizing for industrial production and, depending on the heating system, the continuous heating is more applied to real practice.

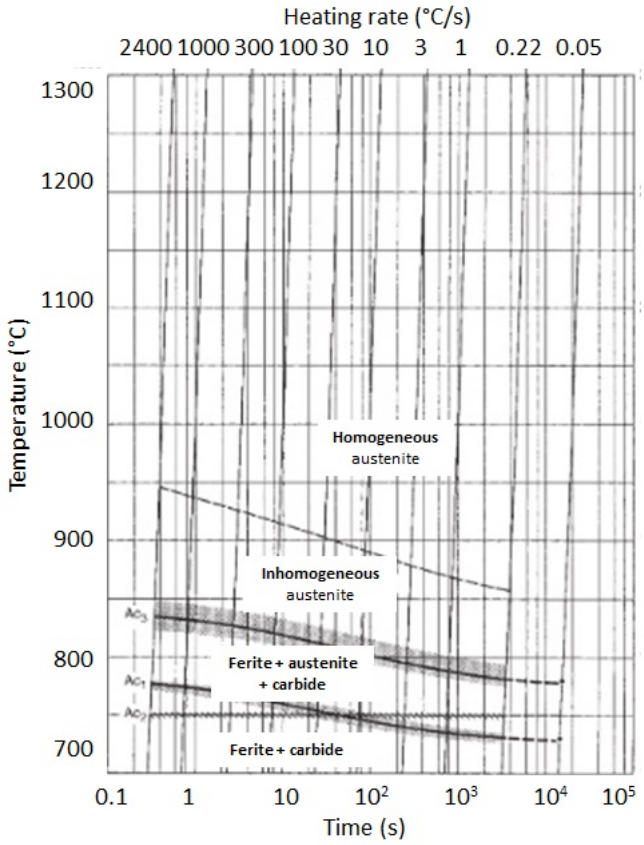

Figure 2.13: Time-Temperature-Austenitizing diagram. Extracted from [8]

There are also many works done using simulation to understand the austenitization process [63, 64], which endures the importance of the knowledge of this transformation.

2.2.2 Austenite to pearlite transformation

The cooling is a decisive part of a thermal cycle because it mainly defines the final microstructure, and thus the final mechanical properties of the product at the end of a heat treatment. Same way as shown for the austenitization process, there are process parameters that affect the cooling transformation, critical temperatures of transformation and diagrams.

The nucleation of pearlite during cooling occurs preferentially at the fourth and triple joints of the austenitic grain boundaries for the same energetic reasons as the austenite. For hypoeutectoid composition, the ferrite nucleates first whereas the cementite nucleates first for the hypereutectoid one. As for the pearlite, the ferrite and cementite are formed, both can serve as the nuclei. By the calculation of the

Gibbs free energy (ΔG), which would be the gain in energy for the the transformation to happen, it was proven that the formation of pearlite would be impossible for a hypereutectoid composition, and the contrary for the hypoeutectoid, while for the eutectoid composition both would have the same energy. [6]

The growing of a pearlitic colony has been a discussion for quite a few years mainly because the modeling of the pearlitic transformation is entirely described neither by diffusion nor interface control growth. Most recently, Pandit and al. have published a very complete work on the theory of the pearlitic transformation where it is proven that it is actually a mixed control [65, 66, 6].

Leaving the kinetics aside, the most accepted mechanism of the pearlitic growth is the one first proposed by Zener-Hillert, in which the pearlite grows in a cooperative manner and the carbon is partionned between the ferrite and the cementite lamella by the interface [67, 10]. In Figure 2.14 is shown an example of the edge growth.

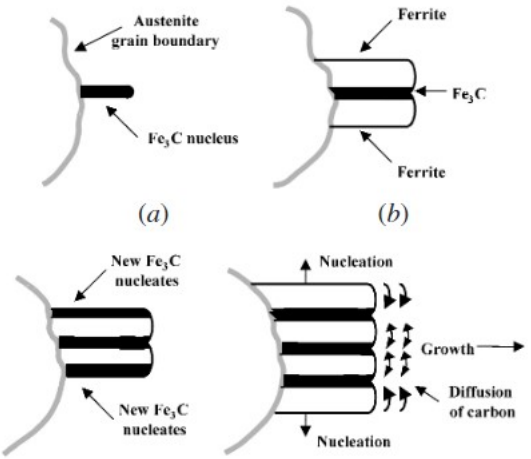

Figure 2.14: Scheme of the edge growth of pearlite. Extracted from [9].

At higher temperatures, the formation of the proeutectoid phases for non fully pearlitic steels happens first. However, with the decrease of the temperature the driving force for the formation of the pearlite is higher than the separated formation of the proeutectoid phases. Therefore, it is not unusual to have hypo or hypereutectoid steels that have completely transformed to pearlite. [10]

The pearlitic microstructure is very complex, which contains a soft phase (α-ferrite) and a hard phase (Fe_3C-cementite). It was previously said that the interlamellar spacing controlling the mechanical properties of pearlitic steels, which is true, however there is also a large contribution of the dislocation density. Apparently the ferrite has a

high amount of geometrically necessary dislocations to contain their inherent difference in crystallographic structures, which creates orientation gradients in the pearlite and contributes to its mechanical properties. [68, 69].

The last important consideration about about the eutectoid transformation is that it might not be lamellar. The spheroidization of the pearlitic microstructure is vastly known and it is a very long heat treatment in which the lamellae become spheroids for diminishing the interface energy of the system [70, 71, 72]. However, if it is shown in the literature that the with the presence of undissolved carbides in the austenite the lamellar transformation can be disfavored, which gives rises to the divorced transformation. An example of divorced transformation is shown in Figure 2.15, and in this case the transformation front advances by the conversion of austenite into ferrite and the carbon diffuses away from the transformation front and it is attached to the previously undissolved carbides. It is seen in Figure 2.15c that there are two regions where the lamellar transformation is favored and another which the divorced transformation is favored. The undercooling, temperature under the eutectoid temperature that the transformation occurs, plays a very important role: the lower the transformation temperature, the lower the chances to have divorced transformation. [65, 73, 74, 75].

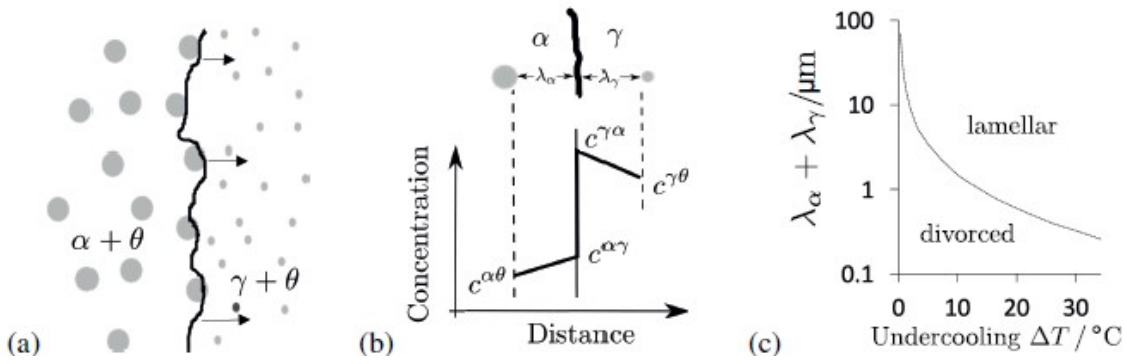

Figure 2.15: Scheme of the divorced transformation with (a) Advance of the ferritic front of transformation into the austenite with undissolved carbides, (b) Carbon concentration profiles in both sides of the interface, and (c) the curve of particle spacing vs undercooling that evidences the conditions where the lamellar transformation is favored and the ones where the divorced transformation is favored. Extracted from [10]

In the dilatometry curve, the transformations are seen in the curve as a change in the expansion. If it is not Bs or Ms as defined before, it can be named as Ar_3 and Ar_1. During the continuous cooling, multiple transformations are often occurring because the transformation does not reach completion. When detected by the dilatometer, as

it is only a small fraction that has formed, it will be seen as small expansions during the cooling [51].

The Time-Transformation-Temperature diagram is widely used to investigate the isotherm transformations. The time in the diagram is counted at the temperature, so it highlights the incubation time for the transformation to happen and the time for the transformation to complete. It is characterized by a C curve, showing longer times for the transformation to happen both at high and lower temperatures with an optimal point at the middle. This shape is related to the kinetics of the transformation that, at high temperatures does not have a high driving force for the transformation to happen, so the incubation time and transformation are long. At lower temperatures the driving force is high but the atoms do not have high mobility, therefore, the transformation occurs more slowly. The optimal point is a combination of the atomic mobility and driving force. [25]. An example of a TTT diagram is shown in Figure 2.16.

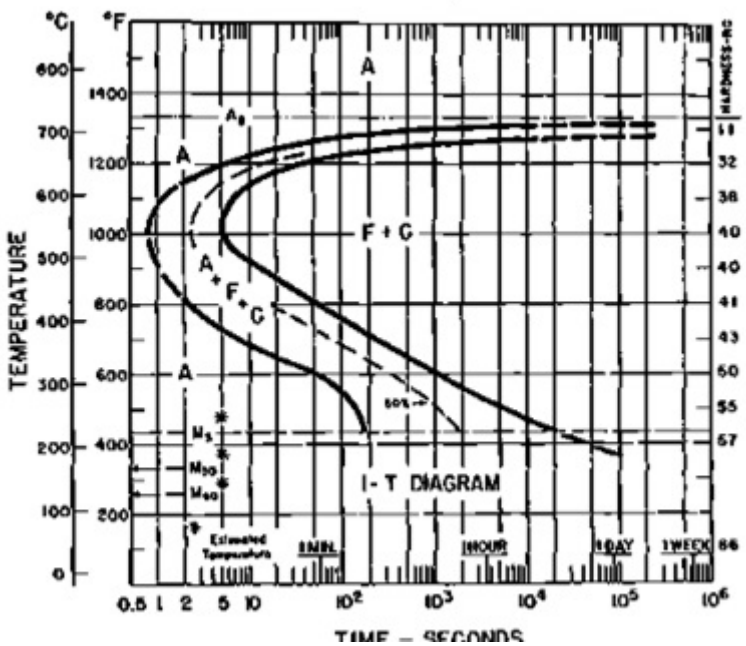

Figure 2.16: Time-Temperature-Transformation diagram of a 0.8%C steel. Extracted from [11]

The analysis of the kinetics of phase transformation during isotherm transformation is done by means of the the S curves, which is a plot of the fraction transformed with time. These curves are used to build the TTT diagram since it is from them that are taken the 1 and 99% of the transformation.

The Continuous-Cooling-Transformation diagram is suitable for the analysis of continuous cooling process since it points up the effect of the different cooling rates in

the final microstructure. There are authors that use the TTT to analyse continuous cooling treatments using a kind of data exportation of the TTT to build a CCT [41]. An example of a CCT diagram is presented in Figure 2.17.

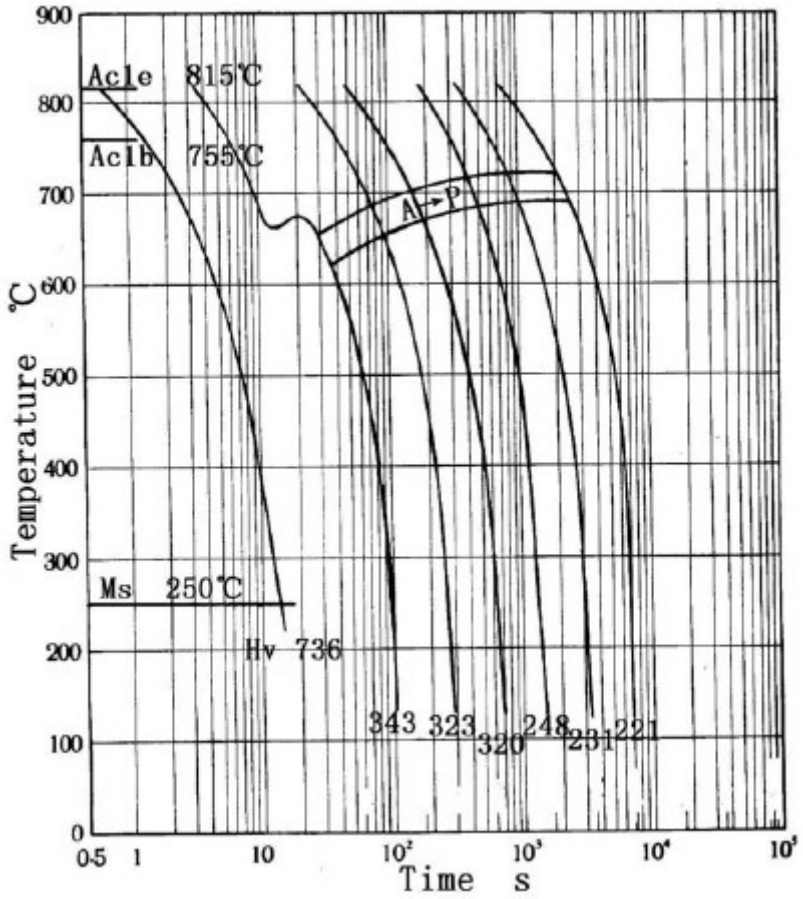

Figure 2.17: Continuous-Cooling-Transformation diagram of a 1%C. Extracted from [12]

It was presented in this section the characteristics of the cooling transformations and its diagrams. The established concepts will represent the essential background to understand the phase transformation during cooling and also to sustain and elucidate the results' discussion.

2.3 Mechanical properties and fatigue behavior

The mechanical properties of pearlitic steels, as previously mentioned, are basically controlled by the interlamellar spacing [28, 14], in which the yield strength increases with decreasing interlamellar spacing following a Hall–Petch type relationship. Figure

2.18 shows the variation of yield strength and the ultimate tensile strength with the interlamellar spacing.

The strain hardening exponent increases sharply with the increase in interlamellar spacing up to a critical value (280 nm), above which further increases in the interlamellar spacing result in no substantial increase in the strain hardening exponent [76, 14].

The colonies have also an impact in the mechanical properties, being the toughness of pearlitic steels dependent of the colony size, which varies with the interlamellar spacing. [77, 31].

The pearlitic steels are also known to present excellent torsion properties [78, 79] especially after drawing.

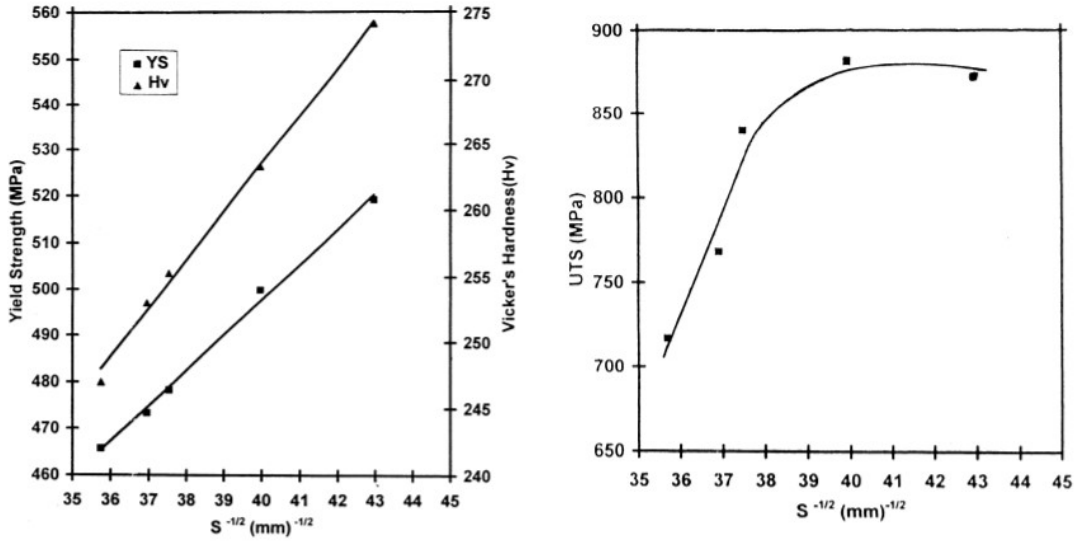

(a) (b)

Figure 2.18: (a) Hardness, yield strength and (b) ultimate tensile strength variation with inverse of the square root of the interlamellar spacing. Extracted from [13]

Although they present ductile fracture under tensile test conditions, during fatigue it presents a brittle fracture [80, 31, 14]. It happens due to the low toughness of pearlitic steels. As the fatigue propagation starts a crack at the surface, as soon as the crack reaches a critical size the specimen fractures. Because of the low toughness, this crack size is very small and it gives rise to brittle fracture in which the crack propagates under in trans-colonial and trans-lamellar path [81]. In Figure 2.19 is seen an example of the fracture surface of pearlitic steels after fatigue test.

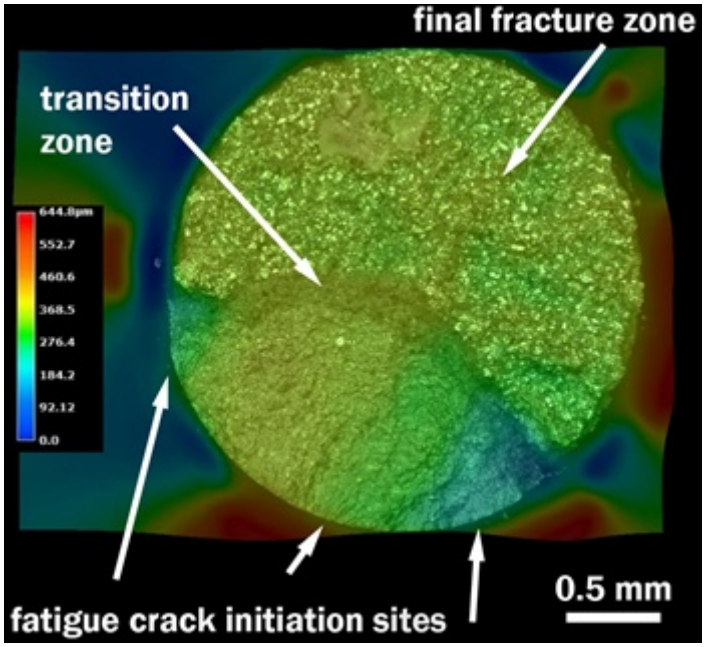

Figure 2.19: Overview of the fracture surface images by digital optical microscopy of a coarse pearlite steel after fatigue at $\Delta\epsilon_t = 1.2\%$ Extracted from [14]

This steel has a yield stress (σ_y) of about 1750 MPa and an ultimate tensile strength (UTS) of 1860 MPa, which is a considerable high strain which can be mostly attributed to the interlamellar spacing and the mechanical and the high carbon of the eutectoid composition. The fatigue behavior of pearlitic steels is affected by the interlamellar spacing [14], in which the stress levels are elevated for the fine pearlite but it presents a lower fatigue resistance, while the coarse pearlite presents a enhanced fatigue resistance and lower stress values.

However the fatigue behavior is of most interest considering all the pearlitic applications, there are not much work on the literature about the fatigue behavior of pearlitic steels. Toribio et al. have done some progress on the knowledge [31, 80, 82] of the fatigue properties but it is need some further studies on the acting mechanism, specially for low cycle fatigue (LCF).

Very few results are available on the LCF of pearlitic steels. In a preliminary study done in UMET in cooperation with Bekaert, it has been already pointed out the role of the interlamellar spacing on the stress response to strain cycling and on the fatigue resistance of a fully pearlitic steels. Examples of the Manson-Coffin curve and the cyclic accommodation of pearlitic steels are shown in Figure 2.20.

Previously were shown the analysis of the fatigue curve, now are reviewed the microstructural response to the fatigue tests. [83]

During the fatigue cycling there are some activity of the dislocations inside the material, which can organize into persistent slip bands and they can later egress on the surface and produce specific slip pattern composed of persistent slip marks. This is an explanation of the formation of the surface relief marks in simple microstructures materials such as austenitic or ferritic steels [83].

The surface relief marks are formed as consequence of intense dislocation slipping, which thus indicates that its formations are related to the enhanced plasticity of the material.

Together with the extrusions are formed the intrusions. They are formed in pairs, which respects the mass balance. These intrusions are precursor the the small cracks.The ease of the formation of these extrusion/intrusion pairs and the ease in evolving the intrusions into larger cracks, are controlled by the cyclic accommodation mechanisms.

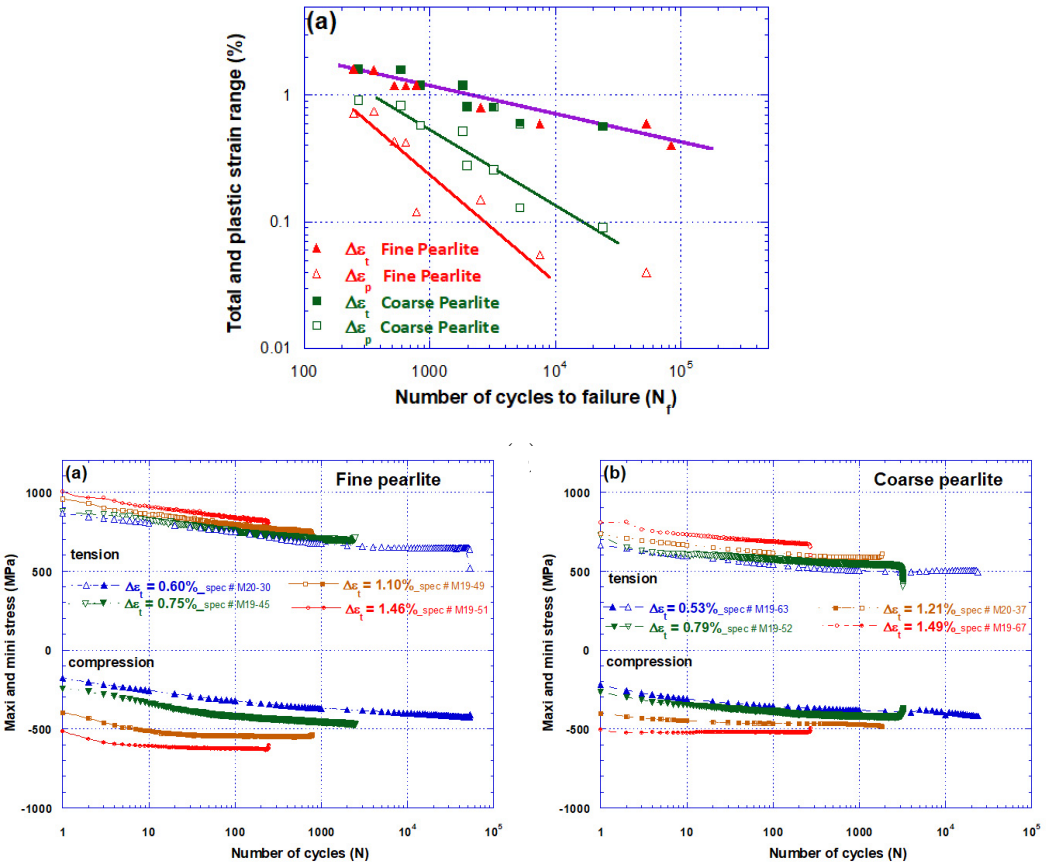

(b) (c)

Figure 2.20: Cyclic accommodation curve and fatigue resistance curve analyzed by the Manson-Coffin diagram [14]

An example of how the extrusions look like on the surface of pearlitic steels is seen in Figure 2.21.

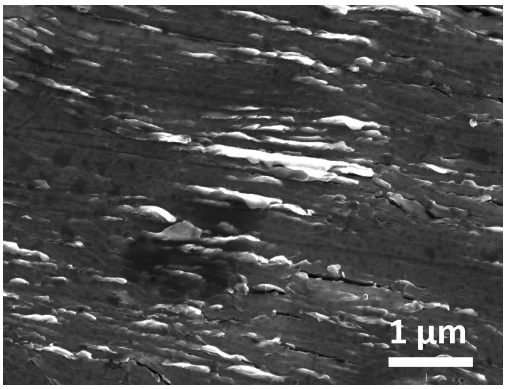

Figure 2.21: Extrusions formed on the surface of fine pearlite pearlite specimen tested at $\Delta\epsilon_t$=1.2%. Extracted from: [14]

2.4 Gradient steels concept

The production of a microstructure gradient as the attempt to evade the trade-off of strength-ductility has been present in the literature for several years. More recently, the so-called gradient structures (GS) concept has been explored with wide range of works and most of them were exploited to austenitic or low carbon steels. The gradient is introduced in the material by means of high deformation at the surface, in which the external deformed layer usually evolved into a nanograined structure, introduces compression forces and deformation gradients from the surface that are capable of increasing the strain hardening.[84] An example of it is shown in Figure 1. Different authors have proved that the gradient structure can effectively increase the mechanical properties responses compared to the homogeneous ones.[85, 86, 87, 88].

The main methods to produce the GS in the literature are surface mechanical attrition treatment (SMAT) and shot-peening, which are both methods to introduce high deformation at the surface creating a hard grained-refined layer while keeping the coarse core. [89, 90, 91].

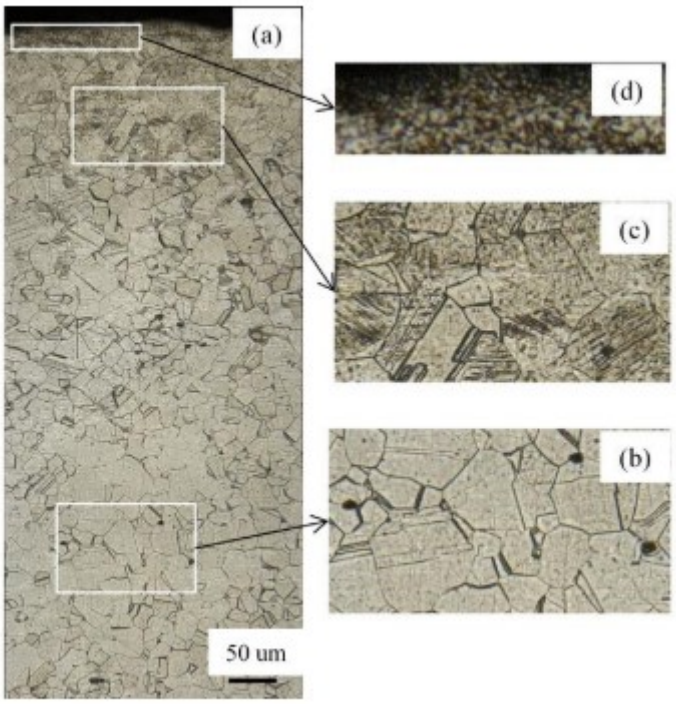

Figure 2.22: Gradient in an austenitic stainless steel done with shot-peening treatment is performed with the air blast shot-peening machine using the impact. Extracted from [15]

In more complex microstructures there are less works on the production of the gradient. A relevant work to be pointed out is the one done on the austenitic steels that proposes a multi-hierarchical hierarchical gradients, with the presence of structurally introducing sandwich structures at both the macro- and nano-scales, the latter via an isometric, alternating, dual-phase crystal phases comprising nano-band austenite and nano-lamellar martensite. [92]. However, this gradient is still done by the introduction of plastic deformation at the surface and plays with the grain sizes among other the hierarchical strain introduced responses.

There is one heat treatment for the pearlitic steels that is produced by thermal means in which is explored the variations in the cooling path to produce the gradients. This heat treatment is a patent called Tempcore [16].

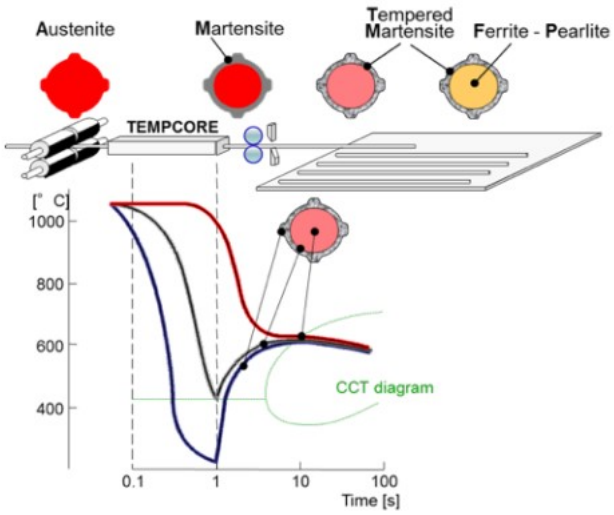

Figure 2.23: Schematic drawing of the Tempcore process. [16]

The Tempcored product is composed of a pearlitic core and a martensitic surface gradient idealized for the production of rebars.In most cases, it concerns steels with a maximum of 0.5%C and it is mainly suitable for very large diameters after the hot rolling.[16] Although, there were some authors that have done tempcore in 8 mm and 12 mm diameter bars [93, 94].

There is also a gradient called delayed quenching, in which the process results in pearlite at the surface and martensite in the core. It is done with discontinuous change of the cooling rate, first producing pearlite then rapidly quenching to form martensite. It is presented as an alternative to tempered martensite and it actually goes in the opposite direction of all the gradient structured materials presented in the literature that bet on a harder surface and a softer core. The other works have presented many arguments that support the improvement in the mechanical properties and the fatigue resistance by introducing a hard deformed layer [88, 85]. This inverse gradient is said to give the best impact toughness, bending fatigue tests with a significant increase of the fatigue life in comparison with tempered non-graded specimens.[95] Yet, there are not much papers to support it and the results are compared to tempered martensite and not so much compared to pearlite.

The gradients of fine pearlite at the surface and coarse pearlite in the core have already been reported, but it was never explored in way to improve the mechanical properties response [30]. So, the production of a pearlitic gradient with this objective is innovative and no records of it were found in the literature.

Some of the works about gradient structure argue that the improvement of the

mechanical properties is limited to a certain thickness of the most external layer of the gradient [87, 86]. Which means that the thickness of the gradient is of great import to reach the synergy between the core and surface properties.

In the case of pearlitic steel wires, it is worth recaping that the drawing process already introduces a non-homogeneous deformation in the wire, since there are more dislocations closer to the surface than the core. It can strengthen the formed gradient, connected with the approach already used by other authors [3].

Chapter 3

Methodology

In this chapter are described the methods used for the study of the phase transformation and the assessment of the gradient production. The dilatometer is the main characterization technique that is used all through the thesis.

In each chapter is specified the used material and the experimental approach, so in this chapter are only shown the general considerations of the techniques.

3.1 Dilatometry

The dilatometer is a precision thermo-simulator instrument for the measurement of dimensional changes in material as a function of temperature. From the dilatometry curve can be extracted a variety of information, including linear thermal expansion, coefficient of thermal expansion, phase transitions, density change, anisotropic behavior and texture evolution. Depending on the extensions added to this equipment it can be divided into different types of dilatometer, such as: quenching dilatometer, high precision dilatometer and quenching & deformation dilatometer, which can perform tension and compression [96].

There are also different dilatometer apparatus that differs by their heating system: induction or resistance heating. The dilatometer in Bekaert is a quenching dilatometer DIL-805, shown in Figure 3.1, from TA instruments, equipped with induction an heating.

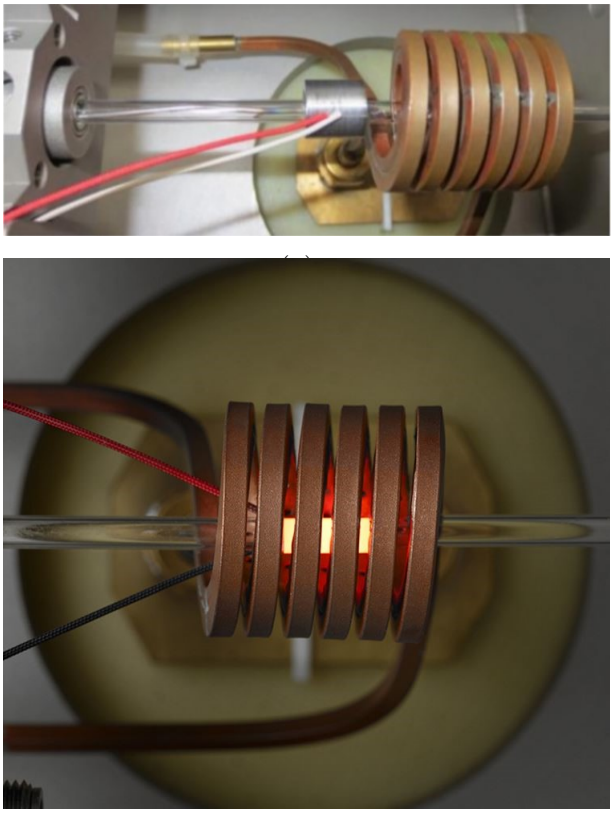

(b)

Figure 3.1: Photos of the dilatometer available at Bekaert with different coil sizes. (a) shows the coil used for thicker diameters with the special feature for measuring the temperature in the core of the sample and (b) standard for 4/5 mm diameter specimen.

It can measure both the change in length or diameter. The displacement in length is measured by the contact of the specimen with the push-rods, that produce the mechanical motions, and the Linear Variable Differential Transformer (LVDT) sensor converts it to electric signals. The diameter is measured by a non-contact system in which a light beam emitted by LED in the sample then it is converted by an optical charge coupled device (CCD) sensor to electrical charges.[96]

The present dilatometer presents a resolution of 0.01 µm in the measurement of the length variation and 0.03 µm when measuring the diameter. The temperature precision is 0.05 °C and it can range from -150 °C to 1300 °C on hollow samples and 20 °C to 1700 °C on solid cylindrical samples.

Following the recommendation of the ASTM 1033-18 [97], (Pt-Rh)-Pt thermocouples (R or S) were welded on the surface of the sample. For the especial case of the large diameter samples, a hole is drilled in the depth of the cylindrical specimen where the second thermocouple is inserted. This assembly allows controlling

the variations in temperature both at the surface and in the core. The test environment is vacuum.

In the calibration cycle, the test specimen should be first heated to 1000 ± 5 °C, with a nominal rate of 1 °C/s, held for 60 s and then cooled at 1 °C/s to room temperature. This procedure is followed by a second cycle that consists in heating to 1000 ± 5 °C, with a nominal rate of 10 °C/s and then cooled at 10 °C/s to room temperature. The standard recommends a high purity nickel to be used as reference material. In Bekaert a platinum sample is used and, as its thermal expansion data has already been documented, it is still in agreement with the standard.

The dilatometer used in this research had two special features that were exclusively design for this work: two size coils, for allowing the analysis of larger diameter (until 22 mm); and it can measure the temperature in the core of the sample. As seen in Figure 3.1b, there is a thermocouple welded to the surface, and another one inserted in the core of the sample. For that, the samples had to have a a drilling hole with a diameter of 1 mm and, approximately, 5 mm deep. In this way, it can measure the temperature both at the surface and the core and the thermal gradients can be tracked.

3.1.1 Dilatometry analysis

The dilatometry test records the variations in length or diameter with the temperature and time. It can give valuable information about the phase transformations for a determined thermal cycle, as previously mentioned.

There are three main causes for the change in length for polycrystalline material: (I) thermal expansion, (II) variation of composition of the phases and (III) the variation due to phase transformation [98, 99, 100], being (I) and (III) the most relevant for the determination of the phase transformation diagrams. The first one appears in the dilatometry curve as a straight line since the expansion varies linearly with the temperature, and the slope is thermal expansion coefficient, which is dependent on the composition and the crystalline arrangement. The cementite, however, presents a ferromagnetic phase transition at $T_c = 480$ K, that affects the expansion coefficient. The expansion coefficient below T_c is much lower than above ($4.1 \times 10^{-5} K^{-1}$ versus $< 1.8 \times 10^{-5} K^{-1}$), which produces a variation in the dilatometry curve at about 200 °C. [101].

The second case can be defined as the lattice parameters since they are composition-dependent. Indeed, depending on the solubility of an element in solid solution, which varies with the temperature, the number of atoms that fit in phase can change and the corresponding lattice parameter will have a different size. For example, precipitation, dissolution or any change in the morphology combined with a local change in composition can have an impact on the curve. This kind of change is seen in the curve as a change in the linear behaviour of the curve, as if it was possible to define two slopes with slightly different inclinations. [102]. Some other deviation of the linear behaviour during heating can be observed and might not be related to this variation of composition. Some authors have shown that they often considered as anomalies, which can be attributed to the annihilation of defects, such as recovery, recrystallization, and to texture evolution.[103, 104]

And the last one is a result of a new crystalline arrangement. In the case of steels, the change of the austenite with the face centred cubic arrangement (FCC) to ferrite with the body cubic arrangement (BCC) appears as a big expansion at a determined temperature during cooling. The FCC phase is denser than the BCC one and, when the transformation from austenite to ferrite starts, it expands to fit the same number of atoms in the new phase arrangement [98, 99, 100, 105].

The knowledge of the dilatometry curve is the first step to allow more complex analysis. In the context of this work, the most useful information that can be extracted from the dilatometry curve are the temperatures of start and end of phase transformation. For the steels, Ac_1 and Ac_3 were shown to be critical transformation temperature during heating and Ar_3, Ar_1, martensite start temperature (Ms) and the bainite start temperature (Bs) are for the cooling. These temperatures are function of the heating or cooling rate and its accuracy is dependent on the method of data extraction. [99, 98]

In the dilatometry curve, Ac_1 is the start of the transformation seeing in the curve as a big contraction in the curve, which happens due to contraction of the BCC structure to the FCC. The end of stage one, defined as Ac_3, is also well defined as the end of this big contraction and the begging of a more linear behaviour but it only ends when the curve starts being complete linear. That means that transformation has reached the end and the only phenomena happening is the thermal expansion of the austenite.

A peculiar example of phase transformation is the bainitic transformation, in which the dilation follows a S-curve type typical of reconstructive transformation, the strain

remains stable and no more transformation is visually detected after the end of the thermal cycle. It would indicate that the transformation has reached completion, however, the austenite has completely transformed. It is, in fact, a multiphase product: bainite and austenite, both stable at room temperature. The later might precipitate and the final microstructure will be bainite and carbides. Either way, it happens because of the incomplete bainite formation, which means that the level rule could not be applyied because it does not vary from 0 to 100 %. Therefore, the transformation to bainite is always a multiphase transformation that must be carefully analysed.[106, 99, 107]

There is a standard ASTM (A1033-18)[97] that defines the practice for quantitative measurements and a procedure to determine phase transformation diagrams of hypoeutectoid carbon and low-alloy steels. It also gives details about the specimens' characteristics, the type of dilatometer, so as its specific calibration, the procedures for analysing the dilatometry and for the construction of both isotherm and continuous cooling transformation diagrams.

The microstructural characterization, such as microscopy and hardness, is complementary and necessary to confirm the dilatometry measurements and provide a quantitative analysis of the transformations. There are many methods described in the literature for analysing the dilatometry data and the data extraction is decisive for the accuracy of the measurements in the dilatometer. To assess the best method analysis, some of the most popular methods are described below.

The lever rule

This method is the most widely used and the literature about it is very rich. It is often used as a standard method and all the other methods reliability are compared to the lever rule. This method consists in a mathematical manipulation of the curve in which two segments, one from the thermal expansion of the austenite and another from the thermal expansion of pearlite giving AB and CD indicated in Figure 3.2. These segments are then extrapolated creating two tangents. These tangents are used to calculate the fraction transformed by the expression $fp = (Y - AB_{extrapolated})/(CD_{extrapolated} - AB_{extrapolated})$, being Y the change in ΔL/L0 value. The critical temperatures of the start and the end of the transformation were defined as 1 and 99 % of the fraction transformed, respectively. [31], [32], [38]

It is an effective analysis, although it has some uncertainties at the start and the end of the transformation temperatures. This method is suitable for one phase transformation during continuous heating or cooling, or for isotherm cycles as long as the parent phase fully converts into the product phase.

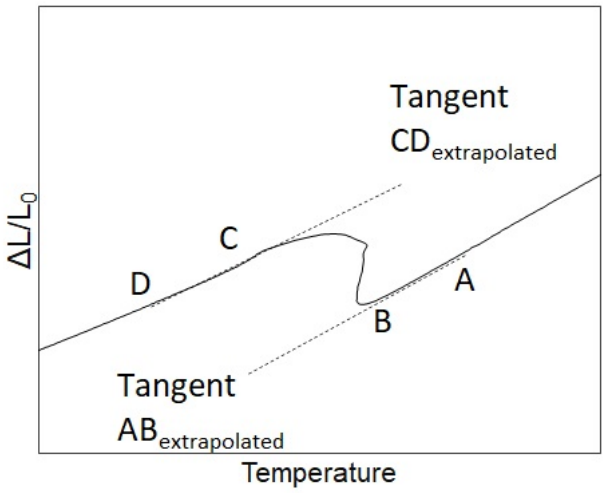

Figure 3.2: Lever rule application example. AB are related to the cooling of the austenite and CD to the cooling of pearlite.

ASTM standard 1033-18

The method recommended in the ASTM for the continuous cooling curve analysis assumes that the progress of the transformation is linearly dependent on the strain and the formation of the microstructure constituent is estimated from inflections in the slope of the cooling. The method used for estimating the progress of the austenite transformation involves the constructions of constant percent transformed and to plot these lines, it is first calculated the difference between the heating and the cooling curve for each temperature. For this method, the progress is considered to be linear and the original heating line would give dilation for the 100% transformed. So, the extrapolated linear fit of the austenite cooling plus the difference valued calculated multiplied by the desired fraction, 10%, 50% or 75%, should provide the line that intercepts with the dilatometry curve on the time and temperature correspondent to the percentage transformed.[97] It is mentioned that this method can be applied for multiple transformation.

It is not clearly described in the standard how to define the temperature of start and end of the transformations, it is only mentioned that it is observed by the inflection,

which is very subjective. The standard also mentions that the diagram is only a quantitative guide and the lines estimate the austenite fraction transformation, which not necessarily indicate the final volume fraction. The metallographic analysis is recommended to determine the relative amounts of various microstructure constituents.

OFFSET method

The offset method is proposed by Bhadeshia et al.[98] as a method to analyse phase transformation from austenite to martensite. It calculates the offset due to the formation of 1% of martensite. The principle should be valid for all kinds of transformation if the strain related to 1% of the new phase is calculated.

The calculation starts defining the offset strain ϵ_0 that is a function of the lattice parameter of austenite, ferrite and the chosen volume transformed as shown in the equations 3.1. to 3.4.

$$(1+\epsilon_0)^3 = a_\gamma^{-3}[2Va_\alpha^3 + (1-V)a_\gamma^3] \tag{3.1}$$

$$\begin{aligned} a_\alpha = {} & \frac{0.28664 + [(a_\alpha - 0.0279x_C^\alpha)^2(a_{Fe} + 0.2496x_C^\alpha) - a_{Fe}^3]}{3(a^2)_{Fe}} - 0.003x_{Si}^\alpha \\ & + 0.006x_{Mn}^\alpha + 0.007x_{Ni}^\alpha + 0.031x_{Mo}^\alpha + 0.005x_{Cr}^\alpha + 0.0096x_V^\alpha \end{aligned} \tag{3.2}$$

$$a_\gamma = 0.03573 + \sum_{(i=1)}^{n} C_i w_i^\gamma \tag{3.3}$$

$$\begin{aligned} \sum_{(i=1)}^{n} C_i w_i^\gamma = {} & 3.3\times10^{-1}w_C^\gamma + 9.5\times10^{-3}w_{Mn}^\gamma - 2\times10^{-3}w_{Ni}^\gamma \\ & + 6\times10^{-3}w_{Cr}^\gamma + 3.1\times10^{-2}w_{Mo}^\gamma + 1.8\times10^{-2}w_V^\gamma \end{aligned} \tag{3.4}$$

ϵ_0 is the offset strain

a_α is the calculated lattice parameter of ferrite

a_γ is the calculated lattice parameter of the austenite

w_i^γ is the weight fraction of species i in the phase γ

w_i^α is the mole fraction of species i in the phase α

V is the volume transformed

This offset strain ϵ_0 is added to the linear fit of the cooling curve, making a parallel slope with an offset of ϵ_0. The intercept between this new slope and the dilatometry curve, calculated is set as the temperature of the start of the transformation (M_S).

This method is more reliable than the lever rule because it involves a theoretical calculation specific for each composition and the value is used in the experimental data to extract the temperature of transformation, while for the lever rule it is just a mathematical manipulation of the data. Moreover, because the transformation is not always finished, the application of the lever rule might lead to mistakes. In the comparison of the two methods, the offset showed a much lower standard deviation.

Unit dilation cell

This calculation has been recently published [99] and it is the most complete characterization for continuous cooling transformation with multi-transformation, although being a theoretical calculation based on the dilatometry data.

Suitable only for continuous cooling experiments, the Unit Cell Dilation is an algorithm that calculates the volume of each unit cell of the phases and considers all the thermodynamics parameters to define when a phase transformation can occur. It is a valuable tool for dilatometry analyses since it can also give present phases, the volume fractions and the amount of carbon in each phase. The algorithm is further described in this paper: [99], and it runs on a python 2.7.

This method was published in 2018, it seems to be a promising method for data analysis and it is especially interesting for the case of complex microstructure. Even so, it still needs to be further studied since there are no much references about and it was never tested for eutectoid or hypereutectoid compositions.

3.2 Microscopy characterization

3.2.1 Scanning electron microscopy

The scanning electron microscopy (SEM) technique is based on the principle of scanning a giving area with an electron beam. Basically, the collected information can give either a chemical composition contrast via backscattered electrons (BSE) or topography by secondary electrons (SE). Various parameters (accelerating voltage, beam size, atomic number of the studied material) affect the interaction volume and then the resolution that can be reached.

In the context of this work, the SEM was extensively used for the measurements of the interlamellar spacing, which used SE, but the BSE contrast can give valuable information and some authors propose to combine the Electron backscatter diffraction (EBSD) and the BSE for the characterization of the pearlitic nodules and colonies [108].

The measurement of the average interlamellar spacing is not straightforward as it is for the main intercept counting techniques, as it is for grain sizes [109]. The apparent distance between the cementite layers does not provide a realistic view of the pearlitic microstructure with pearlite colonies oriented randomly. For this reason, the **true** interlamellar spacing (λ_0) should be considered and it corresponds to a distribution of spacing on a surface normal to the lamellae, as seen in Figure 3.3.

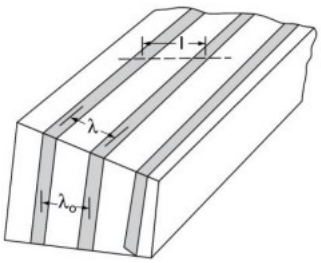

Figure 3.3: Parameters for interlamellar spacing estimation [1].

In this study, the **mean** interlamellar spacing of pearlite was determined according to Underwood's method. It consisted in superimposing an intersection grid of three circumferences in such a manner that the lines intersected the pearlite lamellae randomly in all directions. The mean intercept $\bar{l}$ is thus obtained by dividing the total line length by the number of the lamellae intercepted of each grid line [110]. The **mean** true value of interlamellar spacing $\overline{S}$ is given by the equation below:

$$\overline{S} = \frac{\bar{l}}{2} \tag{3.5}$$

The space between the lamella defines the interlamellar spacing and this distance can be measured by SEM. The colonies are also visually defined, being the unit containing all the parallel lamellae. The nodule, however, presents a crystallographic definition and, therefore, it can only be measured by EBSD.

EBSD is nowadays well known in the field of metallurgy. Considering a sample tilt at 70° for better collection [4], the primary beam hits the sample, and part of the BSE diffracts with the surrounding crystallographic planes.This leads to the formation of diffraction cones whose interaction with a phosphorus screen in front of the sample gives an electron backscatter diffraction pattern (EBSP) constituted of bands named Kikuchi bands. In Figure 3.4 is summarized the generation of the Kikuchi lines. [111]

Note that the obtained pattern is dependent on the crystal structure (for example, bcc and fcc) as well as its orientation. The phase identification and the determination of the crystal orientation are done in an indexing process in which all the recognised bands are converted in points (with a butterfly shape) in the Hough space and indexed through comparison with a data-set.

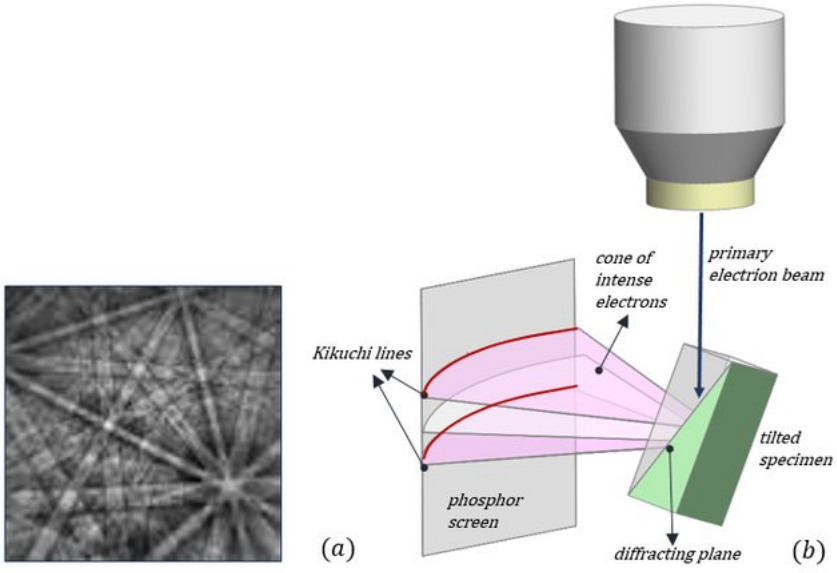

Figure 3.4: Representation of the acquisition of EBSD patterns. [17]

An advantage of the EBSD technique is that it allows the visualization of bulk specimens and can be performed on large zones, providing more statistical data, which

is the down point of standard TEM characterization.

The EBSD analysis is also very convenient for identifying, with high spatial resolution (down to less than 0.1°), the phase distribution of polycrystals, local texture, individual grain orientations at the surface and crystallographic relationships between phases, just to list a few possibilities of this technique [29].

In the considered case, the pearlitic crystallography has been investigated over the years and there are some known orientation relationships(OR) between the ferrite and cementite. Two of the most accepted relations are the Bagaryatskii and the Pitsch-Petch [27]:

The Bagaryatskii OR:

$$(100)_c \,||\, (110)_F$$

$$[010]_c \,||\, [1\overline{1}1]_F$$

$$[311]_c \, 0.91° \; from \; [1\overline{1}1]_F$$

The Pitsch–Petch OR:

$$[100]_c \, 2.6° \; from \; [13\overline{1}]_F$$

$$[100]_c \, 2.6° \; from \; [113]_F$$

$$[001]_c \,||\, [\overline{5}2\overline{1}]_F$$

During conventional EBSD experiments, due to the thickness of the cementite (only a few nanometers [112, 10]), during the regular EBSD experiments, the cementite is not recognized and, therefore, the textures of pearlitic steels have only information about the ferrite phase orientation [113, 49]. In addition, and perhaps due to this issue, there has been no serious attempt to discover any consequences of the different OR on the practical applications of pearlite [10].

As previously commented about the texture, it occurs due to a repetitive alignment of some specific atomic planes with the some specific directions. There are some vastly known textures and, as the texture during drawing is the same as the known rolling texture of ferritic steels [4], it can be analyzed in the same way. The texture is analyzed by means of the Orientation Distribution Functions (ODFs), which basically represents the distribution frequency of the measured orientation. Some of the main texture components are listed below in Figure 3.5, knowing that drawing texture is represented by the $\alpha - fiber$.

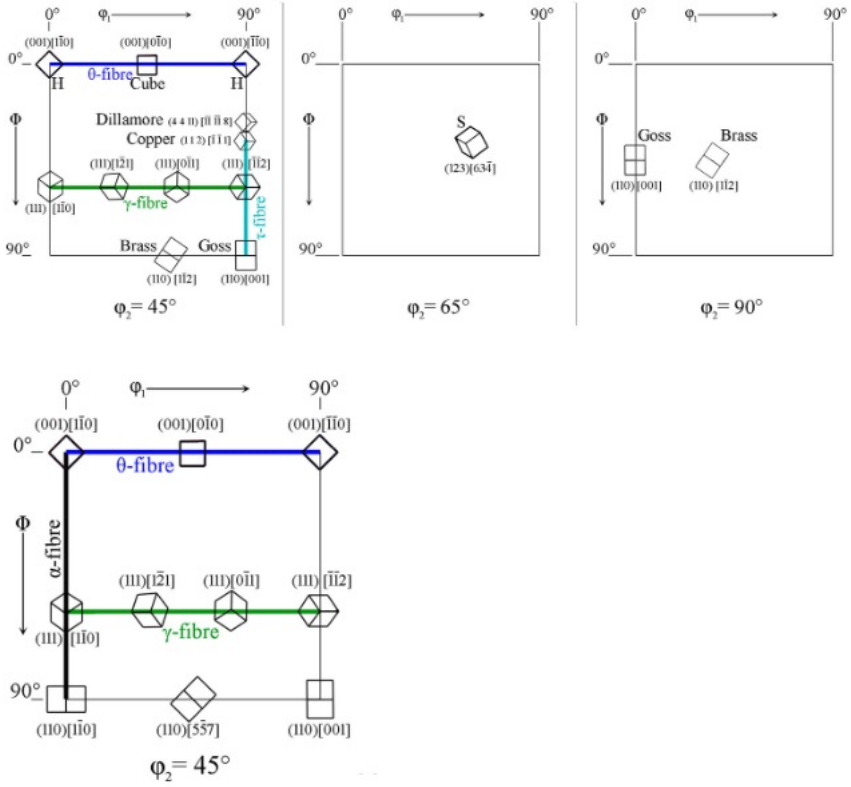

Figure 3.5: Various fibre textures that are of relevance for rolling and annealing textures in FCC and BCC alloys; φ_2= 45, 65 and 90°sections and φ_2= 45° section, representing the characteristic components and fibres of the FCC and BCC rolling and annealing textures, respectively. Extracted from: [4]

To have an information at a nanometric level, the interaction volume has to be reduced so it may allow to differentiate cementite and pearlite and give clear results. A recent development known as transmission-EBSD (t-EBSD) or Transmission Kikuchi Diffraction (TKD) allows the EBSD analysis of a thin foil. Here, the EBSD patterns will be produced by transmission rather than scattering [114, 115]. Despite the Kikuchi patterns are slightly deformed due to camera position, this method, when used on a conventional EBSD system can have almost the same angular resolution as EBSD and the advantage to reach a step size donw to 5 nm by comparison to the 25 nm reached in a FEG-SEM for conventional EBSD.

3.2.2 Transmission electron microscopy

The characterization of nano-structures and substructures is usually performed with the transmission electron microscopy technique (TEM). The high spatial resolution

(and angular resolution, under certain conditions) of TEM allows the characterization of crystal defects like dislocations, stacking faults, and point defects. Nevertheless, TEM presents some drawbacks such as sample preparation, where extremely thin sample disks (about 80-60 µm) are needed, and this method has reduced observation area [116]. When compared to SEM, TEM uses much higher voltages (between 80-300 kV). To generate TEM images, the electron beam incident traverses the thin disk, then the electrons are transmitted through the specimen, being subsequently focused by lenses and collected by a detector. The generated images can be visualized in real-time on a phosphor screen, or by a wide-angle camera. Nowadays, the images are recorded by a CCD camera (electronic charged coupled devices) which is a transductor that converts the electron signal into a pulse per pixel [117].

The use of the TEM characterization for pearlitic steels is specially important for the characterization of the cementite[118, 79, 5, 35], in which was possible to observe that the cementite participates on the plasticity of the pearlitic steels and it presents several slip planes and many dislocations inside the lamella.

The High-Resolution Transmission Electron Microscopy (HRTEM) is another technique that uses both transmitted and scattered beams to create an interference image, generating a phase-contrast image. This technique can analyze crystal structures and lattice imperfections, showing images at the atomic level, with the possibility to reveal details finer than 0.2 nm. Under some imaging conditions, the patterns will correspond to atom positions. If the specimens are very thin, about 100 nm thickness or less, the elastic scattering will be majoritarian in relation to the inelastic scattering. Interference patterns, normally visible starting from 400k of magnification, will be generated by the interaction of the beam and the crystal lattice [119].

In Figure 3.6 it is seen the HRTEM micrographs of two deformed cementite lamella.

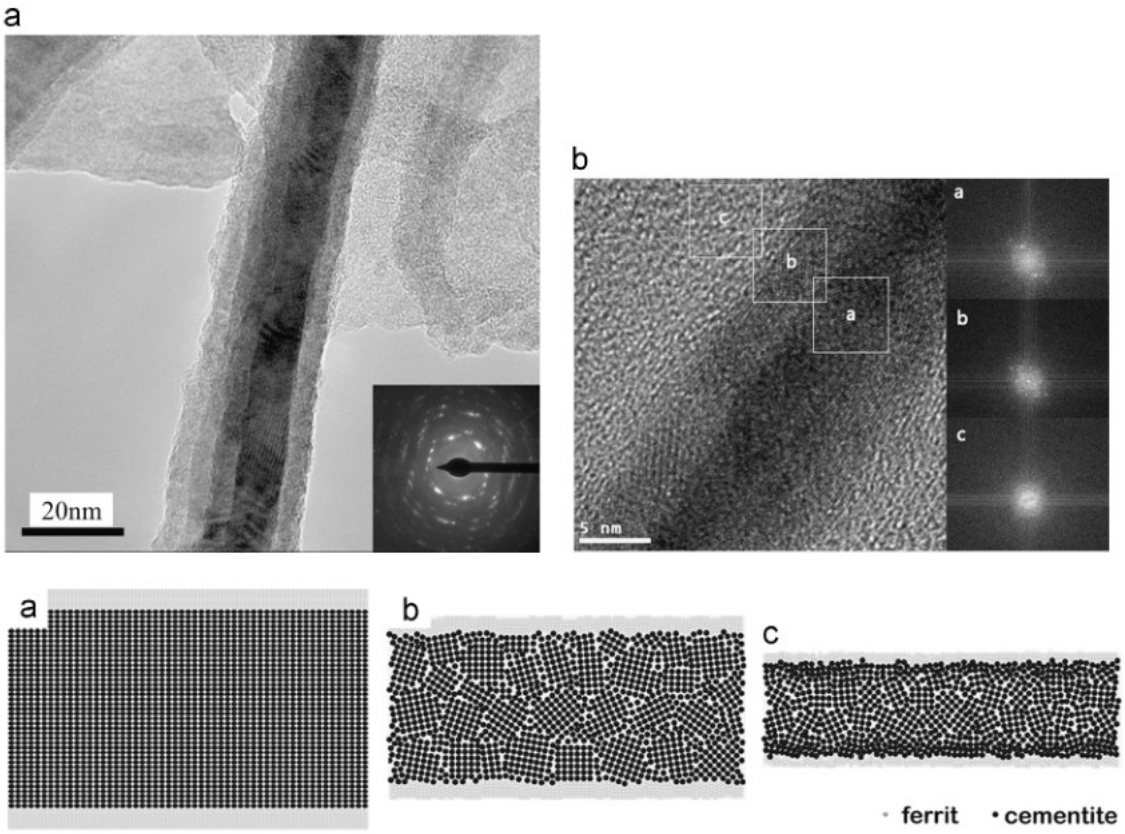

Figure 3.6: HRTEM image of cementite structure in heavily cold drawn pearlitic steel wires. (a) Cementite lamella at ϵ_d =1.6 and (b) atomic structure of cementite layers obtained at ϵ_d = 2.6, along with site-specific diffraction spots. And on the second line, Deformation scheme of cementite in cold drawn pearlite steel wire. (a) Original cementite; (b) low-strain deformed cementite; and (c) heavily deformed cementite. Extracted from: [18]

3.3 Fatigue characterization

3.3.1 Low cycle fatigue

Fatigue can be characterized as a mechanical failure caused by a cyclic loading with a certain stress amplitude, which can be higher or lower than the yield strength, but always lower than the ultimate tensile strength. The fatigue damage can be separated in the following stages:

The low cycle fatigue (LFC) differs from the high cycle fatigue (HCF) by the imposed stresses are higher than the yield strength [120] while for the HCF the material in stays under elastic deformation. The aim of LFC test is to evaluate the stress-strain

response of the material, besides the analysis of the fatigue life. It is often done under strain control, meaning that the strain levels are imposed and the load needed to reach the imposed strain is measured. The stress amplitude can be from strictly positive strains (only in tension) or negative and positive strains (tension and compression).

When done under strain control conditions, some points can be defined, such as the strain range $\Delta\epsilon$ and the strain amplitude $\Delta\epsilon/2$, that can be presented versus the number of cycles to failure (Nf). The total strain range, $\Delta\epsilon_t$ can be decomposed into plastic strain range $\Delta\epsilon_p$ and elastic strain range $\Delta\epsilon_e$. In Figure 3.7 are shown these values on the fatigue loop.

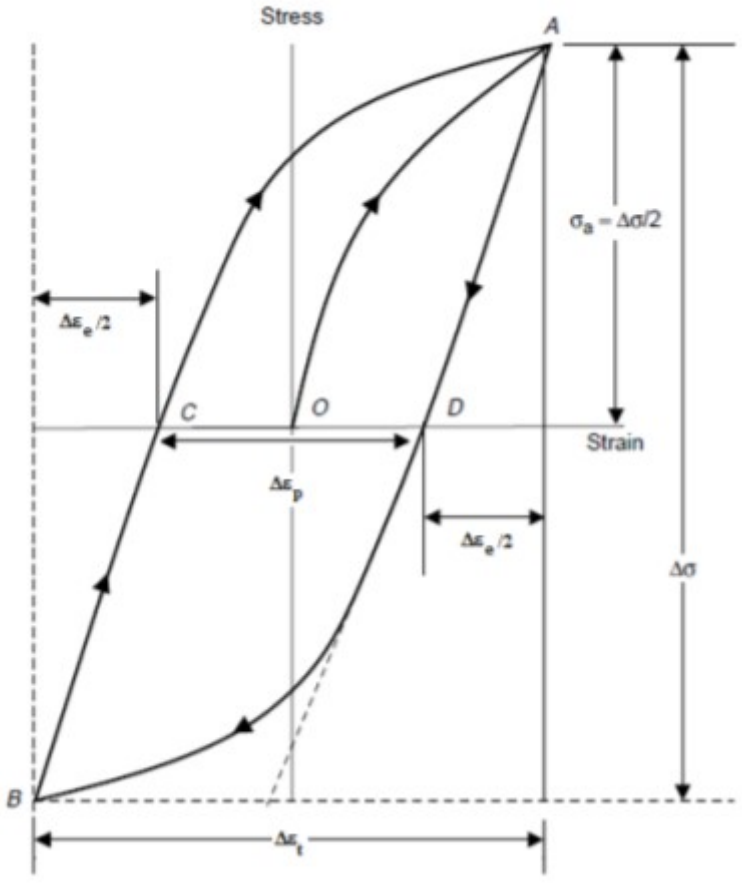

Figure 3.7: Hysteresis loop and the respective total strain range $\Delta\epsilon_t$, plastic strain range $\Delta\epsilon_p$, and elastic strain range $\Delta\epsilon_e$. Extracted from: [19]

Theses values are usually measured at the mid-life of the fatigue test and the values vary linearly with the number of cycles to failure. According to Basquin, Manson, and Coffin, they can be fitted to a power law as follows:

$$\frac{\Delta\epsilon_t}{2} = \frac{\Delta\epsilon_p}{2} + \frac{\Delta\epsilon_e}{2} = \frac{\sigma_f}{E}(2N_f)^b + \epsilon_f(2N_f)^c \tag{3.6}$$

Where $\Delta\epsilon_t/2$, $\Delta\epsilon_p/2$, and $\Delta\epsilon_e/2$ are the total, plastic and elastic strain amplitudes, respectively. 2Nf is the number of load reversals to failure, σ_f the fatigue strength coefficient, E the Young's modulus,ϵ_f the fatigue ductility coefficient, b the fatigue strength exponent, and c the fatigue ductility exponent [121].

Chapter 4

Pearlite formation study

4.1 Introduction

To assess the possibilities of producing a microstructural gradient, it is important to know the parameters that can play a decisive role during the phase transformation and how exactly do they affect the final microstructure. That is why in this first chapter are investigated the effect of the process parameters, during both heating (heating rates, temperature and soaking time) and cooling (cooling rates and isotherm treatment temperature), and the material contributions, such as the effects of carbon content, initial microstructure and its mechanical history.

The quenching dilatometer is used all through this chapter to simulate all the heat treatment conditions while also characterizing its effect on the phase transformations. The microstructural characterization is also extensively used, mainly by light optical microscope (LOM) and SEM investigation and hardness, aiming to,first of all, confirm the results obtained by the dilatometer, and secondly to investigate morphology features not reviewed during the tracking of change in length of the sample, such as morphologies (grain shape or similar feature).

In this chapter, neither the real process conditions nor the dimensions of the real samples are considered. The interest here is to understand how the pearlite formation can be manipulated and modified to produce a gradient.

4.2 Materials and experimental approach

4.2.1 Materials

All the tests in the chapter were done using standard size dilatometer samples, ϕ = 4 mm diameter with 10 mm long, to investigate the basis of the pearlitic transformation. The studied chemical compositions are shown in the Table 4.1. It comprises an eutectoid composition (0.82%) that will be used as the reference, one with a lower carbon contents (0.72%C) and another with higher carbon content (0.87%C). The interest in analyzing different carbon content is to investigate the effect of the proeutectoid phases, which affect the thermodynamics and the kinetics of the phase transformations, and it can produce different microstructural responses during the heat treatments.

For general applications of pearlitic steels wires, there is no need to highly alloy them, since they already present high strength and do not need solid solution strengthening or precipitation hardening. Therefore, only plain carbon steels are analyzed, which is very convenient for this work, so that the effect of the carbon content can be mostly isolated. There are some small contents of manganese and silicon, but it should not affect the transformation to pearlite since, with the present quantities, it can barely affect the steel hardenability (ease to transform to martensite).

Table 4.1: Chemical composition of the 4 mm diameter wires and drawing strains (ϵ_d)

Chemical composition (in wt.%)							
	Wire						
	0.72C	0.72C	0.72C	0.82C	0.87C	0.87C	0.87C
Element \ ϵ_d	0.97	1.39	1.83	0.97	0.97	1.39	1.83
C	0.739	0.709	0.714	0.824	0.885	0.885	0.877
Mn	0.655	0.633	0.615	0.562	0.636	0.629	0.646
P	0.009	0.010	0.016	0.011	0.012	0.013	0.015
S	0.013	0.009	0.012	0.006	0.011	0.012	0.013
Si	0.244	0.252	0.255	0.280	0.260	0.249	0.264
Al	0.001	0.001	0.001	0.001	0.001	0.001	0.001
Cu	0.012	0.007	0.028	0.030	0.007	0.006	0.014
Cr	0.010	0.015	0.020	0.013	0.012	0.014	0.012
Ni	0.015	0.016	0.021	0.021	0.013	0.013	0.020

These compositions were considered for the production of the Time - Temperature - Austenitization (TTA), Continous - Heating - Transformation (CHT), Continous - Cooling - Transformation(CCT) and Time - Temperature - Transformation (TTT) diagrams.

The steel rods (6.5 mm diameter) were produced and delivered by the wire rod supplier, subsequently patented and then drawn in Bekaert. The obtained microstructures with the selected compositions that will be departing point of the study are shown in Figure 4.1. It is seen that all the samples drawn from a diameter of 6.5 mm to 4 mm (ϵ_d=0.97) presented a fully pearlitic microstructure.

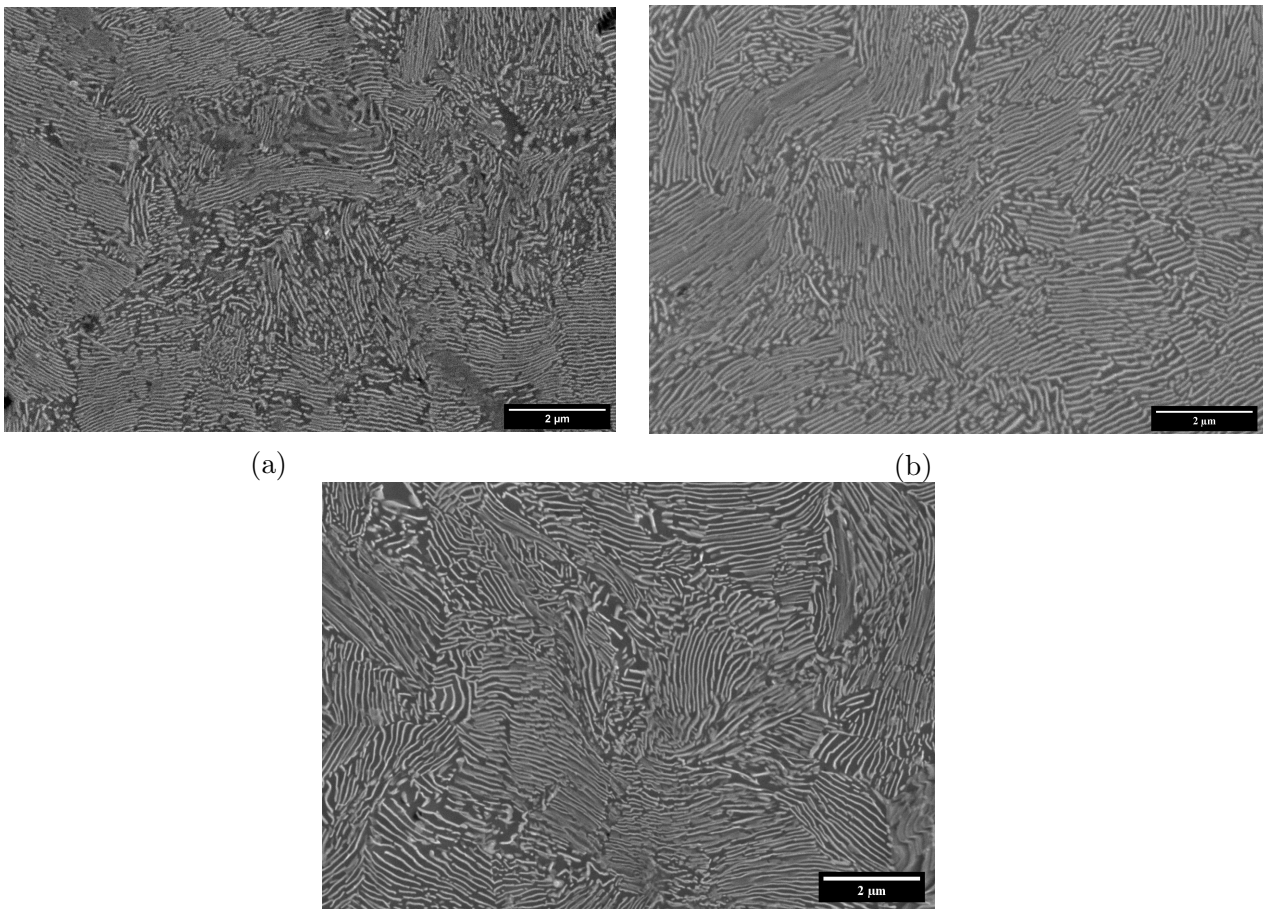

(a) (b)

(c)

Figure 4.1: Initial microstructure of the (a) 0.72%C, (b)0.82%C and (c) 0.87%C wires.

For the diagram assessment, only the wires drawn from 6.5 mm to 4 mm (ϵ_d=0.97) were used. For the investigation of the mechanical history effect, experiments were performed on the wires with different initial amounts of accumulated strain. This was done on the wires with of 0.72%C and 0.87%C, with different amounts of deformation: drawn from 10 mm (ϵ_d=1.83), 8 mm (ϵ_d=1.39) and 6.5 mm (ϵ_d=0.97) to 4 mm,

respectively.

The ASTM standard A1033-18 [97] describes the elaboration of a dilatometry sample and it takes into account the heating apparatus(induction or electrical resistance) and the sample texture. It indicates that, for the induction heating, the samples should be cut from the mid-radius if cut from a bar, and it must have its longitudinal axis perpendicular to the rolling direction. In this work, the drawing texture is parallel to the length because the wires are directly cut into cylinders to produce the dilatometry samples. To avoid misinterpretation of the results, the microstructural investigations were done both at the longitudinal and the transverse cross-section to analyze if the material is isotropic or if there is an effect of the texture on the microstructure. Moreover, to investigate the effect of texture and if represents any harm for the measurements of the change in length, some cycles measuring the variations in length, diameter and volume were done and they are seen in appendix A.

4.2.2 Experimental approach

Dilatometry cycles

First of all, the heating diagrams were produced to analyze the effect of the heating parameters on the formed austenite, which will further affect the pearlitic transformation. These effects are observed in the chemical homogenization of austenite and the PAGS. The parameters can be heating rates, austenitizing temperature, and soaking time. The effect of the heating rates can be assessed in a typical diagram called Continous-Heating-Transformation and the austenitization temperature and time are observed in the Time-Temperature-Austenitization. The used cycles to produce these diagrams are shown in Figure 4.2. Most of the chosen heating rates, soaking times, and temperatures were selected based on the industrial practices, and then some "extremes" were added for better understanding the effect of these parameters.

During heating, the dilatometer chamber stays under vacuum to avoid oxidation and/or decarburization. The ASTM states that it should be not higher than 10^{-3} Pa, but the tests were done under 10^{-5} Pa following the dilatometer supplier advice. This condition was used for both diagrams done with the industrial parameters and the one according to the standard.

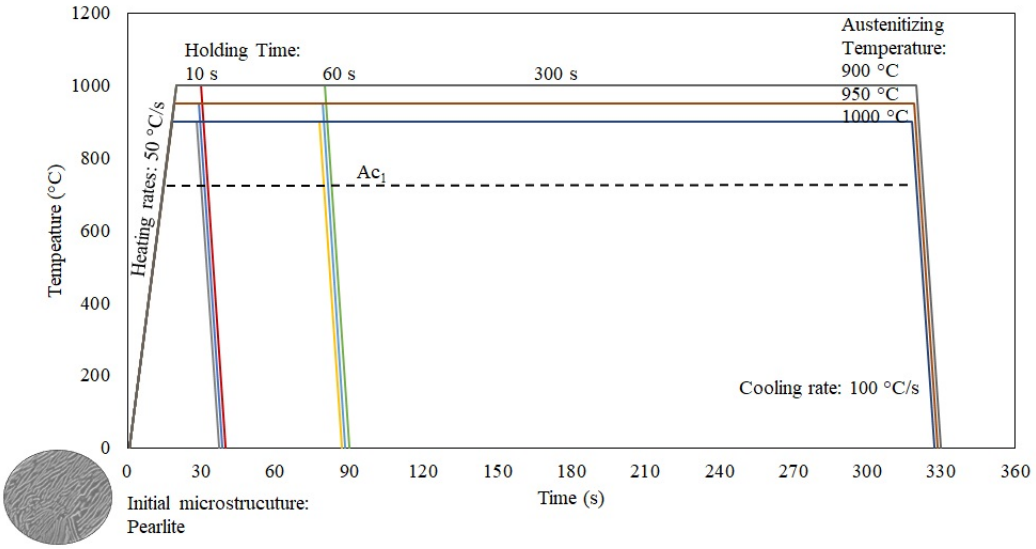

(a)

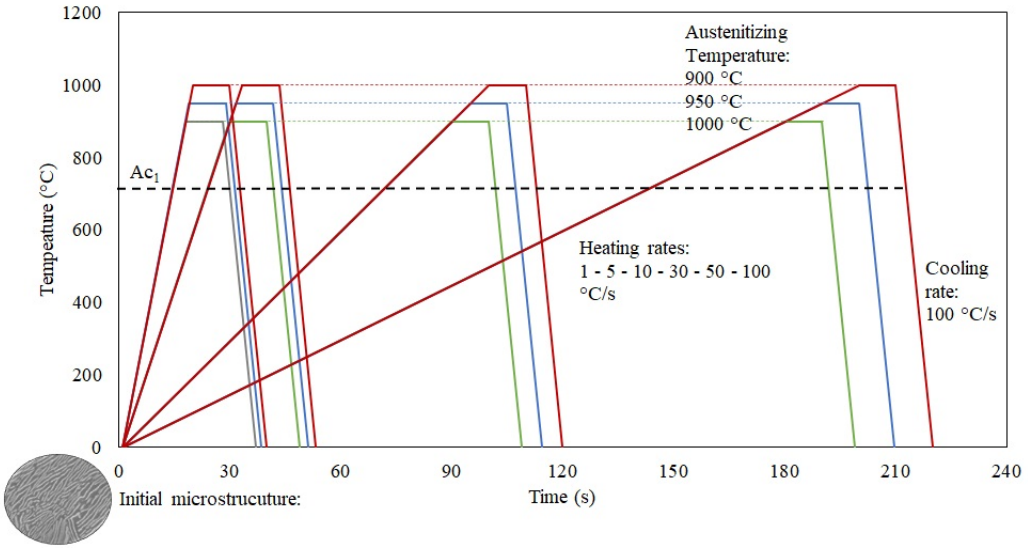

(b)

Figure 4.2: Cycles for the production of the (a) Time-Temperature-Austenitizing and (b) Continuous-Heating-Transformation diagrams with a soaking time of 10 s.

The CHT diagrams were produced for the 0.6, 0.72, 0,82 and 0.87%C with a drawing strain $\epsilon_d = 0.97$, while the TTA was only produced for the 0.82%C. They all started from a deformed pearlitic microstructure as shown in the previous section.

For the effect of the mechanical history on the austenitization (PAGS and the homogenization of the austenite), some continuous heating tests were performed using the wires with 0.72%C and 0.87%C and a drawing strain $\epsilon_d = 1.39$ and 1.83. They all presented a fully pearlitic microstructure, they only differed by the accumulated

amount of deformation.

It is known to happen some recovery and/or recrystallization during heating of deformed materials and the magnitude of its phenomena will depend on the given energy during the heat treatment, i.e. heating rate, temperature, time, and initial accumulated strain that will rule the driving force for the phenomena to occur. Although these phenomena are vastly known and documented for many steel microstructures[122, 123, 124], the exact mechanisms are not very well described for the pearlitic steels. It is not clear if it is only inside the lamella, if the cementite plays a role, if it affects the subsequent transformation to austenite... just to name a few of the unresolved issues.

So, in addition to the study of the mechanical history, it was also investigated the phenomenon occurring in the microstructure before the transformation to austenite. For that, two sets of tests were performed:

1. Interrupted tests at 700 °C with various heating rates (1, 5, 10, 30, 50 and 100 °C/s); It consisted in heating the wires with the different drawing strains ϵ_d to the interrupted test temperature and immediately quenching at 100 °C/s.
2. Two-step heating, in which the samples were first heated to 700 °C at 1 °C/s and then heated to 1000 °C at 100 °C/s; and the contrary, it was heated at at 100 °C/s to 700 °C and then heated to 1000 °C at 1 °C/s.

The purpose of the first test is to understand the exact phenomenon that was happening during the transformation of pearlite to austenite and its relation with the drawing strain ϵ_d and the heating rates.

In the second one, the effect of this phenomenon during the austenitization is investigated. The thermal cycles of the two steps heating are shown in Figure 4.3a.

The last parameter that could still affect the austenitization is the initial microstructure since the different phases and their size can considerably affect the global austenitic homogenization. Therefore, the effect of the initial microstructure was also studied for the 0.87%C steel rod because it has the higher carbon content, which entails the hardest composition to homogenize and uniformly redistribute the carbon. The employed cycle is shown in Figure 4.3b.

As there were no martensitic wire rods, a prior cycle of austenitizing and quenching

was done in the dilatometer to start from a martensitic microstructure. The applied cycle was certainly enough to change the amount of deformation accumulated in the starting microstructure, thus meaning that the comparison between pearlitic and martensitic microstructures does not take into account the mechanical history.

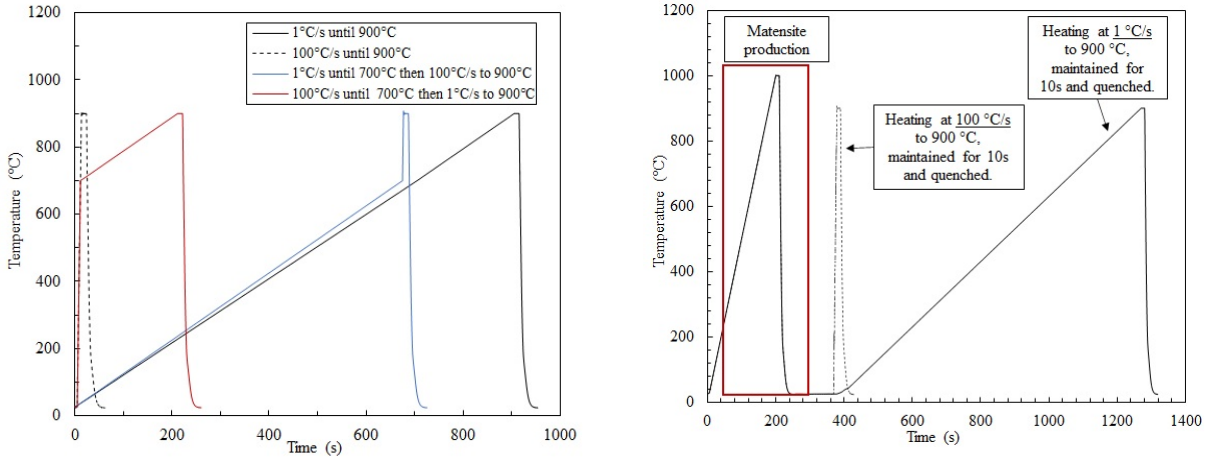

(a) (b)

Figure 4.3: Thermal cycles used for the investigation of (a) the mechanical history and (b) initial microstructure.

The CHT and the TTA diagrams for the four compositions, together with the study of the effect of the mechanical history and the initial microstructure contemplate all the possible features that can change the microstructure through the austenitization.

The following investigation is during cooling which, in practice, can be changed by the cooling technology and its process parameters, e.g. bath temperature and heat extraction coefficient, to name a few. While the cooling technologies will be further discussed in the next chapter. In the present chapter, only ideal cooling conditions are investigated. The pearlite formed by continuous and isotherm cooling is analyzed and the impact of the prior austenitization in the final microstructure is also evaluated.

There is a standard from ASTM (A1033-18) [97] that defines the the conditions to produce phase transformation diagrams, however, the rules dictated by these standards are too far from the real industrial practice. Therefore, to simulate both standard and industrial conditions in the dilatometer, two sets of experiments were done to build the diagrams and they are defined as:

- **Standard Transformation Diagram (STD)**: cycles and procedures done according to ASTM A1033-18. [97]

- **Wire Transformation Diagram**(WTD): done according to the wire heat treatment conditions.

Starting with the conditions for the STD diagrams, it is first necessary to determine the start and end of the transformation from pearlite to austenite, Ac_1, and Ac_3 respectively, which is done by a specific cycle for critical temperature determination. It consists in heating the test specimen to 700 ± 5 °C, at a nominal rate of 10 °C/s, followed by heating at 28 °C/h until the two critical temperatures are identified. This is important because the heating cycle for the STD diagrams is done 50 °C above the Ac_3.

The measured values for the 0.8%C wire were Ac_1=707 °C and Ac_3=747 °C.

Before the test, a stabilization cycle to remove residual stress and stabilize the position of the sample before the heat treatment cycle is done. The test consists in heating the specimen to 650 ± 5 °C, at a nominal rate of 10 °C/s, holding for 10 min followed by the cooling at 10 °C/s to room temperature.

The ASTM standard defines the cycle as:

> "Heating a test specimen to an austenitization temperature of Ac_3 + 50 °C (+/- 5 °C) at a nominal heating rate of 10 °C/s. The test specimen shall be held at the austenitization temperature for 5 min and then cooled to room temperature at nominal cooling rate of 0.05 °C/s to 250 °C/s. It is recommended to do twelve tests over the ranger of just presented cooling rates." [97]

Although the STD were done only for continuous cooling, the standard also defines the conditions for the isotherm tests in which the austenitization is followed by quench to the holding temperature at a cooling rate of at least 175 °C/s. When the sample reaches the holding temperatures, it must not undershoot by more than 20 °C and it must stabilize within 2 s. The holding time should be long enough for the sample to transform completely and it is recommended to do twelve isotherm temperatures between Ac_1 and room temperature. The final cooling to room temperature is done with a maximum cooling rate of 20 °C/s.

The WTD are done closer to the possible industrial applications, thus not having a stabilization cycle or a long austenitization cycle. The chosen conditions for the CCT

and TTT in the WTD are shown in Figure 4.4.

To analyze all the effects of the heating conditions on the transformations during cooling, two heating paths were chosen: a slow heating at 5 °C/s to 1000 °C and fast heating at 30 °C/s to 950 °C.

The lever rule and the offset method, both explained in Chapter 3, were the only two methods used to analyze the dilatometry curve. For the single-phase transformation, $\alpha + Fe_3C \rightarrow \gamma$ during heating or $\gamma \rightarrow \alpha + Fe_3C$ during cooling, the lever rule is enough precise to extract the temperatures of start and end of the transformation, as previously discussed in chapter 3. The offset method was only used for the definition of martensite start temperature (Ms) because the transformation to martensite does not reach its completion at room temperature, hindering the use of the lever rule.

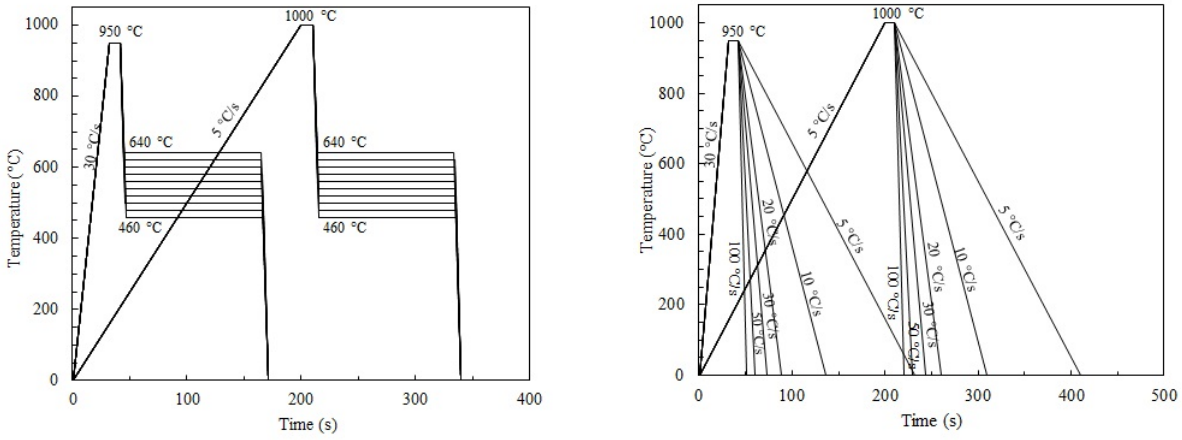

Figure 4.4: Thermal cycles for the production of the phase transformation cooling diagrams. In (a) are the cycles for Time-Temperature-Transformation diagrams, done in ten isotherm temperatures (640, 620, 600, 580, 560, 540, 520, 500, 480 and 460 °C) and hold for two minutes before final quenching; and for the (b) Continuous-Cooling-Transformation diagrams six cooling rates were analyzed (5, 10, 20, 30, 50 and 100 °C/s); And, for both diagrams, two austenitizing conditions were analyzed: heating at 30 °C/s to 950 °C and heating at 5 °C/s to 1000 °C and soaking for 10 s for both conditions.

For the case of the multi-phase transformation, none of the methods is suitable since the transformations might be superposed and they do not reach its completion. The lever rule was used to estimate the transformation temperatures of start and end, and the transformed fraction was not taken into account.

Microstructural characterization

To perform a metallography analysis on the dilatometry samples, they had first to be cut in the precision cutting machine Struers Accutom-100, at the length of 5mm for the transverse cross-section analysis, and then the remaining 5 mm long cylinder was cut in two for the longitudinal cross-section analysis. Finally, they were mounted in a conductive Bakelite in case of subsequent SEM examination.

The metallographic preparation of the samples was carried out with the grinding SiC papers from #320 to #2400 followed by fine polishing with diamond paste until 1 µm.

For the SEM analysis, especially for the ILS measurements, two additional steps were necessary, first a 0.25 µm diamond paste polishing and then the final mechano-chemical-polishing step with the Struers colloidal silica suspension of 0.25 µm (OP-S) for two min and another two minutes of polishing in water. For EBSD preparation, as the OP-S presented to be too reactive,it was used instead another standard colloidal silica suspension of 0.04 µm (OP-U), also from Struers, for ten minutes and then another ten minutes with hot soapy water.

To reveal the pearlitic microstructures, samples for both light optical microscopic (LOM) and SEM analysis, the most suitable etching was Picral 4% (4 g of picric acid in 100 mL of ethanol). While for revealing martensitic, the Nital 2% (2 mL in 98 mL of ethanol) was enough. Both etching procedures were chosen according to the ASTM standard 407-07e1 for good micro etching practices [125]. In the case of mixed microstructure, both etchings were used in the same sample to reveal all its features.

To reveal the prior austenite grain boundaries, the alkaline sodium picrate (ASP) at 90 °C for 10 minutes was used, followed by Nital 2% etching and Picral 4% [126]. Many etching solutions are proposed for measuring of the PAGS, but it is known to be a struggle to have a good definition of the grain boundaries in medium and high carbon steels [127]. The ASP solution was the most successful chemical one.

The other successful method for revealing the PAGS was the thermal etching [127]. It consisted in preparing the sample surface before the thermal cycle by the metallography route described, grinding until reaching the center of the samples and then polishing until 1 µm, before performing the cycle in the dilatometer, so it can preset this free surface. It is explained that there is a flux of atoms out of the samples

by the grain boundaries, making it deeper and creating contrast. Although it has a very nice image result in most cases, it is very time-consuming to prepare before each sample and it affects the variation in length measured by the dilatometer since half of the cylinder was grinned out to create the free surface. For these reasons, this etching procedure was applied only for a few samples.

The comparison between the thermal and the chemical etchings is shown below in Figure 4.5. In both cases, it was possible to manually measure the prior austenite grain size (PAGS).

The method used to measure the PAGS is described in the standard ASTM, E112 [128]. The measurement is done by counting the grains intercepts with the three circles and four other straight lines drawn on the sample as shown below in Figure 4.5. This three-circle mask is known as Abrams three Circle Procedure and it is recommended to use a low magnification to have a final counting of 500 intercepts, which is calculated to give statistical reliable values of PAGS.

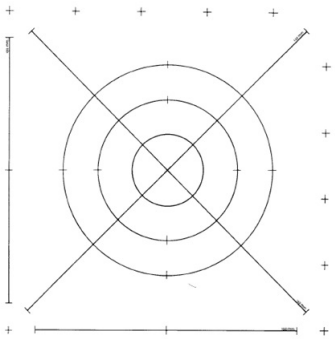

(a)

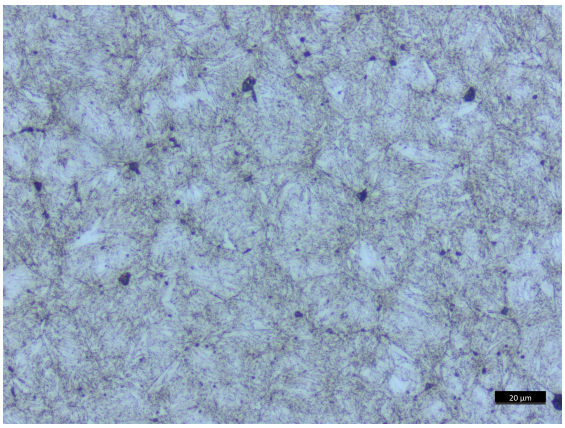

(b)

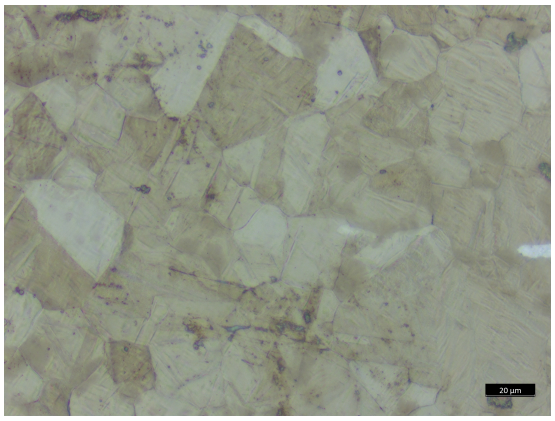

(c)

Figure 4.5: (a) Pattern for intercept counting and the light optical micrographs of the martensitic structures obtained by (b) chemical etching and (c) thermal etching for the measurements of the PAGS

The micrographs for the PAGS measurement were carried out by LOM a ZEISS Axiovert 200x inverted microscope.

The scanning electron microscopy observations were done using three different equipments, one is the Hitachi S3400N that is a tungsten filament microscope used for simpler microstructure investigations; and other two are field emission gun (FEG) microscopes, the FEG JEOL JSM – 7800F located in Bekaert and the Hitachi SU-5000, in which were also performed the EBSD experiments.

As previously discussed in Chapter 2, pearlite is a complex hierarchical microstructure and the interlamellar spacing is considered to be the most important parameter of pearlitic steels. The colonies' sizes are known to vary with the interlamellar spacing and are independent of the PAGS. Whereas the nodules depend on the PAGS and are independent of the transformation temperature [9].

The characterization of the nodules, by definition, can only be done by EBSD since it is the region that presents the same crystallographic orientation [108]. The colonies are defined as the regions in which the ferrite and cementite lamellas are parallel, thus not presenting a crystallographic boundary defined. Although some authors propose chemical etchings for measuring nodules because it reveals the high angle boundaries [129], the final result is not very clear to make statistical measurements. The reason for measuring all the nodules and colony sizes is because they can be affected by the phase transformation [130, 68]. However, the colony size is known to vary the same way as the interlamellar spacing, and the nodules are known to vary linearly with the PAGS [131] and, as the characterization of these features is very time-consuming and they could not be done for all the diagrams conditions, only the interlamellar spacing was measured.

The measurement of the interlamellar spacing can be done by many methods described in the literature [132, 133] and there are some controversial arguments in the way of doing that can under or overestimate its values. In this work, Underwood's method will be used to determine the average interlamellar spacing ($\overline{S}$). The method is employed on at least 20 SEM micrographs with a magnification ranging from 7 000x to 15 000x and to select images in which the pearlite lamellae are parallel to each other and perpendicular to the normal axis. To make a faster and more reliable measurement a post-processing of the images was performed using the ImageJ-Fiji software [134].

The statistical analyses were done in the MINITAB software [135] and the interest

here was to confirm if there was a significant difference between the measured averages. For it, the ANOVA test was the most suitable statistical test since the averages of different sets of experiments are compared. It had a sufficient number of measurements and the variance could be assumed to follow a normal distribution. The null hypothesis of the test was that all the averages were equal, considering a level of 95% significance.

Finally, the vickers hardness measurements were performed with the Buehler micro-hardness test machine with a Vickers indenter, using a load of 500 g held for 10 s.

From the collected data of all the diagrams, it is expected to produce a correspondence guide of pearlitic transformation giving its hardness, morphologies, or interlamellar spacing. In the literature, there are some atlas of phase transformation, however, they are not done in industrial conditions.

For the investigation of the effect of the mechanical history, more specifically for the interrupted tests, a deeper characterization was needed at a nanometric scale. Thus, the Transmission Kikuchi Diffraction (TKD) and transmission electron microscope (TEM) were carried out to observe the dislocation arrangements both in ferrite and cementite and also to find evidences of recrystallization of the ferrite.

In both cases and to ensure the analysed area, a thin lamella was needed and for that, the focus ion beam (FIB) technique was used. Cross-sectional thin lamellae were drawn out perpendicular to the surface with the help of the FIB technique using Ga+ ions in a FEI Strata DB 235 Dual-Beam microscope located at the Institut d'Électronique, de Microélectronique et de Nanotechnologie (IEMN, Lille). The lamellae were extracted at 1 mm of the border of the sample. The surface was later covered by a thin layer of carbon, deposited by electron bombardment, and a thick layer of about 1 µm of platinum by ion bombardment. This allowed protection of the surface against the Ga+ ion insertion employed for the machining of the lamella. The analysis TEM were conducted on a FEI Titan Themis 60-300 kV microscope.

The EBSD acquisition was carried out in a Hitachi SU-5000 FEG-SEM system operated at 20 kV and fitted with an Oxford Instruments Symmetry system. The employed conditions were 200 and 100 nm of step size on a 90 x 95 µm cliche, which entail a angular precision below 1° using the high-resolution camera, which is capable of performing acquisition speed up to 3000 patterns per second [136]. Pattern acquisition was done with refined accuracy and post-processing (mapping) was done using Aztec Crystal or Aztec Channel 5 software. For the TKD analysis, the operating conditions

of 30 kV and the lamella was placed in the pre-tilted sample holder.

4.3 Effects of the process parameters

4.3.1 Eutectoid composition

During heating

In this section are discussed the effects of the heating rates, the austenitization times and temperatures on the transformation of a fully pearlitic eutectoid steel to austenite.

Before the construction of the diagrams, all the dilatometry curves were analyzed and the critical temperatures Ac_1 and Ac_3 were determined. An example of the curves obtained during the continuous heating experiments are shown in 4.6.

It is observed that the transformation temperature increases with the increase of the heating rates. Besides, it is also seen that Ac_1 varies less than Ac_3, which is in agreement with the other authors observations [61].

Another interesting feature to be observed is that, before the transformation, the heating curves are not a straight lines as it would be expected to be since only the thermal expansion would be suspected. Here, a first slope change is observed around 200 °C, which has already been documented to be due to a change in the thermal expansion coefficient of cementite. Indeed, at (480 K) 207 °C, the cementite has its ferromagnetic transition that strongly affects the thermal expansion coefficient [137, 138] and it divides the heating curve into two expansion regimes. Then is seen a bump in the curve that is discreetly dependent on the heating rates. Some authors discussed this type of anomalies of the dilatometry curve during the heating and it is usually attributed to the annihilation of defects within the recovery and/or recrystallization, or the texture evolution of highly deformed ferrite [104, 103]. However, the found studies were done for low carbon steels, thus focusing only on fully ferritic microstructure. The meaning of this anomaly for the high carbon steels will be later investigated and discussed in the effect of the mechanical history section.

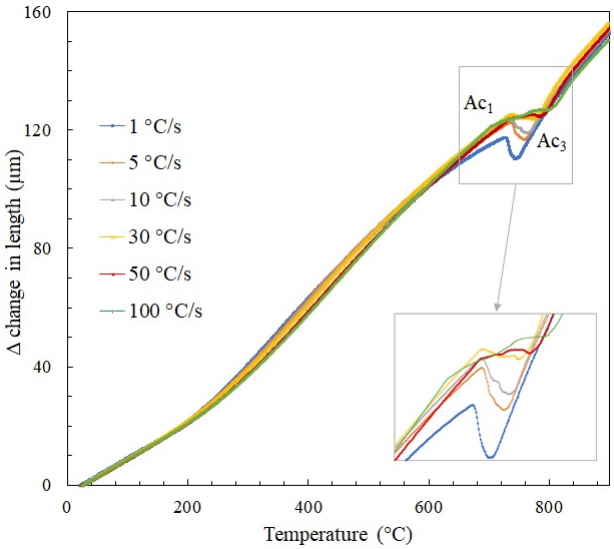

Figure 4.6: Dilatometry heating curves of the 0.82%C wire austenitized at 900 °C for 10 s using different heating rates

With the increase of the heating rate, the transformations occur within a larger range of time since the end is delayed, as seen by the increase of the Ac_3 values. Here, at slow heating rates, the pearlite to austenite transformation and the carbide dissolution happened simultaneously since there are enough time and energy to transform, as seen by the well-defined start and end of the transformation in the sample heated at 1 °C/s.

By contrast, at fast heating, the transformation starts first by consuming the pearlite while the larger carbide particles are later dissolved, thus transforming in two separate steps. This is more evident for the hypereutectoid or hypereutectoid steels because the dissolution of the proeutectoid phase is known to happen after the pearlite is consumed [8]. The growth of the austenite into the pearlite occurs by interface control growth at short distances regarding the carbon diffusion, while the proeutectoid phase is either too rich or too poor in carbon depending if it is cementite or ferrite, respectively, and it will oblige the growth to be by diffusion control.

The derivative of the dilatometry curve during the transformation is seen in Figure 4.7. It is seen that at 1 °C/s the transformation has only one well-defined peak, while at 30 °C/s it appears to have two spread peaks. Indeed, it is surprising to have two peaks in the fully pearlitic transformation since it is expected for the whole pearlite to be consumed by an interface control growth but there is a struggle for the advance of the transformation front with the increase of the heating rate that most likely leads to the change in the transformation kinetics control that entails the two spread peaks.

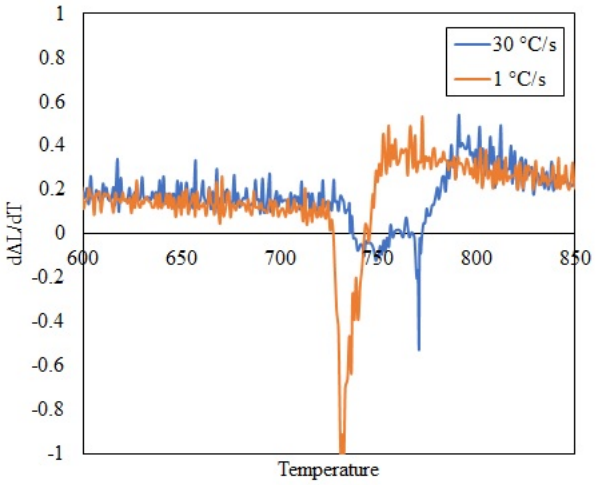

Figure 4.7: Time derivative of the variation in length during the transformation ($\mathrm{d}\Delta L/dT$) at slow and fast heating rates. It evidences that the transformation happens in two stages during the fast heating.

The average values of Ac_1 and Ac_3 temperatures are shown in Table 4.2. Confirming the previous observations in the curves, Ac_1 varies very little with the increase of the heating rates, only 10 °C, and, when heated at 1 °C/s, it starts transforming at the same temperature as the eutectoid transformation temperature (T_E) indicated in the Fe-C diagram, showing to be very close to the equilibrium diagram at this rate.

Table 4.2: Ac_1 and Ac_3 temperatures

	Ac_1		Ac_3	
HR (°C/s)	Average (°C)	Standard Deviation	Average (°C)	Standard Deviation
1	727	2	749	2
5	732	3	760	3
10	734	4	764	4
30	736	5	778	6
50	736	9	793	6
100	Not measured	Not measured	Not measured	Not measured

The Ac_3 temperature has been proved to change greatly, over 40 °C, with the increase of the heating rate. Although by definition Ac_3 is considered to be at the end of the conversion of pearlite in austenite, it is often observed, specially for hypereutectoid and high alloying steels, a temperature above Ac_3 called Ac_c and it is defined as the carbide dissolution temperature. Over this temperature, it is not expected to have any undissolved carbides in austenite.

There are no reliable and certified methods to extract this temperature as an exact value from the dilatometry curve. It is generally said to be the point after which it is only observed the thermal expansion of austenite. Figure 4.8 shows an example of it, in which is seen that between Ac_3 and the linear thermal expansion of austenite there is a gap, which is believed to be the time interval that the carbides are dissolved.

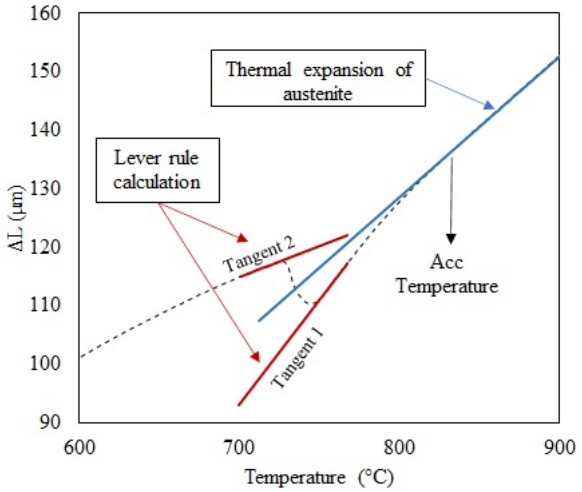

Figure 4.8: Acc temperarture on the dilatometry curve.

The Acc temperature would be around 840 °C as shown by the arrow in Figure 4.8, which stays close to other authors' calculations and measurements of Acc [139]. **Therefore, in all the studied conditions, it is expected to have full dissolution of carbides above 840°C.**.

Regarding the chemical homogenization of the sample, the expected consequence of the fast transformation is to not have enough time to homogenize the carbon distribution in the austenite. It can result in either some regions richer in carbon and others poorer. For the latter case, all the carbon atoms are in solid solution but not uniformly distributed; or, in the case of undissolved carbides, carbon is not dissolved and the overall carbon content in solid solution is not the same as the steel composition, which will diminish the hardness and increase the Ms temperature of the latter formed martensite. Therefore, these two parameters can work as indirect measurements of the non-homogeneity of the austenite. [51].

Hardness tests were performed on all the continuous heating and the isotherm heating tests. The resulting values are displayed in Figure 4.9. For the different times and temperatures of austenitization shown in 4.9 a, b and c, it is seen that the hardness value remains more or less constant for all the tests, which means that the carbon

dissolution has reached its maximum. This can indicate that carbon is homogeneously distributed, or that at least all the carbides are dissolved at all considered temperatures. It also confirmed that the estimated value of the Ac_c temperature (840 °C) is realistic since no evolution of hardness is observed for all the austenitization conditions, which are all above Ac_c.

For the CHT experiments, the hardness does not considerably change even with the heating rates (Figures 4.9 d,e,f), thus endorsing again the full carbon dissolution conclusion.

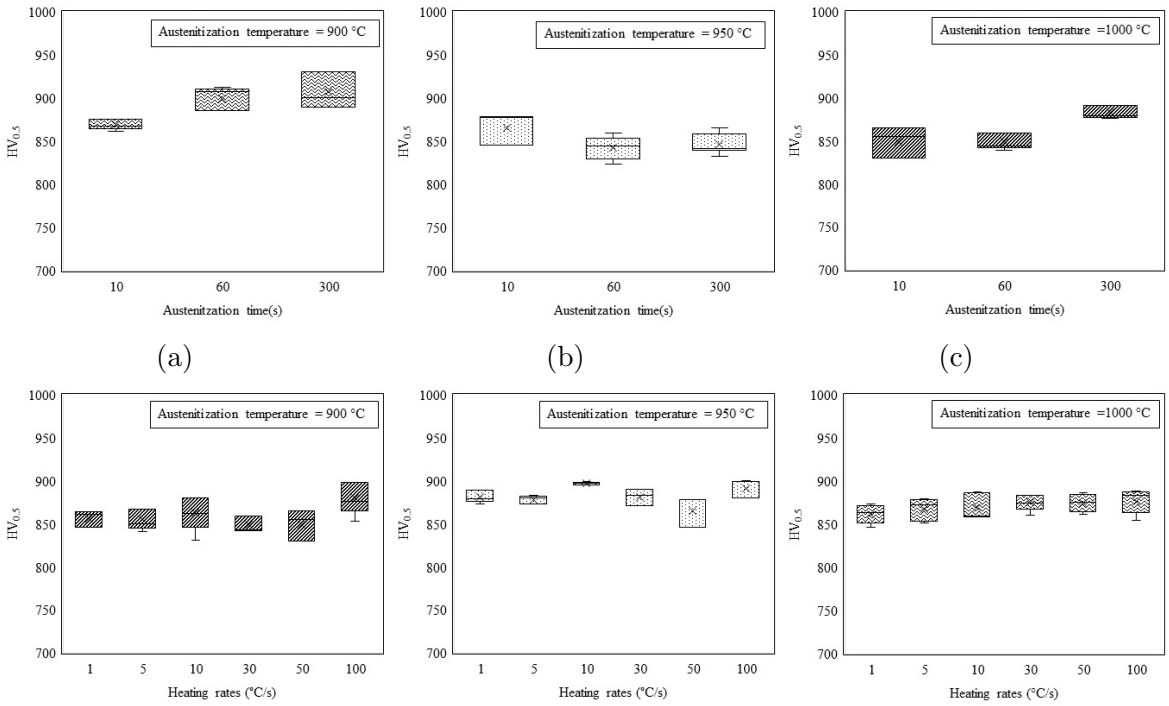

Figure 4.9: Measured hardness of the martensite obtained after austenitization in the (a,b,c) TTA cycles and (d,e,f) the CHT cycles.

As announced before, the Ms temperature can also be an indirect method to determine if the formed austenite is homogeneous. Inversely to the hardness, the Ms diminishes with the increase in carbon in solid solution in the austenite, thus having a higher value when undissolved carbides are present and lower values when the carbon content is the same as the steel composition.

There are some equations proposed in the literature to predict the Ms temperature based on the chemical composition. A very popular one is the Andrews equation [140] which is calculated, as a linear regression, as following:

$$Ms(^{\circ}C) = 539 - 423w_C - 30.4w_{Mn} - 17.7w_{Ni} - 12.1w_{Cr} - 7.5w_{Mo} \quad (4.1)$$

With w_x: the weight percent of element x.

The calculated Ms temperature for the eutectoid composition would be around 165 °C. In the present case, instead of calculating the Ms temperature, this equation will be used here to estimate the amount of carbon in solid solution in the austenite considering the measured Ms temperature. Note that this method assumes that carbon is fully dissolved and homogeneously distributed in the high temperature austenite constituent. The corresponding measure Ms and the respective calculated carbon content values are shown in Table 4.3. As the method that determines the Ms temperature can have a strong influence, the offset method [141], was considered as it gave the least dispersion and the obtained values were closer to the prediction by equation 4.1.

Table 4.3: Table of the measured Ms (°C) for the CHT experiments and the calculated carbon content

	Heating rates (°C/s)											
	1		5		10		30		50		100	
$T_{austenitizing}$	Ms	%C	Ms	%C	Ms	%C	Ms	%C	Ms	%C	Ms	%C
900 °C	161	0.846	152	0.865	153	0.870	160	0.846	163	0.839	156	0.856
950 °C	160	0.846	162	0.844	163	0.839	159	0.849	153	0.865	157	0.854
1000 °C	167	0.830	164	0.837	156	0.858	154	0.861	162	0.842	161	0.844

The calculated values show that the Ms temperature does not remarkably varies neither with the heating rates nor with the temperature. The Ms measured at the test done at 1000 °C for 300 s, which would be the most homogeneous condition, is 160 °C, being about the same value as the ones observed in Table 4.3. Again, this means that **all the conditions do not present undissolved carbides and they all present the same amount of carbon in solid solution as the wire composition.**

The PAGS can also affect the Ms temperature [142, 143], but its effect is more important for very small grains since the variation of Ms with the grain size follows a natural logarithmic function. For the conditions considered in this work, it can be considered that there was no variation of Ms with the PAGS.

It is worth noting that sometimes the calculated carbon content is higher than the measured composition of the steel. It is most likely due to imprecision both of the

Ms measuring method and the calculation. As the obtained values do not present any atypical tendencies or outliers, the fluctuations are considered to be caused by methods uncertainties.

In the analysis of the micrographs (Figure 4.10), some black spots were observed at the grain boundaries, especially on the samples transformed at 900 °C. In the literature, these black spots are said to be either "ghost pearlites" that do not transform during the austenitization [144, 145], or bainite or pearlite formed during cooling [51]. As it was previously determined that carbon was completely dissolved, it cannot be the ghost pearlite. Besides, the black spots are usually observed at the grain joints, which would be the first ones to nucleate a new phase, which thus show a high probability that these spots have been formed during cooling. Some further investigation was carried out and it indicates that these were bainitic islands, which appear because of inhomogeneities in the austenite. This phenomenon occurs more frequently for hypoeutectoid steels, in which the proeutectoid ferrite is the last one to be transformed to austenite and, if there is not enough time for the carbon homogenize, it creates carbon depleted regions.

An example of the observed bainitic regions is shown below in Figure 4.10.

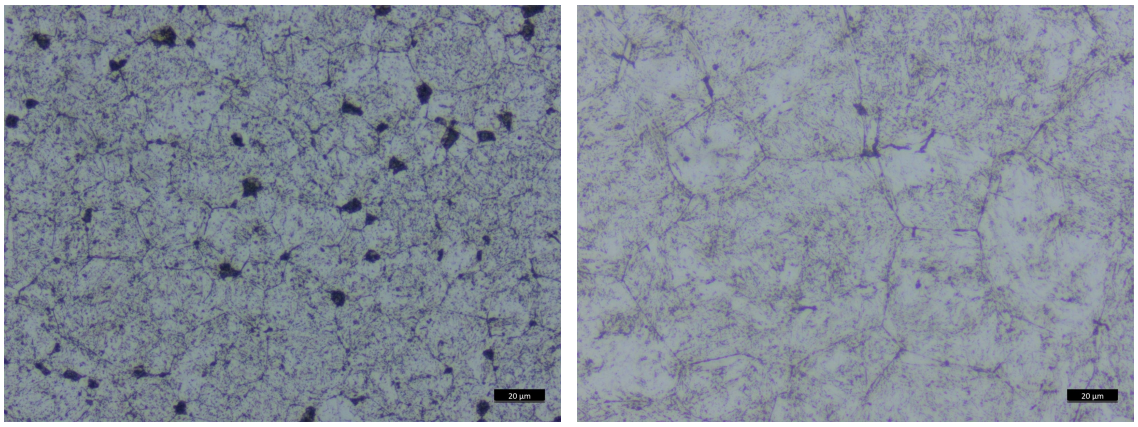

(a) (b)

Figure 4.10: Black spots later identified as bainite in the matrix of martensite in the samples austenitized at (a) 900 °C for 10 s which disappear once the austenite gets homogeneous.(b) Homogeneous sample austenitized at 1000 °C.

As in this section, only the eutectoid composition is analyzed, it is not expected to have this kind of phenomenon. Yet, it is observed to have much more bainite on the microstructure austenitized at 900 °C which gradually disappears with the increase of time and austenitization temperature. Therefore, it is the only evidence of variation of the austenite homogeneity and, hence, it is here defined that the austenite becomes homogeneous once these black spots disappear, which are the cycles for over 60 s at

950 °C or over 1000 °C.

The cooling rates do not play a role in the carbon homogeneity of the austenite since all the samples that were heated with different heating rates and austenitized at the same temperature presented about the same amount of formed bainite.

The last parameter to be analyzed is the prior austenite grain size (PAGS), which is one of the main parameters analyzed during heating. The grain growth happens after the transformation is complete and its driven force is the reduction of the overall energy of the system by diminishing the surface energy of the grain boundaries. The number of grain boundaries and the form of the edges, concave or convex, defines whether grains are going to grow and consume the others or they are going to be consumed. During the grain growth, it happens to change from a unimodal to a bi-modal grain size distribution, that contains large and small grains. The presence of very big grains and small grains can be harmful to the mechanical properties depending on the magnitude of this difference. There is one special ASTM standard, E 1181 [146], which classifies and gives a qualitative description of the grains [147].

The measure values of the grain sizes are observed in the box-plot of Figure 4.11. It is observed that the grain size does not have a great variation with the heating rates, although it varies with the temperature and time of austenitization.

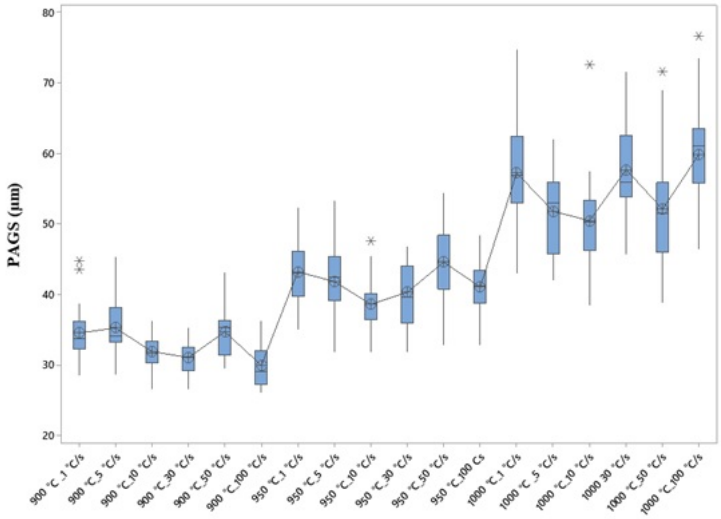

Figure 4.11: Boxplot of the PAGS measurements for the 0.82%C tested under continuous heating conditions to 900 °C, 950 °C and 1000 °C.

The statistical analysis of the PAGS is displayed in appendix A. It is shown that the differences in time and temperature are significant. While for the heating rates,

although they presented some significant variation especially for the extremes (1 and 100 °C/s), they are much less important in magnitude than the ones of time and temperature. Therefore, it is defined that the heating rates do not affect the PAGS.

All the previous analyses about the effect of heating rates, austenitization temperature, and time are reviewed in the Continuous-Heating-Transformation and the Time-Temperature-Austenitization diagrams, respectively. The results are shown in Figure 4.12.

For the TTA, in all the tests, the samples were heated at 50 °C/s, which is a very high heating rate that makes the starting temperature vary greatly from test to test. Therefore the temperatures Ac_1 and Ac_3 appear in a range of values. It is also observed that the temperature and time affect the PAGS, and the higher the temperature and longer the time, the larger the prior austenite grain.

So, the TTA diagram is composed of the Ac_1 and Ac_3 temperatures that indicate the fields of stable pearlite, meta-stable pearlite + austenite and then austenite; next is seen the Ac_c temperature (840 °C) that indicates the temperature over which the heat treatment succeeds in dissolving all the carbides; and, finally, at higher temperatures are indicated the regions in which the austenite is homogeneous. The iso-grain lines indicate the relation of time and temperature that provides the same grain size.

A method of PAGS prediction using Fick's laws of diffusion to compare two different austenitizing cycles at different time and temperatures has been certified with these results and is shown in Reference [14].

For the CHT, the Ac_c temperature is also indicated but the homogeneity and the iso-grain lines were not affected by the heating rates and it only changed with the temperature, that is why the grain size lines indicate that the same PAGS is produced independently of the heating rates in the considered range.

These diagrams serve as a guide for the transformations during heating. However, the conditions considered in the TTA diagram do not match with the industrial practice since it is usually done in a production line in which the wires pass inside the furnace at a certain speed and, therefore, are continuously heated. This process is better described by the continuous heating diagrams.

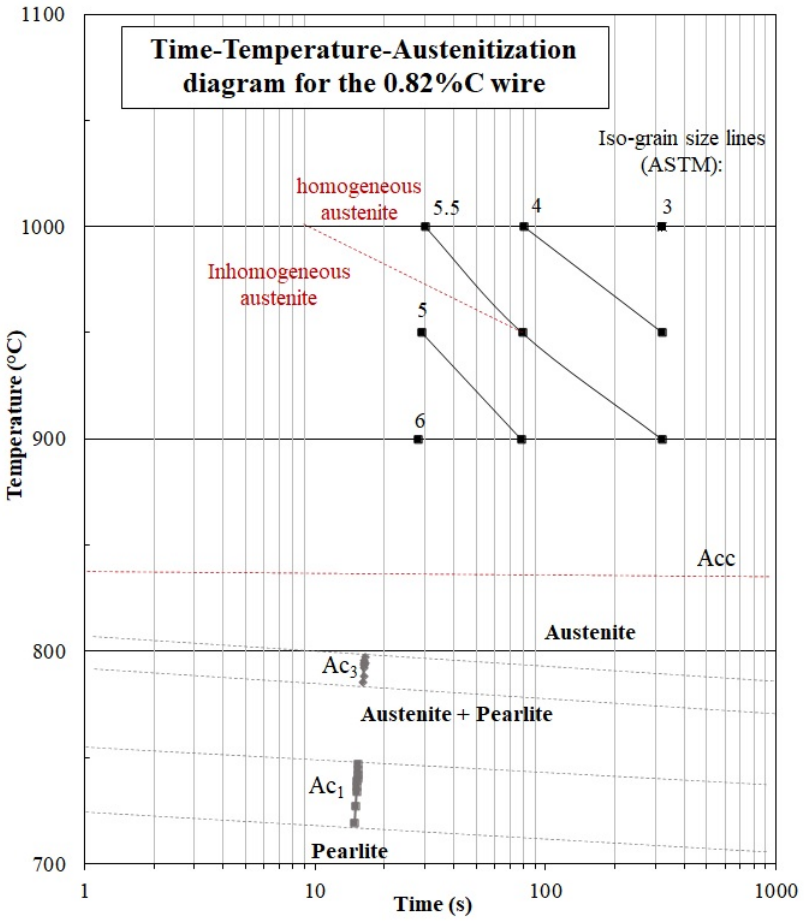
Time-Temperature-Austenitization diagram for the 0.82%C wire
Iso-grain size lines (ASTM):
homogeneous austenite
Inhomogeneous austenite
5.5
4
3
5
6
Acc
Austenite
Ac3
Austenite + Pearlite
Ac1
Pearlite
Temperature (°C)
Time (s)
1100
1000
900
800
700
1
10
100
1000

(a)

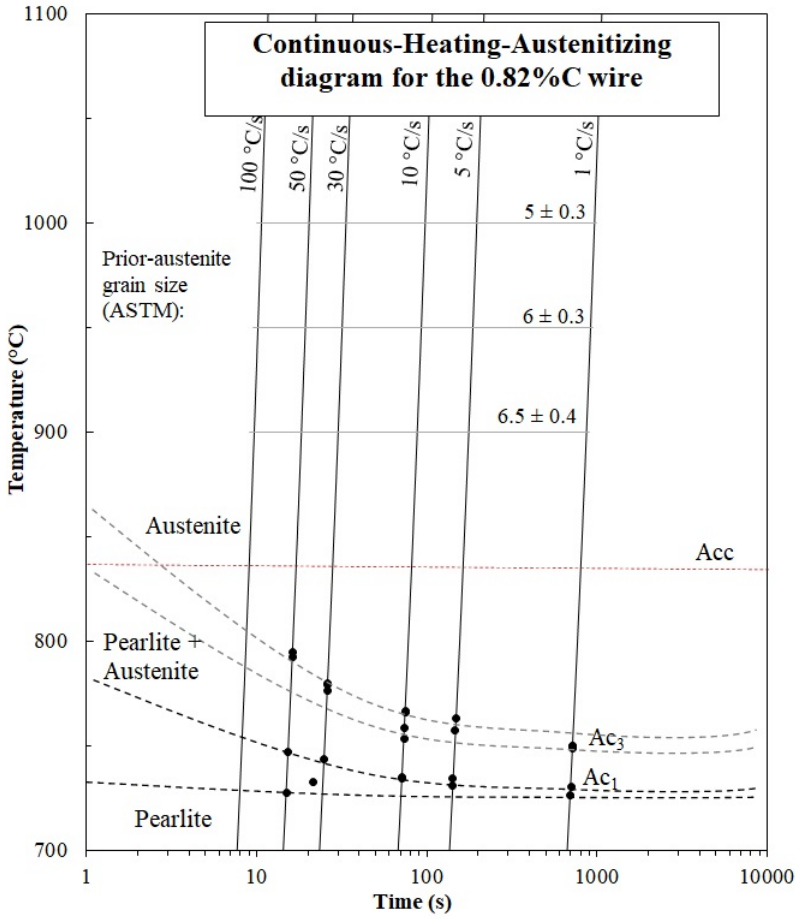

(b)

Figure 4.12: (a) Time-transformation-Austentization diagram and (b) Continuous heating transformation diagram for the 0.82%C.

During cooling

To cover most of the cooling possibilities of producing pearlite, two different types of cooling were tested, the isotherm and the continuous cooling, which is also sometimes called isochronal in the literature [148]. Moreover, the effect of the austenitization on the subsequent pearlitic transformation was also evaluated by starting from two different austenitization cycles. The results of these four conditions, two cooling, and two austenitizations are discussed in this section.

The cooling curves of the two cooling sets are shown in Figure 4.13. For both curves, more remarkably for the isotherm ones though, it is observed that there is a greater change in length during the transformation of austenite to pearlite with the decrease of the transformation temperature. After the transformation, the curves overlap each other, which shows the same behavior during the thermal compression of the products. It occurs because of the difference in the thermal expansion coefficients, higher for austenite than ferrite, $\beta_\alpha = 1.244 \times 10^{-5}\ K^{-1}$ and $\beta_\gamma = 2.065 \times 10^{-5}\ K^{-1}$ [137] respectively. With the decrease of the transformation temperature, the austenite presents a greater thermal compression, so, when it transforms to pearlite at a higher temperature, there is a smaller difference than the pearlite formed at lower temperatures.

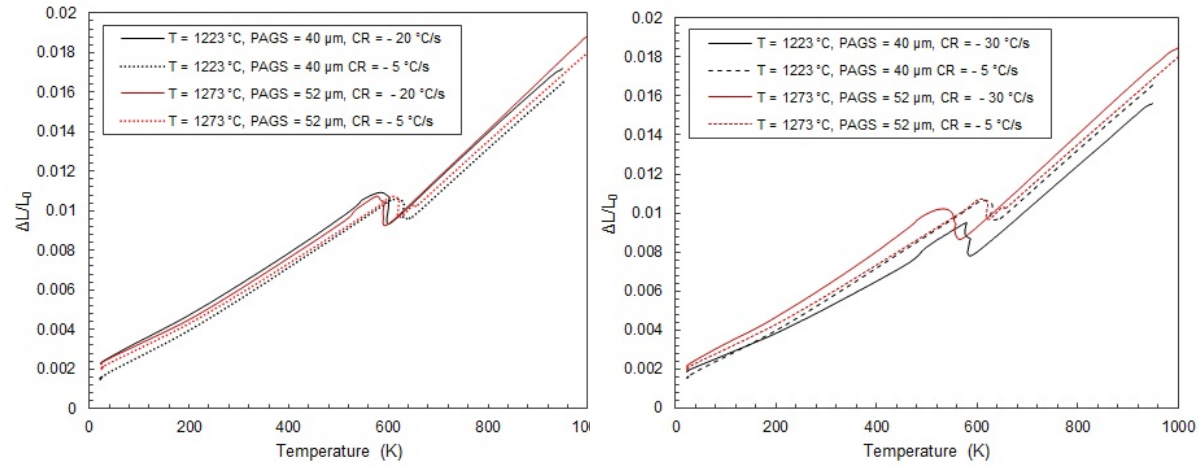

(a) (b)

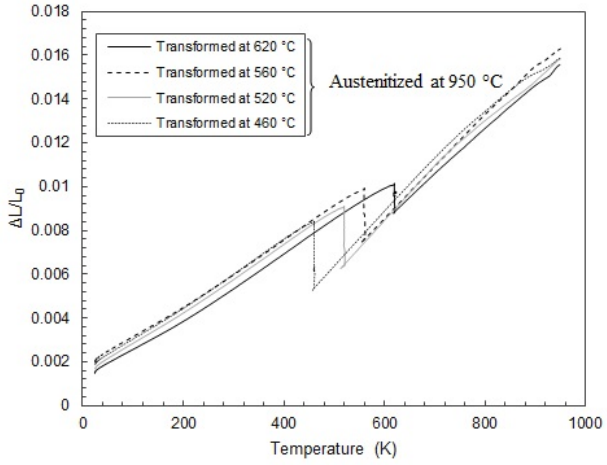

(c)

Figure 4.13: Dilatometry curves of the 0.82%C sample subjected to (a) isochronal cooling mode at (a) -20, -5 and (b) -30 °C/s, and to (c) isotherm cooling mode.

As previously mentioned, the choice of a good method to extract the data from the dilatometry curve is very important and it can considerably affect the interpretation of the results. The lever rule was chosen here to extract the critical temperatures from the isochronal curves due to its simplicity and because it is suitable for single-phase conversion of the parent into one product phase during continuous cooling. The critical temperatures of the start and the end of the transformation were defined as 1 and 99% of the fraction transformed, respectively. As the method of extraction is based on mathematical manipulation, it is important to keep aware that some variations are only due to the method and there are no real physical phenomena related.

The obtained temperature at which austenite starts to transform to pearlite (Ar_3) during continuous cooling based on the extraction method mentioned above and their respective calculated undercooling ($\Delta T_{undercooling} = T_{Eutectoid} - Ar_3$) are shown in Table 4.4. Figure 4.13 shows the two typical responses during the isochronal test: for the cooling rates -5, -10, and -20 °C/s, in which the influence of PAGS is negligible, and at –30 °C/s that presents a noticeable effect of the PAGS. The delay in the transformation can be attributed to the difference in the grain size that entails fewer nucleation sites, thus postponing the beginning of the transformation. The increase in the cooling rates enhances this effect.

In contrast with to the isotherm treatment temperatures, Figure 4.13c, the transformations during the isochronal test, even at the fastest cooling rates, have started around 600 °C. Meaning that below 600 °C, all the isotherm tests were done at higher undercooling than the isochronal ones.

Table 4.4: Temperatures of start of the pearlitic transformation during the isochronal tests and the respective undercooling (ΔT_{under}).

	Transformation start temperature and ΔT_{under}							
Austenitization	30 °C/s		20 °C/s		10 °C/s		5 °C/s	
	Ar_3	ΔT_{under}	Ar_3	ΔT_{under}	Ar_3	ΔT_{under}	Ar_3	ΔT_{under}
Heating at 30 °C/s to 950 °C and soaking for 10 s	591	136	600	127	632	95	642	85
Heating at 5 °C/s to 1000 °C and soaking for 10 s	571	156	598	129	621	106	622	105

To analyze the transformation kinetics, the S-curves were plotted from the previously calculated transformed fraction transformed data and the results are shown in Figure 4.14. During the isochronal treatment, the transformation presented a net S-shape whatever the test conditions, as seen in Figure 4.14a. The batch of curves can be arranged into two sets, one for the highest cooling rates (-20 °C/s and -30 °C/s) and one for the lowest cooling rates (-5 °C/s at -10 °C/s). It most likely occurs due to the transformation temperature that is lower for high cooling rates and higher for low cooling rates, which entails a lower driving force for the transformation at high temperatures, thus delaying its start.

The smallest PAGS samples presented the fastest kinetics of the transformation with the cooling at -20 °C/s. Besides, the progress of the transformation is not the same for the samples with different prior austenite grain sizes. The biggest grains presented a faster transformation rate after about 50% transformed when compared to the smallest grains and it is observed from the slopes variations of the S-curves.

For the isotherm ones (see Figure 4.14b) it is observed that the smallest PAGS material obtained with austenitization at 950 °C exhibits only one maximum of the transformation, which is achieved when the transformation reaches its completion. However, for the biggest PAGS (austenitized at 1000 °C), two steps are observed: one maximum, then the fraction transformed decreases, and finally, it ascends to the final complete transformation.

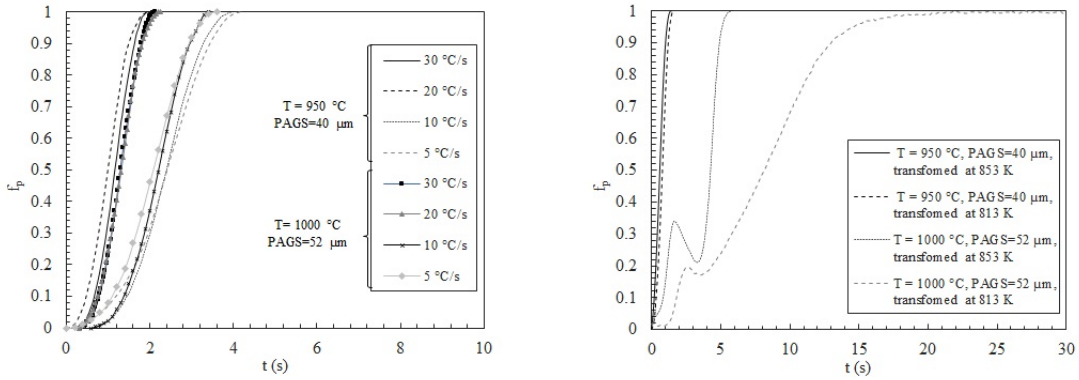

(a) (b)

Figure 4.14: Calculated fraction transformed during the (a) isochronal tests and the (b) isotherm tests for the 0.82%C samples starting from two different austenite grain sizes.

A derivative of the ΔL vs time curve was calculated to obtain the transformation rate (ΔL)/dt. The result is displayed in Figure 4.15. During the isochronal tests, all samples presented one transformation rate maximum.

For the isotherm cooling tests, the response is dependent on the PAGS of the material in the same way as it occurred previously in the transformed fraction vs time of Figure 4.14b. The two transformation maxima are only observed for the material with the biggest PAGS. This phenomena has previously been reported in the literature for pure iron and steel [149, 150, 151] and it is called abnormal transformation behavior. It is characterized by the presence of multiple transformation rate maxima. This is associated to a change of the transformation kinetics whose control arises from the transition between interface kinetic control to diffusion control. The meaning of these peaks for the eutectoid transformation will be discussed in the next section.

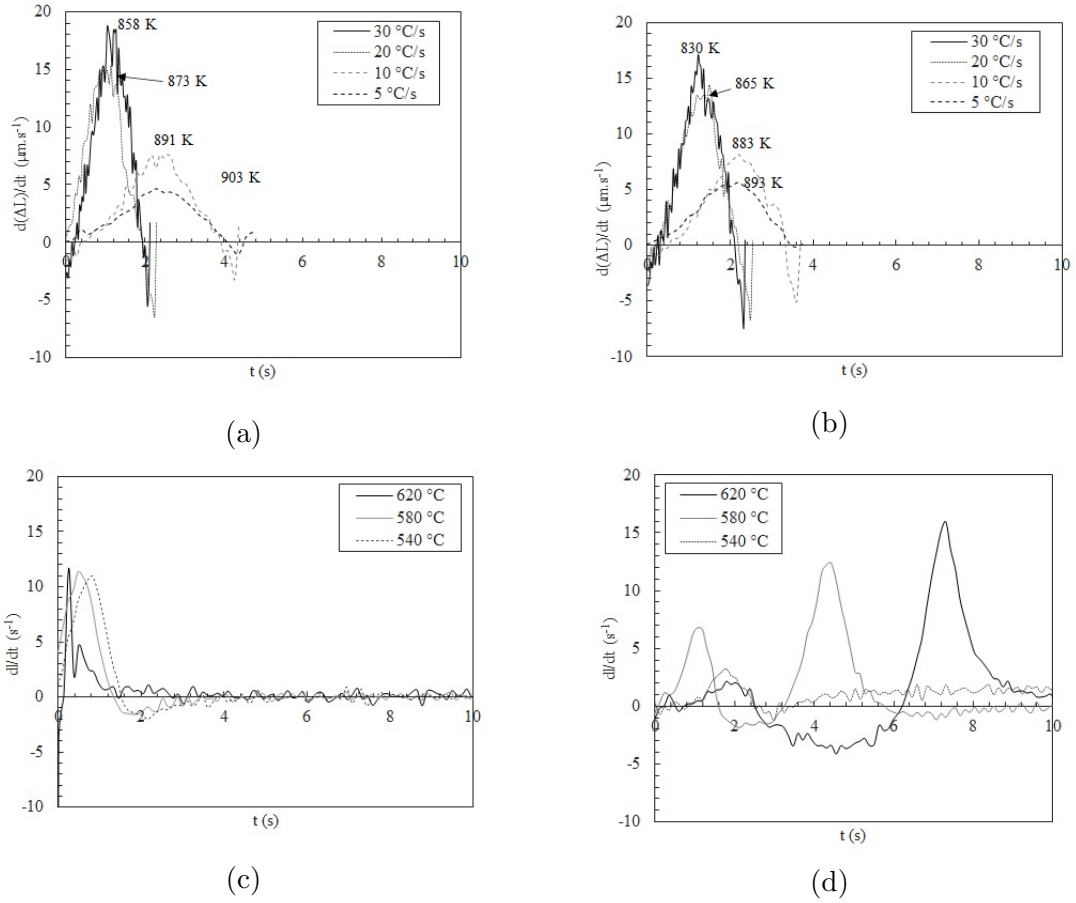

Figure 4.15: Transformation rate of the 0.82%C samples undergoing isochronal cooling, (a) and (b), and isotherm cooling, (c) and (d), starting from a small PAGS (austenitization at 950 °C) ((a) and (c)) and large PAGS (austenitization at 1000 °C) ((b) and (d)).

To associate the kinetics effects and the type of cooling on the microstructure, a metallographic investigation was carried out. The micrographs of the microstructures produced by the isotherm and the isochronal experiments reveal a strong effect of the cooling treatment on the morphology of the pearlite, as seen in Figure 4.16.

The samples transformed by the isotherm treatment (Figures 4.16 a and b) are mainly composed of a divorced microstructure and some lamellar regions, while the ones transformed by the isochronal treatment, 4.16 c and d, presented a rather lamellar microstructure with several branching and bridging between the cementite lamellas.

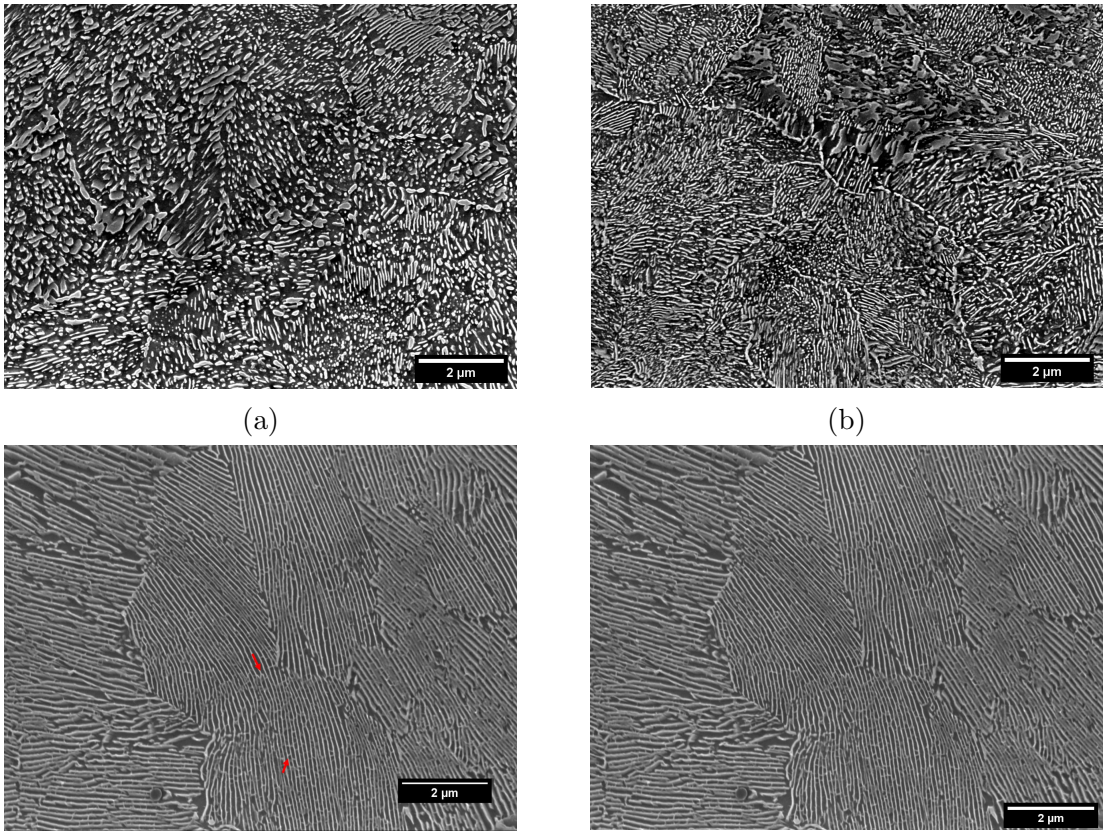

(a) (b)

(c) (d)

Figure 4.16: Representative micrographs of the obtained microstructure from the isotherm heat treatment at 540 °C from the two initial PAGS, (a) PAGS = 40 µm and (b) PAGS = 52 µm; and from the continuous cooled at -5 °C/s, starting from (a) PAGS = 40 µm and (b) PAGS = 52 µm. The gray background matrix is ferrite and in white is the cementite. The isothermally transformed samples presented to be finely divorced, as seen in (a) and (b), while the ones obtained by continuous cooling are long lamellar pearlite presenting a lot of branching and bridging between the cementite lamellae, as indicated by the arrow (c).

Another particular result observed here that deviates from the literature is that the divorced microstructure is independent of the austenitization condition. The finely divorced microstructure observed here is only associated with the type of cooling (isotherm) for both austenitization cycles. Whereas the isochronal test has produced a lamellar microstructure, independent of the austenitization condition and the cooling rate.

As said in chapter 2, the austenitization time and temperature control the presence of the undissolved carbides and a small distance λ between particles favors divorced transformation. When the austenite contains undissolved carbides, they play a role on the progress of the divorced transformation as depicted in Figure 4.17. In this

mechanism, the austenite depleted in carbon transforms to ferrite and the presence of carbides is essential to absorb the carbon that is diffusing away from the transformation front to join the already formed carbides particles and make them coalesce.

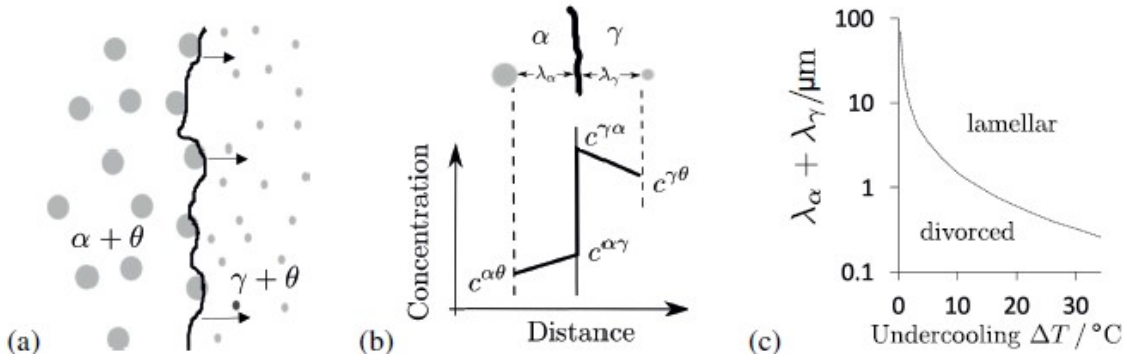

Figure 4.17: Divorced transformation scheme extracted from [10] (a) shows the advance of the divorced transformation front into the matrix of austenite with the divorced carbides, (b) shows the carbon concentrations in both sides of the interface and (c) is the curve that proposes the conditions under which the transformation will happen in a divorced manner.

From the current investigation, the carbide dissolution temperature (Ac_c) was shown to be around 840 °C, which means that the samples austenitized at 950 °C do not have any dispersed particles in austenite. Therefore, the above mechanism cannot be considered and the observed divorced transformation during isotherm cooling must have occurred in another way.

To have quantitative values of the obtained pearlite at the different temperatures and cooling rates conditions, the interlamellar spacing ($\overline{S}$) and the hardness were measured for all the conditions. The results are shown in Figure 4.18. The idea of having both the hardness and the ($\overline{S}$) for all these controlled microstructures is to have a kind of inventory for the latter characterization of the diagrams. Either with one information or the other, it is expected to know at which temperature the pearlite has formed.

It is seen that both the hardness and the interlamellar spacing vary linearly with the temperature of transformation or cooling rate. The lower the transformation temperature, or the fastest the cooling, the smaller the interlamellar spacing and the higher the hardness. It is in accordance with a common agreement that the undercooling is responsible for controlling the $\overline{S}$, and thus the hardness [152, 30, 27, 153, 151].

However, it is clearly seen in Figure 4.18 that the interlamellar spacing ($\overline{S}$) produced by the isotherm treatments is larger than the ones produced by the isochronal cooling, which is a surprising result since the temperatures at which the transformation takes place are higher for the isochronal transformation than for the isotherm ones.

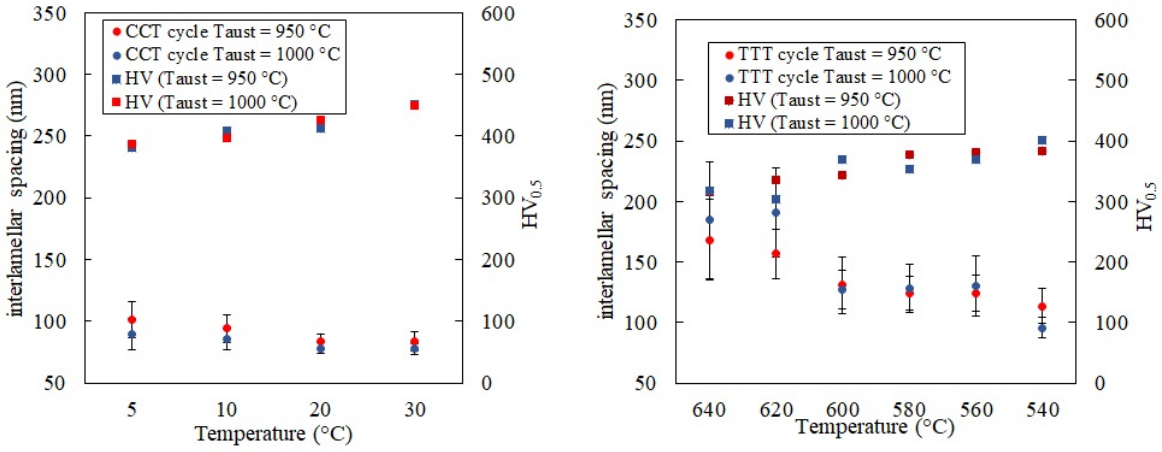

(a) (b)

Figure 4.18: Measure average interlamellar spacing ($\overline{S}$) for the (a) isotherm cooled and (b) continuous cooled samples.

Still analyzing the morphological features of formed pearlite at both cooling sets, an effort to observe the lamellar defects, such as holes in the cementite, was done. The cementite in pearlite is known to be feature-rich. Here the faults can be the presence of holes, gaps, bridging and branching, and variation in thickness, only to name a few. They have been documented to exist, but there is not much explanation on how they are formed.

It was observed that the defects related to holes and gaps were much more present in the material subjected to the isotherm transformation. While in the continuously cooled experiments, there is a massive presence of bridging and branching.

The samples austenitized at 1000 °C (PAGS = 52 µm) and isothermally transformed at 640 °C and 620 °C were deeply etched with Picral for 30 min [27] in order to analyze the cementite morphology in the few lamellar regions. The micrographs are reported in Figure 4.19. As the ferrite is dissolved, the cementite foils get loose and they superpose to each other. So, what is seen in the images are the cementite foils. This micrograph shows that, even in these very few lamellar regions, the pearlite formed during the isotherm cooling presented many large holes (evidenced by the arrows) during the formation of the cementite foil and these holes get even more numerous

with the decrease of the temperature transformation.

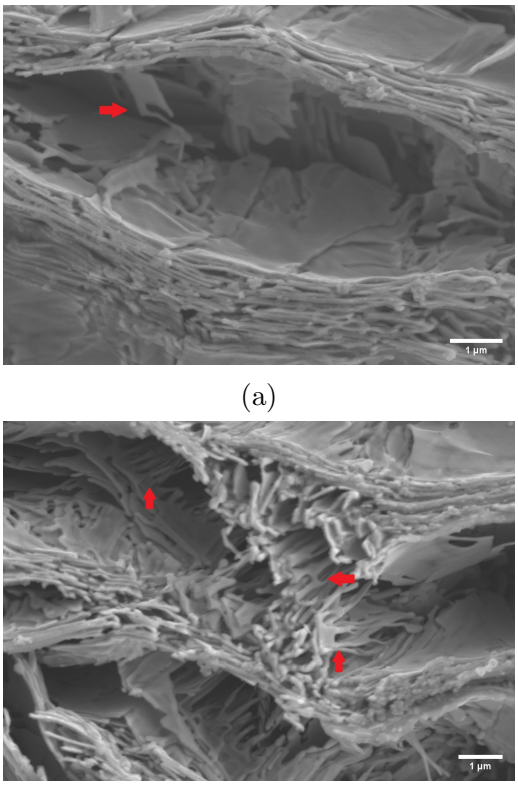

(a)

(b)

Figure 4.19: SEM micrographs of the cementite foils after the deep etching. Samples were austenitized at 1000 °C, PAGS = 52 µm, and isotherm transformed at (a) 640 °C and (b) 620 °C.

As the time set for the isotherm cooling had to be long enough for the transformation to finish and the needed time for the transformation was unknown beforehand, the isotherm cycles were done with 2 minutes of holding time at the transformation temperature to make sure that the transformation could reach its completion. To avoid any misinterpretation as a result of the degradation of the cementite related to the holding time at high temperatures, the tests at 540 °C were redone now with holding times of 1 minute, 30 s, and 10 s. As a result, the same microstructure was obtained independently of the holding time, being mostly divorced, and showing several holes in the few cementite foils.

With all the above data, it is possible to construct the transformation diagrams. It will be first discussed the continuous-cooling-transformation diagrams in the two austenitization temperatures and they are shown in Figure 4.20.

The dashed lines in the diagram, besides the ones indicating Ac_1 and Ac_3, indicate the phase is present but it was not possible to determine the transformation

temperature or that it is in such a small fraction that was not detected by the dilatometer.

The first remarkable difference between the diagrams is the presence of bainite in the diagram austenitized at 950 °C. It happens because the austenite is not homogeneous when austenitized at 950 °C for 10 s, thus leaving a region depleted in carbon that must have favored the local transformation to bainite.

Then, it is observed a difference in the critical cooling rate, which is defined as the cooling rate which the formation of martensite starts. For the sample austenitized at 1000 °C (PAGS = 52 µm), it was already observed some martensitic islands when cooled at -20 °C/s. While the ones austenitized at 950 °C (PAGS = 40 µm) had the first martensitic appearance at -30 °C/s.

This incident must be caused by the difference in PAGS. In large grains, the start of transformation is retarded because there are fewer nucleation sites. It is worth recapping triple or quadruple grain joints are the main nucleation sites for pearlite [6] and they get less numerous with the increase of the PAGS. This way the transformation at lower temperatures (fast cooling rates) has not enough time to finish transformation and the non-transformed austenite later transforms into martensite.

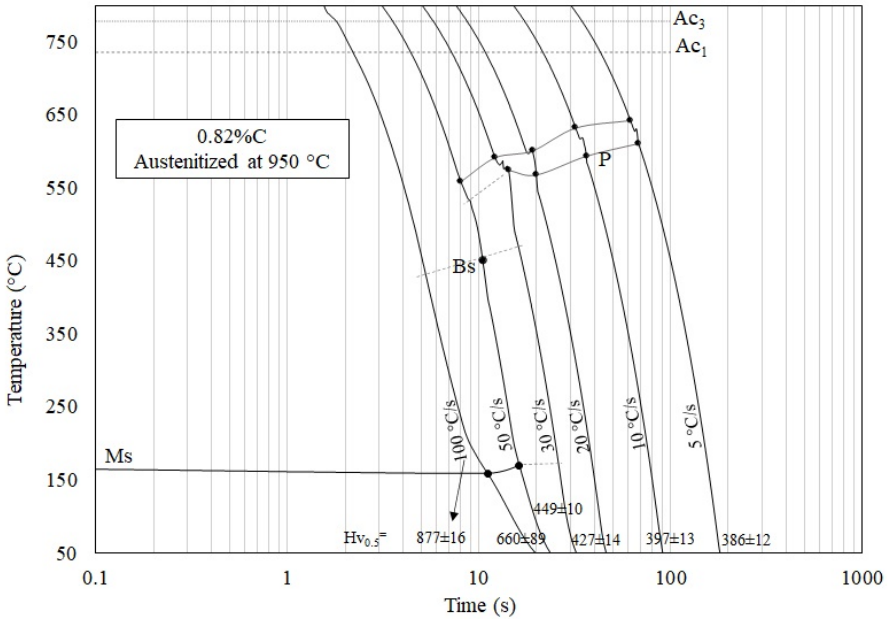

(a)

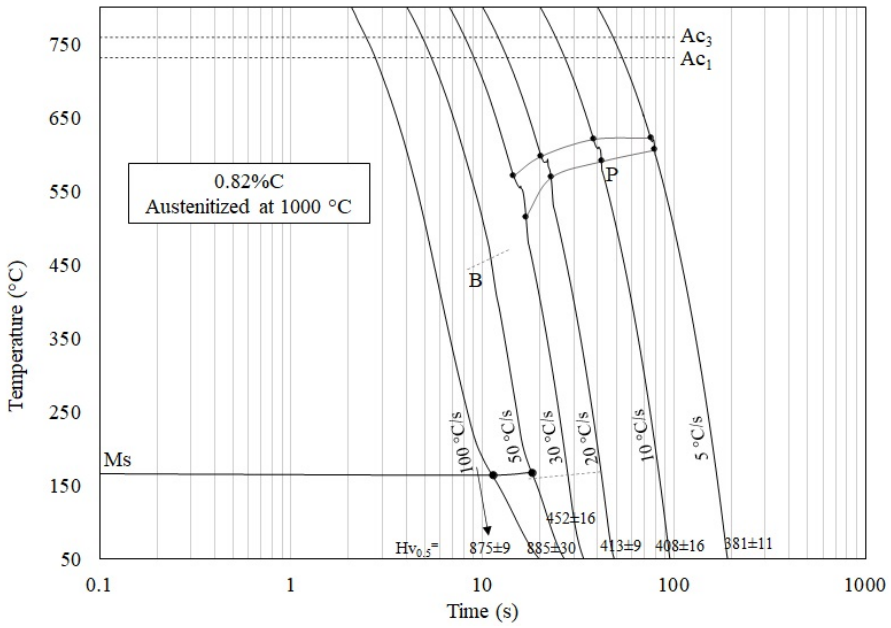

(b)

Figure 4.20: CCT diagrams of the samples austenitized at (a) 950 °C and at (b) 1000 °C.

Endorsing the retarded transformation explanation for the large grains, the amount of pearlite formed when cooled at 50 °C/s is different for the two austenitizing conditions. The micrographs are shown below in Figure 4.21, and it is seen that it is much easier to transform to pearlite when starting from a small grain size.

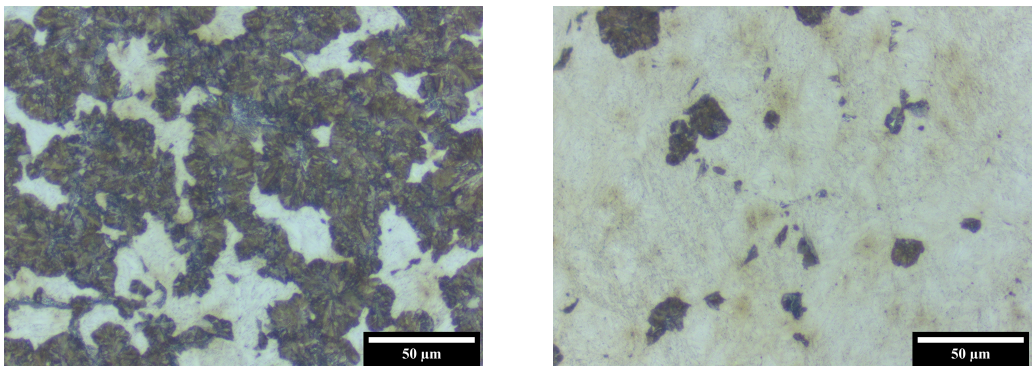

(a) (b)

Figure 4.21: LOM micrographs of the samples cooled at -50 °C/s previously austenitized at 950 °C (PAGS = 40 µm) and 1000 °C (PAGS = 52 µm).

The hardenability can play an important role in the critical cooling rate because it is known to increase with the carbon content [154]. As the sample austenitized at 950 °C presented much more pearlite and the one austenitized at 1000 °C, and it also appeared to be easy to form martensite in the latter than in the formed condition, one might think that it is less hardenable. However, in the previous results, the critical

cooling rates were most likely affected by the PAGS. The smaller grain sizes represent more nucleation sites for pearlite, thus favoring the reconstructive transformation, as observed in the CCTs.

The TTT diagrams are shown in Figure 4.22. The determination of the start and end of transformation was defined as 1 and 99 % transformed, respectively, and they were determined based on the fraction transformed of the S-curve. Since the samples were cooled at 100 °C/s to the isotherm temperature, there were some instabilities at the beginning of the isotherm heat treatment, thus causing some odd results especially at the time of the start of the transformation. Nevertheless, the tests follow the expected C tendency of conventional TTT diagrams and the distributions took last than 1 s to be settled, the information can still be correctly extracted from it.

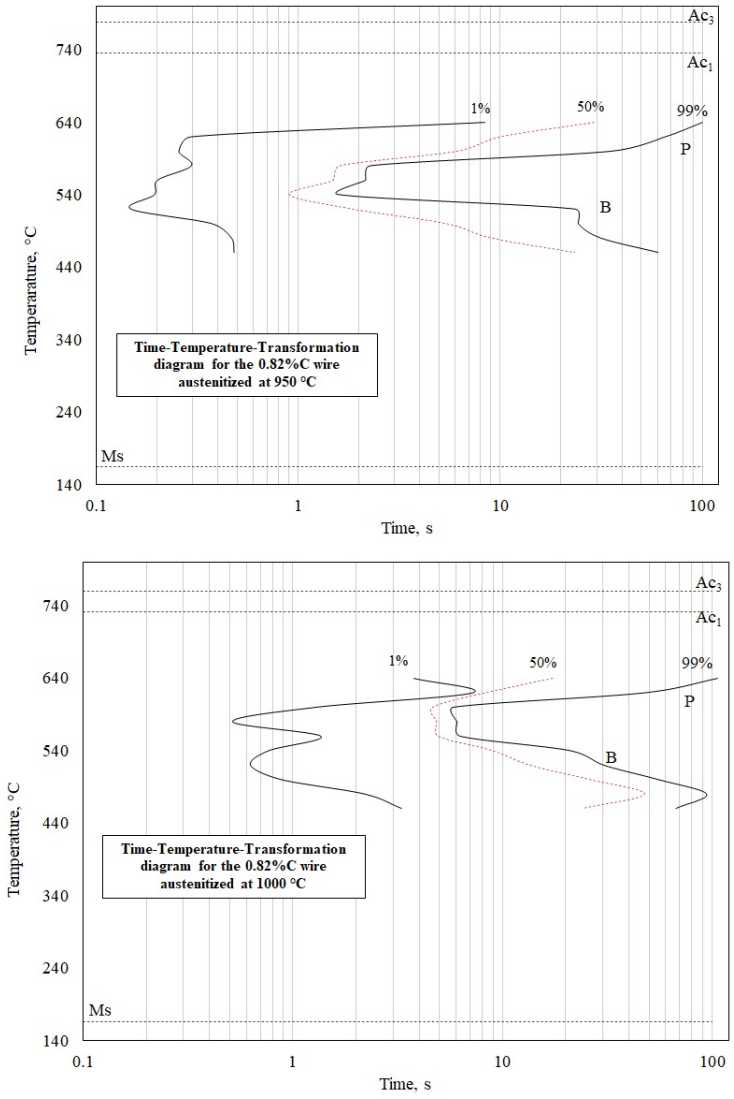

Figure 4.22: Time-Temperature-transformation diagram for the 0.82%C austenitized at (a) 950 °C and (b) 1000 °C.

It is very clear here that the transformation is delayed for the larger grain size since it starts almost instantaneously for the samples austenitized at 950 °C (PAGS = 40 µm) and takes a few fractions of second to start when austenitized at 1000 °C (PAGS = 52 µm).

It seems that the nose of the C curve does not vary with the austenitization, being around 560 - 540 °C. One remarkable thing is that the transformation happens much faster at 620 °C than at 640 °C and there is not so much difference in the $overline{S}$, which means that for the 0.82%C the formation of coarse pearlite would be optimized at 620 °C. It enhances the importance of the knowledge of the phase transformation for the optimization of the industrial process.

4.3.2 Hypoeutectoid and hypereutectoid compositions

In this subsection, the analysis carried out on the eutectoid composition, (effects of the heating rates, austenitizing time and temperature, cooling rates and temperature of isotherm cooling) will be conducted on the hypoeutectoid steel (0.72%C) and the hypereuctectoid steel (0.87%C). The focus here is to emphasize the effect of the carbon content on the considered transformation.

During heating

The CHT diagrams for the hypoeutectoid steel and the hypereutectoid steel are shown in Figure 4.23a and b, respectively. Although the TTA analysis has brought some valuable information about the homogeneity of the austenite, the used conditions are too distant from the real industrial practice, which is most likely described by the fast continuous heating.

Such as seen for the eutectoid composition, it was not possible to delineate the regions over which the austenite is homogeneous. The conclusions are the same based on the presence of the bainitic "black spots": over 1000 °C it is homogeneous.

First, whatever the carbon content, the bainitic islands (dark spots) are always seen. All the samples started from fully pearlitic microstructures, but it was observed that there are more numerous for the hypotectoid condition which is coherent with the fact that it is lowest carbon content studied and it would be the most susceptible to

transform to bainite. Regarding the hypereutecoid steel (0.87%C), the bainite appears when the steel is austenitized at 900 and 950 °C.

The Ms temperature varies with the carbon content and, therefore, the 0.72%C presented a higher temperature, around 180 °C, and for the 0.87%C it was around 150 °C. All the studied conditions led to the same Ms temperature, meaning that the high temperature austenite has the same amount of carbon in solid solution.

The hardness values also indicated the full dissolution of carbon at all austenitizing temperatures since they present about the same value for all the conditions, being around 840 HV for the 0.72%C and 870 for the 0.87%C.

The PAGS is affected by the carbon content, being the larger the grain the lower the carbon content for the same austenitizing condition. It is not such a large difference, 15 - 25 µm, but it is important information to keep in mind.

The diagrams are shown in Figure 4.23. The difference in the Ac_1 and Ac_3 values also have not greatly changed when compared to the eutectoid composition, around 728 °C and 727 °C for Ac_1 and 749 °C and 750 °C for Ac_3 measured during heating at 1 °C/s .

In summary, the effects observed during heating for the hypoeutectoid and hypereutectoid were in the amount of bainite formed during cooling caused by the non-sufficient austenitization time, which decreased with the increase in the carbon content; Then, the PAGS that seems to be sensitive to the chemical composition, thus diminishes in size with the increase of the carbon content.

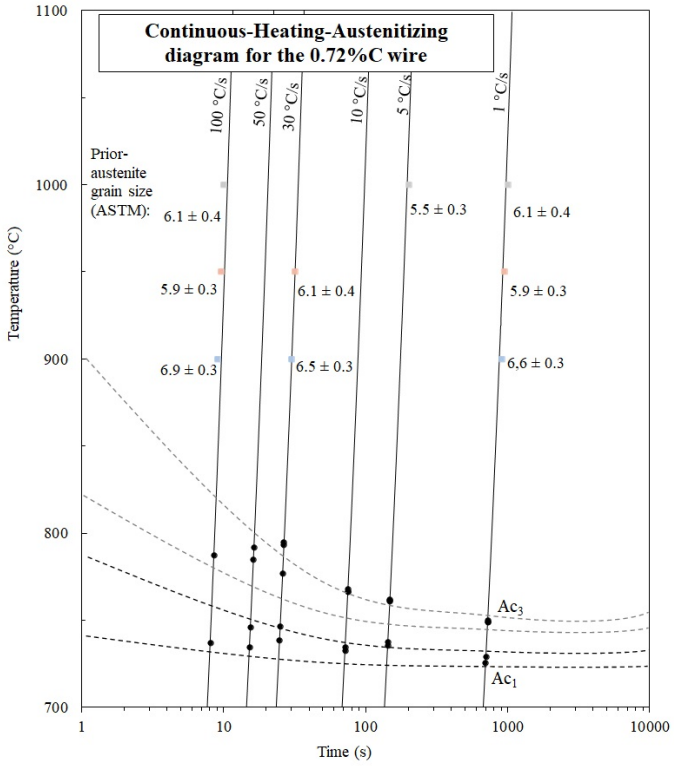

(a)

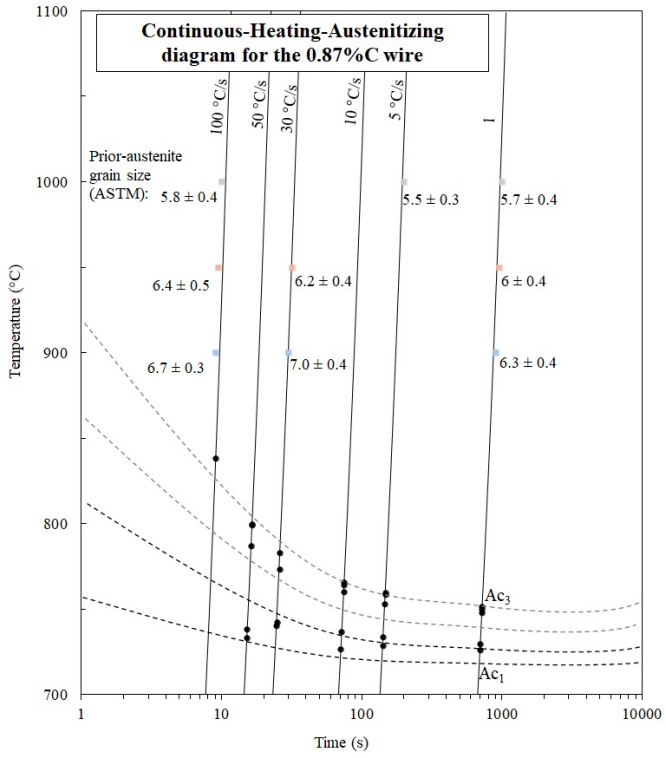

(b)

Figure 4.23: CHT diagrams of the samples austenitized at (a) 0.72%C and at (b)0.87%C.

During cooling

The pearlite transformation sensitivity to the carbon content is studied in this section and some questions are hoped to be answered:

- when the proeuteuctoid phases are formed before the pearlitic transformation during isothermal holding, does the formed pearlite present the same morphology?
- In case of the fully pearlitic microstructure formed in the hypoeutectoid or hypereutectoid steels, which is known to happen at high undercooling, the austenite would be either depleted or enriched in carbon. Would it affect the pearlitic morphology, somehow?
- Do the hypoeutectoid and the hypereutectoid transformations to pearlite are affected by the austenitization cycle in the same way as for the eutectoid composition? e.g. the critical cooling rates and the delayed transformation;

Figure 4.24 shows the micrographs of the microstructures obtained of the samples austenitized at 1000 °C then isothermally transformed at 560 °C and 520 °C for the 0.72%C and the 0.87 %C steel, respectively; and also the ones continuously cooled (isochronal tests) at 5 °C/s. The divorced pearlite was again observed with the isotherm cooling and the lamellar pearlite formed with the continuous cooling. **This result already answers two of the questions: first, the pearlite morphology was formed independent of the carbon content and, second, it was also independent of the presence of proeutectoid phases.**

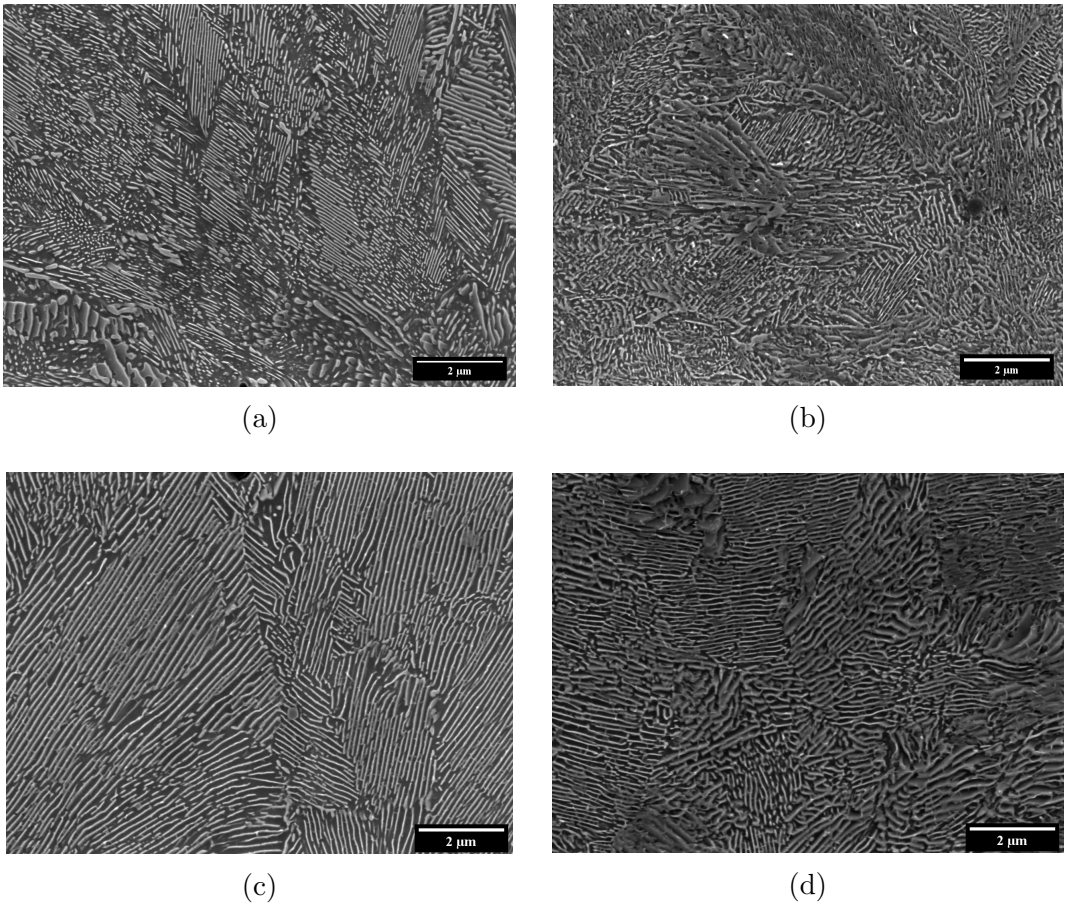

(a) (b)

(c) (d)

Figure 4.24: SEM micrographs of the hypoeutectoid samples (0.72 % C) on the left and hypereutectoid samples (0.87t.% C) on the right austenitized at 1000 °C and isothermally transformed at (a) 560 °C and (b) 540 °C, and (c) and (d) show the samples continuous cooled at 5 °C/s.

The bridging between the cementite lamella seems to be favored by the carbon content, being more densely present for the 0.87%C steel and the 0.82%C steel than in the 0.72%C steel. Even for the isothermal transformation at low temperature, the 0.87%C steel exhibites the lamellar regions with some bridging.

In Figure 4.25 are compared the transformation rates vs the transformation time curves for the hypo and hypereutectoid compositions with the previously analyzed eutectoid sample transformed by isotherm cooling. It is observed that the abnormal transformation happens for all the samples, Figure 4.25a and b, and the first peak seems to be carbon-dependent since it diminishes with the increase of the carbon content in the steel.

When analyzing the evolution of the two peaks in all the results and not only

the ones in Figure 4.25, it was seen that the two peaks are not so evident at high temperatures, then they become well defined in the intermediate temperatures, close to the nose in the TTT diagram; and finally, at low temperatures, the whole transformation occurs all in one peak as seen for the 0.82 %C, as shown in Figure 4.25c and d.

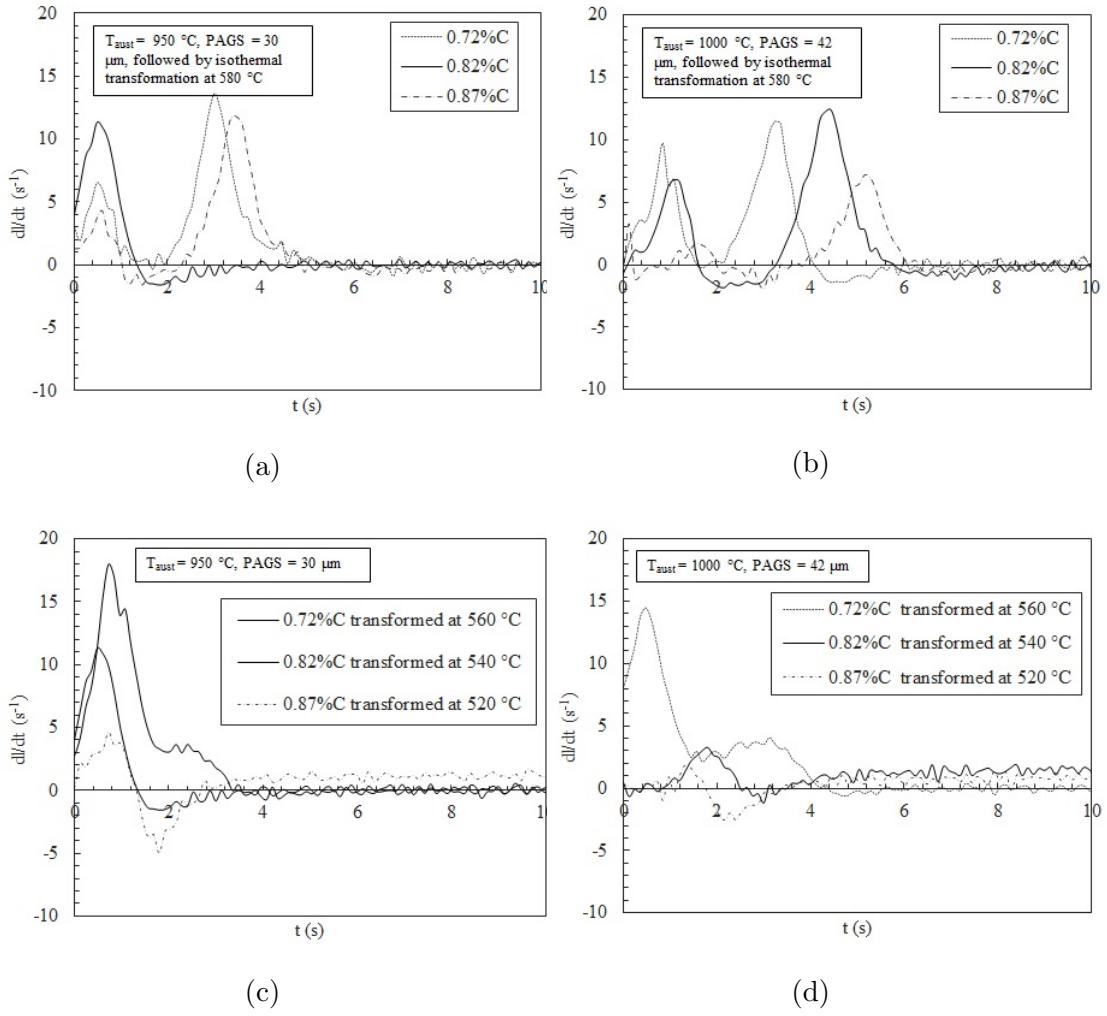

Figure 4.25: Transformation rate of the 0.72%C, 0.82%C and 0.87%C samples transformed at 580 °C (pearlite + proeuctoid phases formed) previously austenitized at (a) 950 °C and (b) 1000 °C; Then the samples transformed at 560 °C, 540 °C and 520 °C (fully pearlitic microstructures) for the 0.72%C, 0.82%C and 0.87%C, respectively, previously austenitized at (c) 950 °C and (d) 1000 °C.

The kinetics of the observed transformation for both the hypo and hypereutectoid compositions occur differently than the eutectoid transformation. The reason for it is clearly related to the formation of the proeutectoid phases and its different phase transformation kinetics, which is diffusion control for the latter and mix controlled for

the pearlite. It will be further discussed in the next section but, what is important to retain is that the two peaks were observed even when transformed from 950 °C; that at low transformation temperatures, the transformation occurs essentially in one peak and the obtained microstructure is almost fully pearlitic; and, finally, that the pearlite morphology was not affected by the presence of the proeutectoid phases, being divorced during isotherm cooling and lamellar during the isochronal one.

Finally,the TTT diagrams of the 0.72 %C and the 0.87 %C are shown in Figure 4.26. The first, and main, noticeable difference is that the start of the transformation is never delayed whatever the PAGS for the hypoeutectoid sample, whereas for the 0.8%C and 0.87%C steels, a strong delay occur as the PAGS increases. These results partially answer the third question about the carbon content, indeed, a high carbon content (hypereutectoid composition) is the only case of delayed transformation.

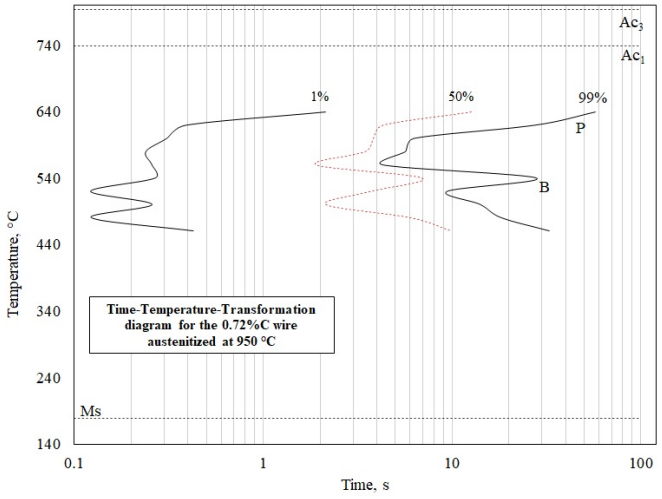

(a)

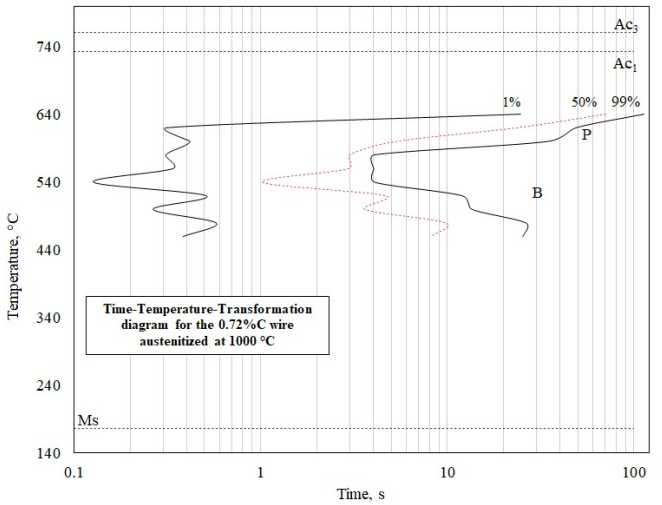

(b)

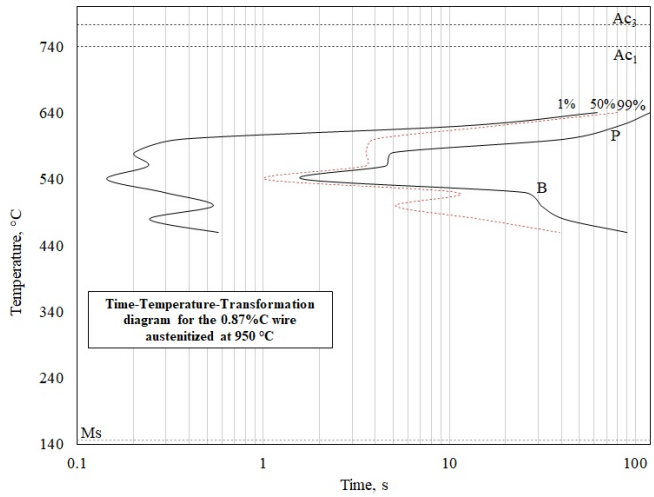

(c)

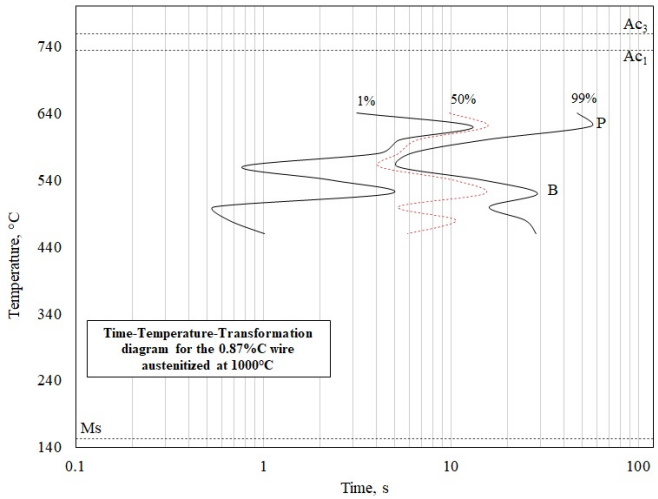

(d)

Figure 4.26: Time-Temperature-Transformation diagrams of the samples austenitized at 950 °C on the left and 1000 °C on the right for the hypoeutectoid, (a) and (b), and hypereutectoid, (c) and (d).

Ms is much higher for the hypoeuctectoid composition than for the hypereuctectoid ones, so as bainite start temperature (Bs), which is not indicated as a line in the diagram because the bainitic transformation progresses as diffusion dependent transformation that reaches its completion during isotherm transformation, even though it starts diffusionless with a defined starting temperature just like it is for martensite.

Lastly, the CCT diagrams have been produced and they are shown in Figure 4.27. The presence of bainite indicates the non-homogenization of austenite, as discussed before, and, therefore, the field of bainite is larger when austenitized at 950 °C than when austenitized at 1000 °C.

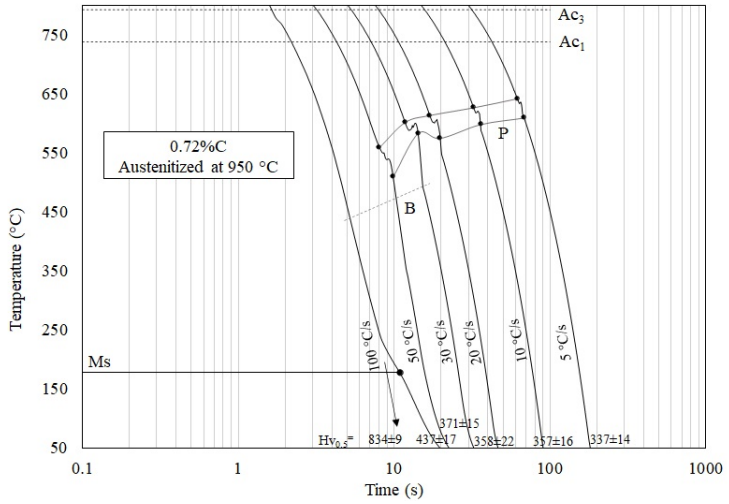
Ac3
Ac1
0.72%C
Austenitized at 950 °C
P
B
Ms
100 °C/s
50 °C/s
30 °C/s
20 °C/s
10 °C/s
5 °C/s
Hv0.5= 834±9 437±17 371±15 358±22 357±16 337±14
Temperature (°C)
Time (s)

(a)

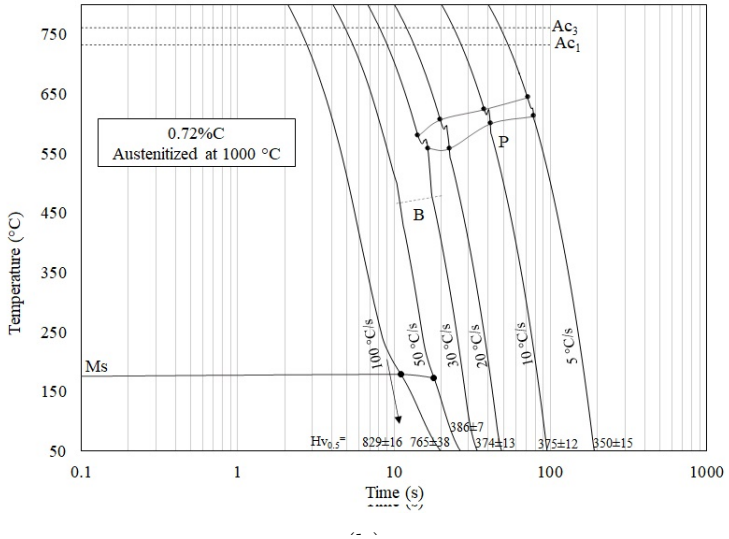
Ac3
Ac1
0.72%C
Austenitized at 1000 °C
P
B
Ms
100 °C/s
50 °C/s
30 °C/s
20 °C/s
10 °C/s
5 °C/s
Hv0.5= 829±16 765±38 386±7 374±13 375±12 350±15
Temperature (°C)
Time (s)

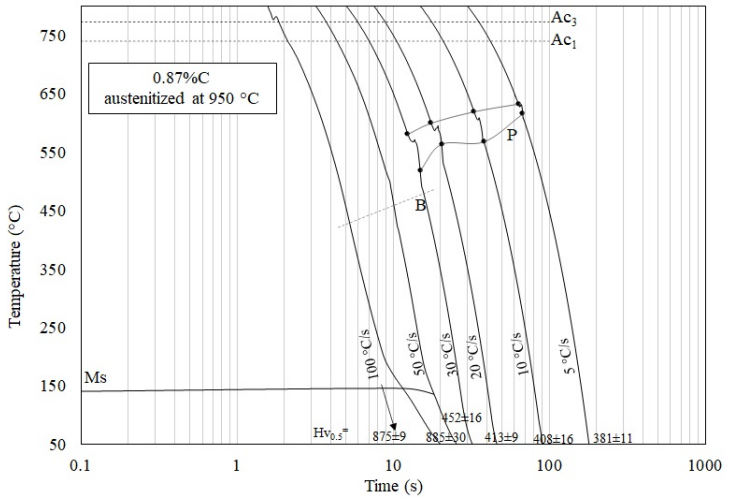
Ac3
Ac1
0.87%C
austenitized at 950 °C
P
B
Ms
100 °C/s
50 °C/s
30 °C/s
20 °C/s
10 °C/s
5 °C/s
Hv0.5= 875±9 885±30 452±16 413±9 408±16 381±11
Temperature (°C)
Time (s)

(c)

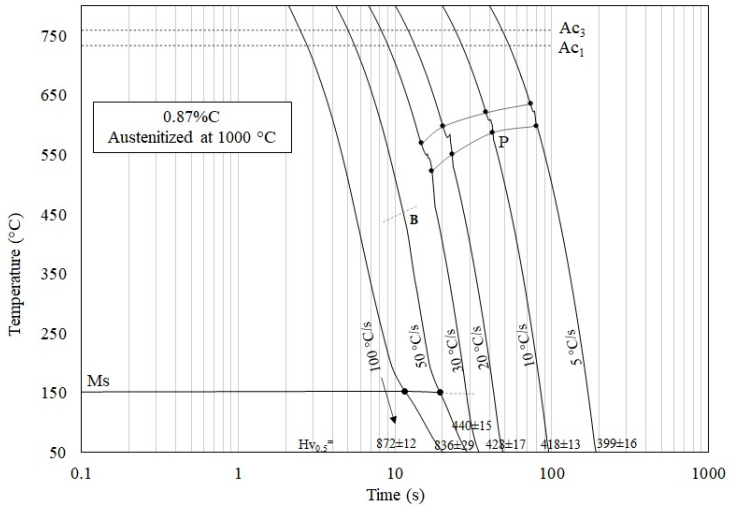

(d)

Figure 4.27: Continuous-Cooling-Transformation diagrams of the samples austenitized at 950 °C on the left and 1000 °C on the right for the hypoeutectoid steel, (a) and (b), and hypereutectoid steel, (c) and (d).

The critical cooling rates, i.e. the cooling rate that triggers the martensitic transformation, changed greatly when compared to the hypoeutectoid steel, being 100 °C/s when austenitized at 950 °C and 50 °C/s when austenitized at 1000 °C; and not so much when compared to the hypereutectoid composition, being around 50 °C/s when austenitized at 950 °C and 30 °C/s when austenitized at 1000 °C. The hardenability has played an important role and, as expected, the hypoeutectoid is less hardenable and it is harder to transform to martensite. However, looking at this martensite formation field, the 0.87%C seems hardenable than the 0.82%C. The formation of the proeutectoid phases must have drained the carbon atoms from austenite during the pearlitic transformation, which does not happens for the 0.82%C. It explains why the transformation at 20 °C/s forms some pearlite and then martensite in the eutectoid composition austenitized at 1000 °C and it transforms completely to proeutectoid cementite + pearlite in the the 0.87%C. It is because after the start of the pearlitic transformation, the remaining austenite for the 0.82%C is richer in carbon than the 0.87%.

This results finally answer the last question about the carbon contents and, indeed, the austenitization cycle affects the critical cooling rates of both the hypo and hypereutectoid compositions with the same tendency of the eutectoid composition: the lower the austenitization temperature, the higher the critical temperature.

The global conclusions of the effect of the carbon content concern the prior austenite

grain size, the kinetics of the transformation during isotherm cooling, and the formation of bainite and martensite during continuous cooling.

4.3.3 Standard conditions

As previously mentioned, there is an ASTM standard [97] created for the production of a transformation diagram of hypoeutectoid steels. To erase all the effects of the mechanical history, it is recommended to perform a prior "stabilization cycle" at 650 °C for 10 minutes. This diagram was also produced for the eutectoid composition to evaluate, first, if the standard is also valid for hypereutectoid samples; second, to observe the effects of the austenitization and the stabilization cycle on the subsequent pearlitic microstructure; third and finally, if the pearlite formed in this condition is any different of the pearlite formed in the wire conditions.

The average PAGS obtained from the ASTM austenitization cycle is 38 $\mu m \pm 5$ μm, which is just a bit smaller than the one obtained when austenitizing at 950 °C for 10 s.

It was previously mentioned about a simple method of prediction of the PAGS using the equivalences of time and temperature of the transformation, based on Fick's law. Basically it allows comparing two cycles with different times and temperatures that result in the same PAGS. The results of section 4.3.1 are in agreement with the calculations, meaning that the predictions were correct, as shown in reference [14]. When calculating the equivalent time at 950 °C to produce the same PAGS as 797 °C for 5 min, the result suggested that it should stay for only 0.5 s, which does not agree with the real obtained result. However, as CHT results were performed with the same mechanical history while the ASTM cycle had the stabilization cycle before the austenitization, one might think that it can have affected the PAGS. The PAGS was then measured in a sample with the ASTM austenitization cycle but this time without the prior stabilization. The obtained average grain size was 37 $\mu m \pm 4$ μm, thus proving that the stabilization cycle does not affect the PAGS grain size, whatsoever.

The hardness was measured with and without the stabilization cycle to see if there is an effect on the general homogenization. The result is shown below in Figure 4.28. From this result, it is possible to conclude that, whatever is happening during the stabilization cycle, this does not hinder the later homogenization of austenite but, in fact, it has actually helped. Indeed, the sample austenitized with the prior stabilization cycle presents the same hardness as the other non-standard austenitization cycles,

whereas the one without presents a lower hardness, thus meaning that it presents less carbon in solid solution.

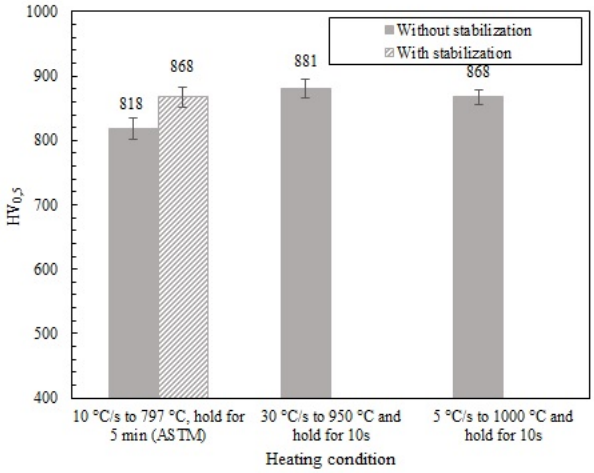

Figure 4.28: Vicker hardness measurements of the pearlite formed after the austenitization cycle in the WTD and STD conditions.

It is worth noting that the austenitization temperature is below the Ac_c temperature, meaning that it could be expected to have the undissolved carbides. As this standard was proposed for the hypoeutectoid steels, the carbide dissolution was not a concern, and it is an important point to be considered for the hypereutectoid steels.

The last characterization of the heating is about the black spots, that were here set to be a sign of non-homogeneity of the austenite. The micrographs in Figure 4.29 indicate that the black spots assigned to be bainite are present in both cases, with and without the stabilization cycle. However, the latter seems to produce less and smaller islands, meaning that the cycle without stabilization would entail more homogeneous austenite. This result is exactly the opposite of the hardness, which most likely means that the one without the stabilization cycle presents some undissolved carbides particles and the ones with the stabilization has more carbon in solid solution, but it is not homogeneous.

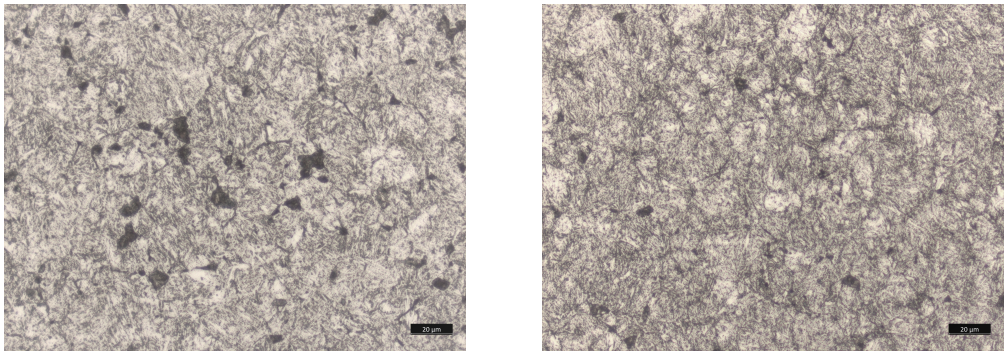

(a) (b)

Figure 4.29: Bainite formed during cooling observed by the black spots in the micrographs (a) with and (b) without the the stabilization cycle.

The previous consideration is only regarding the heating and forthwith are discussed the results regarding the continuous cooling diagram in the standard conditions. The produced diagram is seen in Figure 4.30.

The highest critical cooling rate was measured in the STD condition (80 °C/s) and the bainite is only observed at very high rates. It means that the reconstructive transformation is much favored in this conditions, which is probably due to the presence of the undissolved carbides that entail less hardenable austenite.

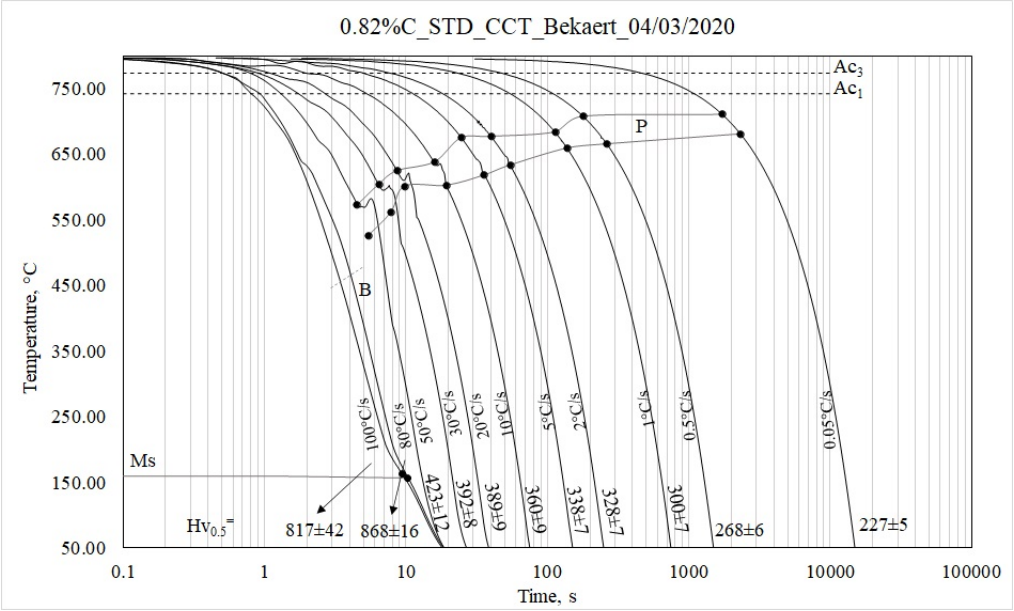

Figure 4.30: CCT diagram done using the standard conditions for the 0.82%C.

Then, the morphology of the pearlite formed in these cycles was analyzed. One representative micrograph is shown in Figure 4.31. The microstructure is lamellar and, differently from the other CCT and TTT, there were no special features such

as divorced microstructures with many holes, nor numerous branching and bridging between the lamellas. Most of the pearlite formed during this cycle is the closest to the "ideal" lamellar pearlite.

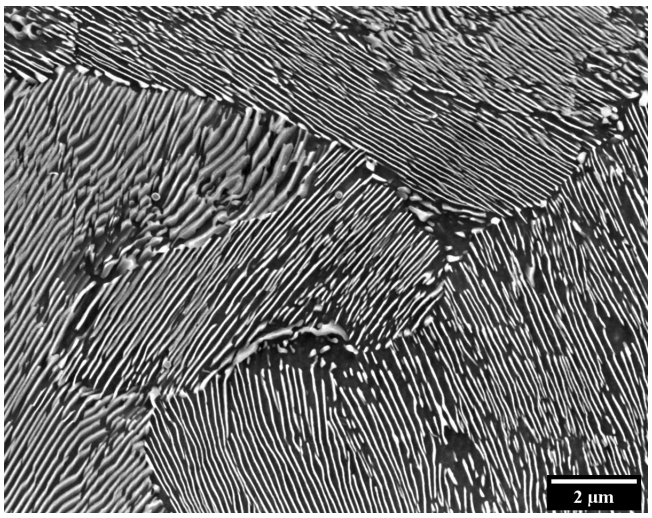

Figure 4.31: Representative micrograph of the lamellar pearlite morphology formed during the CCT in the standard conditions.

Since the cooling cycle is the same as the continuous cooling in the WTD condition, it is proven here that the austenitization effectively affects the pearlite morphology. Besides, another interesting feature observed is that the average interlamellar spacing obtained from the sample cooled with the same cooling rate as the CCT in the WTD are larger for CCT in the ASTM.

The comparison of the $\overline{S}$ obtained in both STD and WTD conditions are displayed in Figure 4.32. The interlamellar spacing is much larger in all the cooling rates, which occurs because the transformation occurs at higher temperatures for the ASTM samples. So, the pearlite transformed at around 640 °C is expected to be coarser than the one transformed at 600 °C.

Essentially, from this section, it is seen that the initial state of the microstructure and the austenitization can greatly change the later pearlitic transformation. Moreover, it can also be concluded that the standard ASTM A1033-18 [97] is not entirely suitable for the hypereutectoid steels, and maybe a higher austenitization temperature would be more reasonable.

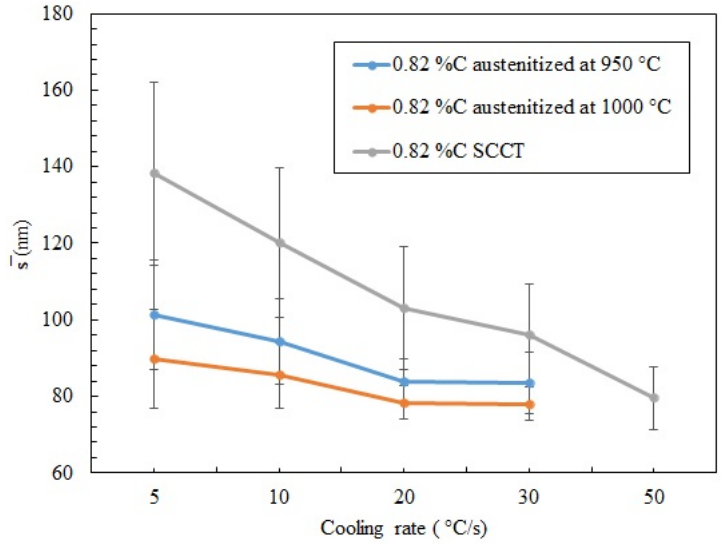

Figure 4.32: Comparison of the average interlamellar spacing ($\overline{S}$) of the pearlite obtained with the two WTD and the STD conditions.

4.4 Influence of initial microstructure

To analyze if there is any effect for the austenitic transformation starting from the pearlite or the martensite, some tests were performed starting from the martensite.

Previous authors have analyzed the austenitization starting from the different microstructures and it was seen that the most important parameter was the particle size, since it would define whether the austenite formation would be more or less diffusion dependent.[51]

The hardness of the samples starting from pearlite and from martensite after the austenitization cycle and subsequent quenching is reported in Figure 4.33. Starting with a pearlitic or martensitic matrix does not affect much the hardness of the final product, except may be at very high heating rates.

This result indicates that the conversion of austenite from pearlite is easier than from martensite since even at fast heating rates the transformation has reached its fulfillment.

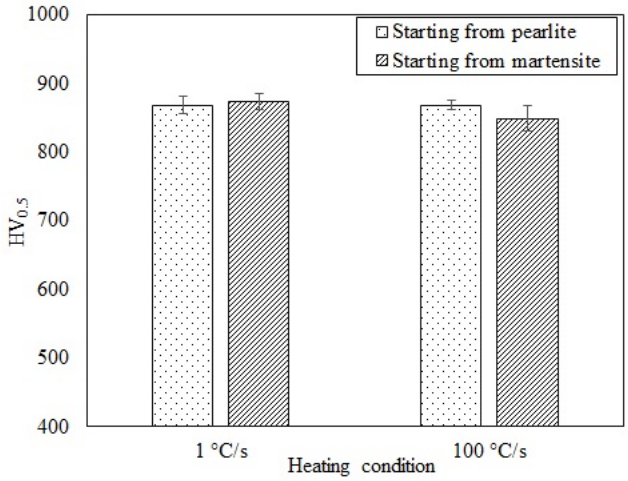

Figure 4.33: Hardness obtained after the austenitization starting from the pearlite and the martensite.

4.5 Influence of mechanical history

The influence of the mechanical history was investigated by carrying out the same heat treatment for the production of the CHT for the three wires drawn at the different initial amounts of deformation (ϵ_d = 0.97, 1.39 and 1.83). The clear question to be answered in this section is: **Can three wires of the same composition, only differing by the mechanical history, present the same final microstructure after the austenitization cycle?**

To answer this question, many aspects can be considered. For instance, if the heating is analyzed, does austenite formed from each of them present the same homogenization? Do they have the same PAGS? And then, if the cooling is analyzed, are the pearlite morphologies, interlamellar spacing, colonies, and nodules size the same? And still, does the final microstructure present any grain texture in the longitudinal or transverse cross-section? and crystallography texture?

As there are too many parameters that can be affected, only a few of them were investigated to give a more pragmatic answer. Therefore the PAGS, the homogenization of the austenite and the pearlite morphology were considered.

The PAGS was measured and no effect of the drawing strain $\epsilon_d = 1.83$ was observed, both at the longitudinal and the transverse cross-section. All the micrographs presented about the same equiaxial grain size of around 35 µm when austenitized at 900 °C and 52

µm when austenitized at 1000 °C for the 0.87%C. And concerning the homogenization, the micrographs were fairly similar, not presenting much difference in the amount of bainite between the different drawing strains ϵ_d. Finally, the hardness, such as the other results, has not shown any variation, being always around $HV_{0.5}$ 880 for the 0.87%C and 800 for the 0.72%C.

For the pearlite formation, there is no effect on the morphology nor hardness, being 350 HV when transformed at 620 °C and 415 HV when transformed at 520 °C for the 0.87%C. It shows, again, that there is no effect of the initial strain.

Therefore, it is conclusive that the austenitization, even at the lowest temperature (900 °C), was enough to erase the effects of the initial amount of deformation.

It already answers the question about the grain texture, because after drawing, the wires present elongated grains, which were entirely restored equiaxial after the austenitization.

The crystallography texture can also be affected by the mechanical history. The increase of the accumulated strain entails a stronger texture in the material. Since the ferrite is known to sometimes produce a memory effect [4], it is important to characterize the drawing texture, then verify if the ferrite lamella presents the memory effect or if the austenitization cycle is also capable of erasing all the texture.

A summary of the performed EBSD analysis is in annex B. It was concluded that all the studied conditions presented a $\alpha - fiber$ texture after drawing, which is characterized by the alignement of the $< 110 >$ plans with the drawing direction, and that this texture disappeared after the heat treatment, showing that there is no memory effect.

Even though there might be a soft effect of anisotropy at the nodule level, it does affect the mechanical properties of the pearlitic steels and, therefore, it is considered here that there is no effect of the mechanical history after the austenitization over 900 °C.

4.6 Recrystallization of pearlite

In the previous sections, some pieces of evidence of phenomena before the austenitization were observed, which means that some recovery or recrystallization are happening in the ferrite lamella or spheroidization, in the case of cementite. However, it is not very clear how exactly it would occur for the pearlitic microstructure. Whatever is this phenomenon, it was seen not to affect the transformation after the austenitization. To understand what is happening and if can affect under other treatment and/or deformation conditions, it was investigated through interrupted tests just before the pearlite to austenite transformation, at 700 °C, to analyze the microstructure before the austenitization.

A very short review of what is known until now in the literature, the recrystallization is only known to occur at very small proportions, only grains with a few dozen of nanometers, inside the pearlitic lamella [155, 156, 157]. The annealing of the pearlitic microstructure is known to promote the spheroidization of the cementite lamella at high temperatures and long times [71] and, as it becomes almost amorphous after high strain drawing, it was observed to occur a type of nano-crystallization at low temperature annealing [112].

The SEM micrographs of the interrupted tests of the wires at 700 °C are shown in Figure 4.34. It is seen a clear advance in the spheroidization of the cementite both at slow and fast heating rates. However, there is not much information to be extracted from the ferrite, since it is only seen as the matrix in the background.

The progress of the spheroidization also changed with the amount of deformation, being more the more deformed the more spheroidized.

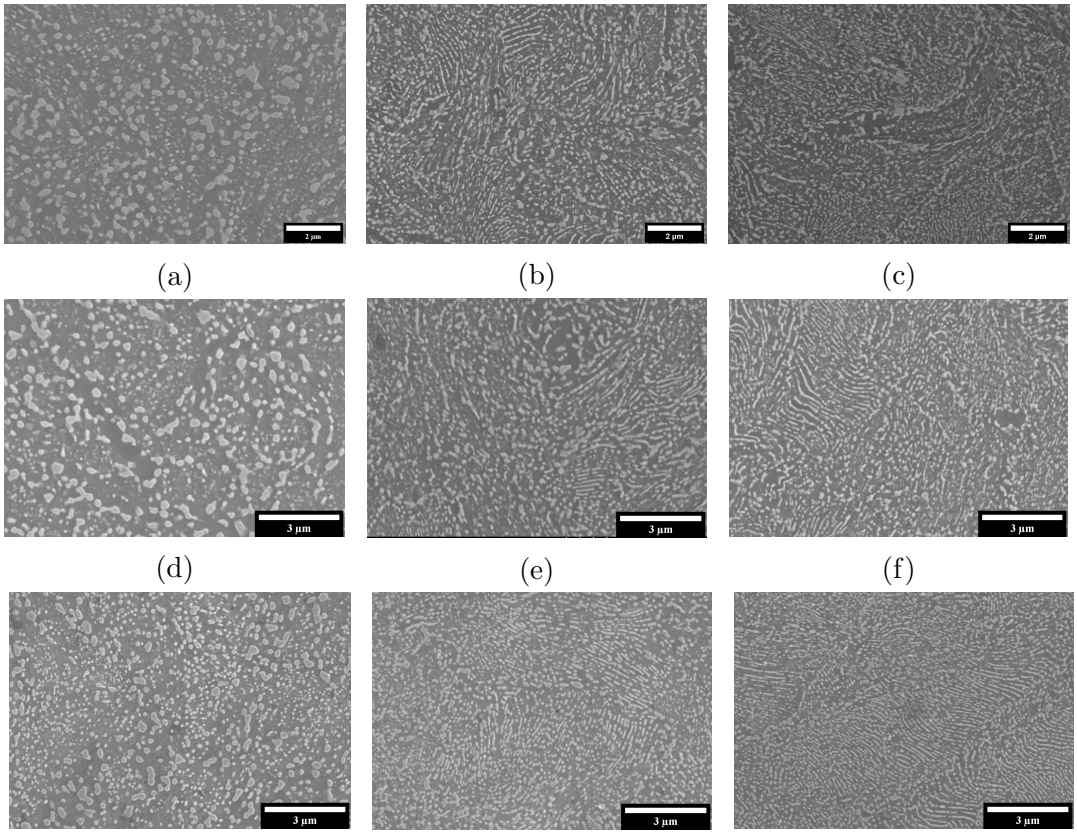

Figure 4.34: SEM micrographs of the 0.87%C submitted to the interrupted tests at 700 °C heated (a), (d), (g) at 1 °C/s, (b), (e), (h) at 30 °C/s and (c), (f), (i) 100 °C/s, being the first line (a, b,c) the $\epsilon_d = 1.83$, the second line (d,e,f) the $\epsilon_d = 1.39$ and last one (g,h,i) the $\epsilon_d = 0.97$

Hardness tests were performed on the samples and the results are seen in Figure 4.35. A great softening is observed in the sample even when heated at 100 °C/s, which again, it does not give direct information about the ferrite, once this tendency is both seen in spherodized samples and also recrystallized samples and the spheroidization is been confirmed to happen.

To have some more precise information about the phenomenon occurring in ferrite it was needed to be investigated at a nanometric level, therefore, TEM and TKD were performed on the 0.87%C wires with $\epsilon_d = 0.97$ and $\epsilon_d = 1.83$. Same way as done for the texture analysis, the TEM investigation started in the deformed state to analyze the evolution of the microstructure.

As previously described by other authors, the cementite after the drawing is almost amorphous, not being possible to identify any long-range crystal organization.[158, 18].

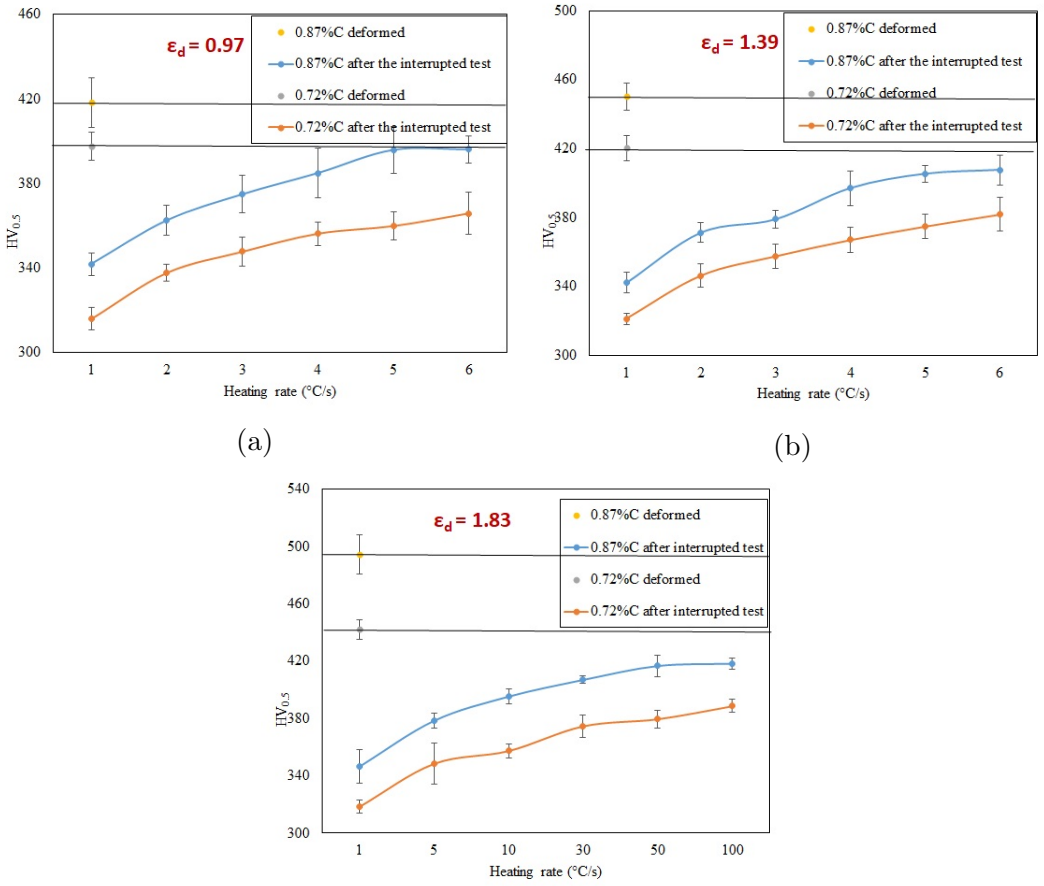

Figure 4.35: Hardness of the 0.72%C and 0.87%C steels with different drawing strains submitted to the interrupted tests at 700 °C heated at (a) 1 °C/s, (b) 30 °C/s and (c) 100 °C/s

HRTEM analysis of the deformed pearlite with $\epsilon_d = 0.97$ and 1.83 are shown Figure 4.36. In both cases is seen that both the cementite and the ferrite are intensely deformed and, for $\epsilon_d = 1.83$ the cementite is indeed highly deformed being almost in an amorphous state which is seen both by Fast Fourier Transform (FFT) and the inverse Fast Fourier Transform (IFFT). It is important to precise that the former gives the image corresponding diffraction pattern, while the latter gives a lattice-fringe representation that corresponds to the selected planes in the FFT. The FFT of the cementite deformed with a $\epsilon_d = 1.83$ looks almost like an amorphous diffraction pattern.

The FIB lamella was extracted both at the surface and the core and no difference was observed regarding the magnitude of dislocations.

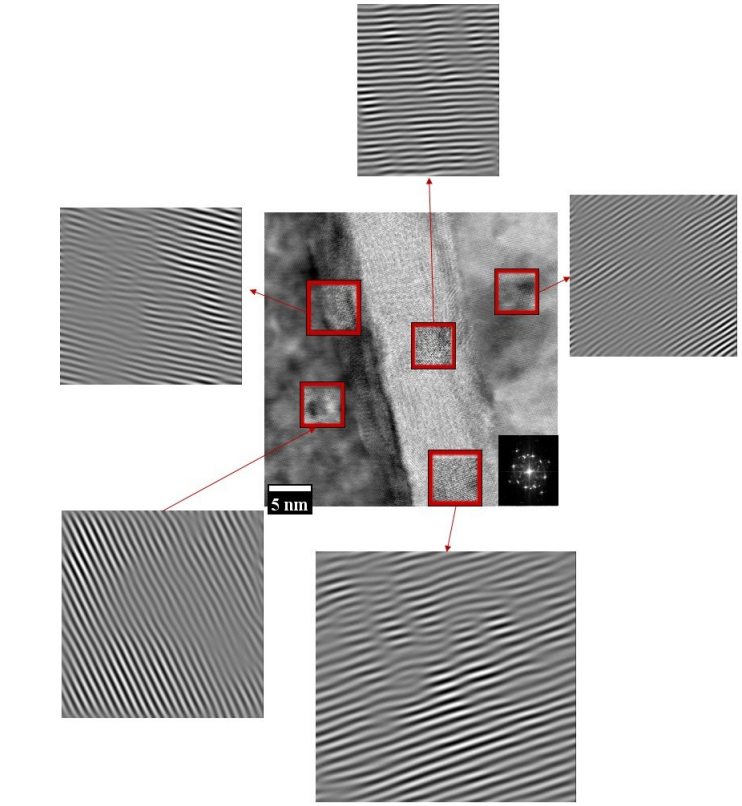

(a)

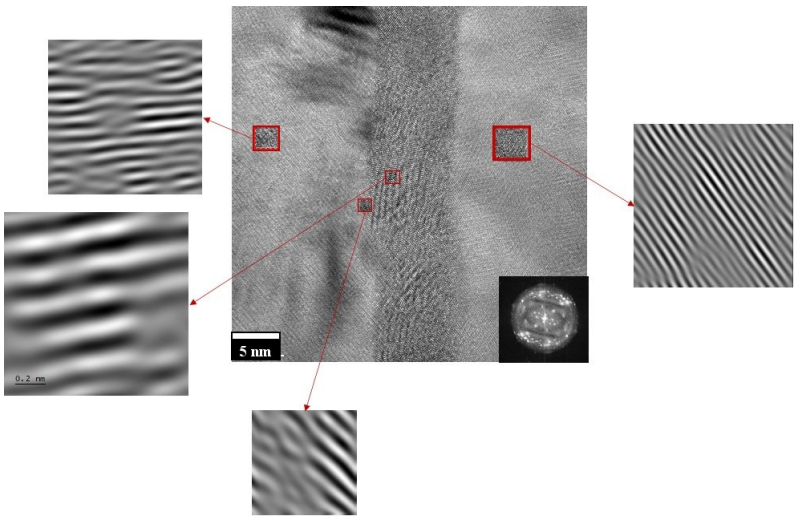

(b)

Figure 4.36: HRTEM analysis of the wires in the deformed state with a drawing strain of (a) $\epsilon_d = 0.97$ and (b) $\epsilon_d = 1.83$. Detailed regions showing the selected area FFT and IFFT images obtained inside the boxed region.

Then the samples heated to 700 °C at 1 and 100 °C/s were also analyzed. The TEM micrograph is shown in Figure 4.37. The cementite, the same way as seen in the SEM micrograph, is completely spheroidized when heated at 1 °C/s and partially spheroidized when heated at 100 °C/s. They could only be identified with the help of

the composition map, as shown in Figure 4.37a. The ferrite is no longer lamellar, and it is now seen in the TEM micrographs as grains.

Comparing the two drawing strains, it is seen for $\epsilon_d = 0.97$ the cementite is less spherodized than $\epsilon_d = 1.83$ heated at 100 °C/s, which indicates that the spheroidization is favored on deformed samples.

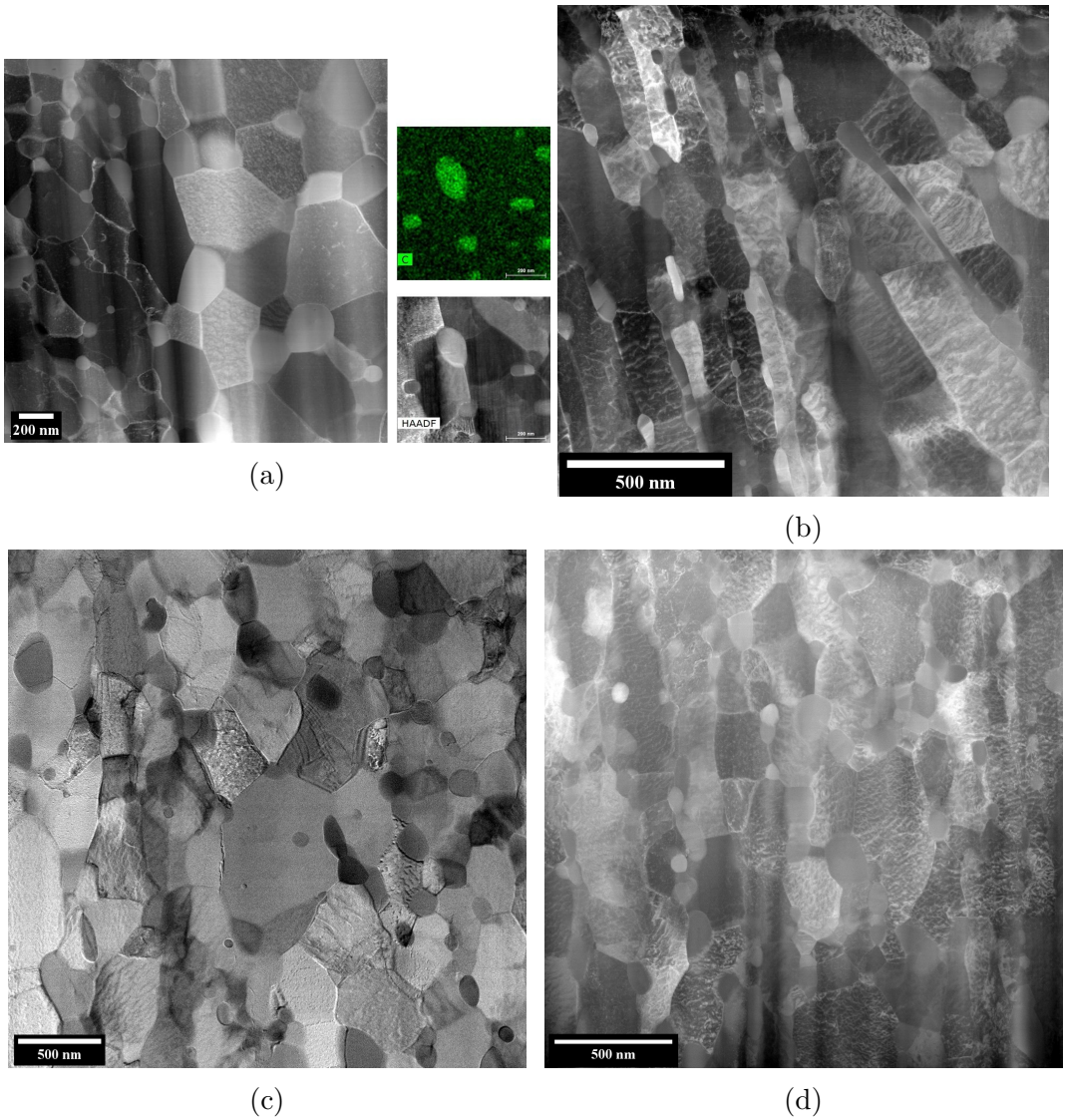

(a) (b) (c) (d)

Figure 4.37: TEM analysis of the wires in after the interrupted tests starting from a drawing strain of (a) and (b) $\epsilon_d = 0.97$ and (c) and (d) $\epsilon_d = 1.83$. On the left are the samples heated at 1 °C/s and on the right are the ones heated at 100 °C/s

Besides, after the heat treatment at 1 °C/s, it is seen the spheroids present a perfect cementite organization without dislocations inside it, thus proving that the cementite has recovered completely. It is seen that there are much fewer dislocations inside the ferrite too and it indicated that new grains are formed.

In the samples heated at 100 °C/s, again, the cementite is recovered. The ferrite is still granular, but with some elongated grains, which still allows finding the initial lamellar microstructure.

Although the ferrite seems to have recrystallized, it is odd that the grains observed in the sample heated at 100 °C/s are similar to the ones observed at 1 °C/s. It seems unlikely for the microstructure to recrystallize in such fast heating since the time and the energy given to the system are smaller. Therefore, the TKD analysis was performed to have a measurement of disorientation between these grains to a better precision it is recrystallization or recovered. The results are seen in Figure 4.38.

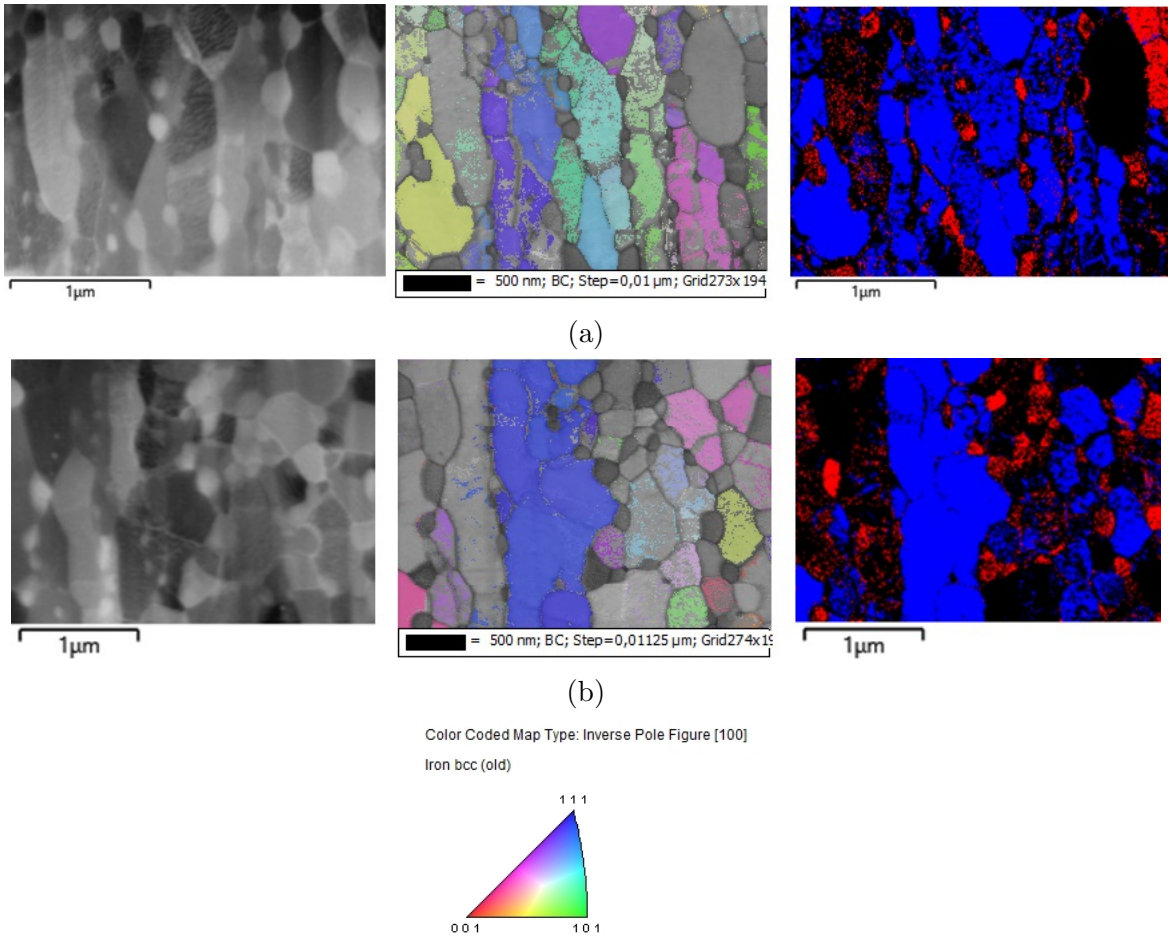

Figure 4.38: TKD analysis of the wires deformed at $\epsilon_d = 1.83$ submitted to the interrupted heating test at 700 °C heated at (a) 1 °C/s and (b) 100 °C/s. From left to the right: FSD image, band contrast superposed with the IPF in Z and phase contrast, in which blue designates ferrite and red designates cementite.

From this result, although it presents a very low indexation, there are adjacent grains that allow the measurement of a misorientation profile. It was observed that,

even though the ferrite looks very grain-like in the TEM micrograph, it does not present a large misorientation between the grains. The misorientation profiles were done between the grains that appear at the different colors and the measured misorientation was always under 1° for both heating rates. From this result is safe to say that the pearlite has not recrystallized and, with the measured misorientations, most likely cells were formed.

There are only few very small grains, with less than a few dozen of nm, which show that the recrystallization can be locally happening, but only at a very small fraction. Since it only occurs on a very small scale and the parallel lamella are not in contact, it does not present an overall effect on the austenitic transformation because it does not entail a higher number of nucleation sites, as it would be the case if new grains are formed.

The importance of the recrystallization for ferritic steels is that the new grains represent new nucleation sites, which will later lead to new nucleation sites for the austenitization and it will change the global transformation. As seen for the pearlitic steels, it is not completely recrystallized, and they do not present any effect for the austenitic transformation, as was observed in the previous results.

The last tests to prove that there is no effect at all, the two-step heating were performed to precise the effect of the phenomena before the transformation and the effect of the heating rate on the transformation.

The results of the measured PAGS and hardness for the two-step heating are shown in Figure 4.39. The PAGS was affected by the heating rate during the transformation, smaller grain size when the transformation happened during heating at 100 °C/s and larger when transformed at 1 °C/s. The heating before the austenitization temperature has not shown an effect on the transformation, whatsoever.

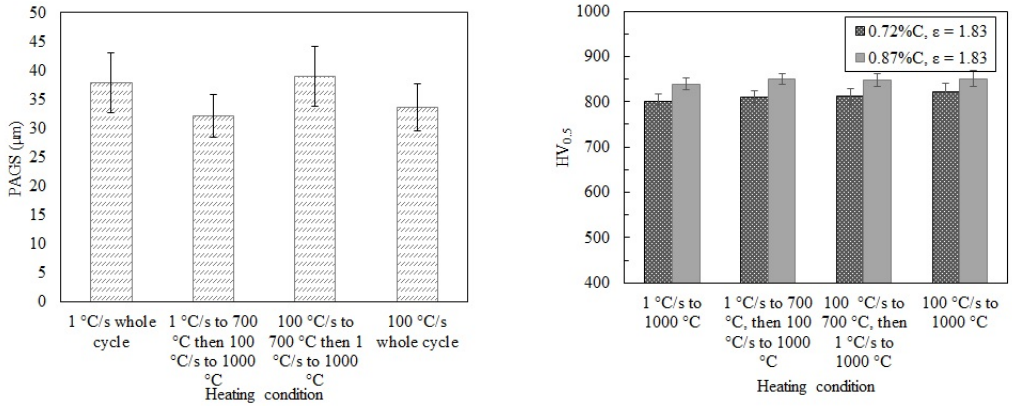

(a) (b)

Figure 4.39: (a)PAGS of the 0.87%C wire heated in the two-step heating and (b) hardness of the two step heating for both 0.72 and 0.87%C

With all the results it is adequate to define that there is no important effect of the phenomena before the austenitization.

4.7 Discussions

The previous sections have presented the results of the possible parameters that can affect, and how they affect, the phase transformation to pearlite.

During heating, it is settled that the austenitization over 950 °C for 60 s or 1000 °C produces homogeneous austenite and the desired PAGS can be chosen given the austenitization conditions in the TTA or the CHT.

During cooling, some odd results were observed, the two cooling routes employed in the present study, isotherm and isochronal, pointed out two phenomena:

- the pearlite morphology is very sensitive to the type of cooling route: a divorced and lamellar microstructure is obtained from isotherm and isochronal tests, respectively, even when transformed at the same temperature.
- the PAGS impacts the kinetics and the nature of the transformation during the isotherm cooling: the largest PAGS material exhibited an abnormal transformation.

The type of cooling was the decisive parameter to define the pearlite morphology, independently of the undercooling or the austenitization. Therefore,

the thermodynamics and the kinetics of the pearlitic transformation are discussed to explain why it is lamellar during isochronal cooling and divorced during isotherm cooling.

It is known by the previous modeling of the pearlitic transformation in the literature that there are two distinct regions in a diagram of spacing between the particles in the austenite (λ) vs undercooling [73, 139, 75]: one where the eutectoid transformation occurs cooperatively and another where the divorced transformation takes place. This modeling works for several eutectoid steels undergoing very slow continuous cooling.

The spheroidization treatment for bearing steels is commercially done based on this principle. Generally, it used low austenitization temperatures, just above Ac_3 or intercritic, to ensure the presence of undissolved carbides with a short distance between them. It occurs because the ferrite growth is favored, since the austenite is depleted in carbon and the energy gain for the transformation of austenite into ferrite + metastable austenite is higher than the gain for transforming austenite into ferrite + cementite ($|\Delta G^{\gamma\rightarrow\gamma'+\alpha}| > |\Delta G^{\gamma\rightarrow\alpha+Fe_3C}|$). In this way, carbon diffuses away from the interface and partitions into the cementite particles present at both ferrite and austenite matrix.

With the increase of the undercooling the$|\Delta G^{\gamma\rightarrow\gamma'+\alpha}|$ transformation starts to be very close to the $|\Delta G^{\gamma\rightarrow\alpha+Fe_3C}|$, meaning that is that the free energy reduction to form only ferrite can be close to the one for austenite conversion into pearlite. This is confirmed by the diagram of Figure 4.40.

Therefore, when it cools fast to the isotherm transformation temperature, there is a sudden large undercooling that does not favors the pearlitic transformation since $|\Delta G^{\gamma\rightarrow\gamma'+\alpha}| > |\Delta G^{\gamma\rightarrow\alpha+Fe_3C}|$. As the ferritic transformation continuously operates, the austenite gets enriched in carbon which favors the non-cooperative growth of pearlite.

During the isochronal cooling, there is a gradual continuous cooling of the austenite that allows some organization which makes the $|\Delta G^{\gamma\rightarrow\alpha+Fe_3C}|$ to be higher. The condition for it to happen under the eutectoid transformation is that it should follow the equilibrium condition seen by the prolongation of the $\gamma+\alpha$ and the $\gamma+Fe_3C$ line, which is known as the Hultgen extrapolation, seen in Figure 4.40b. It states that the $C^{\gamma Fe_3C} > \overline{C}^{\gamma} > C^{\gamma\alpha}$. It means that the state of the austenite before the transformation is decisive for the morphology of the pearlite.

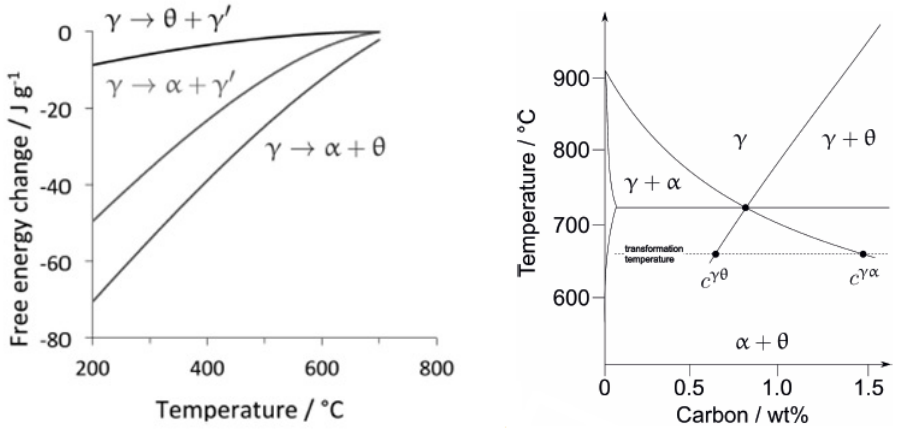

(a) (b)

Figure 4.40: (a)Variation of the free energy with the undercooling temperature for an eutectoid composition sample and (b) the Hultgen extrapolation that states the equilibrium carbon concentration for the pearlitic reaction to happen under the eutectoid temperature. [10]

When the transformation is defined to be cooperative by thermodynamics, carbon is not accumulated in the austenite once the transformation starts because it is directly partitioned into the cementite. This will lead to a constant growth rate, which is finely adjusted by branching of the cementite and by increasing and/or decreasing the interlamellar spacing with the small perturbations. This result was observed in micrographs of the continuously cooled samples.

The fast advance of the transformation interface occurs during the cooperative growth because the carbon atoms only need to diffuse short distances in the transformation front.[65] Meaning that the interfaces advance fast during the continuous cooling while, in the isotherm ones, the ferrite transformation front advances fast but then it will depend on the diffusion of the carbon atoms away from the transformation interface to continue, thus forming a divorced microstructure. This result suggests that during isochronal growth it is mostly done by interface control and during isotherm, it is mostly diffusion-controlled growth.

The presence of the holes on lamellar parts of the mostly divorced microstructure might be explained by an interchange between the pearlitic and the DET growth on a very small scale since there is not a big difference in the ΔG for these transformations. The carbon atoms that follow the cooperative growth might need to diffuse away from the interface when the ferrite lamella grows faster than first previewed for the cooperative growth and it would join the next closest lamella. A systematic interchange of the growth modes, confirmed by the lamellar and spheroidized regions of the isotherm

treatments, would give rise to holes in the cementite.

This result is an interesting example of how the growth mode changes many features in the pearlite which are strongly dependent on the undercooling, but not exclusively dependent on it or the austenitization.

Finally, let's discuss the observed abnormal transformation during the pearlitic transformation of the sample austenitized at 1000 °C. The abnormal transformation phenomenon in steels has been extensively investigated by Liu et al., in which the pure iron, the effect of substitutional and interstitial elements were studied [149, 150, 151]. In the case of pure iron and substitution alloys, the authors suggest that a phenomenon of autocatalysis occurred due to the deformation introduced by the transformation ahead of the transformation front, which creates new active nucleation sites for the ferrite. In the presence of interstitial elements, they observed that the abnormal transformation is caused by a change in the growth control, being first characterized by diffusion control then changed to the massive transformation interface controlled. In all cases, the abnormal transformation entails a bimodal grain distribution, small grains formed in the first part followed by the large grains, and the pre-condition for it to happen is the presence of large prior austenite grain size.

In this above-mentioned work, as it is for the ultralow carbon steel [153], there is a change from the DET, which is a strict diffusion control growth, to the pearlitic transformation that happens by mix control. As the diffusion during the nucleation can be done both by the interfaces, grain boundaries, edges, and corners, after nucleated in austenite with large grain size, there is a struggle of carbon to arrive at the transformation front. As the carbon flow would be done mostly by the austenitic matrix, it is not unrealistic to consider that the first peak is due to a prevailing diffusion growth control or DET with a big interparticle spacing. As the new boundaries are created, the flux of carbon is eased and it gives rise to the second peak of transformation, the mix of interface and diffusion growth.

These discussions only concern the eutectoid composition, however, the related phenomena also occurred for the hypoeutectoid and hypereutectoid steel. It is a special case because there is the proeutectoid transformation.

First analyzing the case in which only pearlite is formed, the closest temperature to have the complete pearlitic transformation occurs during the isotherm tests at 560 and 520 °C for the 0.72 wt.%C and 0.87 wt.%C, respectively. This undercooling

temperature is high enough to disfavor the pro-eutectoid reaction and to promote the pearlitic reaction without being too low to transform to bainite. It means that, at higher temperatures, there is still some nucleation and growth of the proeuctetoid phases and under it, the pearlitic transformation is favored until the point in which the bainitic transformation starts.

As the formation of pro-eutectoid phases is confirmed by the microstructural investigation, the transformation rates for the hypo and hyper eutectoid steels must be carefully interpreted since there is the formation of two phases. Therefore, it will be analyzed by the comparison with the known phenomena happening in the TTT curve and the observed microstructure evolution:

1. At high temperatures there is the high mobility of the atoms and the interfaces and a low driving force for the transformation. There are no well-defined rates maxima at the highest tested temperature (913 K) and the microstructure is rather lamellar.

2. The decrease in the temperature entails the increase of the driving force without yet compromising the atomic mobility. The microstructure starts progressively to be divorced and the two peaks became very well defined.

3. The compromise starts after the nose of the transformation, where the two peaks start to overlap accompanying the gradual disappearance of the proeutectoid phases in the microstructure. It is not reasonable to presume that the first peak in the hypo and hypereutectoid phases happen due to a contribution of the nucleation and growth of the proeutectoid phases.

Since the proeutectoid phases are formed at the grain boundaries, there is no more a struggle for the carbon to arrive at the transformation front, because the new boundaries are created. The flux of carbon is eased being possible to be done both by the austenite, the ferrite, and or cementite and on the network grain boundaries, which gives rise to the second peak of pearlitic transformation by the mix of interface and diffusion growth.

The pearlite morphology continues the same because the conditions for the lamellar pearlite reaction to happen are still not fulfilled, meaning that the presence of the pro-eutectoid phase does not influence the further pearlitic transformation.

Finally, the last discussion is about the recovery of the pearlitic microstructure. It was shown that the pearlite does not considerably recrystallize. Recrystallization does happen, but only at a very small fraction, even though the ϵ_d is elevated.

It happens because the plasticity of the pearlite is confined in the lamella, which does not allow contact with the other lamella and, thus, not accumulate the critical strain for the recrystallization to occur. The energy during heating is used to restore the ferrite, which is confirmed by the presence of the cell walls.

The cementite participates during the deformation, it is known to issue dislocations and also to absorb dislocations from the ferrite [158, 159]. It is seen in TEM micrographs that the cementite after the drawing has many dislocations and, after the interrupted heating, it is mostly spheroidized and also completely restored. Therefore, the given energy was used to restore the cementite.

Therefore, during heating of the deformed pearlite, there is the cementite that is been restored and spheroidized at the same time that the ferrite.

Starting with cementite, it is admitted that spheroidization occurs to reduce the global energy of the system by diminishing the interface energy. The spheroidization heat treatment is known to be very long, taking several dozens of hours, and the main mechanism for the lamella transformation into a spheroid is the fault migration. [71, 160, 161]. There are other two mechanisms, thermal groove theory, and Rayleigh's Perturbation Theory, which are accepted to give greater contributions at the initial and later stages of spheroidizations, respectively. The fault migration is attributed to happen due to the chemical potential gradient between a curved lamellar fault and an adjacent flat interface.

All these considerations are done for the non-deformed lamella, which indicates that the dislocations inside the cementite must have played an important hole in reaching such a degree of spheroidization in such a short time.

Either way, it is seen by the results that the process involves the movement of dislocations in the cementite and it produces a completely restored spheroid. These movements can annihilate the dislocations in the cementite and/or, because the $\alpha - \Theta$ interface is known to be coherent, expel the dislocations which will glide to ferrite and then be reorganized. This process seems to request less energy to happen than the organization in ferrite since in ferrite are observed the cell walls, while the cementite is faultless.

Besides, the spheroidization of the cementite mandatorily connects two deformed ferritic lamellas, which gives a greater free path for the dislocations to reorganize and, hence, diminishes the driving force for the recrystallization.

In the literature, the spheroidization and the recrystallization or restoring of the ferrite are separately studied, whereas they should be considered as mutual and interdependent phenomena. The calculation of the activation energy, the Burgers vectors in the cementite, carbon-defect interaction, and self-diffusion energy values could give a more qualitative measure of this phenomenon.

The stabilization cycle is done for 10 minutes at 650 °C, which most likely progresses the spheroidization to a coalescence point, which explains why the martensite formed in the ASTM cycle without the spheroidization cycle is more homogeneous than the one with. However, the one without the stabilization cycle presents less carbon in solid solution when compared to the one with, which can indicate that the carbon dissolution is eased for the one that was submitted to the stabilization cycle. There must have a relation with the phenomenon happening in the ferrite that has eased the dissolution of the larger cementite particles, maybe by the creation of the grain boundaries that facilitate the flux of carbon atoms. The fact is that at the low austenitization temperature without the prior stabilization cycle, it is not possible to dissolve all the carbides.

4.8 Conclusions

In this dense chapter, the phase transformations to austenite and pearlite were studied and all the aspects that could affect it were considered to allow producing some guidelines for the later production of the gradients.

The main conclusions of this are listed below and then summarized.

- During heating, it was seen that the austenitization over 60s at 950 °C or over 1000 °C is sufficient to have homogeneous carbon distribution in austenite. Even though after 840 °C all the carbides have dissolved, there are still regions that are poorer in carbon that will subsequently transform during cooling. The PAGS was seen to significantly vary with the time and the temperature of austenitization but not so much with the heating rates. The TTA and the CHT were produced

which can work as index book for the austenitization of eutectoid steels.

- During cooling, it was observed that the isotherm and continuous cooling have produced different morphologies: divorced and densely connected lamellar pearlite, respectively. It was discussed that it happens because the austenite does not have time to create a short-range organization when cooled very fast to the isotherm transformation temperature and, hence, does not follow the equilibrium condition to form lamellar pearlite. Whereas the continuous cooling is slow enough to attend the equilibrium condition and, therefore, form the lamellar pearlite. The austenitization, mainly the PAGS, affected the transformation during cooling, affecting the critical cooling rates and delaying the pearlitic transformation with the increase of the grain size. The large grain size has also entailed an abnormal transformation during isotherm cooling, which is most likely caused by the division of a first strictly diffusion controlled stage of the transformation, followed by mixed control. The diagram produced by following the standard conditions presented a lamellar microstructure without many defects and or connections between the cementite lamellas. Although the grain size was about the same obtained for the one transformed at 950 °C, all the transformations happened at a higher temperature.

- The effect of carbon content was observed by the presence of proeutectoid phases, which has not affected the pearlitic morphology. The kinetics of the transformation changes and, in this case, the two peaks are related to the formation of the proeutectoid phases and then by mix-control for the pearlitic transformation. During heating, there is an odd variation of the PAGS with the temperature of austenitization and time and the hypoeutectoid composition is more sensitive to inhomogeneity of the austenite than the eutectoid and the hypereutectoid composition.

- The effect of the initial microstructure was analyzed and it was confirmed that there is no advantage of transforming to austenite from the martensite, since the pearlite has satisfactorily transformed to austenite without leaving undissolved carbide.

- The last is the effect of the mechanical history, which has proven to be negligible since it does affect the austenite formation when the latter is done at over 900 °C. It was shown that it happens because the phenomenon occurring before the transformation does not affect the austenitization. The pearlite before the transformation is spherodized and recovered, and the triple joints of the colonies

continue to be the main nucleation sites for the austenite. The formed spheroids are not so large that it would hinder its dissolution and, therefore, it is not important for the overall transformation.

- The recovery of the pearlite was proven to be different from what is known for the other microstructure because the ferrite and the cementite overcome the process of recovery. They are mutually dependent and it seems that cementite recovers before the ferrite, while it also spheroidize, thus giving the dislocation in ferrite a broader path to recombine and annihilate.

Chapter 5

Gradients

5.1 Introduction

The idea of creating a microstructure gradient arises from a proven concept of nature since they are present in seashells and bones[84, 92]. This concept has been extensively explored, as commented in Chapter 2. The main challenge is to cause a synergy between two distinct properties, e.g. strength and ductility, in a way that the final product presents better properties than the separated components.

The application of a microstructure gradient concept for the pearlitic steel wires is limited by the reduced dimensions of the wires and the robustness of the process. To enlarge the possibilities and explore the limits of the gradient production, the attempts to obtain the gradients took into consideration two wires of different diameters, different types of heat treatments, and also different types of gradients: thermal, mechanical, and thermomechanical.

5.2 Materials and experimental procedures

The production of the microstructure gradients was approached according to three means: by thermal means, by mechanical means and thermomechanical means. The production by thermal means is restricted by the thermal gradient created in the sample, which is inevitably affected by the diameter. Therefore, for the gradients tests, two diameters rods were tested, ϕ=6 and 12 mm, and in Table 5.1 is seen their

chemical composition.

For comparison, some tests were also performed on the 4 mm diameter wire, same as the one studied in Chapter 4 that presents a similar eutectoid composition. It was investigated if in a rod with diameter of 4 mm there is a thermal gradient or if the sample can be considered homogeneous.

Table 5.1: Chemical composition of the wires with 6 and 12 mm diameter used to test the gradient production

	Chemical composition (in wt.%)									
Diameter	C	Mn	P	S	Si	Al	Cu	Cr	Ni	Fe
6.5 mm	0.832	0.517	0.009	0.011	0.195	0.001	0.042	0.069	0.028	balanced
12 mm	0.812	0.531	0.009	0.008	0.148	0.001	0.009	0.053	0.021	balanced

All the tests were performed in the dilatometer that was previously described in Chapter 3. The standard coils of the dilatometer cannot fit such thick samples and, therefore, a medium coil specially made for larger diameters was designed.

As the process for the production of the gradients is part of the scope of this chapter, they will be described in each section.

The obtained microstructures were characterized by SEM and the micrographs were used to measure the average interlamellar spacing ($\overline{S}$) with the Underwoods method, same way as described in the previous Chapter 4.

What concerns the gradients formed using thermal means, for the two main austenitization cycles, the PAGS was measured at the surface and in the core to see if there is a gradient coming from the austenitization cycle. Again, the same procedure previously described in Chapter 4 was used: chemical etching with the alkaline sodium picrate (ASP) at 90 °C for 10 minutes, followed by Nital 2% etching and Picral 4%, then measuring with the ASTM method [128].

For the gradients produced by mechanical means, the employed procedure consisted in drawing the 6.5 mm diameter wire to 6 mm ($\epsilon_d = 0.16$). The deformed zone was analyzed by SEM.

One other way to evidence the gradient in terms of surface repetition was to perform hardness mapping. Here, Vickers microhardness was automatically acquired using a FM-810+ARS900(FT) apparatus, from FUTURE-TECH. The indents were done by employing a load of 500 g and 10 s hold at every 300 µm in x and y keeping a distance of 200 µm from the surface.

5.3 Transition to the real process

Before dealing with the production of the gradients, it is important to make some considerations about the means of simulating and producing the latter.

The dilatometer was used here as a thermal simulator and this means that thermal cycles possibilities are wide open. It is capable of entirely extinguishing the recalescence of the pearlitic transformation, cooling then reheating to any given temperature, increasing or reducing the cooling power during the cooling, only to name a few of the possibilities. Despite all the possibilities accessing through the dilatometer use, the considered parameters must be selected as close as possible to the real industrial process, which is not so flexible.

Then, to rely on the real process conditions and to simulate them, the way they are in a process line has to be thoroughly investigated. Indeed, the immersing cooling technologies, such as lead patenting and salt bath, are considered to be isotherm cooling. While some water-based alternative cooling technologies are better described by continuous cooling. To confirm these features, they were investigated by austenitizing a wire rod of 6 mm or 12 mm in a furnace and then transformed into a production line equipped with molten salt, liquid lead, or water while recording the temperature with a thermocouple inserted in the center of the rod. The results shown in Figure 5.1, indeed, indicate that the cooling in the lead and molten salt can effectively be approximated to an isotherm heat treatment and the alternative cooling is a type of continuous cooling.

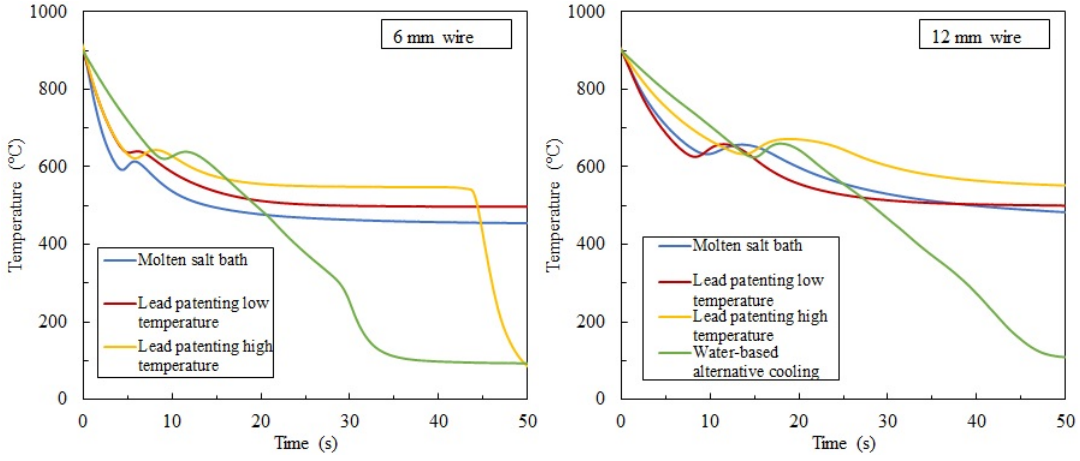

(a) (b)

Figure 5.1: Temperature evolution during cooling in lead, molten salt and water-based alternative cooling measured in 6.5 mm and 12 mm diameter wires.

The only difference with conventional or simulated the TTT and CCT cycles is that the effect of the recalescence is observed for the real process. Therefore, to work around this problem, it is proposed here to use constant gas flow for cooling instead of temperature control. The results obtained for the 4 mm wire cooled with the constant gas flow (100, 80, 60, 40, and 20 % of gas) with the regular and the medium coil are shown in Figure 5.2. It is seen that a kind of continuous-cooling-transformation diagram was produced and that the different sizes of coils were able to provide different cooling powers. The distance of sample to the coil plays an important role, 20 % of gas flow for cooling in the regular coil was strong enough to produce martensite, whereas 40 % in the medium coil was still possible to completely transform to pearlite.

As the cooling power decreases to allow the formation of pearlite, the limitation of the recalescence is also jeopardized. The latter appears to have the same magnitude for the samples cooled with 40 and 20% for gas but, as the containment of the recalescence is stronger at 40%, it indicates that the recalescence was higher when transformed at lower temperatures (fine pearlite).

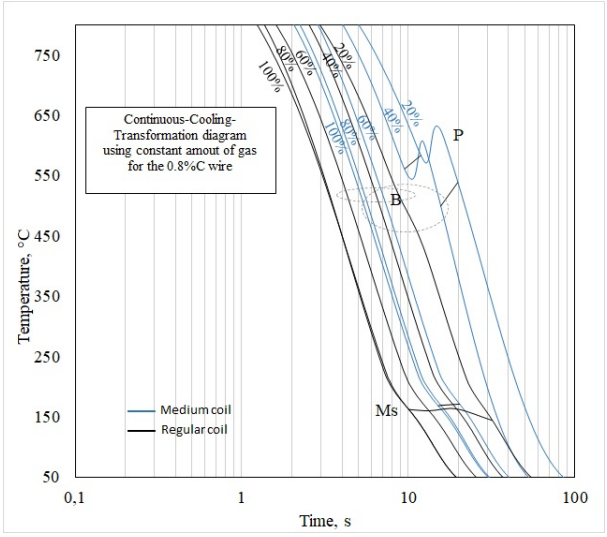

Figure 5.2: Continuous-cooling transformation done for the 4 mm wires using constant gas flow of 100, 80, 60, 40 and 20 % of gas in the regular and the medium coil

For the 6 and 12 mm diameter rods, it was not possible to use both coils, so, the results of the cooling using constant gas flow with the medium coil for the larger diameter is shown in Figure 5.3. Compared with the 4 mm diameter, it is seen that the larger the diameter, the slower the cooling and the easier it is to form pearlite. For the 12 mm it is possible to form pearlite even when using 80% of gas flow.

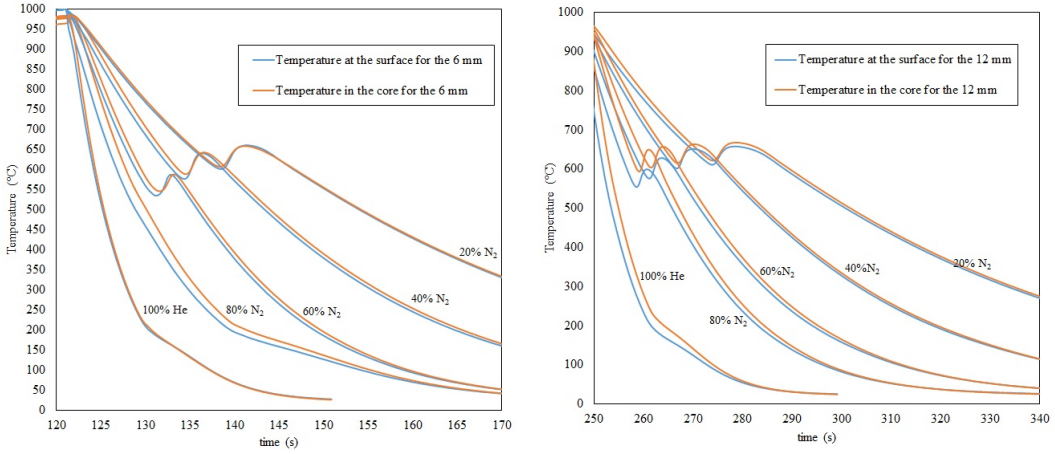

(a) (b)

Figure 5.3: Continuous-cooling transformation done for the 6 and 12 mm wires using constant gas flow of 100, 80, 60, 40 and 20 % of gas in the medium coil.

For the large diameters, the temperature was measured both in the core and at the surface of the samples. As expected, the thermal gradient in the 12 mm diameter rod is much greater than in the 6 mm ones, reaching a difference of 50 °C at the start of the transformation when cooled with 80% of gas flow. For the 6 mm diameter rod, there is a very small difference of temperature between the core and the surface, meaning that the gradient formation in a diameter of 6 mm is quite limited.

Analyzing the shape of the curves during cooling and comparing them with the cooling of the real process (Figure 5.1), it is seen that the transformation using low gas flow is very similar to the real cooling. After the transformation in the lead and molten salt, the wires are kept at the bath temperature, whereas in the dilatometer it continues to cool. It can be adjusted either by cutting completely the gas flow or diminishing it. Either way, it has been proved that it is possible to simulate cooling with constant cooling power.

For a better understanding of how the temperature difference evolves during heating, then at the start of the cooling, and finally during the progress of the phase transformation, it was plotted the difference in temperature between the core and the surface vs the surface temperature, and it can be seen in Figure 5.4. Again, the thermal gradient in the 12 mm is remarkably greater than the 6 mm, being about two times greater.

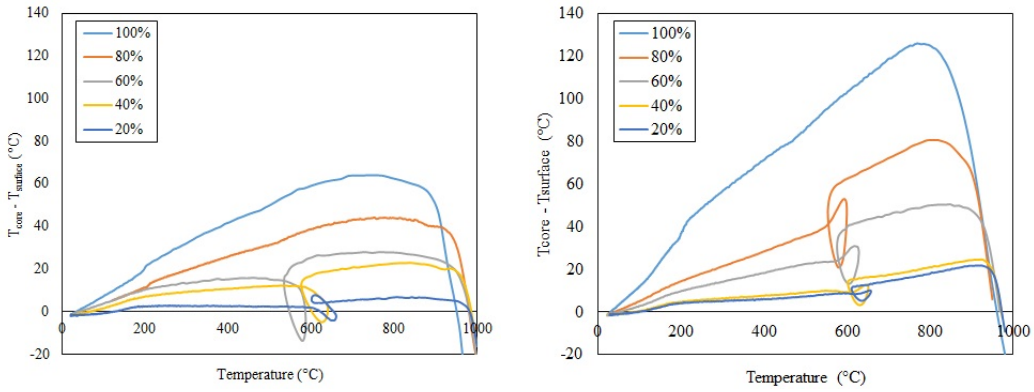

(a) (b)

Figure 5.4: Temperature difference between core and surface in the (a) 6 and (b) 12 mm diameter rod cooled with the constant amount of gas

First looking at high temperatures (around 1 000°C), they all come from a negative difference between the core and the surface, which means that the surface is hotter than the core and, thus, there is already a gradient of temperature from the austenitization. During cooling, the core is always hotter than the surface until reaching the transformation, in which is observed a loop (around 600 °C). This loop is caused by the recalescence because, after the start of the transformation, the temperature difference reduces very fast due the start of the transformation at the surface. As a consequence, the temperature at the surface increases, then the overall difference increases again because now the transformation has started in the core. Finally, it cools until the temperature is homogeneous.

Figure 5.5 shows that the evolution of the difference in temperature between the core and the surface with the gas flow obeys a linear relation. As the difference in temperature between core and surface doubles when the diameter doubles, a factor of 2 is found between the two slopes. It is also seen in the graph that this correlation works better for stronger gas flows.

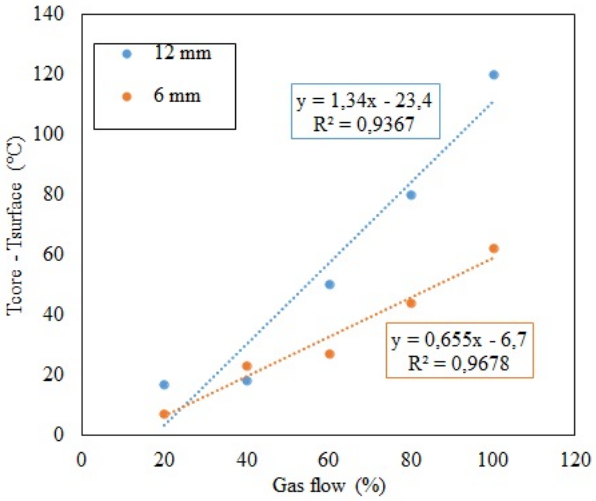

Figure 5.5: Temperature difference variation with the amount of gas applied during cooling for 6 and 12 mm wire diameters.

Some tests under controlled cooling rate (30, 20, and 10 °C/s) were also performed but they did not follow a linear behavior. The temperature differences between the core and the surface were also measured for the 4 mm diameter rod measured in this conditions and, although it can reach 20 °C of difference during the cooling at 30 °C/s, the time for the temperature of the core to reach the same temperature of the surface is less than 1 s and which entails that the transformation takes place at the same temperature in the core and the surface. So, there is a thermal gradient, but it is not enough to produce a microstructure gradient.

This struggle with the time happens the same way for the 6.5 mm diameter rod, which presents a temperature difference of 40 °C when cooled at 30 °C/s and it takes 1.5 s to reach the same temperature, while the 12 mm diameter rod presented a difference of 50 °C and then it takes almost 2 s to reach the same temperature. Once more, the 6 mm is very limited to produce the gradient but it is manageable to have coarse pearlite formed in the core and finer at the surface. It was seen in the Chapter 4 that 40 °C of difference produces considerably different interlamellar spacings.

5.4 Gradient production

Three types of gradients are proposed to be produced, they will be called the "targeted gradients". The microstructural radial distribution will define each of the three types, thus being:

- Soft + hard: Coarse pearlite at the surface and fine pearlite at the core.
- Hard + soft: Fine pearlite at the surface and coarse pearlite at the core.
- Hard + soft *: Bainite at the surface and pearlite, whether coarse or fine, in the core.

It is seen in the results of the previous section that the formation fine pearlite at the surface and coarse pearlite at the core is the most evident one since the surface is cooled first than the core, thus producing the hard + soft gradient. This type of gradient is characterized by a higher hardness at the surface than in the core, which means that all the mechanical gradients, such as shoot penning, SMAT, and even drawing, are also of this type.

The "soft + hard gradient" is the most complicated to be produced for two reasons: first, because it can only be done by thermal means; and second, the nucleation of the coarse pearlite has to be restricted to the surface even though the whole cross section has a mostly homogeneous temperature during slow cooling.

The "hard + soft *" is a kind of remodeling of the process as known as "Tempcore" [16], which is a gradient of tempered martensite at the surface and pearlite in the core that is used for thick reinforcement bars. This type of gradient was reviewed in Chapter 2 and it cannot be applied here because this patent is used for medium carbon steels, and in this work only the high carbon steels are studied. The Ms temperature is much lower in the high carbon than the one of medium carbon, thus making it impossible to produce martensite at the surface without transforming the core. Besides, they are only capable of doing this because the bars are 22 mm thick, which allows a much greater thermal gradient. Therefore, it is proposed here to keep the 6.5 and 12 mm diameter of the wires to assess its feasibility and change the martensitic transformation to a bainitic transformation, since the Bs of high carbon steels is close to the Ms of medium carbon.

These are three types of gradients that were studied and the trials to obtain them were divided by the means of production: thermal, mechanical, or thermomechanical means.

5.4.1 Gradient production by thermal means

In this section, all the trials are based on the temperature gradients created between the core and the surface during heating and cooling. It is worth noting that they will be very diameter-dependent.

The gradient in the larger diameter will be stronger but, as in the real production the wires are later drawn to 2.25 mm diameter, it would be very hard to draw this wire because of the very high strain hardening caused by such large diameter reduction. Therefore, 6.5 mm diameter rod is preferred for the practical production of the wires and, since they have a more limited temperature gradient, they will be deeper investigated.

First, it is investigated if there is a formation of a PAGS gradient during the heating. For that, the samples were heated in the same two heating conditions of CCT and TTT mentioned in chapter 4 and then quenched. The conditions are:

- Heating at 5 °C/s to 1000 °C, soaking for 10 s then quenching at 100 °C/s.
- Heating at 30 °C/s to 950 °C, soaking for 10 s then quenching at 100 °C/s.

For these thick samples, the dilatometer was not capable of quenching at 100 °C/s, only reaching a maximum cooling rate of 85 °C/s, which was enough to avoid the formation of pearlite.

The results of the PAGS are shown in Figure 5.6. It is seen that the 12 mm diameter presented a difference of PAGS at the core and the surface, whereas for the 6.5 mm diameter rod, there is not such a difference when austenitized at the same condition (heating at 5 °C/s to 1000 °C). However, when heated at 30 °C/s to 950 °C, it did present a difference in the grain size measured in the core and at the surface.

To have some statistical results, the t-test was used to compare if there was a difference between the means of the measured PAGS with a level of significance of 95%. For the 6.5 mm diameter rod, when austenitized at 1000 °C, it was proven that there was no difference between the means ($p - value$=0.424). However, when austenitized at 950 °C, there is a significant difference of 5 µm between the core and the surface ($p - value$=0.015). For the 12 mm diameter rod, a significant difference of 10 µm between the core and the surface was also observed ($p - value < 0.001$).

For the 6.5 mm diameter rod, the PAGS is larger at the surface than in the core, which is expected given that the surface is hotter than the core. However, for the 12 mm diameter rod, the PAGS is smaller at the surface. A big difference to be taken into account is that the heating rates are different and it explains for the 6.5 mm diameter rod (heated at 30 °C/s) why the surface is hotter and, thus, why it presents a larger PAGS at the surface. For the 12 mm diameter rod (heated at 5 °C/s), the wire is homogeneous during heating but, during cooling, the thermal gradient allows the grains to continue to grow in the core while the surface is already cooled. This effect was not observed for the 6.5 mm in the same conditions, which means that **the heating rates play the most important role for the gradients during heating for the 6.5 mm diameter rod.**

Either way, it might have a meaningful effect for the 12 mm diameter rod that reached a difference of 10 µm but, for the 6.5 mm diameter rod, the difference of 5 µm will not entail any effect in the later pearlitic transformation.

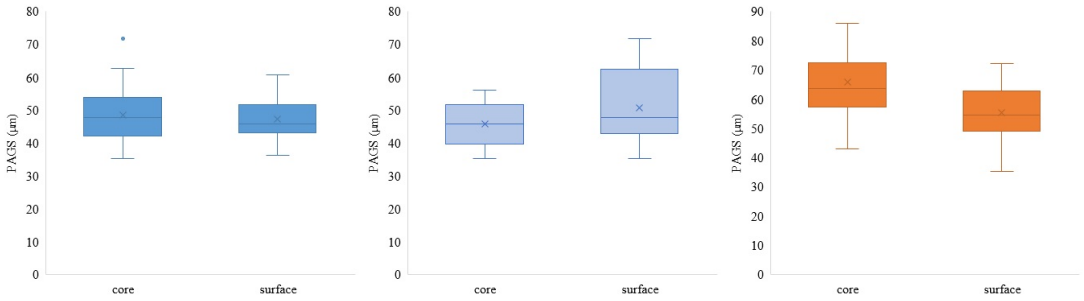

Figure 5.6: PAGS measured at the core and at the surface of the 6.5 mm diameter rod heated at (a) 5 °C/s to 1000 °C and (b) 30 °C/s to 950 °C, both soaked for 10 s; and (c) 12 mm diameter rod also austenitized at 5 °C/s to 1000 °C.

The formation of the gradients **only during cooling** is now considered. The cycles for the production of the target gradients are shown in Figure 5.7. The used principle was similar to the Tempcore, the transformation starts at the surface, and then the condition is changed to transform the core. Therefore, to form coarse pearlite at the surface, it is first used a very slow cooling until the start of the formation of the coarse pearlite and then the gas flow is increased to form fine pearlite at lower temperatures.

Contrarily, to form fine pearlite or bainite at the surface, a stronger cooling is applied right from the end of the austenitization until the start of the fine pearlite formation, then the gas flow is either stopped to have a natural cooling or the cooling is changed to a very slow cooling to allow the effect of the recalescence to naturally

increase the temperature and, thus, form coarse pearlite.

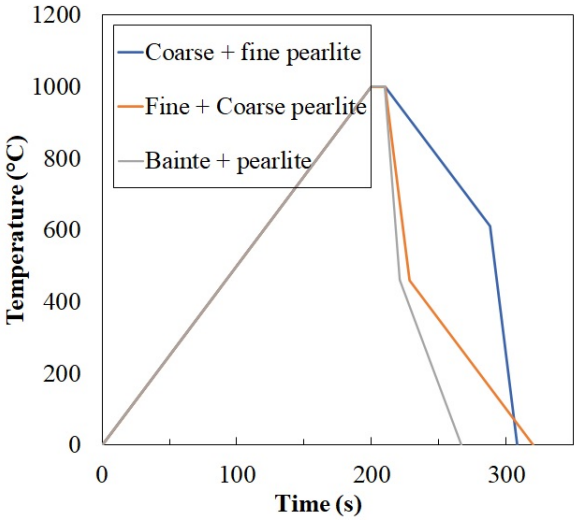

Figure 5.7: Thermal cycles for the production of the target gradients.

The decision of the exact time for changing the cooling path will define the thickness of the gradient. It is a complicated decision because the temperature of the start of transformation measured from the dilatometry curves is not very precise since a certain fraction transformed is needed for the dilatometer to recognize that the transformation has started. The fraction transformed calculated by the level rule is not very reliable.

Therefore, just to have an idea of **real** fraction transformed under controlled conditions, some interrupted tests were performed. The time needed to transform 10% to pearlite or bainite at the isothermal conditions at 640, 540, and 460 °C was estimated using the lever rule. The interrupted tests were carried out by cooling the sample to the transformation temperature, holding for the estimated time and then quenching. For the pearlitic microstructures, it was not even possible to stop at 10%, it has completely transformed to pearlite during cooling. The result of the bainite is shown in Figure 5.8. What is seen in white is bainite and the gray matrix in the back is the martensite. It is seen that a gradient was effectively formed, however, it is clear that it has transformed much more than 10% (around 21%) of bainite in form of a homogeneous distribution of the bainitic islands within the whole surface and a non-uniform external layer of around 25 µm.

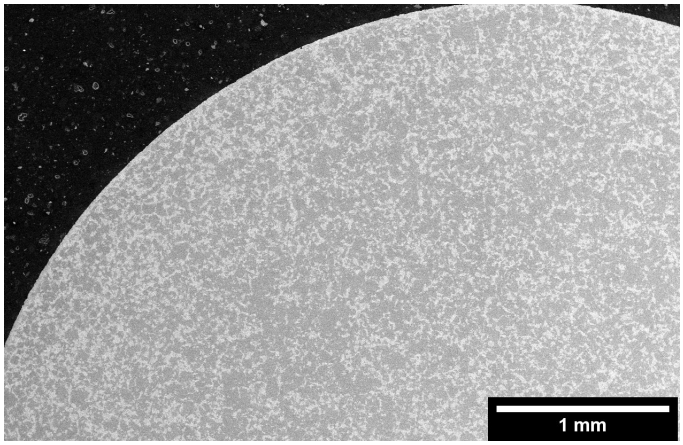

Figure 5.8: SEM micrograph of the interrupted trial at 460 °C. The sample was cooled to 460 °C, stayed the measured time to transform 10% and subsequently quenched. The white areas are bainite and the gray matrix is martensite

This result also evidences that it was not possible to selectively transform only the surface since some bainite formation is observed even at the core. Therefore, as soon as it reaches the transformation temperature, it should be strictly changed the cooling without holding time. This is the only strategy that might allow the possibility of creating a gradient.

With the knowledge of the fraction transformed and the previous results concerning the microstructures formed with the different gas flows, some cycles for the production of the gradients were proposed:

- Soft + hard = cooling with 20% of gas until 239 s (around 600 °C) then quenched with 70 % of gas.
- Hard + soft = cool with 60% of gas until 224 s (around 540 °C) then continue to cool with 40%
- Hard + soft * = cool with 80% of gas until 222 s (around 500 °C) then continue cooling with 40%.

These tests were applied on the 6.5 mm diameter rod and the dilatometry curves are shown in Figure 5.9. As the transformation temperature to coarse pearlite increased too much due to recalescence, it was also tested an increase of the cooling power a bit sooner, around 232 s, to diminish the effect of recalescence, it is called Soft + Hard modified. For the 12 mm diameter rod, only the modified one was done.

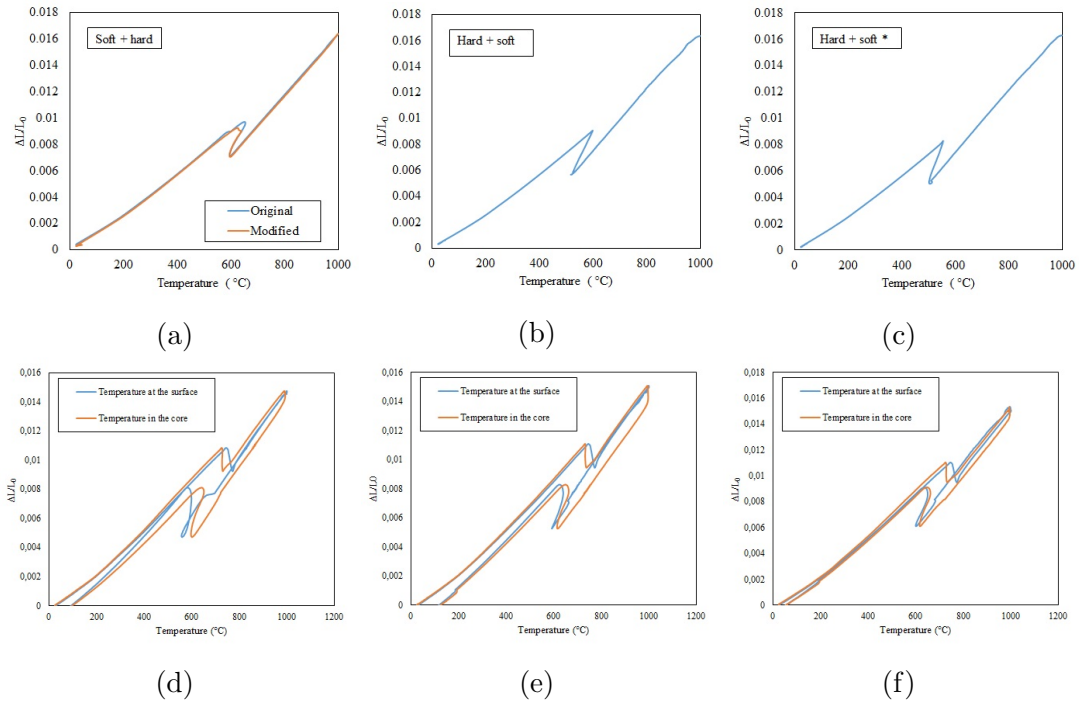

Figure 5.9: Dilatometry cooling curves of the samples transformed with the (a) Soft + Hard and Soft + Hard modified, (b) Hard + soft and (c) Hard + soft * cycles on the 6.5 mm diameter wires, and the whole cycle (heating and cooling) with the temperature measured both at the surface and the core on the 12 mm diameter wires cooled with the (d) Soft + Hard, (e) Hard + soft and (f) Hard + soft * cycles.

For the 6.5 mm diameter rod, the temperature at the core was not measured and the only conclusion that can be taken from these results is that the wires have transformed at the different temperatures and that the recalescence is observed in all cycles. For the 12 mm diameter rod, the temperature was measured both at the surface and core and it is seen that the transformation has taken place at different temperatures at the surface and the core, thus indicating that a gradient was formed.

To evaluate the gradient, the interlamellar spacing was measured every 1 mm, being one measurement at the surface, one in the middle, and one at the core. The micrographs and the measured interlamellar spacing are shown in Figure 5.10 and Table 5.2, respectively. The coarse pearlite formed during Soft + Hard is long and lamellar, while the fine pearlite formed both at Hard + soft and Hard + soft* are very short and partially divorced.

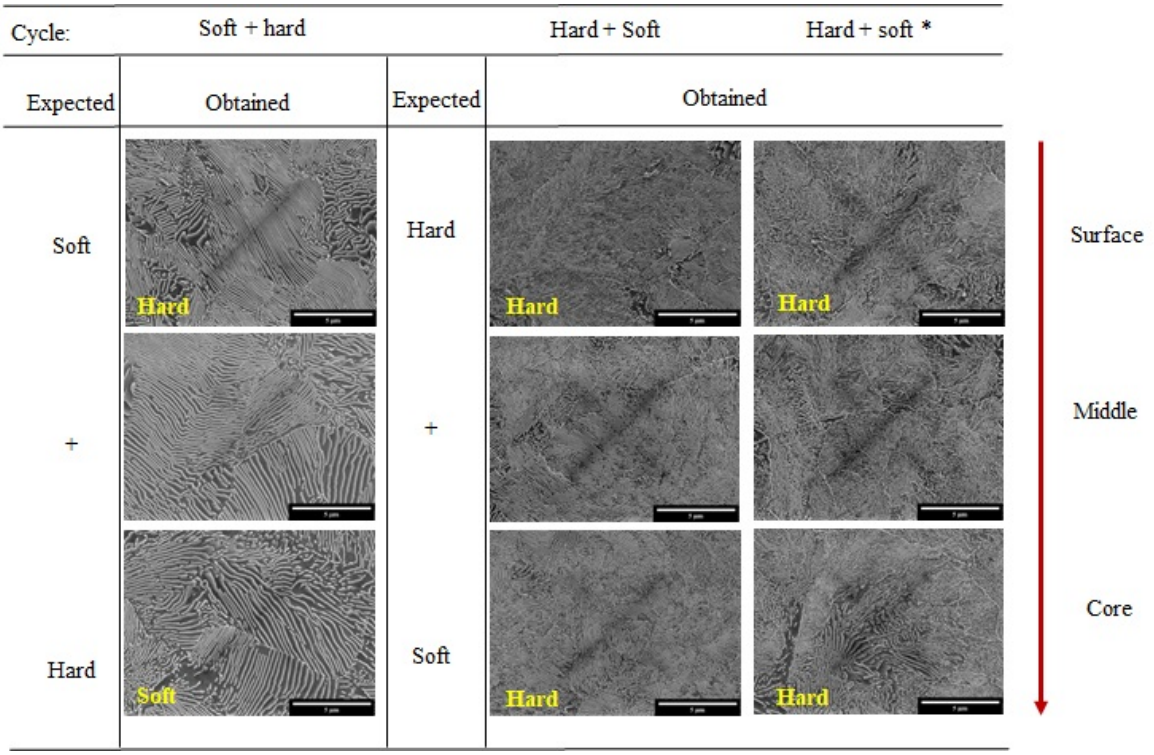

Figure 5.10: SEM micrographs from the core, the surface and the middle in between for the target gradients produced by the cycles soft + hard, hard + soft and hard + soft* on the 6.5 mm diameter rod.

The bainite is observed to form in the core for both the 6.5 and 12 mm diameter rods, which again indicates that it is not possible to have a controlled transformation of only bainite at the surface and pearlite at the core.

From the results in Table 5.2, it is seen that, for the 12 mm diameter rod, all the tests have produced gradients of Soft + Hard. For the 6.5 mm diameter rod, the cycle for Soft + Hard, which should produce coarse pearlite at the surface and fine pearlite at the core, has actually produced the exact opposite. The cycle of Hard + soft and Hard + soft* have produced homogeneous samples, which are probably more homogeneous than a normal 6.5 mm diameter rod that is cooled with only one cooling rate.

Table 5.2: Average interlamellar spacing $\overline{S}$ measured for the target cycles for 6.5 and 12 mm diameter rods.

	Average interlamellar spacing $\overline{S}$ (nm)					
	6 mm			12 mm		
	Soft + Hard	Hard + soft	Hard + soft *	Soft + Hard	Hard + soft	Hard + soft *
Surface	110	84	85	117	105	79
Middle	135	86	83	147	134	94
Core	125	85	82	165	133	119

The last characterization of these target gradients was the hardness mapping and it is shown in Figure 5.11. The first remarkable feature is that the dilatometer has produced non-symmetrical gradients. The 12 mm rod presents the most evident gradient of Hard + soft , which was actually produced by Soft + Hard cycle, followed by the 6.5 mm rod. The modified cycle was successful in diminishing the formation of coarse pearlite.

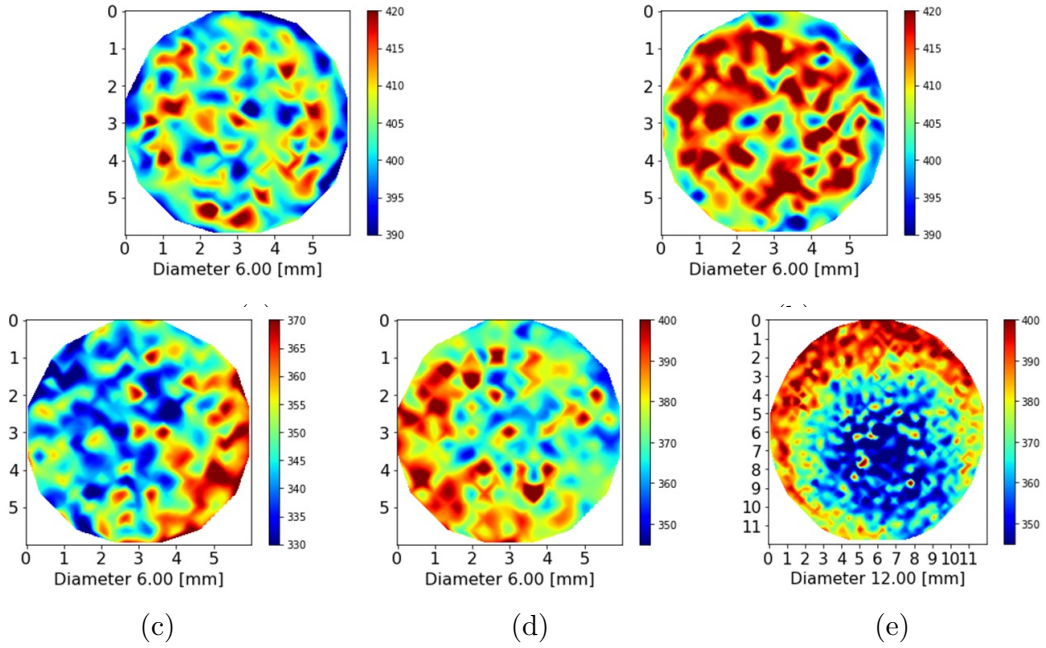

(c) (d) (e)

Figure 5.11: Hardness mappings of the samples transformed by the target cycles of (a) Hard + soft , (b) Hard + soft * for the 6.5 mm diameter rod, the Soft + Hard (c) and I modified for the (d) 6.5 mm and finally Soft + Hard for the 12 mm diameter rod.

Finally, the Hard + soft cycle has produced the hardness profiles of Soft + Hard, even though they actually seemed more homogeneous by the $\overline{S}$ measurements.

It is important to consider the used parameters for the hardness measurements since the first indents are done 200 µm from the surface and, therefore, the most external crown is not analyzed. Any gradient smaller than 200 µm is not analyzed.

All the formed gradients present a very thick external layer, being 1 mm of outer crown of fine pearlite that represents 55% of the wire cross-section. Therefore, the mechanical properties of the gradient are going to be strongly affected, if not completely controlled, by the microstructure of the external layer of the wires.

To enlarge the possibilities of producing a microstructural gradient by thermal means, the influence of the austenitization was again considered. As seen from Chapter

4, the temperature of austenitization, which effectively changes the PAGS, can affect the nucleation and the kinetics of the pearlitic transformation. Moreover, as previously in this section,the heating rates can play a role in the production of the gradients by increasing the temperature difference between the core and the surface.

Therefore, the same target cycles were done with different austenitization parameters to see if a gradient from the heating can, in fact, enhance the gradients formed during cooling. The results of the interlamellar spacings are shown in Table 5.3 and the hardness mappings in Figure 5.12.

From the results in Table 5.3, it is seen that, again, the soft + hard cycle has produced gradients that are hard at the surface and soft at the core, and hard + soft cycle has produced basically homogeneous samples. The intensity of the gradients is about the same difference in the $\overline{S}$ values, about 10 nm between the core and the surface, however they are more refined (smaller $\overline{S}$) when heated at 30 °C/s, specially when austenitized without soaking.

Table 5.3: Average interlamellar spacing $\overline{S}$ measured for the target cycles for 6.5 mm diameter rod with different austenitizations

	Average interlamellar spacing $\overline{S}$ (nm)								
	30 °C/s to 950 °C, 10 s soaking			30 °C/s to 1000 °C, 10 s soaking			30 °C/s to 1000 °C, no soaking		
	Soft + Hard	Hard + soft	Hard + soft *	Soft + Hard	Hard + soft	Hard + soft *	Soft + Hard	Hard + soft	Hard + soft *
Surface	100	87	86	99	91	84	88	83	79
Middle	107	81	79	103	97	84	96	83	77
Core	111	82	83	109	94	97	98	84	77

The one austenitized at 950 °C is the least interesting because it has formed many bainitic islands uniformly distributed all over the surface in all cycles. Recapping the results in Chapter 4, the austenitization at 950 °C for 10 s is not homogeneous, which is a consequence of regions that are richer in carbon than others and, during cooling, the regions depleted in carbon will later transform to bainite.

The hardness mappings of the gradients heated at 30 °C and then austenitized at 1000 °C with 10 s soaking and no soaking at all are seen in Figure 5.12. The soft + hard cycle seems to have formed mainly coarse pearlite with the 10 s holding, while the one without holding has formed about the same gradient of hard + soft cycle as the one formed by the one heated at 5 °C/s.

The cycle without soaking has formed a non-symmetrical gradient of hard + soft type, but most likely because of the non-symmetrical cooling, otherwise, it would be all homogeneous. The same explanation works for Hard + soft *.

The Hard + soft cycle done with the one soaked for 10 s produced a gradient of Soft + Hard and Hard + soft * that is, again, very similar to the one heated at 5 °C/s.

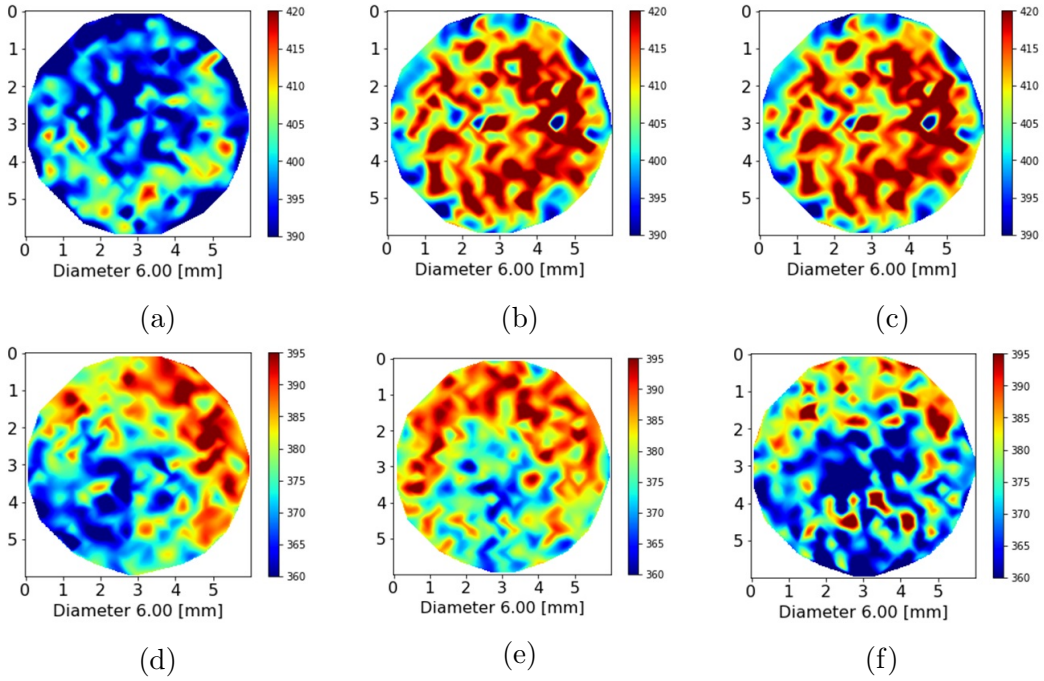

Figure 5.12: Hardness mappings of the cycles Soft + Hard, (a) and (d), Hard + soft , (b) and (e), and Hard + soft *, (c) and (f). They were all heated at 30 °C/s to 1000 °C and the (a), (b) and (c) were soaked for 10 s while (d), (e) and (f) had no soaking and were directly quenched.

One detail is that the overall hardness values at the sample austenitized without soaking time are lower than the ones with the the soaking, which might indicate the presence of undissolved carbides since it comes from fast heating. It was analyzed in Chapter 4 and it was concluded that the austenitization at 1000 °C is homogeneous independent of the time or heating rate but, in all the tested conditions, the austenitizing always had a soaking time of at least 10 s.

The global conclusion is that it is possible to produce a gradient in the 6.5 mm wire, both of Soft + Hard and Hard + soft. These gradients are enhanced with the increase of the diameter but not so much by the austenitizing in the tested conditions.

5.4.2 Gradient production by mechanical means

Another way to produce a gradient is by mechanical means. The way of producing it would be by introducing a greater plastic deformation at the surface than in the core

for providing a gradient of Hard + soft .

These types of gradients are the most common ones and, as thoroughly discussed in section 2.4, there are many technologies to do so, such as the shot peening and the SMAT [90]. These gradients are produced on simpler non-hierarchical microstructures, meaning that they played mostly on the grain size, which is nanometric at the surface and micrometric in the core.

For pearlitic steels, the production of a gradient is not so evident since the plasticity of the pearlitic steels happens at a nanometric scale, which means that the introduction of a gradient is mostly expected to play a role on the interlamellar spacing and, eventually, on the dissolution of the cementite.

The drawing is known to introduce a radial gradient that is higher at the surface than in the core [162, 48, 68]. Therefore, the strategy here was to do one drawing pass to reduce the diameter from 6.5 mm to 6 mm ($\epsilon_d = 0.16$) to see if it can effectively introduce a gradient. The die angle is a decisive parameter whether there is high or low deformation in the surface. The effect of the die angle was analyzed by using the die in its regular form, with 12° of entrance angle and 20° exit angle, and then the die was mounted inverse. These two assemblies define the two drawing conditions: drawing by the normal die or the reverse die. As the entrance angle in the reverse die is higher, it is expected to introduce a larger amount of deformation at the surface.

The samples after drawing were analyzed by SEM and, although it presented some typical twisted pearlite morphology after drawing, it was hard to identify the affected layer between the core and the surface. From the micrographs shown in Figure 5.13, it was very hard to identify a gradient only based on the interlamellar spacing or on the pearlite morphology. At the longitudinal cross-section, it was possible to observe some alignment of the pearlite colonies with the drawing, which is a common feature of drawn pearlitic steels which can help to identify the external deformed layer that composes the gradient. This alignment was still observed until 0.5 mm below the surface for the normal die and over 1 mm for the reverse die. Although the overall reduction was the same (19%), the strain distribution on the wire appears to be different.

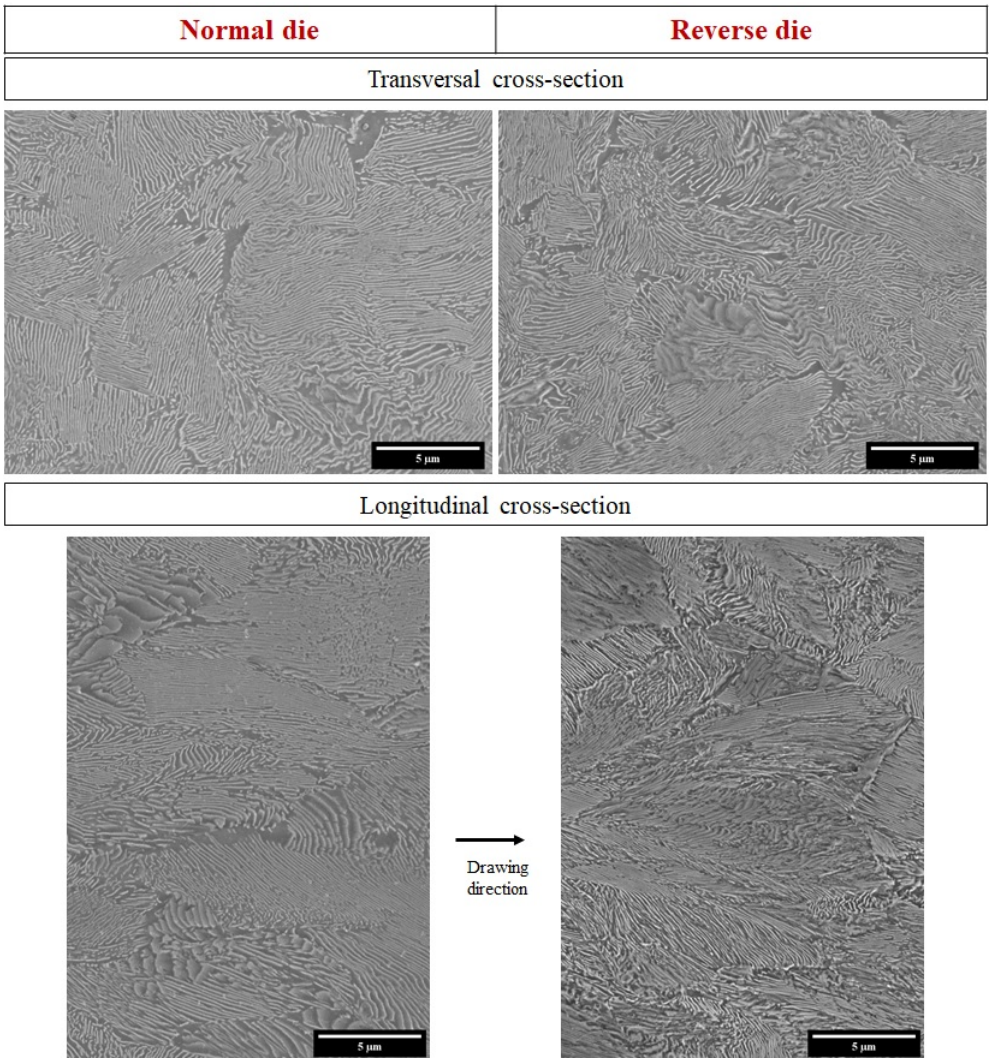

Figure 5.13: SEM micrographs of transverse and longitudinal cross-section of the samples obtained after drawing at $\epsilon_d = 0.16$ with the normal and the reverse die.

Globally, the gradient produced by drawing followed the same principle as the other gradients since it has deformed at a grain scale.

5.4.3 Gradient production by thermomechanical means

The samples that were previously drawn were then submitted to the heat treatment used for the production of the target gradients to analyze if the deformation can enhance the gradients. The austenitization cycle was done by heating at 5 °C/s to 1000 °C and then soaking for 10 s and, in these conditions, considering the previous results shown in the Chapter 4, it was seen that the mechanical history did not affect the sample after the austenitization.

The surprising result was that the pearlitic transformation was disfavored. Hard + soft * transformed to a mix of bainite and martensite in the same cycles that have previously transformed to pearlitic gradients. It was especially disfavored in the reverse die, which was the strongest deformation, and only during the cycle of Soft + Hard pearlite was formed. Yet, the formed pearlite is homogeneous and there is no sign of a gradient, whatsoever.

The samples drawn with the normal die have transformed to pearlite with the cycles of Soft + Hard and Hard + soft and had the interlamellar spacing measured, so as the one drawn using the reserve die and then transformed by the cycle of Soft + Hard, and the results are shown in Table 5.4. Soft + Hard has transformed basically to a homogeneous microstructure since the surface and the core have about the same interlamellar spacing. And Hard + soft has transformed to a mostly uniform interlamellar spacing, however, it has formed many bainitic islands.

Table 5.4: Average interlamellar spacing $\overline{S}$ measured for the target cycles for ϕ= 6 mm done in the deformed samples

	Average interlamellar spacing $\overline{S}$		
	Reverse die	Normal die	
	Soft + Hard	Soft + Hard	Hard + soft
Surface	98	102	78
Middle	100	109	72
Core	102	104	75

In the hardness maps shown in Figure 5.14 it is seen that the pearlite was formed for both types I but no clear gradient is observed. Hard + soft has still formed pearlite when drawn using the normal die but it is seen that the hardness is much higher, which can most likely be attributed to the presence of bainite. Finally, it appears to have a hardness distribution of Soft + Hard. Hard + soft * is basically characterized by the homogeneous transformation to martensite.

With all these results, it is possible to conclude that the deformation has not enhanced the gradient formation and the deformation, which was thought to entail an increase of the nucleation sites which would favor the nucleation of the pearlite at the surface than in the core, has presented the opposite effect. Whatever is the effect of the deformation, it has hindered the transformation to pearlite the most of the gradient cycles have transformed to martensite.

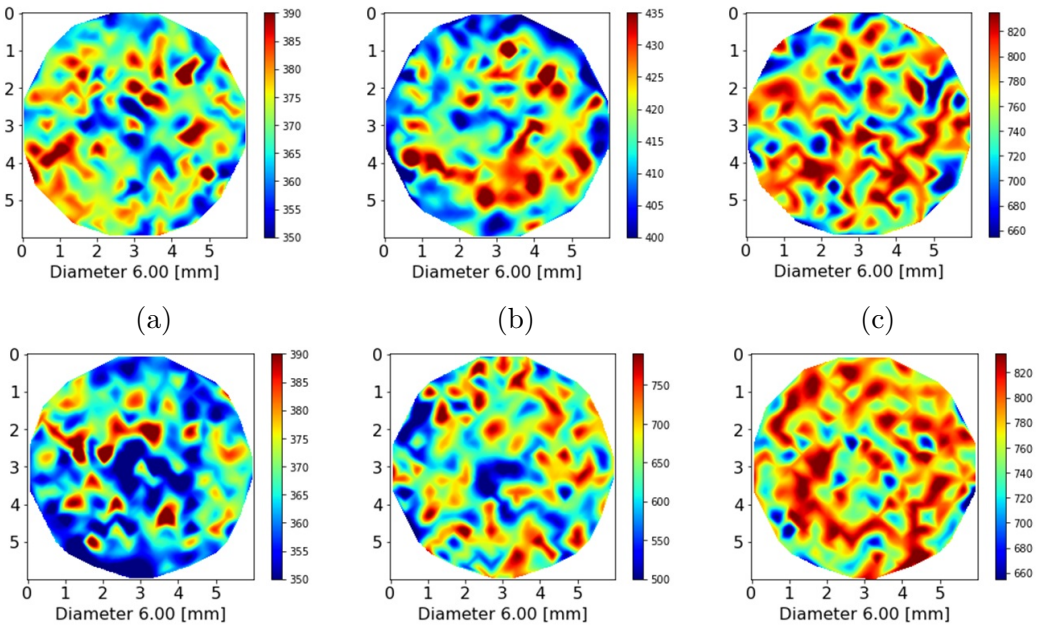

Figure 5.14: Hardness maps of the thermomechanical trials of the samples deformed by the normal die and subsequently transformed by type (a) Soft + Hard, (b) Hard + soft and (c); and the ones deformed by reverse die and then transformed by type (c) Soft + hard, (d) Hard + soft and (e) Hard + soft*.

5.4.4 Discussion

The possibilities of creating a microstructural gradient were evaded within this chapter. It was first seen that the real process involves recalescence that cannot be completely suppressed; second, that the lead patenting and the molten salt bath can be approximated to an isotherm heat treatment and the alternative water-based cooling is characterized by continuous cooling; and finally, it was proved that the real cycles can be simulated in the dilatometer and that its diameter is the main limitation for the thermal gradients, especially for the 6 mm.

Then the gradients production was proposed with the three targeted gradients cycles formed during cooling:

- soft surface and hardcore (Soft + Hard),

- a hard surface and softcore (Hard + soft), and

- different harder microstructures at the surface and a softer pearlitic core (Hard + soft *).

But, before they were tried, the effect of possible gradients formed during heating was first evaluated. It was seen that the heating rates can play a role in the strengthening of the thermal gradient during heating, which has allowed to form larger PAGS at the surface and finer at the core of the 6.5 mm diameter rod. The PAGS formed for the 12 mm diameter rod was unexpected since the surface was expected to be hotter during heating, however, as the heating cycle was done using a slower heating rate, the temperature had time to get even at the whole diameter which has allowed the heating to be homogeneous. So, the fast cooling has actually played the most important role because it has caused a large temperature difference between the core and the surface that has stopped the growing at the surface, but not in the core.

In the end, it has entailed a difference of 10 µm in the PAGS for the 12 mm diameter rod and 5 µm for the 6.5 mm diameter rod, which represents around 14% and 10 % of the difference, respectively. The role of the PAGS is important for the nucleation of pearlite during cooling. Considering that the smaller grain size represents around 14% or 10 % greater nucleation sites than the larger grains, it does not seem to be a very strong effect.

The equation of the nucleation rate proposed by the classical nucleation theory, which defines that the nucleation will start after the nuclei reach a supercritical size that decreases the overall energy of the system [163], comprises the density of nucleation sites with the nucleation. The equation is calculated as follows:

$$N(T(t)) = C\omega exp(-\frac{\Delta G^*(T(t)) + Q_N}{RT(t)}) \tag{5.1}$$

where $\Delta G^*(T(t)$ is the critical free energy of nucleus formation, R is the gas constant, T the temperature, C the number density of suitable nucleation sites, ω the characteristic frequency factor and Q_N the activation energy for the jumping of atoms through the interface.

It is seen that the nucleation rate varies linearly with the density of nucleation sites. For a sake of simplicity, it will be considered that the PAGS decrease of 14% represents a decrease of 14% on the nucleation rate. Therefore, it does not change the previous conclusion that this is not a drastic difference, and the PAGS have a very bland effect on the gradient production.

Finally, the real production of the gradients can be discussed; it was divided by the

means production: thermal, mechanical, and thermomechanical.

By the thermal means, it was seen that it was more or less "easy" to form a gradient of hard + soft , mostly because it comes from a natural distribution of the heat in thick samples. For instance, in the 12 mm diameter rod, that is the thickest one, independently of the applied cycle, a gradient of finer pearlite at the surface and coarser pearlite in the core has formed. However, the 6.5 mm diameter rod has presented some unexpected results: the soft + hard cycle has produced gradients that are hard at the surface and soft in the core, and the types hard + soft and hard + soft* formed a homogeneous interlamellar spacing distribution and, from the hardness results, it even seems to be a gradient of soft + hard type of gradient. From these results, the first and most evident conclusion is that it is not possible to prevent the transformation in the core of the wire because the thermal gradient is not sharp enough. Secondly, and now deeply analyzing this result, when slowly cooled to the beginning of the transformation which will thus transform to coarse pearlite, it does not matter if the cooling power is increased because the overall temperature will increase because of the recalescence. It is seen that the sample transformed with the soft + hard cycle is globally coarser and it happens because it has formed coarse pearlite at the surface and subsequently it has pearlite formed in the core, but it has formed at a higher temperature. Whereas for the transformation of hard + soft , the start of the transformation occurs at very low temperatures, in which the driving force for the transformation is very high and, once the transformation starts, the nucleation sites are fast taken. As fast cooling has to be employed for the transformation to occur at low temperatures without forming coarse pearlite, the core will reach the transformation temperature before the recalescence increases the temperature to form coarse pearlite. The inverse hardening profile observed, which has presented that the core was harder than the surface, might have been produced as consequence of an aging since the subsequent cooling is less powerful and it would leave the core at higher temperatures for a longer time.

The conclusion is that for the production of the gradients, first the inverted gradient, coarse pearlite at the surface and fine pearlite at the core, seems impossible because of the recalescence that is intrinsic to the pearlitic transformation. Next is the modified bainitic version of the Tempcore that was not possible to form a gradient and also not possible to avoid the bainitic transformation in the core of the wire. It is not interesting to have a mix of these two microstructures that have different deformation mechanisms. Besides, from the

industrial practice, it is known to be problematic to have a percentage of bainite in the wire because it fractures during drawing. Finally, only the gradient hard + soft seems feasible.

Afterward, the mechanical gradients were analyzed. It was seen that it has produced a gradient hard + soft since it has introduced a higher amount of deformation closer to the surface.

It was also observed the effect of the die angle on the microstructure. The normal die has affected a smaller portion of the microstructure than the reverse die. The die angle is known to increase the drawing force and the texture, most likely because of the shear deformation caused by the increased interaction between the wire and the die [164, 48]. Therefore, it would be expected to increase the amount of deformation close to the surface and but, in fact, with the used angle of the reverse die, it has affected the whole diameter. Still, it presented a deformation gradient, but the whole microstructure was deformed, differently from the normal die that has only introduced the deformation under 0.5 mm of the surface.

Finally, the thermomechanical gradients were analyzed and, at first glance surprisingly, it has not enhanced the pearlitic gradients. But, when considering the study of the "recrystallization" of pearlite shown in Chapter 4, it becomes obvious that the deformation of the pearlite cannot entail more nucleation sites since, independently of the applied deformation, the nucleation of the austenite continues to be at the colonies triple joints. Therefore, a deformation cycle should be done in the austenitic domain to have this type of effect. However, it is curious that the pearlitic transformation has been disfavored and the martensitic transformation has taken place. The only explanation must be during the austenitization, however it remains understood and some further investigation must be done to have it explained.

5.5 Conclusions

The assessment of the production of a pearlitic microstructural gradient has been done in this chapter. Two diameters were analyzed, 6.5 and 12 mm, to have a better understating of the dependence of the gradient with the diameter. These wires were transformed using a medium coil in the dilatometer, which was set up and validated to simulate the real process of pearlitic production (lead patenting, molten salt bath,

and water-based alternative cooling).

The targeted gradients were proposed and they can be defined given its hardening distribution, being soft surface and hardcore (soft + hard), a hard surface and softcore (hard + soft), and different harder microstructures at the surface and a softer pearlitic core (Hard + soft *). The possibilities of producing these gradients by thermal, mechanical, and thermomechanical means were evaluated.

Summing up the most relevant results, it was seen that:

- The real process cooling can be approximated by isothermal cooling (lead patenting and salt bath) and continuous cooling (water-based alternative cooling). In all the processes it is seen an increase of temperature during the transformation that is caused by the recalescence that is not controlled/suppressed by the cooling power. The dilatometer was set up to simulate the real process with the control of the gas flow instead of the control of the sample temperature and it was proven to effectively simulate the real process.

- The heating and austenitizing conditions were investigated and no important effect on the formation of the gradient was observed. For the 6.5 mm diameter rod it was possible to create a difference in the PAGS of 5 µm larger at the surface than in the core by using a heating rate of 30 °C/s. For the 12 mm diameter rod was created PAGS 10 µm larger at the core than at the surface. The observed difference was not important, but maybe if heating at extremely high rates by induction heating are used in the real process, it can produce improved gradients. Either way, the heating rate was discovered to be the most important parameter.

- The production of the targeted gradients of hard + soft by thermal means was accomplished with the 12 mm diameter rod independently of the employed cycle. For the 6.5 mm diameter rod, the soft + hard cycle has produced a gradient hard + soft , and the cycles for the production of hard + soft types have produced a more homogeneous sample. It is not possible to produce a fine pearlitic gradient with the 6.5 mm diameter wire because the thermal gradient is not sharp enough.

- The mechanical gradients were produced by drawing with different entrance angles of the die and they have both effectively produced a gradient of hard + soft . The lower angle has affected 0.5 mm under the surface while the higher angle has heavily deformed for over 1 mm.

- The thermomechanical tests did not produce any gradient thus proving that the deformation of the pearlite does not strengthen the gradients. Using the same cycles of the thermal target gradient on the deformed samples, the pearlitic transformation was disfavored and martensite was obtained instead. The deformation of the sample still in the austenitic domain might be a better option for the production of the gradients.

Chapter 6

The role of pearlite morphologies on the Low Cycle Fatigue

6.1 Introduction

It was shown in chapter 2 that the average interlamellar spacing ($\overline{S}$) is often considered as the key parameter controlling the mechanical properties of pearlitic steels. However, it was also shown that the pearlitic microstructure is a complex hierarchical microstructure and, therefore, it is questionable whether other characteristics of the microstructure than the average interlamellar spacing ($\overline{S}$) should not be considered to better describe the mechanical properties and, in particular, the fatigue behavior.

Within this chapter will be shown the results of the fatigue specimens especially transformed in the dilatometer, which will be here only used as an advanced heat treatment tool. Some monolithic pearlite with different interlamellar spacings and different morphologies will be first considered and the fatigue behavior of these monolithic pearlitic steels will be analyzed and then compared to the gradient steels. The aim is first to assess the changes in microstructures that can entail an improvement of the fatigue and mechanical properties. Second, the cyclic plasticity of pearlitic steels and the sensitivity of the pearlite morphology on the crack initiation mechanism will be investigated.

6.2 Materials and experimental procedures

To produce fatigue specimens with strictly controlled microstructures and to test different heat treatment parameters on a small scale, it was needed to design a new drawing of a fatigue specimen that can be treated in the dilatometer and still respect the fatigue specimen dimensions. So, the challenge consisted in creating a specimen that is light enough to be held between the two ceramic rods, that is shaped with a gauge part large enough to accept the fatigue strain gauge extensometer, that has to enter in the dilatometer, follow the good proportions dictated by the ASTM standard [165] and thick enough to produce a gradient. The successful specimen design is shown in Figure 6.1a. It has a gauge part with a diameter of 6 mm and a length of 12 mm which can be homogeneously heated by the coil and seen in 6.1b.

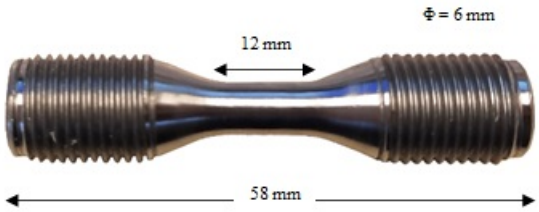

(a)

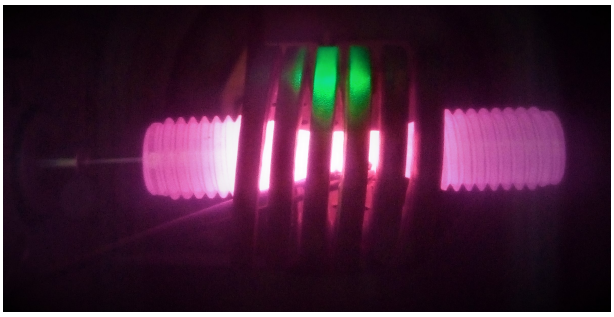

(b)

Figure 6.1: (a)Fatigue specimen design and (b) fatigue specimen glowing in the dilatometer during heat treatment.

The specimens were machined at Bekaert from a 14 mm eutectoid pearlitic wire. The exact chemical composition is displayed in table 6.1.

Table 6.1: Chemical composition of the fatigue specimens

Chemical composition (in wt.%)									
C	Mn	P	S	Si	Al	Cu	Cr	Ni	Fe
0.808	0.555	0.011	0.007	0.176	0.001	0.016	0.045	0.022	balanced

The surface condition of the sample is very important for fatigue testing because fatigue cracks are known to start from the surface. This means that the gauge part of

the specimen cannot have any machining defects or scratches. Therefore, the specimens are usually prepared before fatigue experiments by polishing the gauge part with SiC paper, diamond paste, and, sometimes, electropolishing. In the present case, this surface preparation was done before the heat treatment in the dilatometer to avoid the reduction of the heat-treated diameter due to excessive grinding. It allowed preserving the outer part of the specimen since grinding the fatigue specimen after the heat treatment could result in minimizing or even suppressing one part of the gradient specimen. Still, some polishing was needed after passing by the dilatometer because the thermal couple is welded to the sample surface and because there was some oxidation at the surface after the heat treatment that would hinder the later analysis of the surface.

In short, the gauge part of the specimen was first mechanically polished with grinding SiC paper until grade 2400 before the dilatometer and afterward polished with diamond paste until 1 µm to have the mirror-like aspect.

The modification of the microstructure was successfully achieved by the different heat treatments to obtain four monolithic samples and three gradients samples.

The monolithic pearlitic steels were processed as follows:

- Coarse pearlite: heated at 5 °C/s to 1000 °C with 10 s of soaking time then cooled at 100 °C/s to the isotherm cooling (IC) temperature at 620 °C, such as the ones done for the TTT in chapter 4; It presents a rather divorced microstructure.
- Fine pearlite 1: heated at 5 °C/s to 1000 °C with 10 s of soaking time then cooled at 100 °C/s to the isotherm cooling (IC) temperature at 540 °C, such as the ones done for the TTT in chapter 4; Such as the previous one transformed in the isotherm condition, it presents a divorced microstructure.
- Fine pearlite 2: heated at 5 °C/s to 1000 °C with 10 s of soaking time then transformed by a continuous cooling (CC) at -5 °C/s from the austenitic domain to the room temperature. It presents the same $\overline{S}$ as fine pearlite IC but with a different morphology, now lamellar with interconnections between the cementite lamella.
- Fine pearlite 3: first is done a stabilization cycle at 650 °C for 10 min, then it was heated at 10 °C/s to 797 °C, soaked for 5 min and finally continuous cooled to room temperature at 30 °C/s. This cycle is the same ASTM cycle shown in

Chapter4 and the selected fine pearlite has the same $\overline{S}$ as fine pearlite IC. This is the "perfect" lamellar pearlite.

The first three microstructures present the same heating set at 5 °C/s to the austenitization of 1000 °C for 10 s, while the ASTM counts with a prior stabilization cycle at 650 °C for 5 min then austenitization at 797 °C for 5 min. At the end of each cycle, it is always obtained a fine pearlitic microstructure of around 95 nm of interlamellar spacing, even though they differ from each other by the austenitization and/or the cooling parameters.

Figure 6.2 shows the micrographs of each monolithic pearlitic steel. It is worth recapping that the fine pearlite obtained by isotherm cooling presents a finely divorced microstructure, while by continuous cooling it has a roughly lamellar with a high density of branching and bridging. The ASTM presents to be the most perfect parallel and aligned lamellar structure. The formation of these microstructures will be discussed in chapter 4.

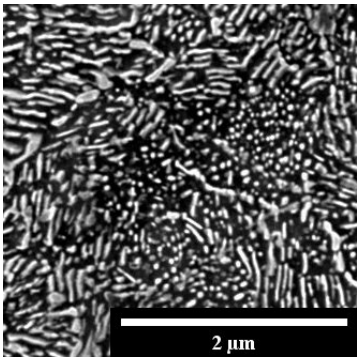

(a)

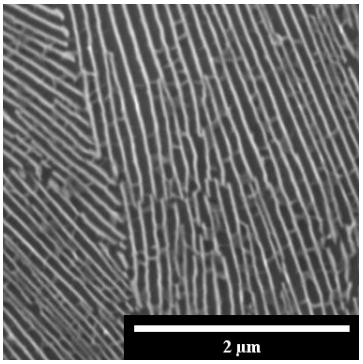

(b)

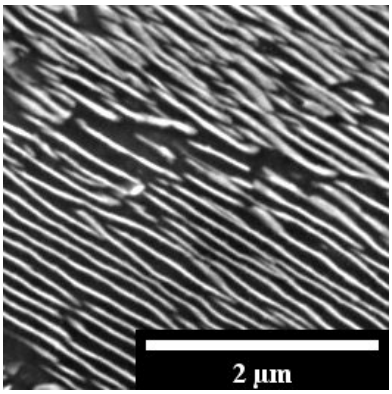

(c)

Figure 6.2: Fine pearlite morphologies: (a) mostly divorced obtained by isotherm cooling, (b) lamellar interconnected obtained by continuous cooling, and (c) lamellar closest to perfect pearlite obtained by the ASTM transformation cycle.

The choice of the gradient was done based on the analysis of the gradients in chapter 5. As explained in the previous chapter, the cycle to produce gradients of type 2, i.e., fast cooling then slow cooling to produce fine pearlite at the surface and coarse pearlite at the core, ended up producing more homogeneous samples. As it can represent a technological interest, its mechanical properties were also tested and compared with the gradients. To avoid mix up with the monolithic samples or the gradients, it will be here called the "most homogeneous" specimen.

The gradients 1 and 2 were produced by the same cooling path, i.e., slow cooling to 600 °C followed by fast cooling, and for this reason, they present the same $\overline{S}$. Their main difference remains in the fact that they were austenitized at different temperatures, which entails different PAGS between the core and the surface. This means that the two tested gradients present fine pearlite at the surface and coarse pearlite at the core and it is expected to observe the effect of this gradient in interlamellar spacing and also compare the effect of the prior austenite grain size.

The summary of the chosen heat treatments is shown in Table 6.2.

Table 6.2: Fatigue samples names, heat treatments, average interlammelar spacing ($\overline{S}$) and PAGS

Specimen	**Austentization**	**Cooling**	**Microstructure**	$\overline{S}$ **(nm)**	**PAGS (µm)**
Coarse pearlite IC	5 °C to 1000 °C and 10s of hold	Isotherm cooling at 640 °C	broken coarse pearlite	191 ± 37	
Fine pearlite IC		Isotherm cooling at 540 °C	broken fine pearlite	96 ± 9	52 ± 7
Fine pearlite CC		Continuous cooling at -5 °C/s	connect fine pearlite	90 ± 13	
Fine pearlite ASTM	10 °C/s to 797 °C, hold for 5 min *	Continuous cooling at -30 °C/s	perfect fine pearlite	96 ± 13	37 ± 4
Most homogeneous	5 °C to 1000 °C and 10 s of hold	20 % of gas until 600 °C then 40%	Fine pearlite homogeneous	83 ± 10	
Gradient 1	30 °C to 1000 °C and 10 s of hold	40 % of gas until 540 °C then 20%	Fine (surface) + Coarse (core)	$100_{surf}\|110_{core}$	52 ± 7
Gradient 2	30 °C to 950 °C and 10 s of hold		Fine (surface) + Coarse (core)	$100_{surf}\|110_{core}$	40 ± 4

*prior stabilization cycle at 650 °C for 10 min.

The microstructure was characterized by SEM taking micrographs every 500 µm to measure the transition of the $\overline{S}$ in the core and the surface. The result of the $\overline{S}$ is also seen in Table 6.2.

The hardness mappings of the samples were also measured to confirm the presence of the gradient. The automatic microhardness Vickers tester FM-810+ARS900(FT), from FUTURE-TECH, was employed with a load of 500 g and 10 s hold. The indents were done every 300 µm in x and y keeping a distance of 200 µm from the surface. The

produced mappings for both monolithic and gradient samples can be seen in Figure 6.3.

The fine pearlite ASTM presents the less homogeneous partition of hardness but was still enough to consider the specimen as monolithic.

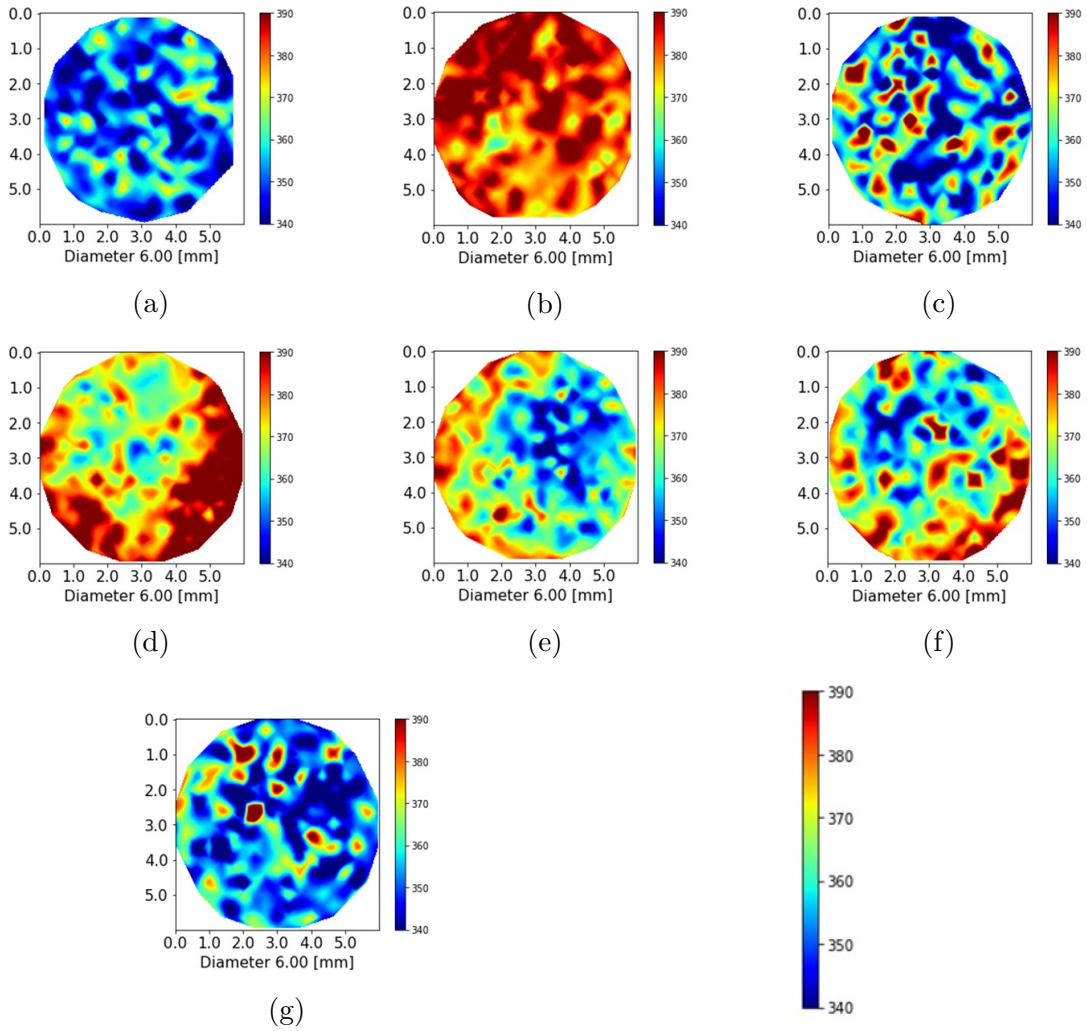

Figure 6.3: Hardness maps of the fatigue specimens. (a) Coarse pearlite, (b) fine pearlite IC, (c) CC, (d)ASTM, (e) gradient 1, (f) gradient 2 and (g) the most homogeneous

The fatigue tests were performed on a Schenck Instron machine at room temperature under strain control. It means that the strain levels are imposed and the needed stress to obtain the required deformation is recorded. An extensometer Instron of 8 mm gauge was used to precisely control the imposed strains.

For the monolithic samples, the total strain ranges were $\Delta\epsilon_t = 0.6$, 0.8 and 1.2%. For the gradients, only tests at $\Delta\epsilon_t = 0.6$ and 1.2% were performed. A triangular strain

waveform was employed at a constant strain rate of 4.10^{-3} s^{-1} as shown in Figure 6.4. All the tests were performed in duplicate to validate the result as reproducible.

The sample is considered to fail, whether it is broken in two parts or not when the stabilized stress drops 30 %. Therefore, this is the criterion to pick the number of cycles to failure.

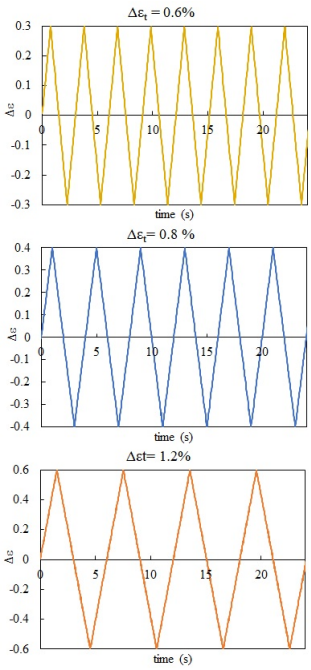

Figure 6.4: Triangular strain waveform signal of the tests under strain control at $\Delta\epsilon_t$=0.6, 0.8 and 1.2%

After the tests, the external surface investigation and fractography analysis were carried out in the SEM. Afterward, the samples were cut to analyze the longitudinal cross-section. This post-treatment was systematically applied to all specimens to investigate the presence of relief marks, longitudinal cracks, and finally its fracture surface. This way, the effect of the $\overline{S}$, the morphology, and the gradients could be thoroughly analyzed taking into account all the possible responses to the fatigue tests.

6.3 Cyclic accommodation

6.3.1 Monolithic microstructures

The stress response to strain cycling of coarse pearlite and fine pearlite in three morphologies are first over-viewed from the fatigue loops recorded at the first cycle

and the mid-life, see Figure 6.5.

First, it is important to highlight that the tests have been well executed. As it can be observed in Figure 6.5, the targeted strains in tension as in compression were reached since the first cycle and remained controlled during the entire test. It validates the veracity of the observations and avoids misinterpretation due to experimental flaws. This is also strengthened by the observation of cracking in the gauge part of the specimen.

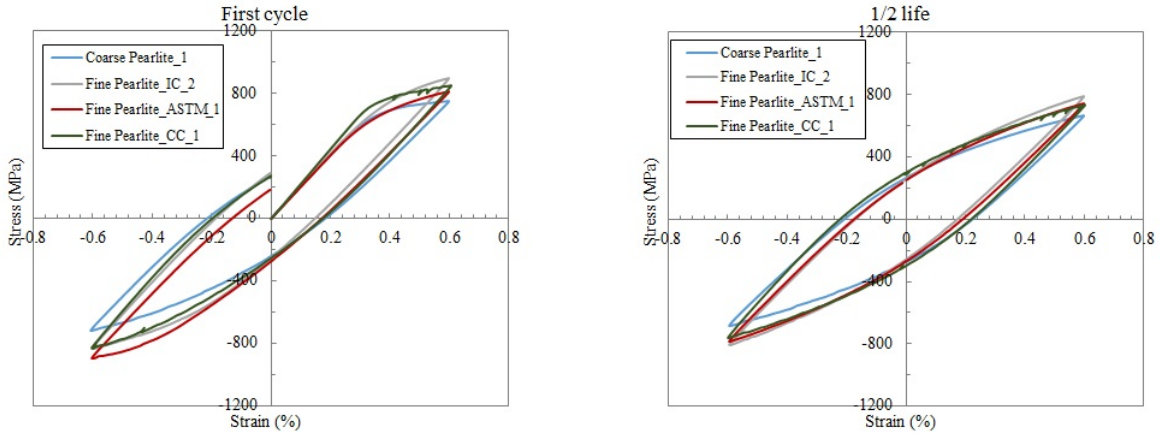

(a) (b)

Figure 6.5: Fatigue loops of the tests performed at $\Delta\epsilon_t$=1.2% recorded at (a) first cycle and (b) mid-life in the monolithic samples.

Now analyzing the mechanical behavior, at the first cycle, all the specimens presented different responses. Although there is not such a sharp difference between the maximum values for fine pearlite, the maximum stress is observed for the fine pearlite IC and the lowest value is observed for the coarse pearlite IC.

The analysis of the stress-strain response at the first cycle informs about the monotonic behavior in tension within a limited strain. All the microstructures presented about the same Young modulus, around 200 GPa. But, in the plastic domain, it is clear that all the specimens presented different responses. It is seen that the yield stress (σ_y), here evaluated by the moment where the curve leaves the elastic straight line, is the smallest for the coarse pearlite steel, as it could be expected. However, σ_y varies from one fine pearlitic steel to another, as seen by the lower stress values of the fine pearlites ASTM and CC when compared to the fine pearlite IC. This indicates that the interlamellar spacing is not the only parameter to consider for the assessment of plasticity properties. Moreover, there is a remarkable difference in the shape of the curve during the tensile load indicating a strong work hardening behavior expressed

by parameters of the Hollomon equation depending on the microstructure.

The macroscopic stress was decomposed into the effective stress σ^* (thermal component) and the internal stress σ_G (athermal component) using the Handfield-Dickson's method [166, 167]. It enables the determination of the effective stress from analysis of hysteresis loops recorded during fatigue without interruption of the fatigue test, which is an advantage in comparison to relaxation tests.

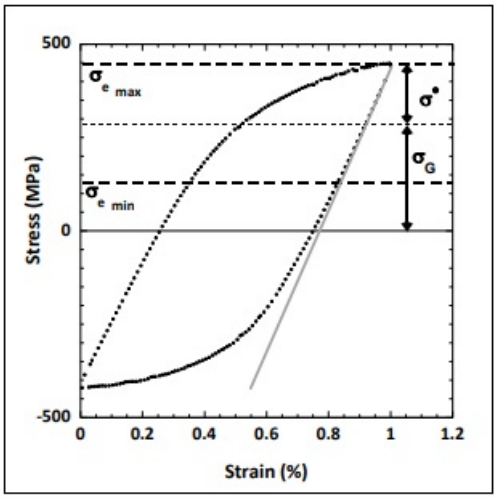

Figure 6.6: Dickson's method for hysteresis loop analysis. [19]

The effective stress, σ^*, is related to short-range interactions and internal stress, while σ_G is related to long-range interactions. They are calculated from the elastic domain delimited by the two frontiers: $\sigma_{e_{max}}$ and $\sigma_{e_{min}}$. The effective stress is then obtained by the equation 6.1 and the internal stress by equation 6.2.

$$\sigma* = \frac{(\sigma_{e_{max}} - \sigma_{e_{min}})}{2} \tag{6.1}$$

$$\sigma_G = \frac{(\sigma_{e_{max}} + \sigma_{e_{min}})}{2} \tag{6.2}$$

Table 6.3 summarizes the calculated values of Young modulus, yield stress, effective stress, and strain hardening. As commented before and now qualitatively confirmed, the different fine pearlite morphologies present different strain hardening and yield stress, which will certainly entail different cyclic responses.

Table 6.3: Young modulus, yield stress (σ_y), effective stress ($\sigma*$) and monotonic strain hardening exponent (n) and maximum stress (σ_{max}) obtained from the first quarter of cycle for the monolithic samples

	Coarse pearlite IC	Fine pearlite IC	Fine pearlite ASTM	Fine pearlite CC
Young Modulus (GPa)	205 ± 8	205 ± 7	209 ± 9	206 ± 8
σ_y (MPa)	557 ± 39	607 ± 21	606 ± 48	633 ± 44
σ_{max} in the 1^{st} loop (MPa)	734 ± 16	888 ± 11	833 ± 19	830 ± 32
$\sigma*$ in the 1^{st} loop (MPa)	80.5	312	250	95
σ_{max} at mid-life (MPa)	663 ± 8	767 ± 21	740 ± 1	717 ± 21
$\sigma*$ at mid-life (MPa)	33	94	91	25
Strain hardening exponent (n)	0.46	0.74	0.62	0.4

Table 6.3 also contains the values of the effective stress measured from the mid-life loop. The comparison clearly points out a strong effect of the interlamellar distance and the pearlite morphology on the effective stress. Indeed, among the three fine pearlitic steels, the one obtained by continuous cooling has the lowest effective stress while the maximum stress reached during the first loading is not so different between these three materials. Moreover, the decrease in the effective stress with cycling is well defined. As the effective stress reflects the short-distance interactions, such as friction lattice, one can assume that the dislocations present in ferrite which are responsible for the plastic deformation of the starting microstructure, are facing lattice obstacles to move. At mid-life, the reduced values of the effective stress suggest that some modification in the microstructure at the atomic scale has occurred giving more freedom to dislocations for motion. A decrease in the effective stress with cycling has already been reported in high nitrogen stainless steels [167], stating strong interactions between solute atoms and dislocations, that can change with cyclic loading. The reason why the different morphologies present different effective stresses will be later discussed.

Another interesting point that differentiates the materials is the response in compression. The maximum stress is very dependent on the material during the compression after the first loading in tension. However, at mid-life, all the fine pearlite steels have nearly the same value. The asymmetry in compression after a tension load occurs due to a decrease of the yield strength in compression as a result of a phenomenon known as the Bauschinger effect, which has been reported to happen for pearlitic steels [82, 168]. This effect indicates differences in the dislocation movements at compression and tension or, as better precised in the [169]:

> "the dislocation model involving asymmetrical potential wells resulting from surmountable barriers appears the most likely explanation of the Bauschinger effect."

It means here that maybe there is some asymmetry in the dislocation movement between coarse and fine pearlite. Nevertheless, a deeper analysis should be undertaken to validate this assumption.

The stress response to strain cycling with the number of cycles will be first analyzed to specify the effect of the average interlamellar spacing $\overline{S}$ without considering any effect of morphology or type of heat treatment. Therefore, the results from the coarse and fine pearlite obtained with the isotherm cooling tested at the three strain levels are shown in Figure 6.7. The graphs include the peak stress measured in tension and compression.

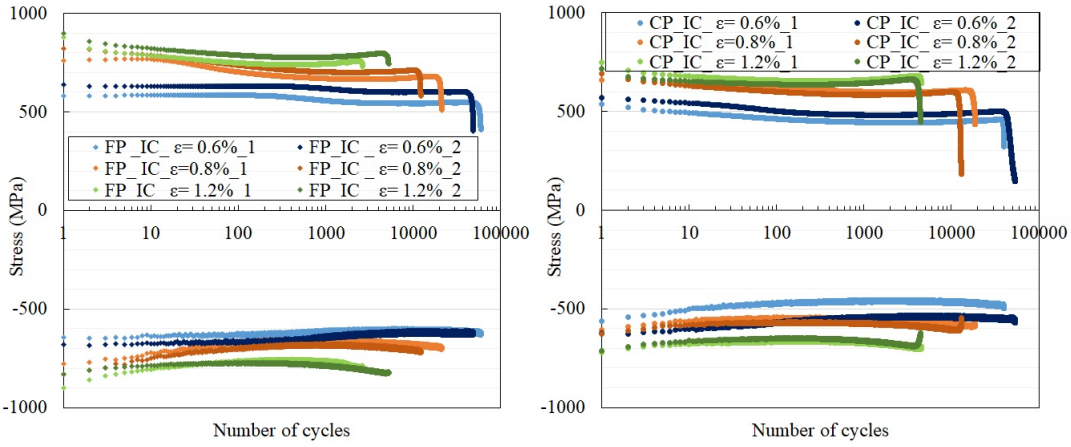

(a) (b)

Figure 6.7: Maximum and minimum stress vs number of cycles for fine (a) and coarse (b) pearlite specimen tested at $\Delta\epsilon_t$ = 0.6, 0.8 and 1.2%.

For each material, the peak values in tension and compression are more or less of the same order of magnitude, giving rise to symmetric curves in tension and compression. Thus, the stress amplitude vs number of cycles curves will serve now for comparison of the coarse and fine isotherm cooled pearlite (Figure 6.8a and b)

The first and most outstanding difference between the two microstructures is evidenced by the stress amplitude. For a considered strain range, the stress amplitude is higher for the fine pearlite steel. This reflects the beneficial role of the interlamellar spacing on yield stress.

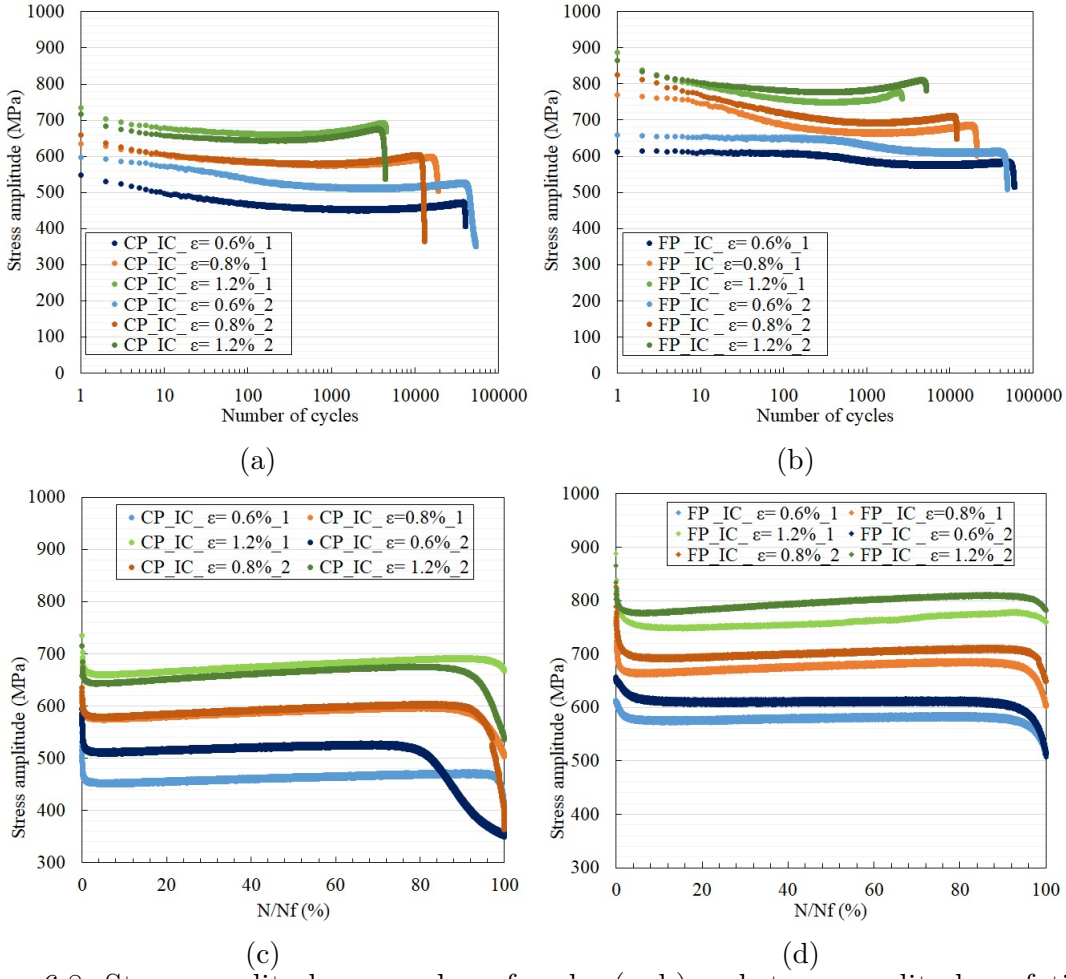

Figure 6.8: Stress amplitude vs number of cycles (a, b) and stress amplitude vs fatigue life fraction (c,d) for coarse and fine pearlite specimen tested at $\Delta\epsilon_t$ = 0.6, 0.8 and 1.2%.

Second is the general tendency in a cyclic softening followed by a hardening for both pearlitic microstructures. But, at a low strain range ($\Delta\epsilon_t$=0.6%), the stress response starts with a net and flat plateau for the fine pearlite steel (for around 300 cycles) and a less pronounced one (for 30 cycles) for the coarse pearlite during which the stress remains stable before the drop initiating the softening period. Increasing the strain range results in the reduction of the initial plateau until it completely disappears at $\Delta\epsilon_t$=1.2% and characterizing the straight softening followed by the onset of a cyclic hardening. The hardening period represents most of the fatigue life as can be seen in Figure 6.8c and d. The hardening rate increases with the applied strain range and is a little bit higher for the coarse pearlite than the fine pearlite. Even with the cyclic hardening, the stress value never reaches the initial one (that of the beginning of the test).

So, to summarize, the effect of the interlamellar spacing is mainly reflected by

the stress values and more roughly by the softening/hardening duration period and magnification.

For the morphology study, the fine pearlite was transformed by different production routes but always keeping the same $\overline{S}$. The results of the cyclic accommodation of the different fine pearlite morphologies are seen in Figure 6.9.

Basically and at a first glance, the cyclic accommodation of the fine pearlite steels obtained with the CC and ASTM routes does not differ frankly from the one processed with the IC route. They are still featuring the cyclic softening and hardening response since the beginning of cycling with only a small plateau observed at low strain $\Delta\epsilon_t = 0.6\%$. As for the coarse and fine pearlite IC, the softening period represents a very short fraction of the fatigue (less than 5%), see Figure 6.9e and f.

It is very important to identify materials that exhibit the softening behavior when exposed to cyclic load because, as the design of products is usually done based on the information provided by the tensile tests, the first cycle is not representative of the global mechanical behavior of the material in its real application since it drops after a few cycles of cycling.

The present investigation shows that the monolithic pearlitic steels present a rather stable stress response to cyclic loading at low strain (weak and slow hardening), but at high strains it presented a continuous hardening right after the end of the softening. The only detail is that the first cycle does not represent its average behavior. After around 5% past the start of cycling, the mechanical properties change a little and the designer should have to consider these values of mechanical properties for designing the structures.

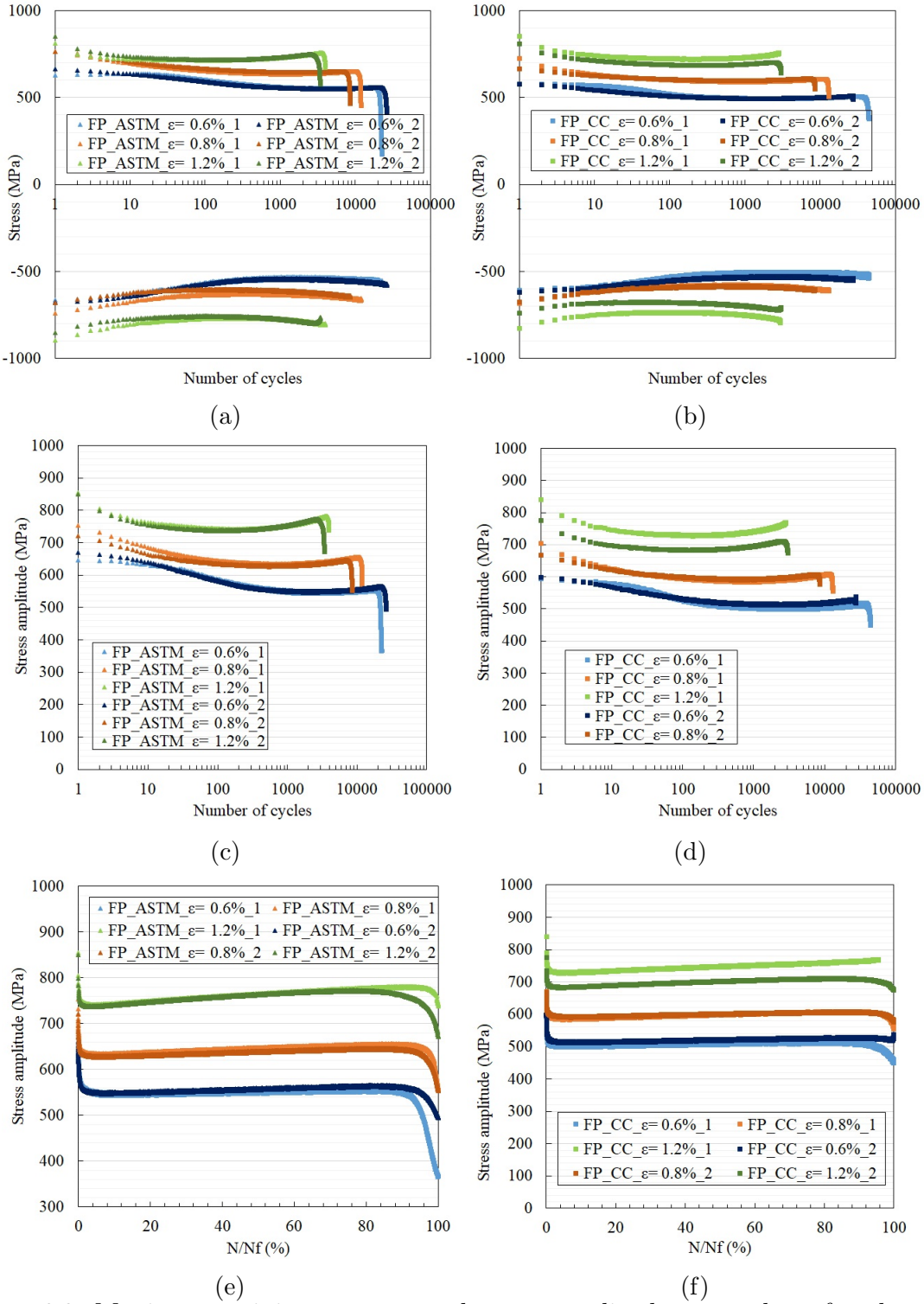

Figure 6.9: Maximum, minimum stress and stress amplitude vs number of cycles, and stress amplitude vs fatigue life fraction for the different pearlitic morphologies: fine pearlite ASTM (a), (c) and (e); and fine pearlite CC (b), (d) and (f); tested at $\Delta\epsilon_t$ = 0.6, 0.8 and 1.2%.

The cyclic stress-strain curves are compared with the monotonic stress-strain curves,

see Figure 6.10.

Despite the very large dispersion and Table 6.4 for the monotonic curve, the cyclic softening is strongly highlighted.

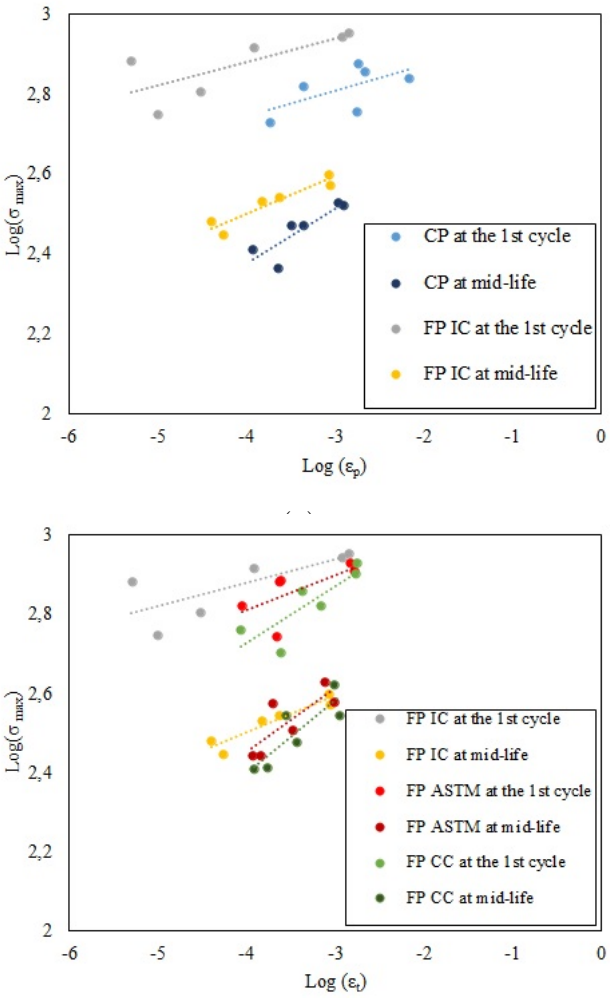

(b)

Figure 6.10: Cyclic hardening of the (a) Coarse pearlite and fine pearlite (b) and fine pearlite with the different morphologies: divorced (IC), perfect lamellar (ASTM) and interconnected lamellar (CC).

Regarding the plastic strain at the end of the first cycle, which is seen by the extreme points of the loops zero load, albeit it looks smaller for the fine pearlite ASTM, it is not a statistical result. When analyzing the duplicate tests, they all presented about the same plastic strain at the first cycle.

Table 6.4: Cyclic strain hardening for the monolithic samples

	strain hardening coefficient (n)			
	1st cycle	R^2	mid-life	R^2
Coarse pearlite	0.06	0.4	0.1385	0.74
Fine pearlite IC	0.06	0.6	0.094	0.89
Fine pearlite ASTM	0.09	0.4	0.16	0.64
Fine pearlite CC	0.14	0.7	0.19	0.73

6.3.2 Gradient microstructures

After having analyzed the key points of the fatigue behavior of the monolithic microstructures, it is now possible to discuss the effects of the gradients. The recorded loops at the first cycle and mid-life are displayed in Figure 6.11.

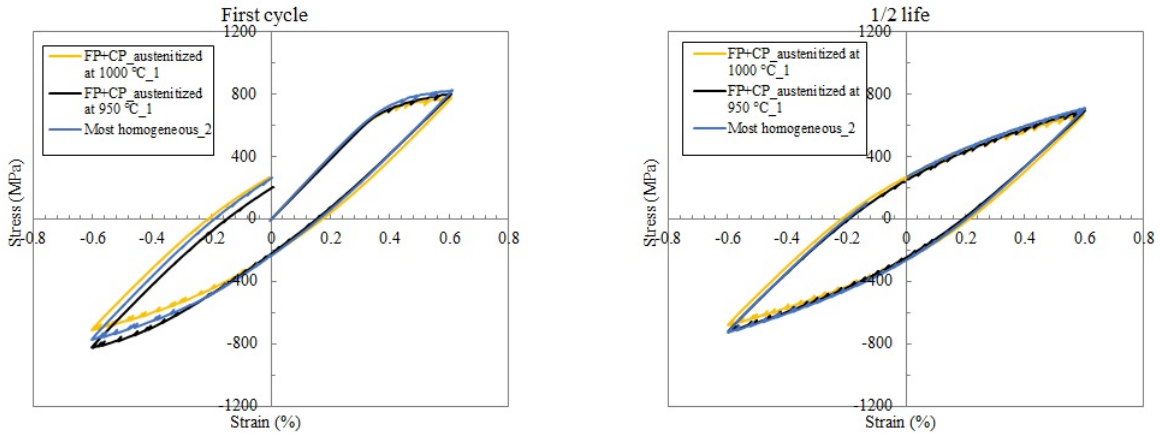

(a) (b)

Figure 6.11: Loops recorded at the first cycle and mid-life for the gradient microstructures and the most homogeneous test under $\Delta\epsilon_t = 1.2\%$.

The Young Modulus, the yield stress, and the effective stress obtained from the loops are shown in Table 6.5. Although the loops appear the overlap, they present important differences such as the yield strength, which changes greatly according to the type of gradient gradients.

The values of the effective stress do not change much neither at the first cycle nor at the mid-life, in which they all reduce in half. This means that the dislocation movement is about the same in all these three microstructures.

Comparing these values with the ones of the monolithic samples, it is seen that the effective stress is more than seven times larger in the fine pearlite of monolithic samples. The analysis of the gradients is rather complicated because the measured effective stress

represents the average of the whole wire, but not separately the contributions of the core and surface. Considering the obtained value of $\sigma*$, it seems to have a greater contribution of the coarse pearlite or the fine pearlite contribution is more like the fine pearlite CC.

Table 6.5: Young modulus, Yield stress (σ_y), and the effective stress ($\sigma*$) for the gradient samples

	Most Homogeneous	Gradient 1	Gradient 2
Young Modulus	192 ± 21	202 ± 3	200 ± 5
σ_y	592 ± 0	505 ± 11	640 ± 8
σ_{max} in the 1^{st} loop	734 ± 16	888 ± 11	833 ± 19
$\sigma*$ in the 1^{st} loop	77	84	79
σ_{max} at mid-life	712	677	720
$\sigma*$ at mid-life	34	35	45

During compression, the samples presented some disparity. The gradient 1, the one austenitized at 1000 °C, had the lowest absolute value, followed by the most homogeneous, and the gradient 2, austenitized at 950 °C, being the last one the most symmetric. This result evidences again the Bauschinger effect and, more specifically here, it seems to be related to the prior austenite grain size, since both austenitized at 1000 °C presented this asymmetry. Again, it can represent a contribution of the fine pearlite.

At mid-life they all presented almost overlapped loops with no important disparity between the values, as seen in Figure 6.11b. These results revealed that these special microstructures present the same behavior, regardless of their differences in the hardness distribution.

The cyclic accommodation behavior of the gradients is analyzed and the curves are seen in Figure 6.12. Since the tests done at $\Delta\epsilon_t$=0.8% with the monolithic specimen did not provide any new information, it was excluded from the gradient analysis and, hence, only the 0.6 and 1.2% strains were tested.

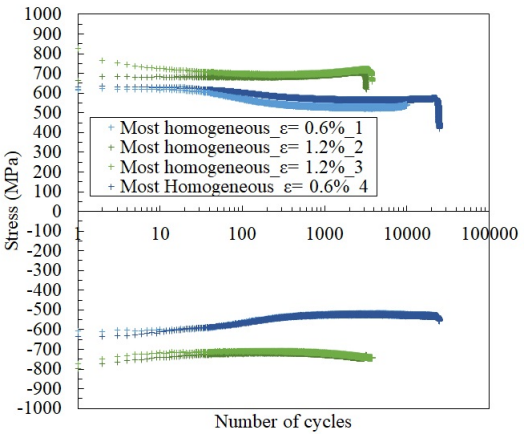
Most homogeneous_ε= 0.6%_1
Most homogeneous_ε= 1.2%_2
Most homogeneous_ε= 1.2%_3
Most Homogeneous_ε= 0.6%_4
Stress (MPa)
Number of cycles

(a)

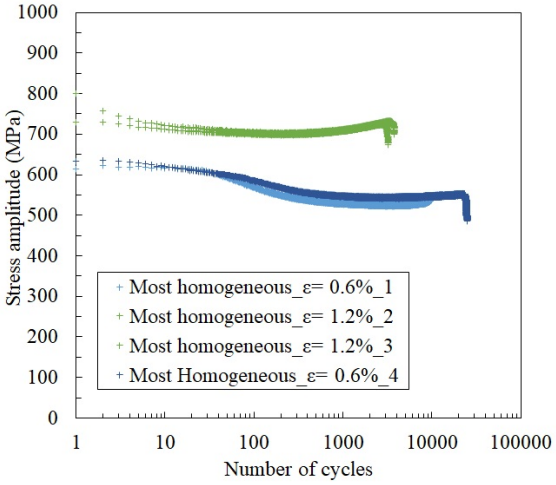
Most homogeneous_ε= 0.6%_1
Most homogeneous_ε= 1.2%_2
Most homogeneous_ε= 1.2%_3
Most Homogeneous_ε= 0.6%_4
Stress amplitude (MPa)
Number of cycles

(b)

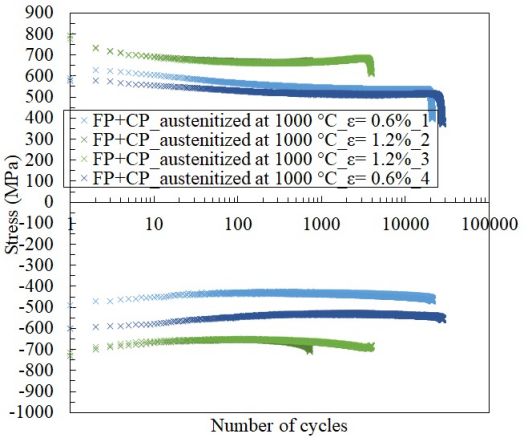
FP+CP_austenitized at 1000 °C_ε= 0.6%_1
FP+CP_austenitized at 1000 °C_ε= 1.2%_2
FP+CP_austenitized at 1000 °C_ε= 1.2%_3
FP+CP_austenitized at 1000 °C_ε= 0.6%_4
Stress (MPa)
Number of cycles

(c)

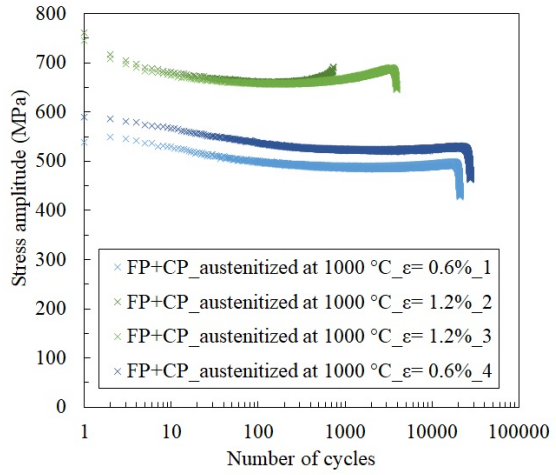
FP+CP_austenitized at 1000 °C_ε= 0.6%_1
FP+CP_austenitized at 1000 °C_ε= 1.2%_2
FP+CP_austenitized at 1000 °C_ε= 1.2%_3
FP+CP_austenitized at 1000 °C_ε= 0.6%_4
Stress amplitude (MPa)
Number of cycles

(d)

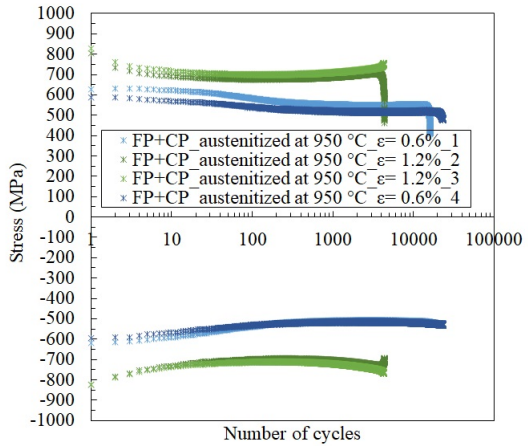
FP+CP_austenitized at 950 °C_ε= 0.6%_1
FP+CP_austenitized at 950 °C_ε= 1.2%_2
FP+CP_austenitized at 950 °C_ε= 1.2%_3
FP+CP_austenitized at 950 °C_ε= 0.6%_4
Stress (MPa)
Number of cycles

(e)

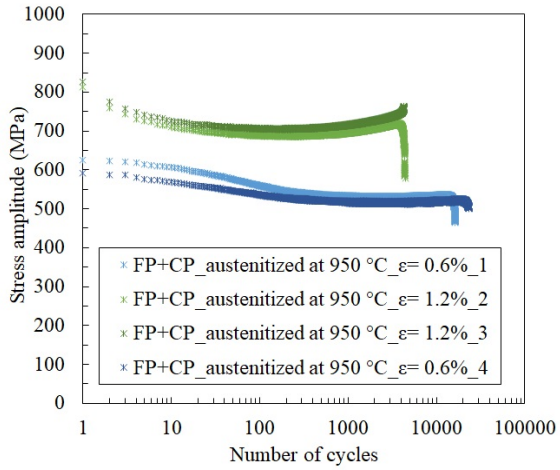
FP+CP_austenitized at 950 °C_ε= 0.6%_1
FP+CP_austenitized at 950 °C_ε= 1.2%_2
FP+CP_austenitized at 950 °C_ε= 1.2%_3
FP+CP_austenitized at 950 °C_ε= 0.6%_4
Stress amplitude (MPa)
Number of cycles

(f)

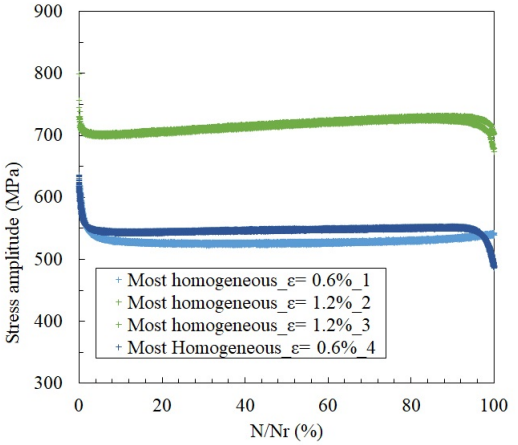

(g)

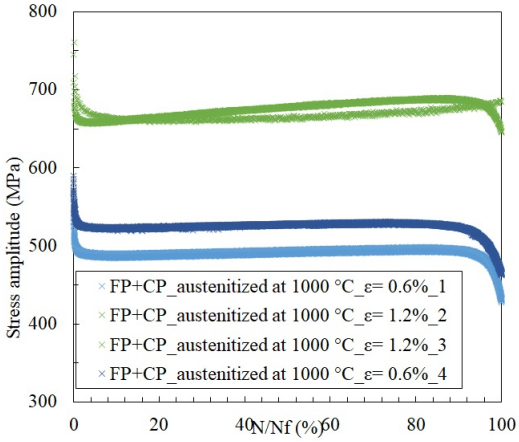

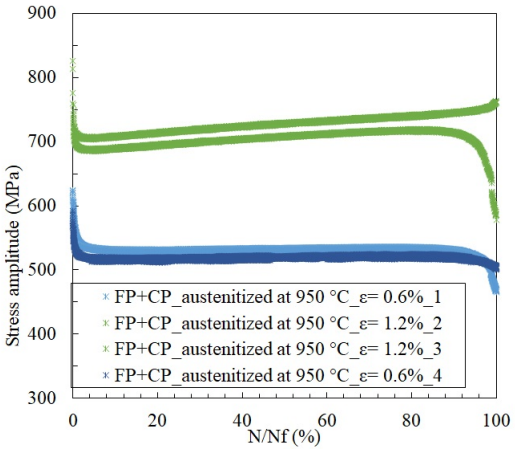

(i)

Figure 6.12: Maximum, minimum, and stress amplitude vs number of cycles, and stress amplitude vs the fatigue life fraction for the more homogeneous,(a) and (b); the gradient 1, (c) and (d); and gradient 2, (e) and (f); specimens tested at $\Delta\epsilon_t = 0.6$ and 1.2%.

At low strain, the most homogeneous microstructure presents the same behavior as seen for the monolithic samples at low strain: the stability period followed by the softening. The gradient samples have a similar behavior between them but, differently from the monolithic microstructures, it is not observed a stability plateau before the softening. Instead, it presents a gradual softening from the beginning, which also represents only a very small fraction of the fatigue life (again, less than 5%).

At high strain, they all present the immediate softening at the beginning followed by the hardening. The plot of the stress amplitude with the fatigue life fraction (Figure 6.12g, h and i) show that the softening period is very short (a few %). By contrast with the low strain test, they exhibit a non negligible hardening when fatigued at high strain.

6.4 Fatigue resistance

The Manson-coffin diagram is a plot of the plastic strain ($\Delta\epsilon_p$) vs the number of cycles before failure (Nf) and it is used to analyze the fatigue resistance of the materials. It defines the highest fatigue resistance either as the higher plastic strain for the same amount of cycles to failure or the highest amount of cycles for the same plastic strain.

The Manson-Coffin diagram for the monolithic and gradient structure are shown in Figure 6.13.

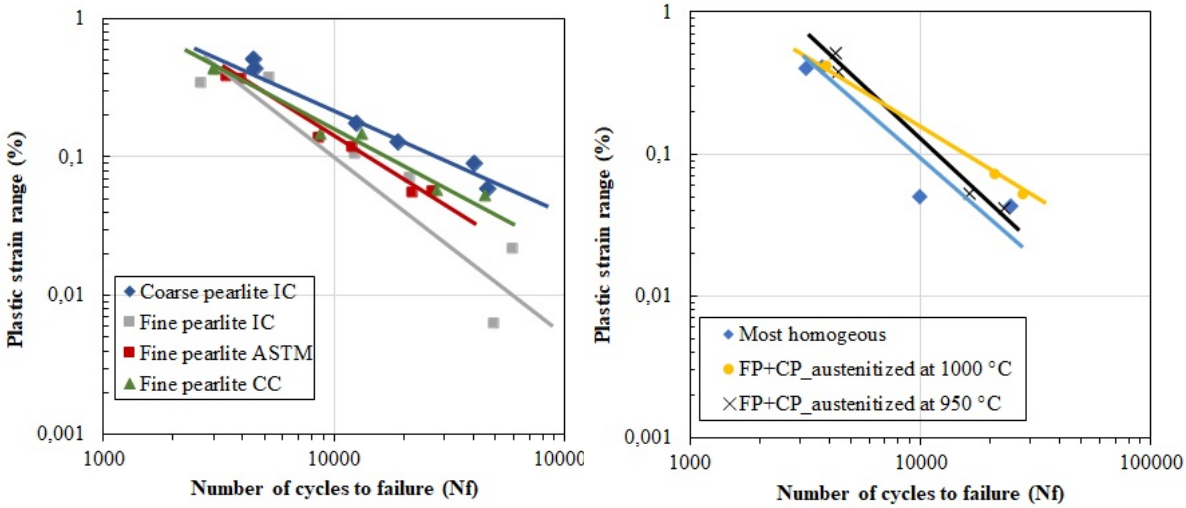

(a) (b)

Figure 6.13: Manson-coffin diagram of the (a) monolithic samples and the (b) special microstructures

Between the monolithic samples, the coarse pearlite presents the highest fatigue resistance seen by the blue line in Figure 6.13a, while the divorced fine pearlite (IC) presents the worse one, being the gray line on the bottom of the figure. The other fine pearlite morphologies stay in between the coarse and fine pearlite.

This result shows that the fatigue resistance of pearlitic steels, analyzed by the Manson-Coffin curve, is not only dependent on the interlamellar spacing since the changes in the pearlite morphology were capable to increase its fatigue resistance. This discovery has a huge technological importance since the morphology modification has improved the fatigue resistance without strongly degrading the maximum stress reached, e.g. comparison of the divorced (IC) and perfect (ASTM) fine pearlite.

It is worth recapping that the connected fine pearlitic (CC) has much lower stress values at low strain, but not so lower at high strains. So, it can also be considered an improvement of the divorced fine pearlite (IC) since it has increased the strain hardening.

The final application of the pearlite will define whether high stress is needed or higher fatigue resistance. In any case, there is a better production route to reach the desired properties.

Because of the small number of tests performed on the gradients, the results must be very carefully analyzed. To take into account the dispersion in fatigue tests, the gradients presented approximately the same behavior as the fine pearlite IC, thus not providing any improvement (6.13b.

6.5 Slip marks and short cracks analysis

All the tested microstructures were able to accommodate plastic deformation apparently with the same easiness, given the width of the hysteresis loops. It results in an evolution of the surface relief marks, the so-called extrusions. Extrusions are accompanied by intrusions to form pairs. The latter are considered to be the precursor of a crack, thus being important to characterize the location of its formation, the amount, the ease which the material has to form it, and also the ease to evolve from an intrusion to a micro crack and a long crack.

As seen in a previous study of the formation of extrusions in pearlitic steels, it

was observed that the extrusions are formed close to the cementite interface while the intrusion is formed in the middle of the lamella. It shows that the interface must play an important role in confining the dislocations in the ferritic lamella, which is the only responsible phase for the plasticity of the pearlitic steels as seen in extracted image 6.14.

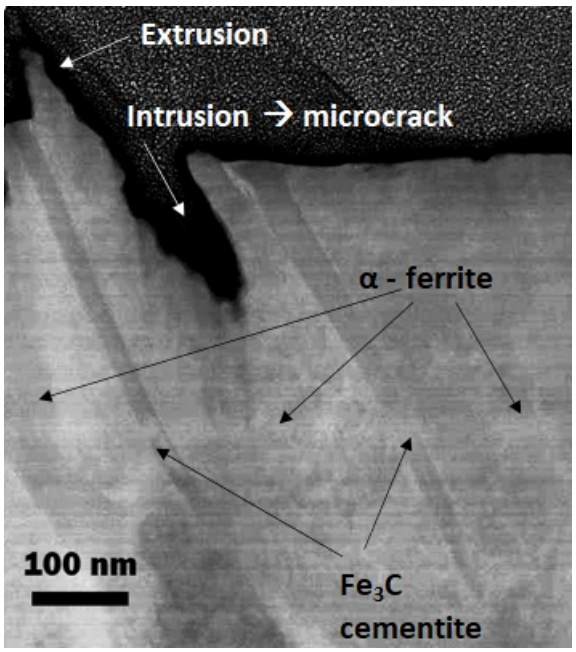

Figure 6.14: Extrusion-intrusion formation in pearlitic steels. [20]

The external surface of all specimens of the different microstructures were analyzed to observe how it affects the formation of the extrusion-intrusion pairs. The following descriptions arise from the observations of the relief after fatigue at $\Delta\epsilon = 1.2\%$.

The effect of the interlamellar spacing is shown in Figures 6.15a and 6.15b. The coarse pearlite presented a high density of well-developed extrusions, meaning that there is a considerable amount of material that was expelled during its formation. These extrusions were found in agglomerations here called packages, they were distributed all along the specimen surface, close and far from the main crack, and only very few small cracks were observed at the surface.

The fine pearlite, on the other hand, presented very few extrusions and almost no crack. The present extrusions were not developed and the few ones were located very close to the main crack.

The change in the pearlite morphology entailed an increase of the extrusions both

connected (CC) and perfect (ASTM) pearlite, as seen in Figures 6.15c and 6.15d, and also an increase of micro-cracks at the surface as observed for the connected fine pearlite (CC).

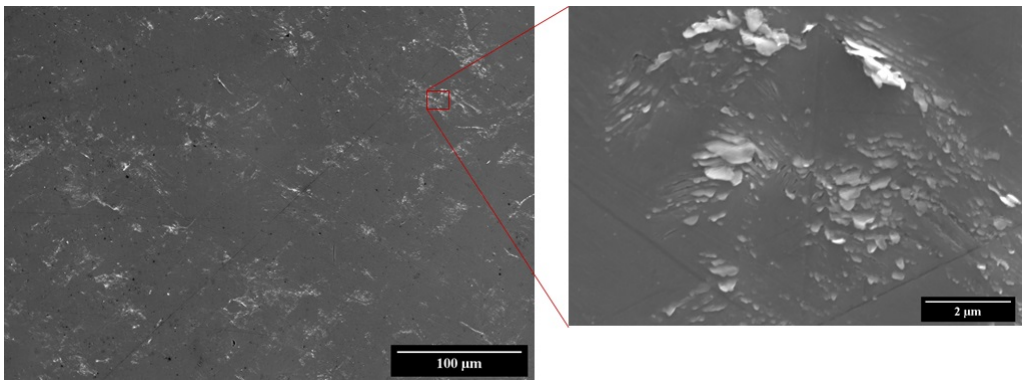

(a)

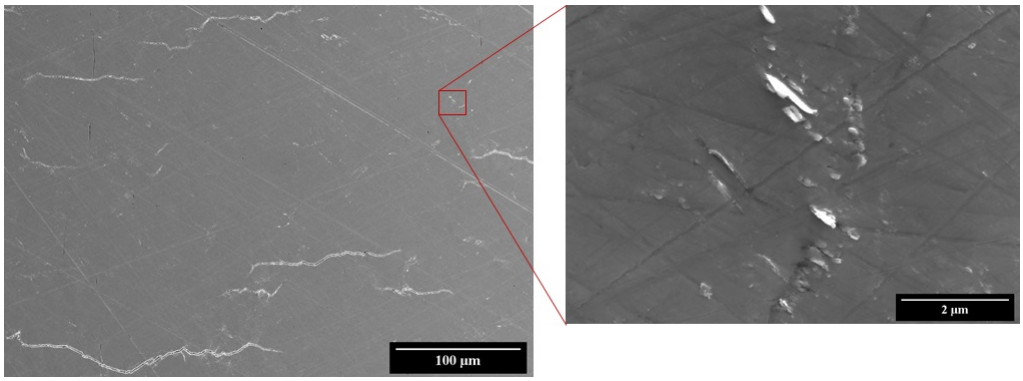

(b)

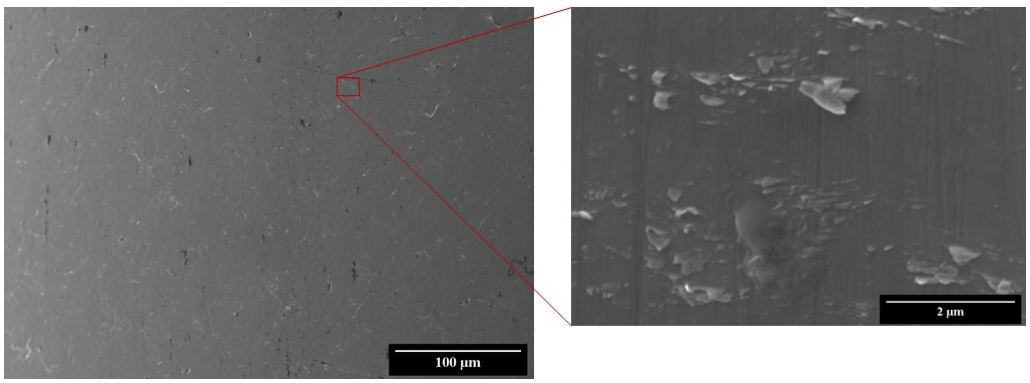

(c)

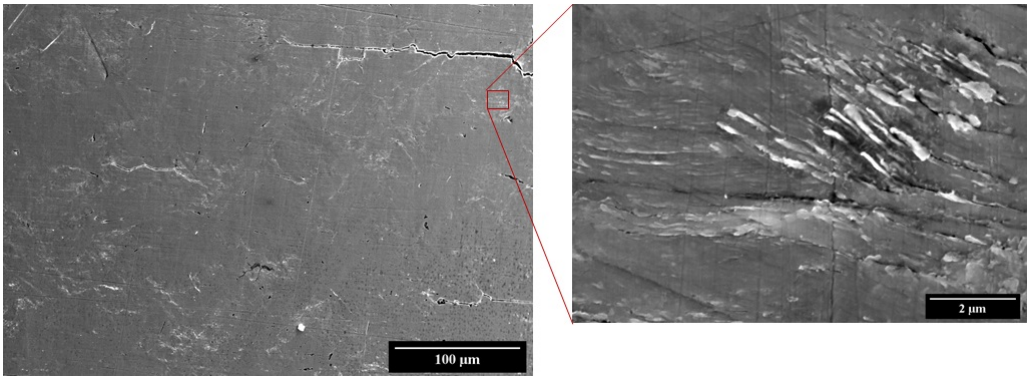

(d)

Figure 6.15: Extrusions of the (a) coarse pearlite, fine pearlite (b) IC c) ASMT (d) CC.

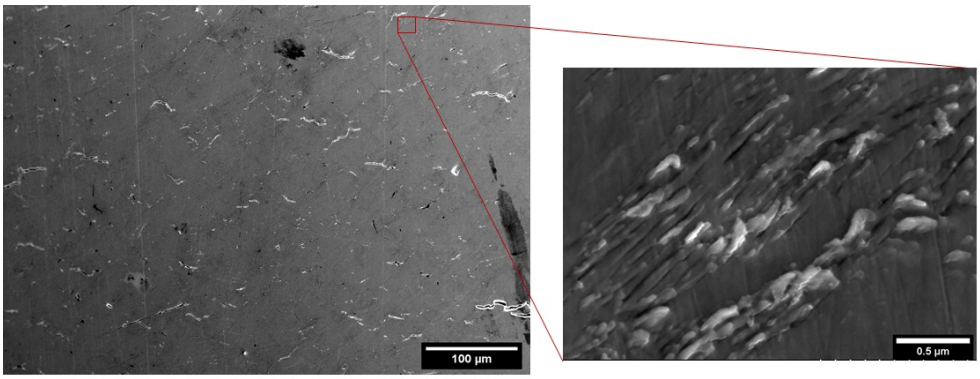

(a)

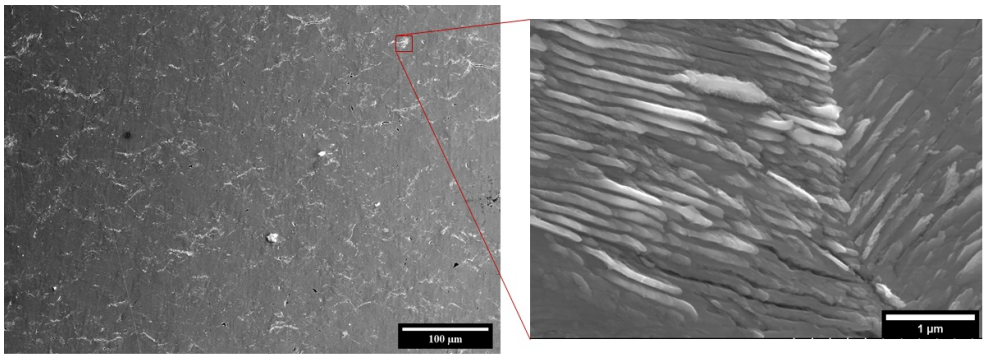

(b)

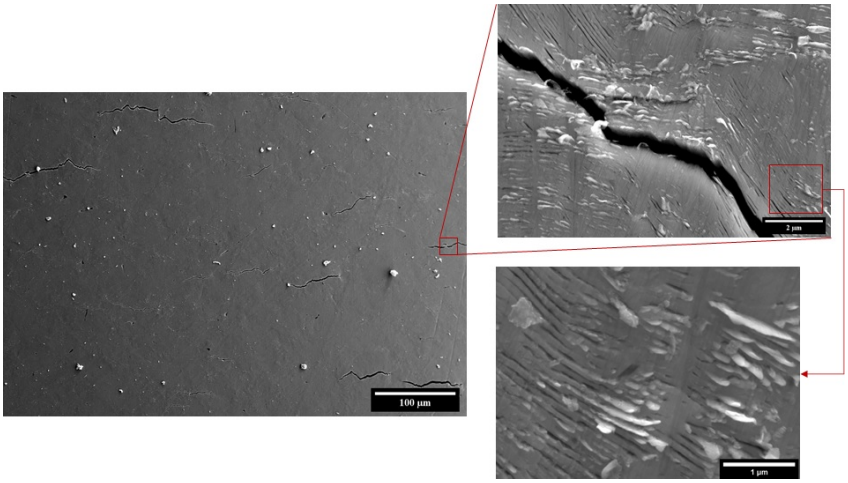

(c)

Figure 6.16: SEM image of the extrusions of the (a) most homogeneous, (b) gradient 1 and (c) gradient 2.

The observations on the gradients are shown in Figure 6.16. Gradient 1 presented a huge amount of very well-developed extrusions distributed all along the specimen surface. While gradient 2 presented a higher amount of small fractures at the surface and some extrusions only close to the small cracks.

The most homogeneous one has quite a few extrusions and cracks. They were developed and in packages.

The extrusions are proved to form at the ferrite and cementite interface, as just previously reviewed. The extrusions are formed due to the gliding movement of the dislocations. For that, they need to be well-oriented to the applied load axis to be able to slip. It is known that within a pearlite nodule the ferrite has nearly the same crystallography orientation, thus, it is expected that all the plans are activated in one well-oriented nodule with all its different directions of parallel lamellas within the colonies and, as the dislocations are confined between two cementite lamellas, the extrusions can be formed in each lamella.

It explains the formation of the packages of extrusions observed in the micrographs. More interestingly, figure 6.16b shows two different colonies that were activated and both produced extrusions. Most likely, they belong to the same nodule that was well aligned since the beginning.

After the intrusions are formed, they can evolve to short and long cracks without necessarily fracturing the material. Because it is not possible to appreciate the depth of a crack (as well any defect of such type), it is necessary to analyze them by the

longitudinal cut of the fatigue specimen. Figure 6.17 shows an example of a crack propagating into the bulk.

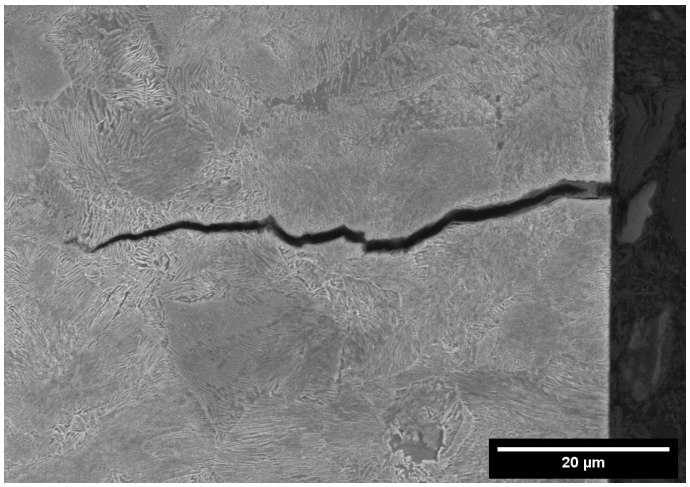

Figure 6.17: Longitudinal crack observed in the gradient 1 longitudinal analysis.

The cracks were measured, counted and classified according to their length "L_c" as follows: small cracks ($L_c < 15$µm), medium cracks (15µm> $L_c > 60$µm), medium-large cracks (60µm> $L_c > 100$µm) and large cracks ($L_c > 100$µm).

The amount of cracks measured at the end of the fatigue test at $\Delta\epsilon_t = 1.2\%$ as a function of their size in the monolithic and the gradient samples are shown in Figure 6.18.

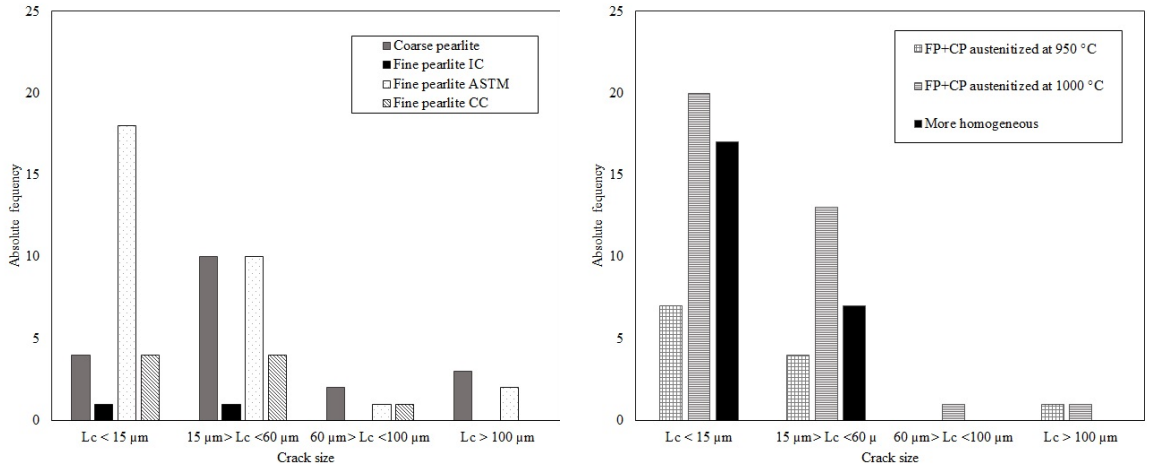

(a) (b)

Figure 6.18: Crack size distribution after fatigue at $\Delta\epsilon_t = 1.2\%$ in (a) monolithic microstructures and the (b) gradient microstructures

The density of small and medium cracks is very high in the perfect fine pearlite

(ASTM) and the coarse pearlite, thus suggesting that the many small cracks, formed in pairs with the extrusions, have encountered barriers stopping their propagation. This is especially pronounced for the perfect fine pearlite. The connected fine pearlite CC also presents many small and medium cracks though in less amount. By contrast, the divorced fine pearlite (IC) contains the shortest crack density and, essentially, the long crack that propagated very deeply into the bulk and has fractured the material. As soon as a short-medium crack develops, there are no barriers to prevent its growth into the bulk and they rapidly evolve to a long crack that fractures the material.

The surface of the most homogeneous specimen is covered with a huge number of small and medium cracks as was observed for the fine pearlite CC, thus appearing to be an improved version of it.

In Figure 6.18b, it is remarkable how the gradients can contain a lot of small cracks and some medium cracks that do not evolve to long cracks. This indicates that the gradient is capable to delay the formation of the long crack and its propagation into the bulk, thus proving to be efficient in improving the plasticity and the endurance of the wires during fatigue.

6.6 Fractography

The last analyzed feature affected by the microstructure is the fracture surface. Briefly summing up, the failure by fatigue happens in three steps:

1. short crack nucleation and growth at the surface;
2. fatigue crack propagation of the long crack in the bulk;
3. final rupture under ultimate tensile loading;

Therefore, the ways to improve the fatigue behavior of materials are related to the first two stages, in which the aim is to retard as long as possible the final irremediable rupture.

The specimen fatigued at low strain, $\Delta\epsilon_t = 0.6$ and 0.8 %, did not break in two parts. Therefore, the analysis of the fractography has only been done on the specimen that failed after fatigue at $\Delta\epsilon_t = 1.2\%$.

The fracture surface was the same for all the microstructures in the sense that it presents two regions: fatigue propagation zone and final fracture in tensile mode, as shown in Figure 6.19. The surface corresponding to the crack advance by fatigue is in general much smaller than the final fracture. The former contains fatigue striations, which were sticky to point out. The latter appears to be flat and typical of a brittle transgranular fracture. Even if this could be surprising since the materials appeared to be plastically deformed, it is a common feature of pearlitic steels as reported by [80, 14]. These observations underline the low toughness of pearlitic steels and it is hoped here that the changes in the microstructure can optimize this characteristic.

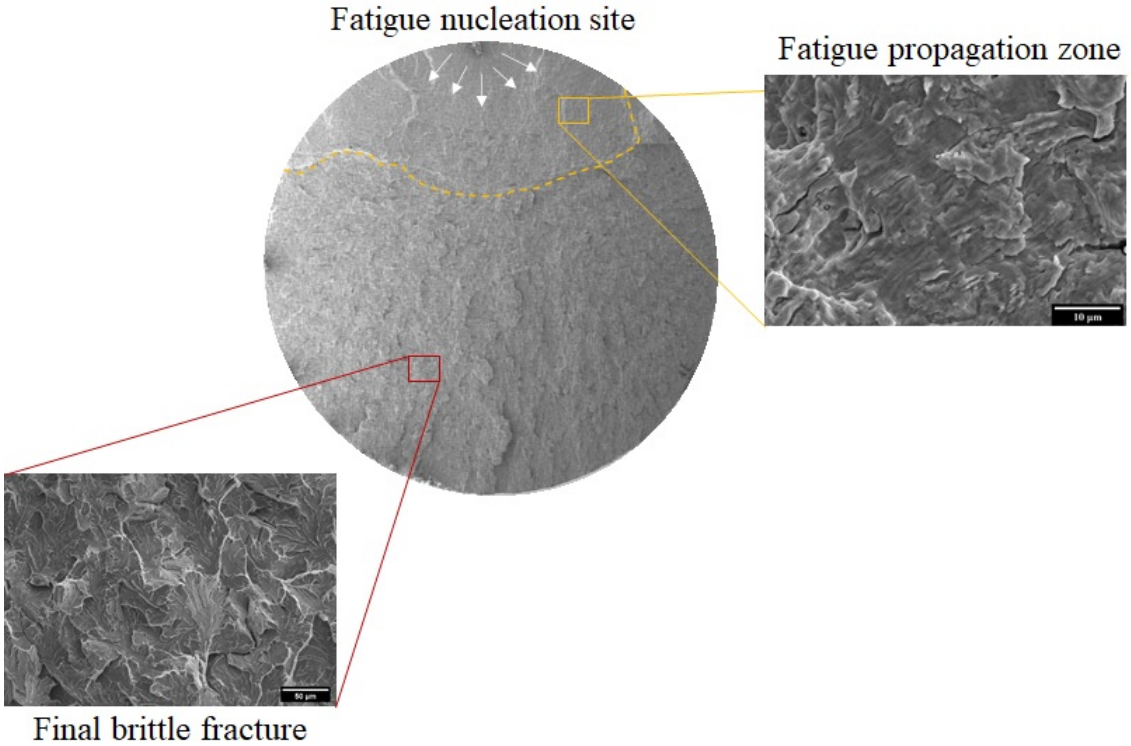

Figure 6.19: Typical fracture surface after fatigue failure observed for all tested materials

For comparison, the fracture surfaces of all the specimens after testing at $\Delta\epsilon_t$ =1.2% are shown in figure 6.20. The monolithic samples cover Figures 6.22a to 6.22d and the gradients Figures 6.22e to 6.22g.

There is not much difference between the fracture surfaces of the monolithic microstructures except the perfect fine pearlite (ASTM), which presented a wider fatigue propagation zone, hence improving the toughness of the pearlitic microstructure. Taking into account the stress just before failure and the fatigue crack

length, it is seen that the ASTM increases in almost 20% the toughness. Moreover the fine pearlite ASTM as well as the coarse pearlite exhibit more numerous fatigue crack initiation sites than the fine pearlite (IC).

The most homogeneous sample presented also a larger fatigue propagation zone and numerous crack initiation sites when compared to the fine pearlite CC, for example. It shows an improvement of the pearlitic microstructure formed during continuous cooling.

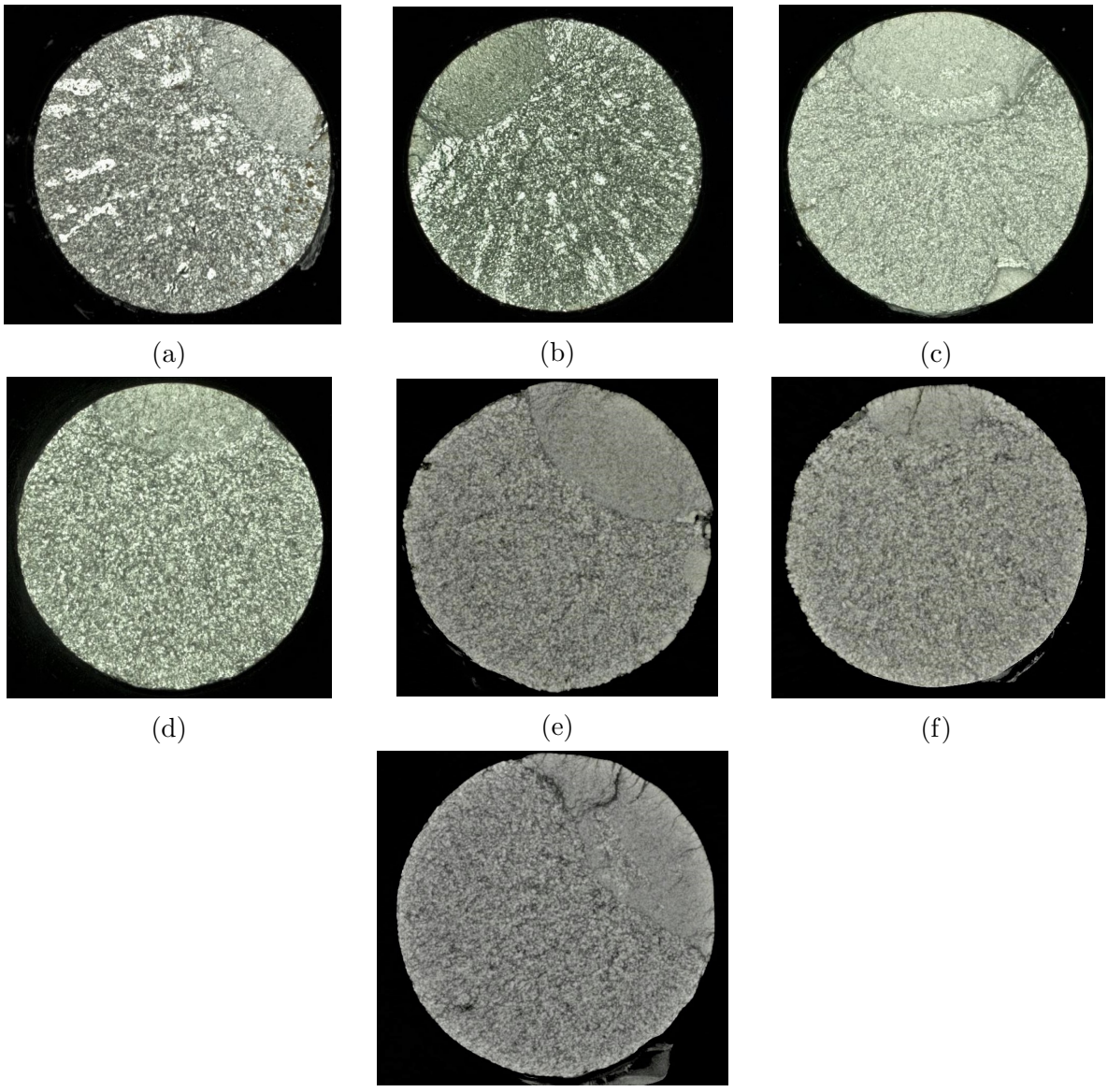

(a) (b) (c) (d) (e) (f) (g)

Figure 6.20: Fracture surface of the monolithic samples: (a) Coarse pearlite, (b) divorced fine fine pearlite (IC), (c) perfect fine pearlite (ASTM) and (d) connected fine pearlite (CC). And the gradient samples: (e) gradient 1,austenitized at 1000 °C, (f) gradient 2, austenitized at 950 °C, and the (g) most homogeneous.

The fracture surfaces of the gradients shown in Figures 6.20e and 6.20f reveal an effect of grain size on fracture toughness. There is a much shorter fatigue zone in gradient 2 when compared not only to the gradient but to all fatigue specimens. This microstructure was the only one austenitized at 950 °C, which implies that the toughness must be dependent on the PAGS.

The most homogeneous appears again as an improved version of the connected fine pearlite (CC) since it has also presented a higher toughness.

The fracture surface of gradient 1, shown in Figure 6.20e, has a larger fatigue zone, which also endorses the interest of producing a gradient hence it presents here a higher toughness in addition to the other improvement compared to the monolithic samples. Considering the calculation of the toughness, $K_{IC} \sim \sigma\sqrt{a}$, being a the length of the crack, it is seen that the materials presented different σ and different crack lengths. Calculating the toughness, it was seen that the both the ASTM and the gradient 1 the gradient presented a real improvement of the toughness, reaching 20 % for the former.

6.7 Discussions

In this section, it is proposed to explain the different mechanical responses concerning the microstructures resulting from the different cooling routes.

Starting by a comparative analysis, Figure 6.21 allows the comparison of the different stress responses to strain cycling of all tested materials.

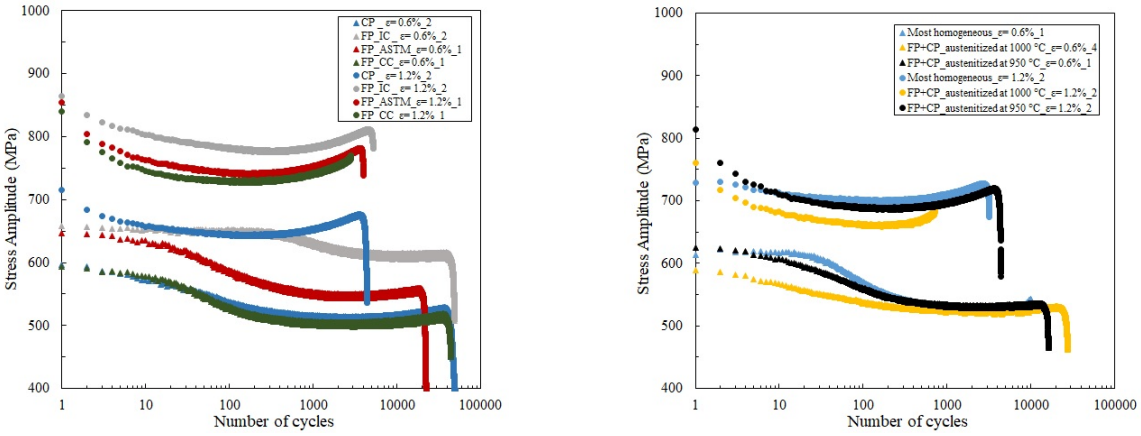

(a) (b)

Figure 6.21: Comparison of the stress amplitude with the number of cycles of the (a) monolithic and the (b) special microstructures.

A common response that features all the investigated steels is the cyclic softening which occurred right at the beginning of cycling at high strain levels and a bit delayed by a plateau at low strain. These different stages depend on the pearlite morphology. The second common point is the limited duration of the softening which is followed by a cyclic hardening. The occurrence of the cyclic hardening seems to be more strain dependent than microstructure dependent.The divorced fine pearlite (IC) keeps its stress superiority at all strain levels.

The gradients' behavior is closer to the coarse pearlite, not showing a big increase in tension with the increase of total strain from $\Delta\epsilon_t = 0.6$ to 1.2%, showing to have the low cyclic strain hardening. From this primary comparison, there is no advantage in producing the microstructural gradient.

To help the identification of the most sensitive material to cyclic strain softening, a softening parameter "τ_s" will be used and it is defined as:

$$\tau_s = \frac{\sigma_{max1} - \sigma_{mid-life}}{\sigma_{mid-life}} \tag{6.3}$$

Figure 6.22 shows the obtained results for monolithic and gradient samples. First analyzing the monolithic samples, two behaviors are observed:

(I) for the divorced fine pearlite (IC), characterized by low softening at low strain which increases with the increase of the strain.

(II) for the coarse pearlite (IC), high softening at low strain that decreases with the increase of the of strain.

This same behavior is observed for the perfect fine pearlite (ASTM) and the connected fine pearlite (CC).

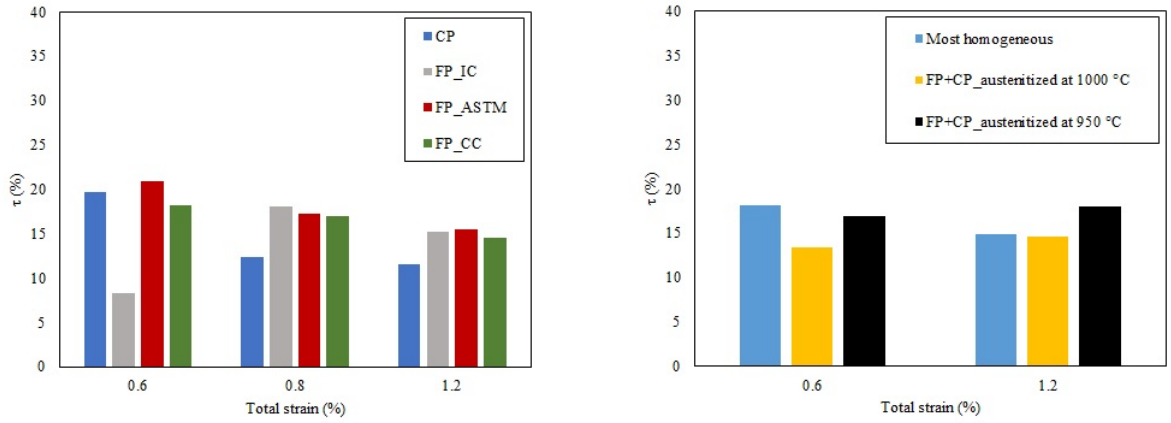

(a) (b)

Figure 6.22: Qualitative analysis of the cyclic softening observed in the (a) monolithic and the (b) gradient microstructures.

In previous works on ferritic steels [170], it was observed that the softening decreased with the increase of strain, same as the coarse pearlite seen here.

Finally, analyzing the especial microstructures, the most homogeneous presented the same behavior as the coarse pearlite, decreasing softening with the increase in strain. Gradients 1 and 2, have the same softening at low and high strain, being the softening in the gradient 2 (austenitized at 950 °C) greater the gradient 1.

At first, the discussion will focus on the coarse and fine pearlite steels obtained with the IC treatment. Their microstructure only differs in the spacing between cementite lamella, which in the present are broken, i.e. divorced pearlite was formed.

The first hysteresis loop shows a difference in the yield stress between these two materials which fits well with the expected effect of interlamellar spacing. However, the evolution of the stress between the yield stress and the peak stress strongly diverges. One can see that the hardening rate is higher in the fine pearlite steel than in the coarse one, meaning that it is easier to get plasticity from the ferrite of the coarse pearlite steel. It is known that for ferritic steels, the strain hardening exponent, n, is grain size-dependent for grain size superior of 1-2 µm [171]. For pearlitic steels, the interlamellar spacing does not appear or weakly affects the strain hardening component [131]. The contrasting results of our work can be simply explained by the range of strain in which n has been calculated. Indeed, the n exponent is usually calculated with plastic strain values of large deformation which makes sense because it is a useful parameter for metal forming. The range of plastic deformation for the calculation of n considered in the present Ph.D. work allows emphasizing the individual behavior of dislocations

in plastic deformation. The highest value of n in the fine pearlite must be associated with the high value of the effective stress measured on the unloading portion of the first hysteresis loop. Both values indicate strong short-distance obstacles.

One phenomenon also to be considered here is static aging, which is been widely investigated in the literature for the cold drawn pearlitic steels [172, 173, 174]. Two stages of aging are defined, one that happens by the pinning of the dislocations by the interstitial atoms, such as C and N, and the other one is related to the locking of dislocations at the ferrite-cementite interface by carbon atoms. The latter is known to happen at higher temperatures, being the second stage of static strain aging. During isotherm cooling (IC), the sample stayed at the transformation temperature for 2 min, which is not a problem for the coarse pearlite that takes very long to form at 640 °C but, for the fine pearlite, the transformation is finished within 10 s. It would give enough time to provide high-temperature aging.

Before cycling, ferrite contains the geometrically necessary dislocations (GND) resulting from the transformation and they are responsible for accommodating the expansion of cementite. Of course, the cyclic deformation is accommodated by dislocation displacement in ferrite, either initially preexisting ones or the ones being emitted from the interface between cementite and ferrite. Upon loading, when the critical shear stress to trigger the dislocation motion is reached, these pre-existing dislocations start moving. It can be assumed that carbon atoms are not very homogeneously partitioned in the ferrite lamella and tend to be segregated in a narrow band at the vicinity of the cementite interface, such as seen in the second stage of static aging. It turns out that a ferrite lamella of pearlite comprises enriched carbon lateral bands parallel to the cementite lamella and core bands less enriched in carbon, as depicted in Figure 6.23.

The smaller the interlamellar spacing, the narrower the core band. This way, the first loading and unloading involve essentially dislocations strongly anchored by carbon atoms in the ferrite bands of the fine pearlite. For the coarse pearlite, rather more mobile dislocations are available, those in the middle of the ferrite bands (the core bands). They are less anchored and more mobile than those in the lateral bands close to the cementite lamella. The decrease of the effective stress with cycling suggests that the repetitive and alternative gliding of dislocations leads to the formation of a track where dislocations now do not seem so strong short-distance obstacles as a result of carbon atoms redistribution away from the dislocation paths, similar as it has been observed in austenitic stainless steels enriched in nitrogen interstitial atoms [167].

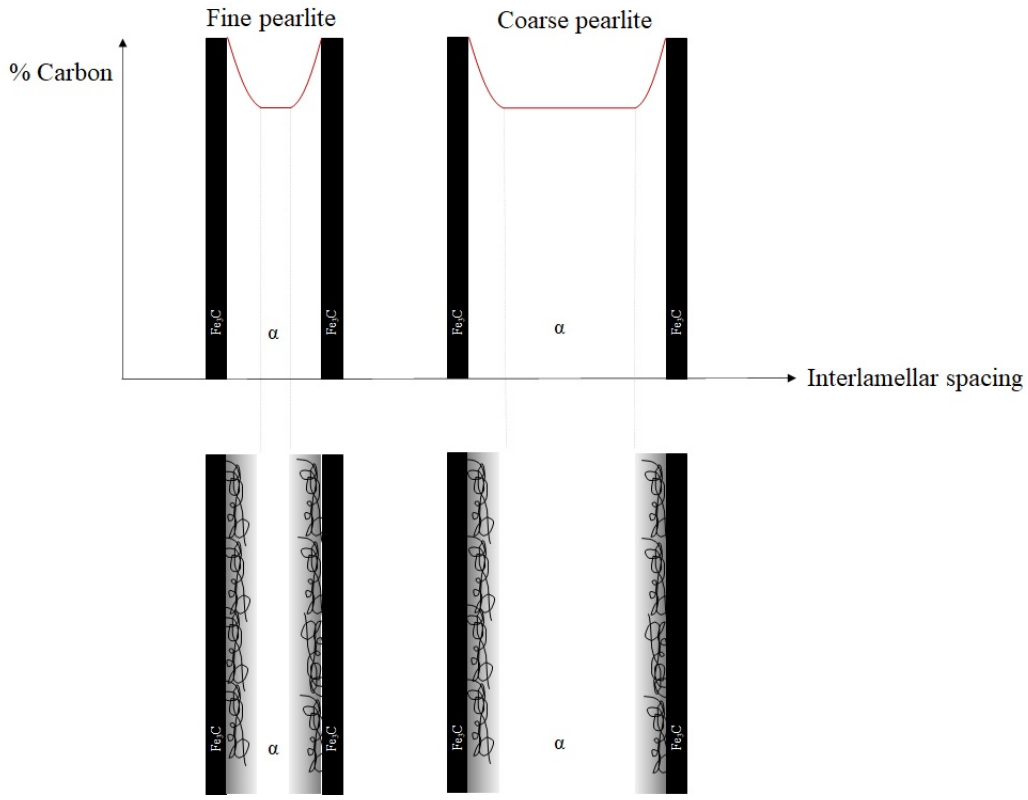

Figure 6.23: Expected carbon atoms distribution in ferrite according to the interlamellar spacing after IC treatment and corresponding partition of locked dislocations in ferrite.

The unlocking process of dislocations from carbon atoms and the carbon atoms redistribution allows the dislocations to move in localized tracks which leads immediately to the softening since the beginning of the test followed, later on, by a cyclic hardening. These two accommodation periods of the stress recorded during cycling are related with the competition between the rate of dislocations creation with the rate of dislocations annihilation, i.e. when $\rho_{annihilation} > \rho_{creation}$, the cyclic softening occurs and when $\rho_{annihilation} < \rho_{creation}$, the cyclic hardening is observed. From this assessment, the difference in the responses between coarse and fine pearlite steels can be easily explained.

Both coarse and fine pearlite steels are sensitive to cycling softening. However, it occurs easier in the coarse pearlite steel, in which the cyclic softening is observed from the first cycle for each strain level tested in agreement with the proposed theory of wide channels containing weakly anchored dislocations which under even a small loading can unpin and glide. Once they move, they can interact and annihilate up to a given number of cycles after which it turns to a cyclic hardening. The higher the applied strain, the shorter the softening period. At low imposed strain, the distance displacements

requested to accommodate the deformation by the preexisting dislocations are rather small, implying that their interaction results in moderate annihilating. At high strain, the requested distance displacements are much higher, in which case the annihilation events occur more frequently. The annihilation rate seems to be much superior to the creation rate that the ferrite lamella are quickly "cleaned" and it needs to reactivate new dislocations sources to accommodate the deformation, which now interlocks with new dislocations and gives rise to the hardening.

This description is also valid for the fine pearlite steel at the highest strain test, but not for the two lower strain tests. For the latter, the stress vs the number of cycles starts with a plateau, longer for the test performed at $\Delta\epsilon_t$ =0.6% than for that at $\Delta\epsilon_t$ =0.8%. The reason for this is the reduced size of the soft lane of dislocation gliding in the ferrite lamella. Since it contains mainly strongly anchored dislocations, the displacement distance of moving dislocations is so small that the annihilation process requires more loadings and unloadings to produce significant softening. The smaller the applied strain, the smaller the displacement movement, which explains the difference observed in the plateau at $\Delta\epsilon_t$ =0.6 and 0.8%.

Apart from the coarse pearlite, the other three investigated materials have about the same interlamellar distance between ferrite and cementite but not the same morphology, thanks to the different thermal treatment routes. Once more, the measurements of the effective stresses from the hysteresis loops bring discriminating results. The fine pearlite obtained with the CC treatment exhibits much lower effective stresses than the two other ones, which most likely indicates that carbon atoms are not distributed in the ferrite lamella the same way as it is in the fine pearlite IC and ASTM pearlite. In the fine pearlite CC, with the continuous cooling not involving any aging effect, the pearlite lamella are well aligned but connected by very thin cementite strips connections. It is, therefore, reasonable to believe that these strips have been formed by capturing the carbon atoms of the ferrite resulting in less carbon-enriched ferrite than for the two other ones. The rather low values of the stress amplitude at $\Delta\epsilon_t$ = 0.6%, comparatively close to the coarse pearlite, reflects simply the weak requested displacements of dislocations that do not undergo friction stresses.

The ASTM pearlite, which is the one with a perfect and well-aligned lamella, exhibits stress values at the very beginning of the test that are very close to the fine pearlite IC (divorced pearlite), but it presents a similar shape in the stress amplitude vs the number of cycles curve to the fine pearlite CC. The displacement of dislocations is disfavored because of the pinning effect by carbon atoms but once they start gliding,

they are guided by the cementite barriers and forced to remain along straight ferrite channels. Thus annihilation events as a result of moving dislocations interactions are more likely to happen than in the IC pearlite. And this explains the earlier softening.

This explanation for the fine pearlite IC is reasonable if the pearlite is thought as the definition given by Matt Hilert, one as an interpenetrating bi-crystal of cementite and ferrite [175, 176], it means that the ferrite is connected wherever there is a hole in the cementite or if the cementite is disconnected. In the case of the divorced fine pearlite, the dislocations have a much longer mean free path when compared to the ones confined between two cementite lamella.

The proposed mechanism of the accommodation of cyclic plasticity fits well with different observed networks of extrusions. The divorced fine pearlite did not present almost any developed extrusions. It can be explained by the fact that even if dislocations gained mobility once unlocked, they can move in wide gliding areas. On the other hand, in the samples that had a more restricted space for the movement of dislocation, such as the perfect and the connect fine pearlite, in each ferritic lamella there was an accumulation of defects that favors the formation of the extrusions. They were observed in packages, meaning that there was an intense activity of the slip plans in the parallel lamella, they were all activated and they did not have contact with each other.

Figure 6.24 illustrates the displacement of the dislocations in each microstructure. It becomes clear that the interactions are much facilitated in the divorced fine pearlite and hindered in the perfect and connected fine pearlite.

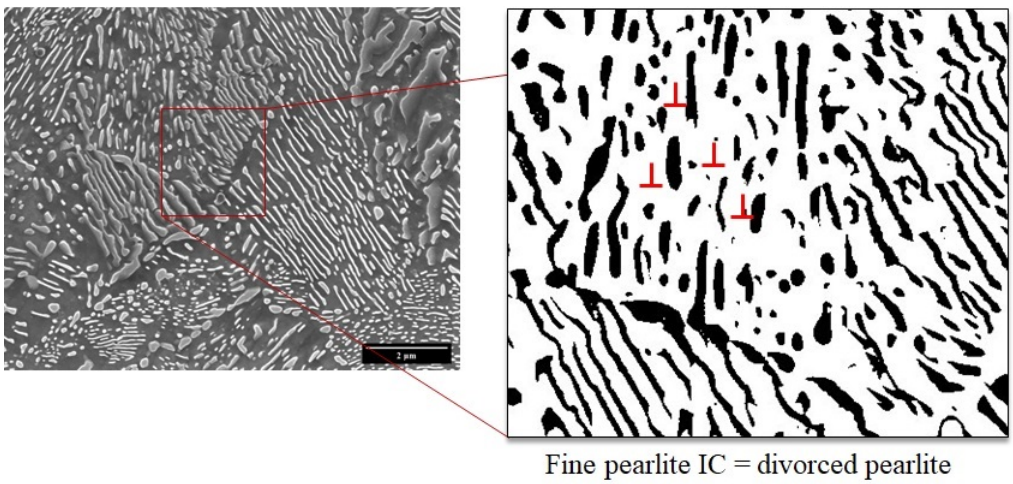

(a)

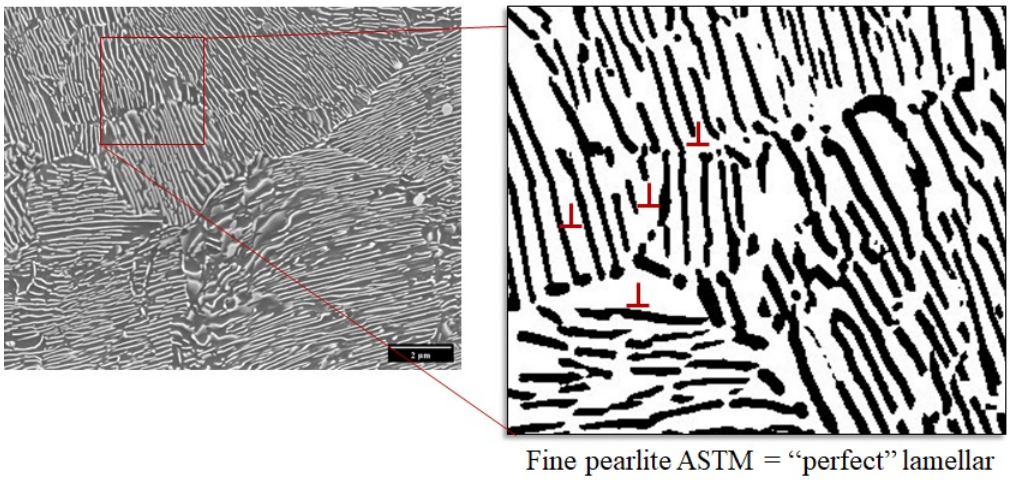

(b)

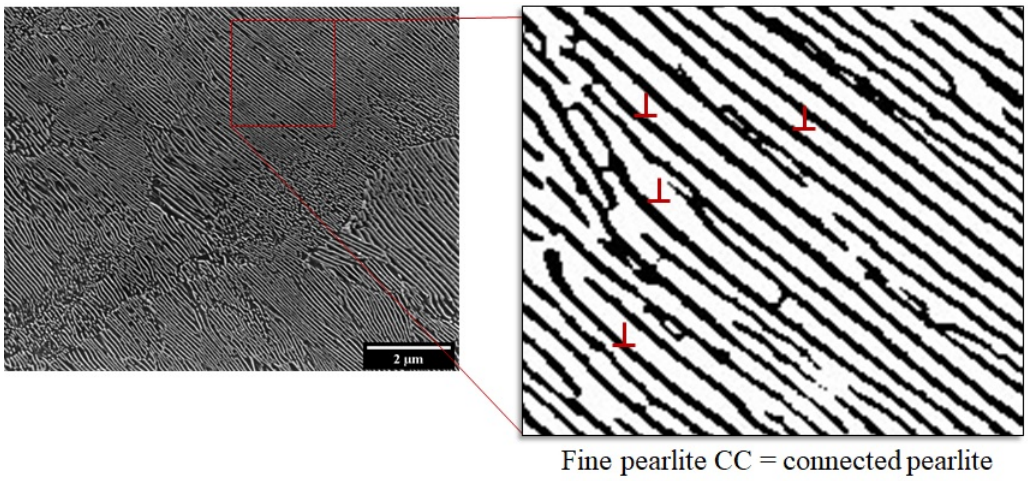

(c)

Figure 6.24: Dislocations path for the (a) divorced fine pearlite (IC), (b) perfect fine pearlite (ASTM) and (c) connected fine pearlite (CC).

The analysis of the gradients is much more complicated since there is a contribution of coarser pearlite in the core and a finer pearlite at the surface. Therefore, as it presented enhanced plasticity and it was observed in the micrographs that the fine pearlite at the surface presents well-defined lamella, it is assumed to have the same behavior of the fine pearlite CC: a softening due to the intense interaction caused by the confinement in a ferritic lamella. However, as the core is composed of coarse pearlite, there is an intense creation of dislocations in the core for the whole wire to undergo the applied strain. So, on average, the gradients present the same behavior at low and high strain because of the different responses within the same cross-section, $\rho_{annihilation}$ and $\rho_{creation}$ are always being balanced.

Now assessing the contribution of the gradients in the fatigue behavior, the overall

results of the gradients, 1 and 2, show an improvement of the plasticity especially related to the contention of cracks. However, for the production of a bridge cable, it is important to keep a high strength, which was considerably lower for the gradients. The optimization of the external layer thickness can entail better results for the stress.

The comparison of the Manson-Coffin curve and the stress amplitude at mid-life vs number of cycles curve is shown in Figure 6.25, and it is seen that the coarse pearlite has the best fatigue resistance among all the samples and the fine pearlite together with the most homogeneous has the worse results. However, when looking at the stress amplitude (Figure 6.25b), the fine pearlite has a much higher stress amplitude, proving to be undeniably advantageous.

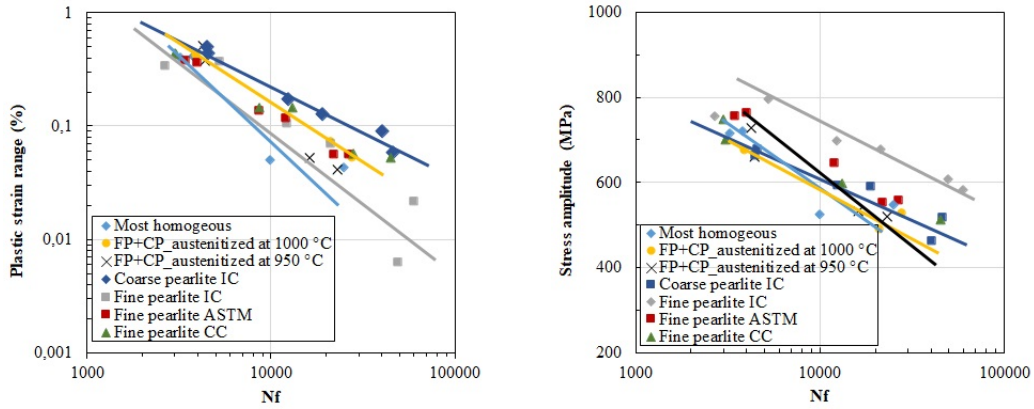

(a) (b)

Figure 6.25: (a) Manson-coffin and (b) stress amplitude results measured at mid-life for all the tested conditions assembled.

Therefore, the gradients do not show any convincing advantage to justify its production, not even compared to coarse pearlite. The optimization of the gradient thickness is needed to improve the overall gradient properties.

6.8 Conclusions

The study of the fatigue behavior of both monolithic and gradient pearlitic steels has allowed the identification of the cyclic accommodation, suggestion of cyclic plasticity mechanisms of pearlite and to accomplish the effect of the gradients. The successful design of the fatigue specimen suitable be treated in the dilatometer is already an accomplishment since it has restricted the analyzed variables only to the heat treatment.

The results of the monolithic pearlite obtained by the different processes have shown some very interesting results. They all have the same interlamellar spacing, which is generally accepted to be the one parameter that controls the fatigue properties of the pearlitic steels, and, yet, they presented completely different fatigue behaviors. The understanding of the basis of how these morphologies are changed and why, together with the knowledge of its effects on the mechanical properties, represents a huge technological possibility for the optimization of the pearlitic microstructure to produce high strength materials with higher mechanical properties.

The proposition of producing microstructure gradients comes from the need to diminish the trade-off between strength and ductility. It has been proved in this chapter that it can be done by the production of the gradients and also by the change in the morphology.

The results have evidenced the main conclusions:

- It is possible to make heat treatment of the fatigue samples in the dilatometer. The microstructure was successfully changed and the fatigue tests were satisfactory.
- The fine pearlite with the same $\overline{S}$ produced by different routes presented different morphologies and different mechanical properties, such as different yield stress and strain hardening. Besides, the fatigue behavior was considerably changed by the morphology, the fine pearlite obtained by isotherm cooling was rather divorced, and it presented the highest stress levels and worse plasticity. While the ones obtained by continuous cooling and by the heat treatment proposed by the ASTM, which are the connected and the perfect morphology, respectively, presented lower stress responses but enhanced plasticity.
- The monolithic results prove that the interlamellar spacing is not the only parameter controlling the mechanical properties and the fatigue behavior and that the change of pearlitic morphology represents an advance on the heat treatment design of pearlitic steels since, after all, it has done what the gradients were proposed to do: combine improved strength and ductility.
- The gradients presented lower stress responses, comparable to coarse pearlite and, although having improved plasticity, being able to contain the crack propagation, have many slip marks and improved toughness. In the Manson-Coffin diagram it presents a low fatigue resistance, just a bit better than the fine pearlite.

Therefore, optimization of the gradient to assure that it can attain as high-stress levels as the monolithic fine pearlite is needed to reach the desired improved microstructure with high strength and diminished trade-off with the plasticity.

- The most homogeneous presented similar results to the connected fine pearlite but, as the gradients, it presents improved plasticity and cracks contention. However, the obtained stress values are comparable to the coarse pearlite and the fatigue resistance is as low as the ones for fine pearlite, which thus allows concluding that is not advantageous to produce a more homogeneous sample.

- The mechanisms of the pearlite behavior at low and high strain were pointed out with the aid of the stress effective analysis and it had allowed explaining the difference in the fatigue responses for the different interlamellar spacings and different morphologies.

Chapter 7

Transposing the gradient concept

7.1 Introduction

During the conception of the gradients, many assumptions of how the treatment were made and, even if all of them are right and the proposed gradients can be produced, there is still the remaining question of the effect of these gradients after the drawing. Besides, there are many cooling technologies, such as lead patenting that is roughly isotherm, and some water-based technologies that are mostly continuous, that would interfere in the created gradient and its properties.

Along this chapter are shown the results of the coils treated in the pilot production line located at Bekaert that were tested with three real cooling technologies to allow acknowledging the feasibility of a gradient by the different methods and two initial microstructures from the 6 mm diameter of the eutectoid wires. Subsequently, these wires were cold drawn to a diameter of 2.25 mm, and the mechanical properties were evaluated before and after drawing, giving an overview of all the possibilities and achievements of the gradient production.

7.2 Materials and experimental procedures

Three coils of similar eutectoid compositions were chosen to perform the different heat treatments. The exact chemical compositions of coils 1, 2 and the wire rod are shown in table 7.1. Different coils were used due to a material limitation, but they can

be considered as equal for the comparing matters.

The difference between the coils and the wire rod (WR) is that the coils came with a larger diameter, thus needing to be drawn to 6.5 mm before the heat treatment, while the wire rod had already the right diameter 6.5 mm.

Table 7.1: Chemical composition of the 6 mm coils used in the pilot line (Fe bal.)

Chemical composition (in wt.%)			
	Coil 1	Coil 2	WR
C	0.812	0.802	0.812
Mn	0.599	0.562	0.550
P	0.011	0.015	0.010
S	0.011	0.013	0.006
Si	0.230	0.255	0.224
Al	0.001	0.001	0.001
Cu	0.03	0.014	0.065
Cr	0.021	0.020	0.063
Ni	0.025	0.026	0.028

As explained before in Chapter 2, the main industrial process to produce pearlitic steel wires is known as patenting. It consists in cooling the wires by submerging them in a hot molten lead bath and the transformation temperature is considered to be the same as the bath temperature, thus defining whether is going to be fine or coarse pearlite. The patenting is considered to be an isotherm heat treatment and it is known to be a very reliable process, this means that it does not have strong variations in the final microstructure if the bath temperature is controlled. However, because of the environmental issues related to it, other cooling technologies have to be considered.

Among the many methods present in the literature, another known reliable method to produce pearlite is also by immersion, but this time in a hot molten salt bath. There are nitrate-based and chloride-based salts. Here it has been used the mix of $NaNO_3$ – KNO_3 and is considered as a quasi-isotherm alternative cooling. This technology also presents some environmental and safety issues, but it is less problematic than lead patenting.

There are many other possibilities, but the last one considered in this work is the water-based technology, which is the only continuous cooling condition analyzed here. The process is not so stable, which means that little variations in the process parameters can potentially entail substantial variations in the mechanical properties of the wires. Hence, this technology demands strict control of the process.

In short, these three cooling technologies were tested in this work: Alternative water-based cooling, molten salt bath, and lead bath. The specific conditions of each heat treatment are shown in table 7.2. Coil 2 cooled in lead will be used as the reference microstructure since it represents the large majority of pearlitic steels produced around the world.

Table 7.2: Coils and thermal treatment conditions of the pilot line trials

Specimen description	Coil	**Bath temperature (°C)**	$\overline{S}$ **(nm)**	**Coarse pearlite (%)**	**Bainite (%)**
Water based cooling	1	90	97	2	1.8
Salt bath	2	480	110	1.1	1.2
Lead bath	2	560	121	1.8	1.2
Lead bath	wire rod	560	118	1.9	1.2

The heat treatment in the pilot line proceeds in the same way for the four tests: starting by the austenitization cycle at a continuous furnace at 1000 °C, followed by the cooling in the different conditions. Then the wires were submitted to a dry cold drawing done in ten passes until reaching a final diameter of 2.25 mm, accumulating a total strain ϵ_d= 2.12. The scheme of the pilot line is shown below in Figure 7.1.

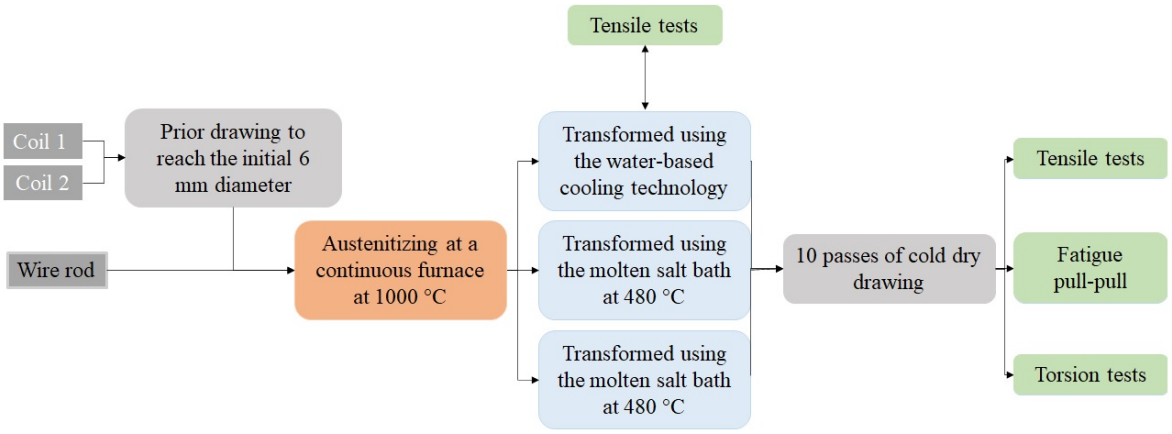

Figure 7.1: Industrial pilot line flow

Some samples were extracted before the start of the drawing and after each drawing pass to analyze the strain hardening and the evolution of each microstructure.

The drawing is a complex mechanical conformation method that produces both compression and shearing stress in the material. The reduction in the cross-section defines the strength of the drawing and two parameters can be used to calculate it: the true drawing strain (ϵ_d) and the area reduction (r), and they can be calculated as follows:

$$r = (1 - \frac{A_1}{A_0})x100 \tag{7.1}$$

$$\epsilon_d = ln(\frac{A_0}{A_1}) = 1 - 2ln(\frac{D_0}{D_1}) = ln(\frac{1}{1-r}) \tag{7.2}$$

In which D_0 and A_0 are the starting diameter and cross-section area, respectively, and D_1 and A_1 are the finishing ones.

The diameter reduction per pass, the area reduction, and the accumulated drawing strain is shown in table 7.3.

Table 7.3: Diameter reduction through the ten passes with the respective accumulated ϵ_d and area reduction

Diameter (mm)	Drawing pass	Drawing strain (ϵ_d)	Area reduction (%)
6.5	0	-	-
5.89	1	0.20	18
5.16	2	0.46	37
4.61	3	0.69	50
4.12	4	0.91	60
3.64	5	1.16	69
3.32	6	1.35	74
2.98	7	1.56	79
2.7	8	1.76	83
2.47	9	1.94	86
2.25	10	2.12	88

The mechanical properties were characterized after each pass by a tensile test and the final 2.25 mm wire was also characterized by the fatigue pull-pull test and by torsion tests. All the tests were done at least in triplicate to validate the observations.

The fatigue pull-pull test is a type of test that is done using strictly tensile loads. These tests were performed in the robust Instron 8801 axial fatigue machine that can go to a maximum load of 100 kN. The test was done under stress control, with a stress amplitude of 20 % of the ultimate strength (Rm) and a mean stress of 35% of the ultimate strength, at a frequency of 35 Hz.

The tensile tests were performed in the machine Zwick Z250 with a pre-load of 500 N and the test proceeded at a displacement velocity of 30 mms^{-1}. An extensometer was used, a model multiXtens extensometer also from Zwick and it is fully controlled by the test equipment.

The torsion tests were done in a machine TL200 torsion tester also from Zwick that is capable to apply torque until 200 Nm. The tests were performed at a speed of 30 r.p.m and an axial load of 12 kg on a 225 mm long sample. The stress and the number of rotations before rupture were recorded.

To obtain some evidence about the effect of the heat treatments on the mechanical responses, the samples had their fracture surface analyzed by SEM.

7.3 Pilot line trials

7.3.1 Microstructural characterization

The microstructures obtained right after the heat treatments are shown in Figure 7.2. No particular pearlite morphology was observed in the used heat treatment conditions and no gradients were observed between the surface and core by the analysis of the interlamellar spacing.

The only special feature observed in the after-transformed microstructure is seen in the wire started from the wire rod, which presented a 20 µm decarburization layer seen by both the longitudinal and the transverse cross-section. The decarburized area is only less than 1% of the total area, which might look insignificant but, as the fatigue starts at the surface, it is expected to have affect it.

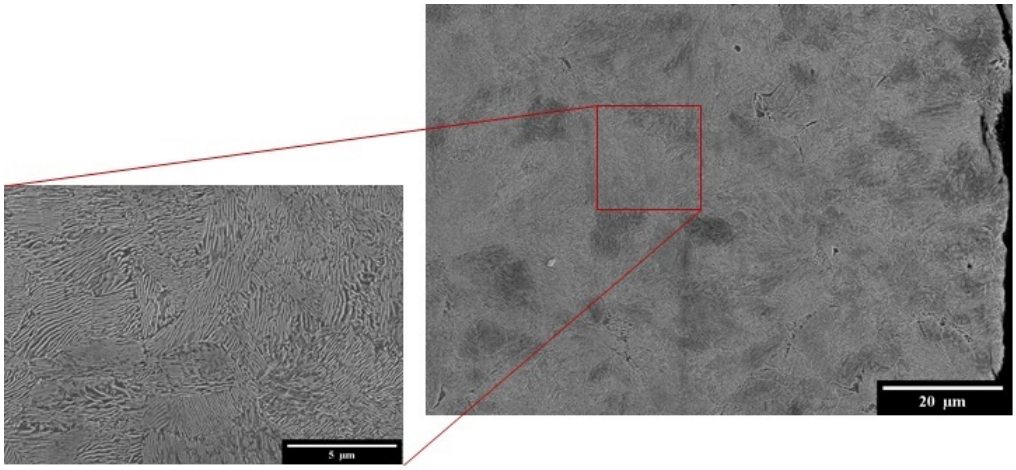

(a)

The transverse cross-section was analyzed for all the tested conditions and the observed microstructure is the same as in the longitudinal, proving that the wires are isotropic before the drawing because the austenitization was capable to produce equiaxial grains before the new transformation to pearlite.

To investigate the presence of microstructural gradients, the hardness mappings were recorded and the results are displayed in Figure 7.3. The conditions used to produce these mappings are the same as described in chapter 6, the automatic microhardness Vickers tester FM-810+ARS900(FT), from FUTURE-TECH, was used and the load of 500 g and 10 s hold was applied with indents every 300 µm in x and y keeping a distance of 200 µm from the surface.

The water-based cooling technology is characterized to be a continuous cooling alternative and it is the one that has produced the most evident gradient. Although the formed gradient is very thick, the outer crown has a thickness of 2 mm. It means the observed mechanical properties are most likely similar to the surface alone than to the core.

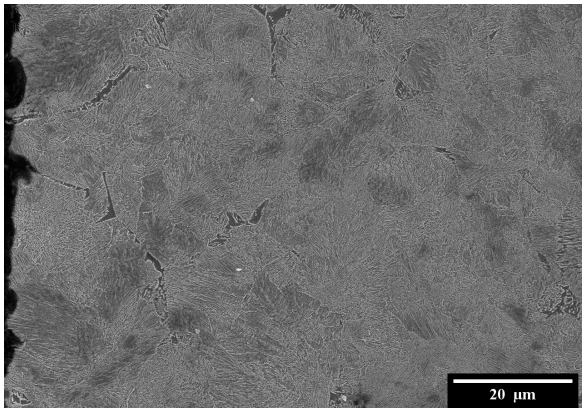

(b)

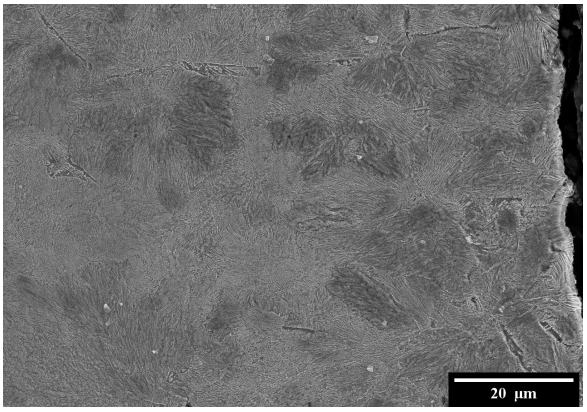

(c)

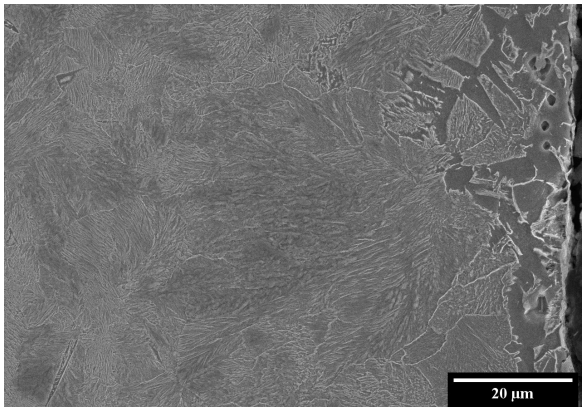

(d)

Figure 7.2: Longitudinal views of the microstructures of the wires after being patented by the different cooling technologies: (a) Water-based cooling, (b) salt bath, (c) reference lead patenting from the usual coil and (d) lead patenting from the wire rod.

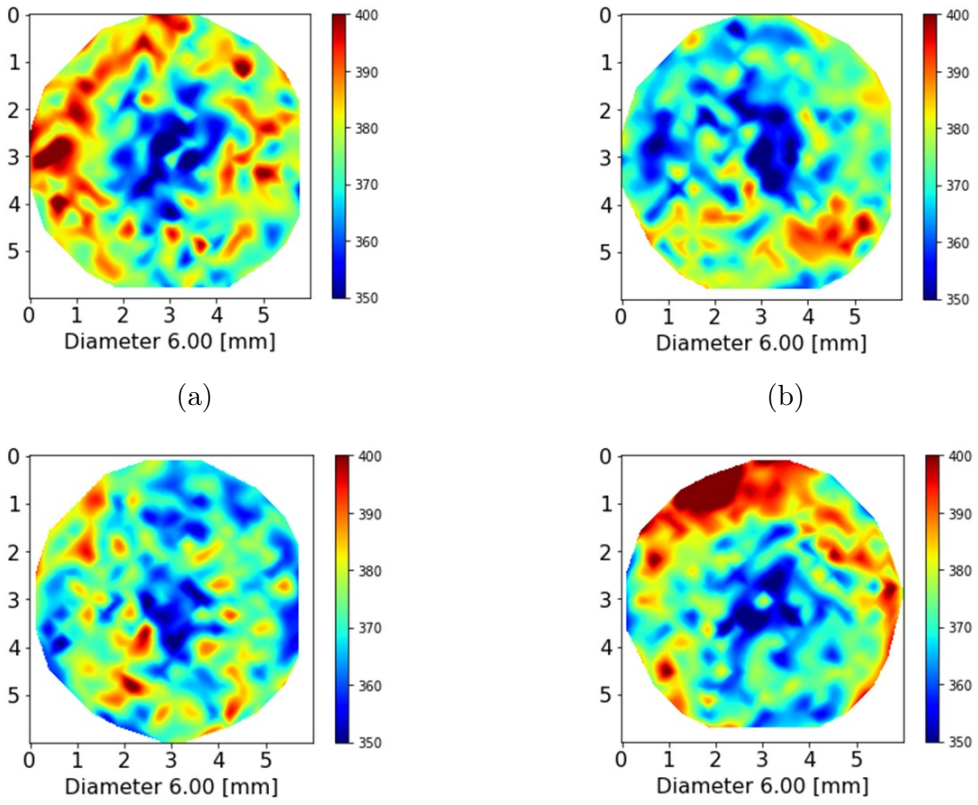

(a) (b)

(c) (d)

Figure 7.3: Hardness mapping of the samples after being transformed in the (a) water-based cooling, (b) salt bath, (c) lead in the coil 2 and (d) lead in the wire rod.

The sample starting from the wire rod also presented an asymmetric gradient, which is a surprising result since the same heat treatment in lead at 560 °C done in the coil has shown to be homogeneous in Figure 7.3c.

What is also important to remark is that the external layer of the wire rod was not analyzed in the hardness measurements, because it is smaller than the 200 µm distance from the surface. So, if there is any other gradient smaller than 200 µm, it is not observed.

The microstructure was again characterized by SEM after the 10 passes drawing and the results can be seen in Figure 7.4. It is observed that the pearlite colonies have strongly rotated to align with the drawing axis after the 10 passes and they appear in their majority parallel to the drawing axis after the drawing.

The wire rod sample has maintained its external decarburized layer, although it has thinned to around 7 µm. It continues to represent less than 1% of the total surface, which shows that the gradient has kept its proportions after drawing.

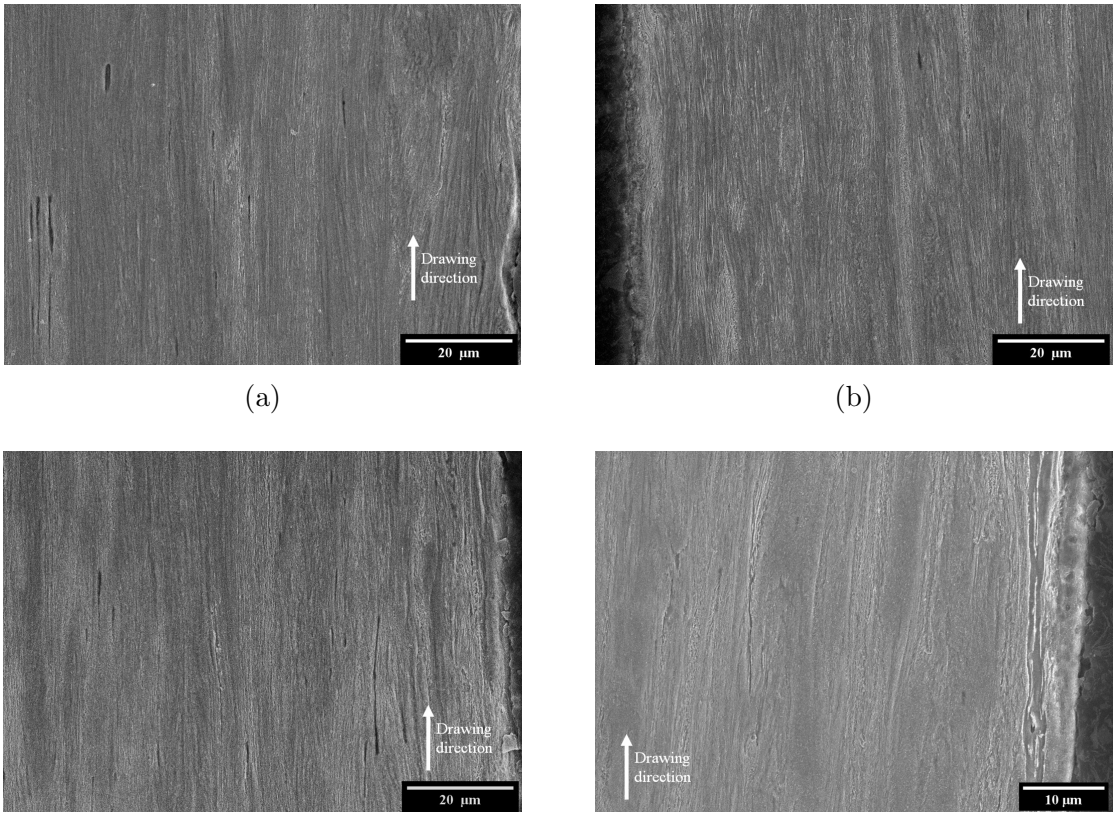

Figure 7.4: Microstructure after drawing for the wire previously transformed by (a) water base cooling, (b) molten salt bath and lead patenting for the (c) regular coil and (d) wire rod.

The samples also had their transverse cross-section analyzed and it presented a kind of typical pearlitic microstructure after drawing: twisted and fragmented cementite lamella. This happened because the colonies that were not favorably oriented to rotate and align with the drawing axis undergo severe shear deformation and it caused the cementite lamella to twist or fragment.

Figure 7.5 shows the possible cementite lamella forms after drawing relative to its initial orientation. Then it is shown how it was observed in the samples both at the longitudinal and the transverse cross-sections. The most frequent morphology observed is the very long and thin cementite lamella, as number (1) indicated in Figure 7.5a, followed by the often seen sheared cementite such as the number (3) in the scheme.

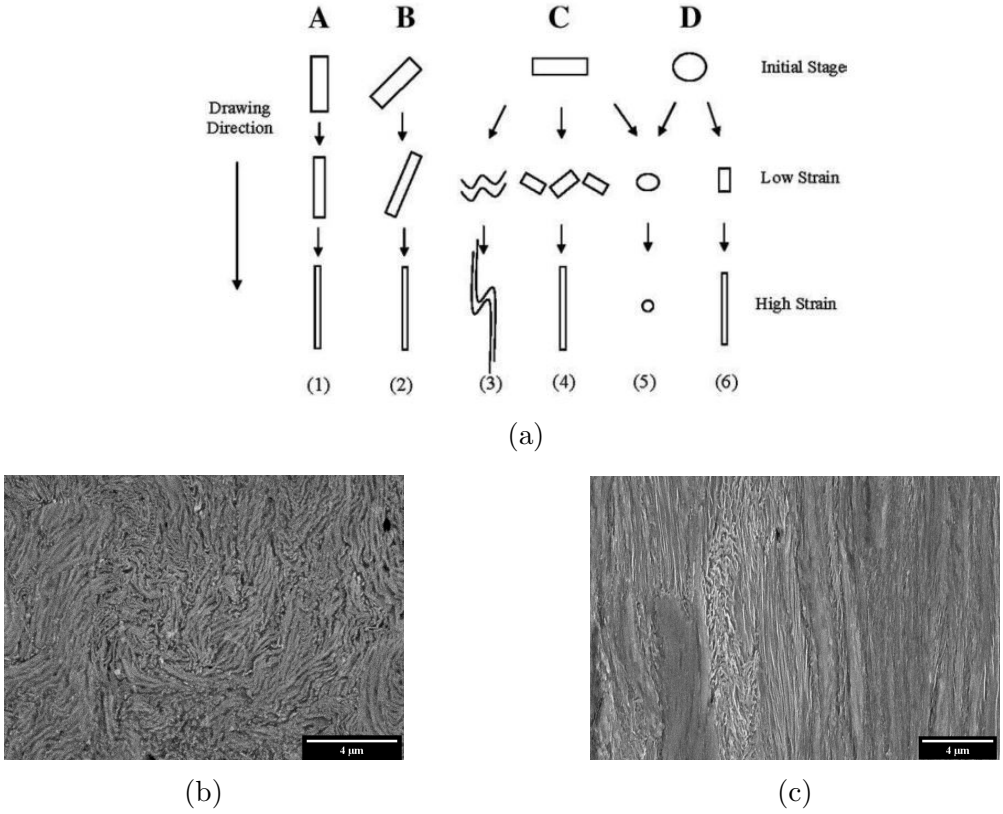

Figure 7.5: (a) Cementite morphology after drawing depending on its orientation relation with the drawing axis and real examples of the microstructures obtained after drawing for the wires at the (b) transverse and the (c) longitudinal cross section.[21]

Summarizing the results obtained from the different production processes, the hardness mapping has shown a thick gradient on the wire transformed by the water-based cooling and an asymmetric gradient on the wire rod, although the SEM investigation has not evidenced any difference between the microstructure obtained by the tested patenting alternatives before and after drawing, whatsoever.

The only difference observed in the micrographs is the decarburized external layer of the wire rod.

7.3.2 Mechanical behavior

Tensile test

As previously explained, some samples were extracted after each drawing pass to allow the characterization of the mechanical properties. The ultimate tensile stress

obtained for each of the four wires after each drawing pass is displayed in Figure 7.6.

As expected due to the severe deformation introduced during drawing, the increase of the drawing strain entailed an increase of the ultimate strength (Rm), so as the yield strength (σ_y), while the ductility decreases drastically.

Not much difference was observed between the values of Rm for the different heat treatments. Although the salt bath appears to be in the superior line and the lead from the coil on the bottom, the differences are not physically meaningful.

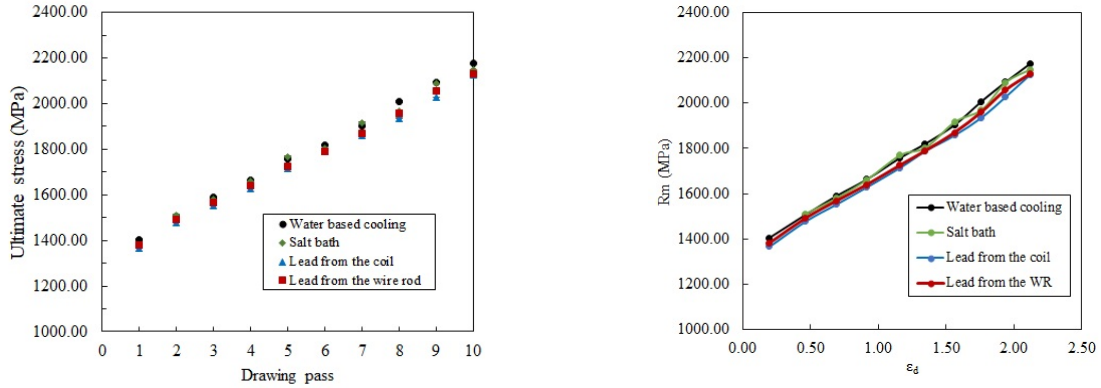

(a) (b)

Figure 7.6: Ultimate tensile stress measured after each drawing pass for each of the three tested cooling technologies versus (a) the drawing pass and (b) the drawing strain.

The same evolution of the stress after each drawing pass was plotted versus the drawing strain, as shown in Figure 7.6b, and it gives to the same conclusion that there is a strain hardening with the increased drawing strain. And, again, no significant difference was observed between the samples transformed by the different methods.

The difference between the stress values right before and right after the drawing can give a hint of the overall strain hardness obtained by each microstructure. The results are shown in table 7.4 and samples cooled in the water-based alternative present the highest strain hardening, although it is only 10 MPa higher than the one obtained by the lead patenting in coil 2.

Table 7.4: Ultimate tensile strength before and after drawing and the difference between them

	Rm before drawing	Rm after drawing	Increase in Rm
Water-based	1277	2175	898
Salt bath	1266	2147	881
Lead (coil 2)	1239	2127	888
Lead (WR)	1245	2128	883

One might think that the difference between the Rm values before and after the drawing is enough to settle the "superiority" of a given heat treatment but to confirm it and understand what is happening during is important to follow the evolution of the deformation to understand if different mechanisms are acting in each microstructure.

Even though the strain hardening has an exponential relation with the drawing strain, the calculation of the strain hardening coefficient is proposed here to analyze the drawing hardening to emphasize if the pearlite obtained by different processes presented different strain hardening coefficients. To recap, the strain hardening coefficient calculation is based on the Hollomon equation as follows:

$$\sigma = k\epsilon^n \tag{7.3}$$

$$log(\sigma) = nlog\epsilon + logk \tag{7.4}$$

Being k the strength coefficient and n the strain hardening exponent. This is usually applied at the stress-strain curves within the homogeneous deformation part. During drawing, the type of loading is much more complex, but for sake of simplicity, it is used here to evaluate the hardening during drawing. From the plot log Rm vs log of drawing strain, it is possible to calculate the strain hardening during drawing. These results are shown in Figure 7.7 and table 7.5.

There is a change in the strain hardening behavior, a weak hardening noted at low strain and a stronger one at higher strain. It is most likely related to the changes in the microstructure, it is possible that when the cementite starts to dissolve into the matrix it changes the stress response of the material since the dislocations become less mobile. The strain under which the cementite starts to decompose is reported in the literature to be around $\epsilon_d = 2$ [5, 49], thus agreeing with the above mentioned proposition.

Thus, it can be fitted two slops, one at the low strains and another at higher strains. It is seen by the high R^2 value that these well describe the different strain hardening regimes.

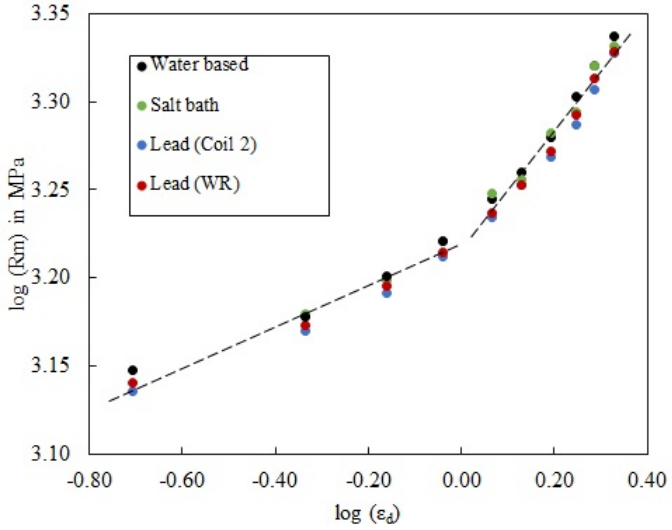

Figure 7.7: Strain hardening calculation with the drawing strain

Table 7.5: Strain hardening exponent values (n) at low and high drawing strains

	low strain		high strain	
	n	R^2	n	R^2
Water-based	0.12	0.97	0.36	0.98
Salt bath	0.14	0.98	0.34	0.97
Lead (coil 2)	0.11	0.98	0.35	0.98
Lead (WR)	0.11	0.98	0.35	0.98

Finally, it is seen that the n values are very similar whatever the cooling method. The ones treated in the salt bath presented slightly lower values, but if the dispersion is considered, it is not enough to conclude that it presents a different behavior. It proves that the strain hardening was not affected by the production means.

Pull-pull fatigue test

The analysis of the tensile curves gives the monotone behavior of the wires and, to analyze the cyclic behavior, the fatigue pull-pull tests were performed. The results are seen in Figure 7.8.

The water-based cooled microstructure has indeed presented a higher value of

strength followed by the salt bath and the lead. The WR did not present any effect of the external decarburized layer on the stress response of the wire.

The average stress values and the fatigue life resistance are shown below in Figure 7.8. The stress values of the microstructure were obtained by the water-based, followed by the salt bath and the lead ones. The wire rod again has not shown an effect on the stress values.

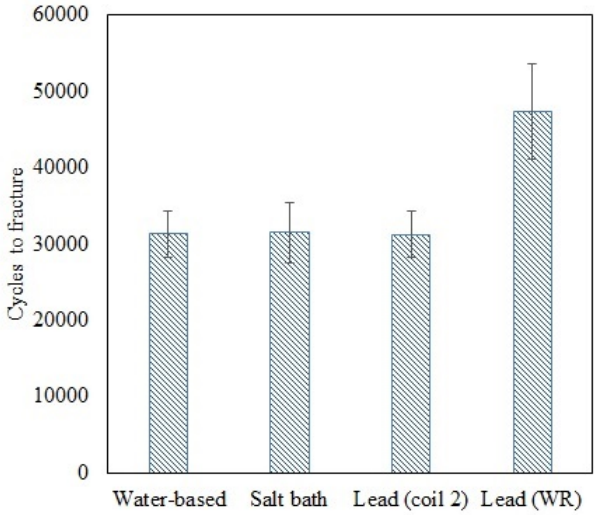

Figure 7.8: Fatigue pull-pull results of the fatigue resistance.

For the fatigue life resistance, it is seen that, while no difference was observed due to the heat treatment, the fatigue life has been greatly increased in the sample that started from the wire rod. Confirming the expectations, the presence of the 7 µm external layer was successful in improving the fatigue life, most likely by improving the crack formation and propagation.

The fractography of the wires was also done in an attempt to observe any difference due to the heat treatment in Figure 7.9.

The fracture surface comprises two zones first a fatigue propagation zone, which represents more or less 50% of the crack surface, then a final fracture under ultimate tensile loading. By contrast with the low cycle fatigue experiments, the final fracture appears to be ductile. It can be explained by the test parameters set, which here is characterized by the low strain applied that slowly opens the crack, thus allowing it to be ductile.

Another interesting feature observed here is the presence of deep cracks in the fatigue propagation zone. Some of these cracks are shown in detail in Figure 7.10.

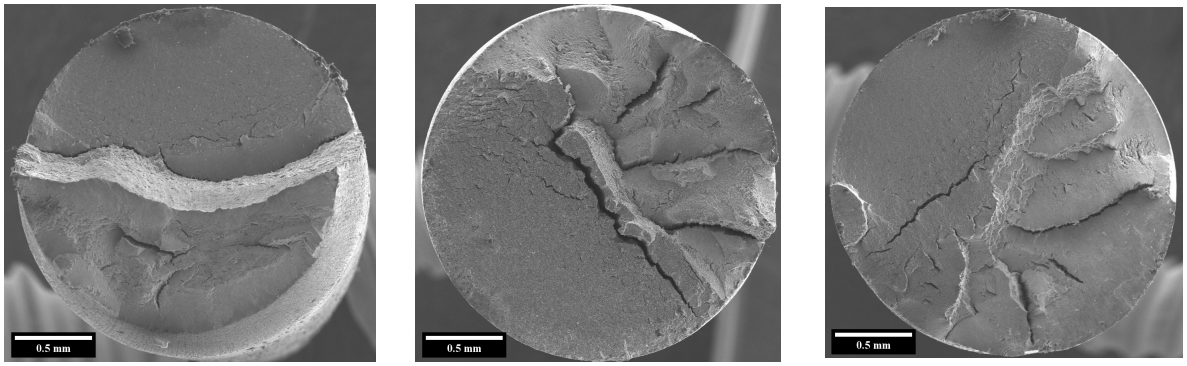

(a) (b) (c)

Figure 7.9: Fracture surface of the pull-pull fatigue tests of the samples transformed by (a) water-based patenting, (b) salt bath and (c) lead patenting on the coil 2. On the top of each micrograph is seen the flat fatigue propagation zone and on the bottom is the final ductile fracture.

They are known as secondary cracks.

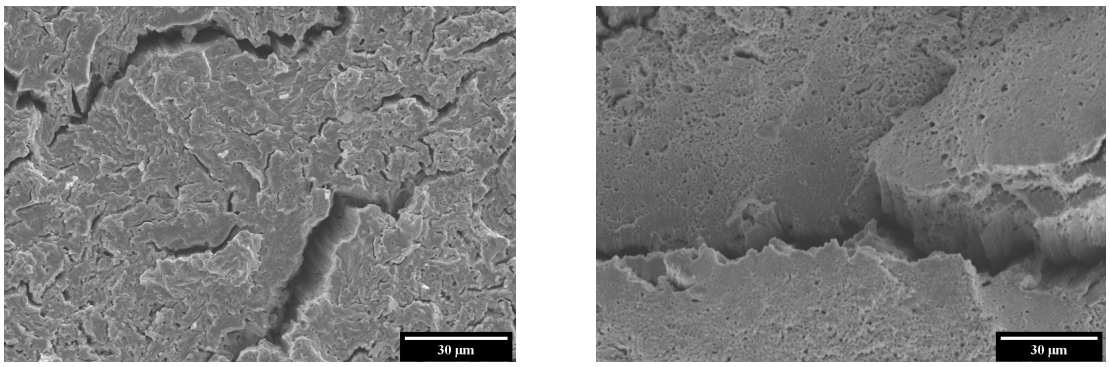

(a) (b)

Figure 7.10: Fracture surface detail of the (a) fatigue propagation region and the (b) final ductile fracture extracted from the fracture surface of the sample tested transformed by the water-based cooling.

These secondary cracks are formed parallel to the wire axis, 90° deflected from the crack plane, and it appears due to stress relief on the tip of the existing radial cracks. In Figure 7.11 is shown the formation mechanism of these secondary cracks, which has been previously proven in the literature [22] to happen due to a three-dimensional stress state at the tip of the crack and it is relieved by the propagation of the cracks in the Y-axis direction at the colonies boundaries.

After the formation of the secondary crack the main crack is still growing perpendicular to the wire axis but not necessarily at the same plane. That is the reason why the fracture surface presents some topography.

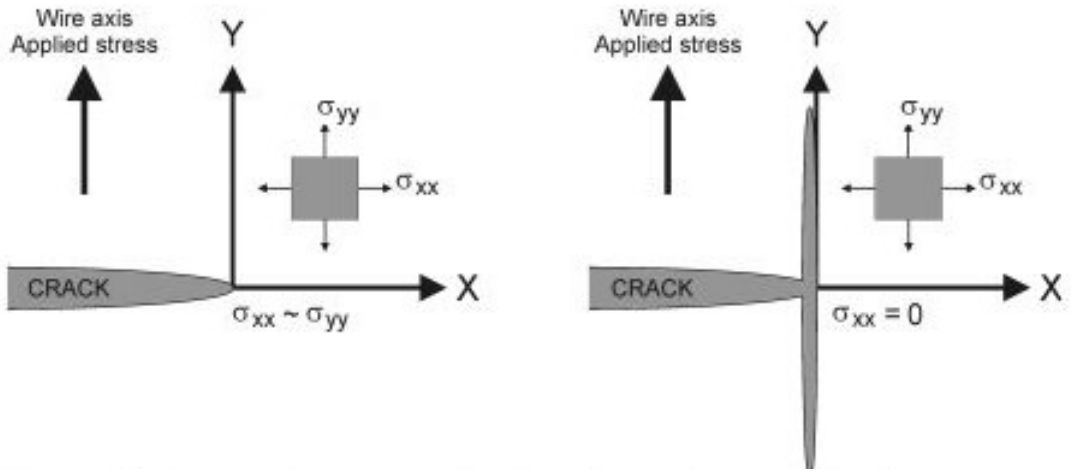

Figure 7.11: Secondary crack relief mechanism [22]

The sample treated in the molten salt bath has more secondary cracks, followed by the ones treated in lead and the water-based patenting, although the overall fatigue behavior remains the same. It indicates that these microstructures were capable to produce more radial cracks that were relieved by the secondary cracks, which evidences an improved contention of the crack propagation.

Torsion test

The last characterization of the mechanical behavior is under torsion. It is a different type of loading and the response to shear stress can be different than for the traditional uniaxial testing. As said in Chapter 2, the torsion is especially important for wire ropes.

During the torsion test, it is recorded the necessary torque T (N.m) to twist the sample at a deflection angle ϕ (rad). As it is for the usual tensile curve that the load and variation in length are converted to stress (σ) and strain (ϵ), the torque is converted in τ, which is the shear stress and the angles are converted into γ, shear strain. This conversion is shown below:

$$\gamma = r\frac{\phi}{l} \tag{7.5}$$

$$\tau = G\gamma = \frac{T.r}{J} \tag{7.6}$$

Where l and r are the length and radius of the test wire, respectively, and J is the polar moment of inertia given by $\frac{\pi r^4}{2}$ for a solid circular shaft.

During the torsion tests, there is a stress distribution within the radius of the sample, as shown below in figure 7.12. The maximum shear stress is applied at the surface such as the maximum strain. Thus, as the surface is much more solicited than the core, the gradients could present an important improvement of the torsion behavior.

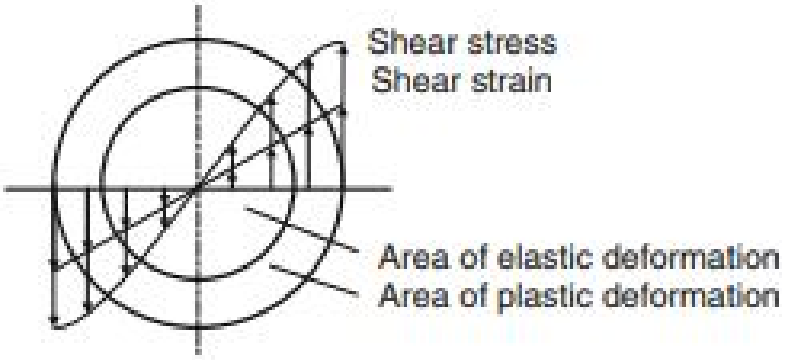

Figure 7.12: Cross section distribution of stress and strain.

An example of stress versus strain curve during torsion is shown in Figure 7.13. Comparing the wires results, no large difference was observed between the torsion behavior due to the different production processes. The one produced from the wire rod seems to undergo a higher number of rotations before fracture, going over γ= 1.2. It shows that the 7 µm external layer also improves the torsion behavior.

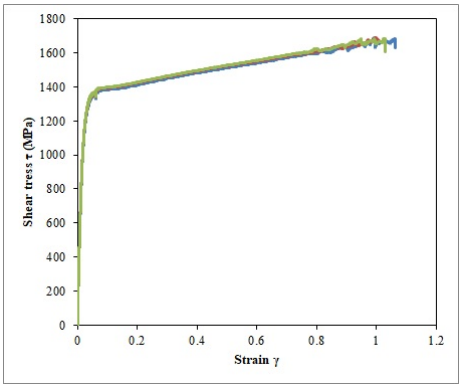

Figure 7.13: Shear stress- shear strain curve of the the torsion tests done in the sample cooled in the molten salt bath.

Similar to tensile loading, the strain hardening can also be calculated for torsion. It is lower than the strain hardening in pure uniaxial testing but the values obtained for all the samples do not vary substantially with the production method.

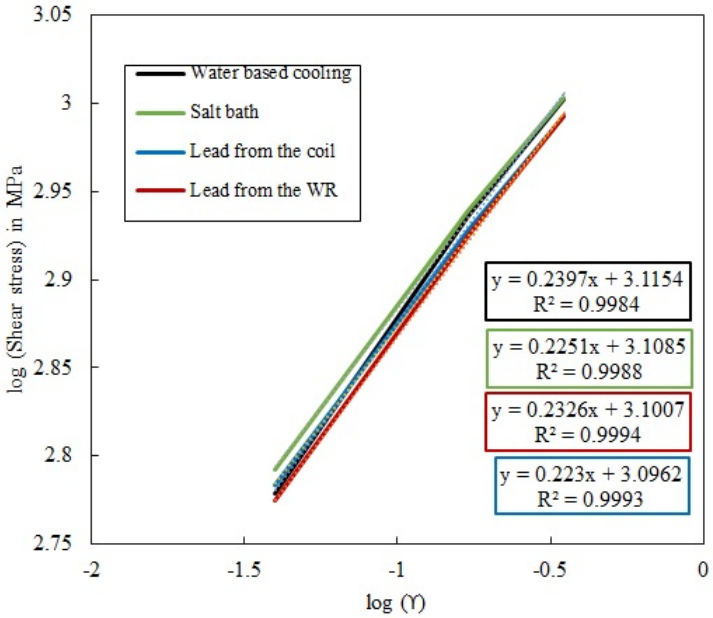

Figure 7.14: Strain hardening calculated for the torsion tests.

Finally, the fractography was also done for the torsion tests. As expected for ductile materials, they all presented flat fracture surfaces. The only exception is when the samples had delamination, in which case they do not present either brittle or ductile fracture, it is simply the detached colonies that separate from each other following the 45 ° of the tension application.

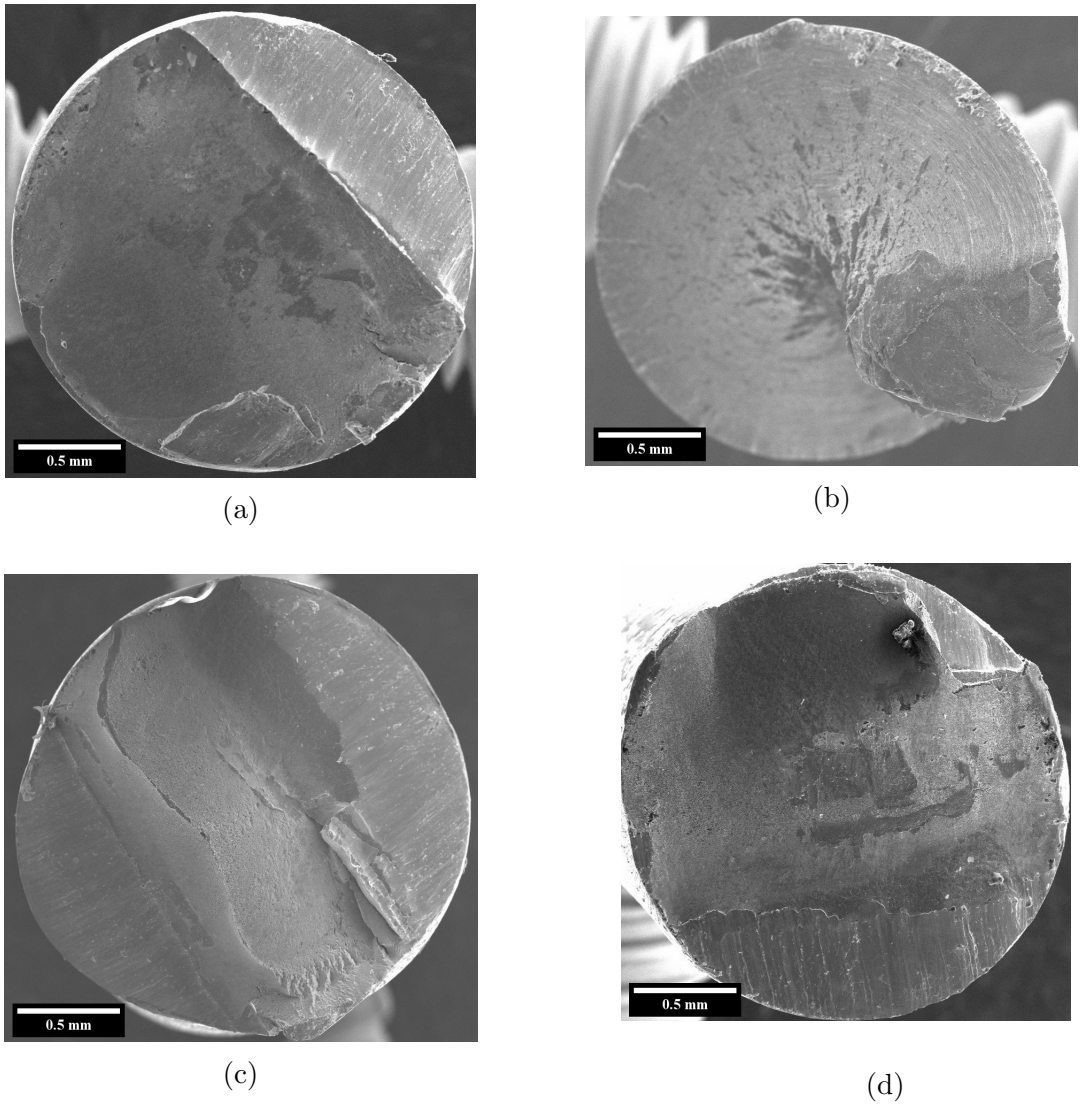

(a) (b)

(c) (d)

Figure 7.15: Torsion fractography of the samples transformed in the salt bath (a) with a normal response and a (b) delaminated example; and the ones transformed in lead (c) from coil 2 and (d) the wire rod.

In the sample starting from the wire rod (Figure 7.15 d), it was questionable if the fracture was initiated from the presence of a defect such as inclusion (see upper part of the micrograph) aka "fish-eye". It was further investigated and it is not the case, since the fracture has started at the surface.

Different from the fatigue results, the presence of the gradient in the wire rod did not show any improvement in the torsion response of the wire. It did not show any harm neither. All wires had about the same response independent of the initial microstructure or heat treatment.

7.3.3 Discussion

The production of wires by the different technologies and the effects of a gradient on the mechanical properties after ten drawing passes were assessed in this chapter.

It was observed that there is no large difference between the obtained values of interlamellar spacing nor morphology, giving an understanding that the samples were equal. Although, the hardness mapping has already evidenced a thick gradient produced by the water-based cooling technology.

During drawing they all had the same behavior and the microstructure looked the same: strongly aligned with the drawing axis with a very thin fiber structure. The gradient of the sample starting from the wire rod has kept its proportion, which has given good perspectives for the improvement of the gradients in the 6 mm since they proportionally are kept.

Then the mechanical characterization has shown some more interesting results regarding the differences between the production methods. The overall strain hardening for the pearlite obtained by the water-based cooling was higher, but at the beginning, the salt bath had a higher and at the end presented the lowest strain hardening coefficient. There must be some hardening mechanisms acting differently on these microstructures, which can be related to the fraction amount of bainite or coarse pearlite dispersed in the fine pearlite matrix. Most likely, it is not dependent on the interlamellar spacing.

The pull-pull fatigue tests endorsed the most interest of producing a gradient because there is no effect at all due to the production method, but the 7 µm external layer was capable of almost double the fatigue life resistance. This result was again confirmed in torsion tests, in which the wire rod initial sample was able to undergo a larger number of cycles.

The production of a gradient as proposed in the previous chapters seems feasible either by the classical lead patenting or by the other cooling technologies. The temperature gradient must be refined to produce an interesting gradient which would demand some process adjustments in the austenitizing, or decreasing the bath temperature at the starting temperature. Either way, it is still, nevertheless, possible to produce high-strength pearlite by any of the proposed methods. There is no important harm in the pearlite produced by any of the cooling technologies and there is also not

a huge distinction of the best process, meaning that there is not much loss or gain in changing the cooling technology.

The real bright result here that magnifies the whole work proposed in this thesis is the presence of a microstructural gradient. Here, the gradient was composed of a very thin softer phase that did not show any effect on the obtained stress values, meaning that it does not participate in the overall strength of the material. However, when the surface was solicited, it has been able to drastically improve the material resistance.

As said in the previous chapters about the optimization of the thickness of the exterior layer, here is shown a great example of optimized thickness. The previous knowledge obtained about phase transformation can still be applied here and maybe be added to the successful decarburized layer gradient.

7.4 Conclusions

The production of pearlite by the various cooling technologies was assessed in this chapter. The different initial microstructures with and without a gradient, continuous, and isotherm cooling before and after drawing were all analyzed. The conclusions from this assessment are:

- The production of pearlite by the different cooling technologies was successful in all the cases with very few variations in the amount of bainite and coarse pearlite.
- All the formed pearlites were randomly oriented after the pearlitic transformation and they all presented a strong texture at the end of the drawing, with all the lamella parallel to the drawing axis.
- The production method did not seem to significantly affect the mechanical properties of the wires. The hardness during drawing was observed to vary differently for the microstructures, but the overall result is the same.
- The 20 µm decarburized external layer observed on the wire rod just after the patenting was still present after drawing, but having only a 7 µm thickness in the final 2.25 mm wire. It had about the same mechanical behavior as the other pearlite microstructures, but it presented an enhanced fatigue resistance during the fatigue pull-pull tests. This result is encouraging for the production of

microstructural gradients since a very small modification under the surface was enough to almost double the fatigue life resistance.

Chapter 8

Conclusions

First, it is worth coming back to the initial challenge of how improving the mechanical properties of components made of an "old" microstructure, the pearlite. The driving force of the present research project was to consider the possibility of producing a microstructural gradient in rods or wires. In addition, because the number of primary metallurgical variables is limited in general by the interlamellar spacing, other metallurgical features, such as the pearlite morphology, were also considered.

The strategy of the present thesis was to carry out a deep global study of the eutectoid steels from the phase transformation and the parameters that can affect it, the production assessment of a microstructural gradient in wires with 6.5 mm diameter, the real production assessment of the gradients produced by the different cooling technologies, to the final analysis of its effect on the mechanical properties and fatigue response of the different morphologies with and without gradients. In addition, the research having been conducted in an industrial context, the technical means to tentatively reach these items must be as close as possible to those existing on the industrial lines, especially the patenting. Therefore, heat treatments and mechanical treatment were the guidelines of the experimental route. It included heating, cooling, austenitization soaking, and, drawing deformation. Understanding some of the observed responses is also required to investigate parameters that are purely material-dependent such as the carbon content and mechanical history.

Heating step

The heating rate did not impact the final microstructure, either by PAGS or the

chemical homogenization. Although it is the key parameter to create a thermal gradient during the heating, in the studied parameters it did show an effect.

Austenization step

From the phase transformation study, it was seen that the austenitization can have a great impact on both the formation of the phases during the subsequent cooling, which is seen by the formation of bainite that indicates inhomogeneity of the austenite and the ease of the martensite formation that is observed by the change in the critical cooling rates. It can also affect the morphology of the pearlite since the samples formed after the ASTM standard cycle (stabilization cycle + 797 °C for 5 minutes) presented a perfect larger lamellar microstructure, while the ones obtained by continuous cooling at the same cooling rate are a kind of interconnected lamellar. Besides, the large grain size is seen to cause the abnormal transformation during isotherm cooling, thus also affecting the kinetics of the $\gamma \rightarrow \alpha + \theta$ transformation.

Cooling step

The pearlite morphology appeared to be dependent on the type of cooling, being mostly lamellar during continuous cooling and divorced during isotherm cooling. It was shown to happen because the transformations have happened under different kinetics control, being under a diffusion-controlled growth in the divorced case, and interface control for the ones transformed during continuous cooling. Furthermore, by the construction of the diagrams, it was evidenced that the transformation is a bit delayed when transforming from a large PAGS which is not so significant since the transformation still starts with less than 1 s. The hardness was observed to vary with the interlamellar spacing by also with the morphology, being lower for the spheroidized sample.

Effect of carbon content

The deviation from the eutectoid composition resulted in the formation of proeutectoid phases but it did not affect the pearlite morphology, thus being again divorced during isotherm cooling and lamellar during the isochronal cooling. The kinetics were also investigated and, although it also presents an abnormal behavior also caused first by the diffusion control and then by mix control, the two peaks observed during the transformation rate are related to the formation of proeutectoid ferrite or cementite and the second peak is related to the pearlitic transformation. At lower temperatures, during which only the pearlite is formed, the transformation rate is

observed in only one peak. In addition, the hypereutectoid was seen to present closer tendencies to the eutectoid sample than the hypoeutectoid, such as the effect of the PAGS on the delay for the transformation. However, the increase of the carbon content has not increased the critical cooling rate, as would be expected, and it happens because of the formation of the proeutectoid cementite.

Effect of mechanical history

The effect of the influence of the mechanical history was also investigated and it was not identified to produce any effect on the final microstructure after the austenitizing. As there were some pieces of evidence that there were some recovery-related phenomena before the austenitic transformation, it was investigated using interrupted heating tests at 700 °C with different heating rates. It was seen the cementite recovers first and then spheroidizes and that the ferrite forms cell walls during the recovery process. A very small fraction of recrystallization was observed, being only a few nanometric grains that were observed inside the ferritic lamella. Therefore, it explains why there is no effect either in the PAGS or the later pearlitic transformation. It happens because the related phenomena occur at a lamellar scale, while the austenitization could be affected at a colony or nodule scale. Hence, when the transformation to austenite starts, it continues to nucleate at the triple joints of the colonies and consumes the lamellae independently if they are recrystallized or not. Even spheroidization is not an obstacle since the formed spheres are small and quickly dissolved.

Gradient assessment

Once the factors controlling the phase transformation were identified and understood, the gradients assessment was successfully done in the dilatometer on the wires of 6 mm and 12 mm diameters. It was shown that the gradients formed during austenitization did not entail any difference in the final gradient, at least not with the tested conditions.

By thermal means, it was obtained a gradient of interlamellar spacing that is fine at the surface and coarse at the core. The inverse gradients, coarse pearlite at the surface and fine pearlite at the core have shown to be impossible to produce because the formed temperature gradient is not sharp enough to promote a selective transformation at the surface and avoid the core transformation.

By mechanical means, it was possible to do a gradient that is harder at the surface than the core. However, considering that the sample is going to be drawn until

2.25 mm, it is not useful, especially because the production of pearlitic gradients was seen to be hindered when done by the thermomechanical means. The pearlitic transformation was not favored and the same target gradients cycles performed on the thermal gradient production have transformed to martensite. This allows concluding that the mechanical gradients do not enhance the thermal gradients. The reason why it has hindered the pearlitic transformation is not yet understood, considering it does not follow the previous explanation about the recovery phenomena that happen before the austenitization.

Fatigue response

Then the effect of the formed gradients and pearlitic morphologies on the low cycle fatigue behavior was investigated. The results have shown that the gradients, although presenting more slip marks than the monolithic samples and being capable of containing small cracks propagation, have not presented convincing results to justify their production. The obtained stress values were closer to the coarse pearlite and the fatigue resistance was comparable to the fine pearlite, thus taking the least interesting feature of each microstructure. Changing the interlamellar spacing produced an expected effect on cyclic stress and surface plasticity. But more interesting was the strong impact of the pearlite morphology with the same interlamellar spacing obtained by different thermal routes on the cyclic plasticity behavior. It led to a discussion on the interactions of dislocations with carbon atoms that vary according to the heat treatment. It has allowed explaining the start and the extent of the cyclic softening and also of the cyclic hardening. The divorced fine pearlite has surprisingly shown the highest stress levels and the worse fatigue resistance, while the coarse pearlite has shown the lowest stress levels and highest fatigue resistance. An expectation of increasing the toughness through the morphology, perfect lamellar or interconnected lamellar, has appeared. Therefore, it is concluded that the pearlite morphology has a much more interesting effect than the gradients on the improvement of the fatigue behavior of the pearlitic steels.

Gradients on production line

Finally, the real gradient production was assessed by processing two coils and one wire rod, which presented a decarburized 20 µm thickness layer, under three different cooling technologies and then drawing these wires to a final diameter of 2.25 mm. This investigation has shown that the decarburized gradient is kept after drawing and it has increased by two the fatigue life of the wires, thus showing to be very advantageous. The

obtained microstructure by the three different cooling technologies has not presented any significant difference neither at the microstructure or the mechanical properties and thus showing a favorable assessment of the substitution of the lead patenting by other less environmental hazardous cooling technologies.

8.1 Thesis questions

Besides the main objective of assessing the production of a microstructural gradient, this work also intended to address some secondary and more specific questions that were listed in the introduction.

Here below are found answers and the issues brought up with them.

1. **Is it possible produce a pearlitic gradient?**

   Yes, it is possible to produce it by thermal means, being both by the formation of fine pearlite at the surface and coarse pearlite in the core or by creating a decarburized layer under the surface of 6.5 mm wires.

2. **Does the gradient structure represent an advantage compared to the homogeneous wires?**

   The pearlitic gradients have been shown to improve the plasticity of monolithic wires by the increase of slip marks and contention of small cracks, however, it has presented to attain lower stress and low fatigue resistance as the worse monolithic wires. Therefore, it is not advantageous to produce it. It is not hazardous either, it just does not bring advantages.

   The decarburized gradient presents the same mechanical properties as the wires without gradient but it presented enhanced fatigue resistance, thus being advantageous.

3. **Can the thickness of gradient be controlled? Is there an optimal thickness?**

   In the pearlitic gradient, it was very complicated to produce it and does not seem possible to control its thickness on the 6.5 mm wire because the produced thermal gradient is not sharp enough.

   In the case of the decarburized gradient, it must be possible of controlling its thickness but the 20 µm layer formed on the 6.5 mmm wire seems to be optimal

4. **Does drawing help to strengthen the gradient?**

   From the production of the thermomechanical gradients, it was seen not to enhance the gradient but, instead, hinder its formation.

5. **What are the limitations for gradient production?**

   The main limitation is the diameter, which defines the extent of the thermal gradient and, thus, the sharpness difference between the transformation formed at the core and the surface.

6. **Is it possible to reproduce a gradient microstructure by temp core in high carbon with smaller diameter wires? And control the thickness of the external martensite layer?**

   No, it is not possible because the variation in temperature between the start of the martensitic transformation and the lowest temperature that the pearlite can form are two distant and it would not possible to avoid the transformation in the core. It was tried to produce a bainitic version of the tempcore, however, it was not possible to keep the transformation only close to the surface, and bainite was formed in the core for both the diameter of 6 and 12 mm.

7. **Can it be industrially produced by lead patenting? And using the alternative cooling technologies?**

   The production of the gradients is quite possible by real industrial production means, although it would need some adjustment of the temperature at the beginning of the bath and the end, it seems feasible. The other cooling technologies have produced the same microstructure and same final mechanical properties as the lead patenting, giving positive perspectives for the production of gradients by alternative cooling technologies. And, what concerns the decarburized gradients, it for sure possible to produce both by lead patenting and the other alternative cooling.

Bibliography

[1] R. E. Reed-Hill, R. Abbaschian, and R. Abbaschian, *Physical metallurgy principles*, vol. 17. Van Nostrand New York, 1973.

[2] D. P&C, "wire manufacturing process." [Online], Available: http://www.dhstl.co.kr/skin/page/process_e.html (visited on 18.04.2022).

[3] R. N. Wright, *Wire technology: process engineering and metallurgy*. Butterworth-Heinemann, 2016.

[4] L. Kestens and H. Pirgazi, "Texture formation in metal alloys with cubic crystal structures," *MATERIALS SCIENCE AND TECHNOLOGY*, vol. 32, no. 13, pp. 1303–1315, 2016.

[5] Y. J. Li, P. Choi, C. Borchers, S. Westerkamp, S. Goto, D. Raabe, and R. Kirchheim, "Atomic-scale mechanisms of deformation-induced cementite decomposition in pearlite," *Acta Materialia*, vol. 59, no. 10, pp. 3965–3977, 2011.

[6] A. S. Pandit, *Theory of the pearlite transformation in steels*. PhD thesis, Citeseer, 2011.

[7] F. G. Caballero, C. Capdevila, and C. García De Andrés, "Influence of pearlite morphology and heating rate on the kinetics of continuously heated austenite formation in a eutectoid steel," *Metallurgical and Materials Transactions A: Physical Metallurgy and Materials Science*, vol. 32, no. 6, pp. 1283–1291, 2001.

[8] U. Prisco, "Case microstructure in induction surface hardening of steels: an overview," *International Journal of Advanced Manufacturing Technology*, vol. 98, no. 9-12, pp. 2619–2637, 2018.

[9] A. Elwazri, S. Yue, and P. Wanjara, "Effect of prior-austenite grain size and transformation temperature on nodule size of microalloyed hypereutectoid steels," *Metallurgical and Materials Transactions A*, vol. 36, no. 9, p. 2297, 2005.

[10] H. K. Bhadeshia, *Theory of Transformations in Steels*. CRC Press, 2021.

[11] G. F. Vander Voort, *Atlas of time-temperature diagrams for irons and steels*. ASM international, 1991.

[12] J. G. Zhang, D. S. Sun, H. S. Shi, H. B. Xu, J. S. Wu, and X. F. Wu, "Microstructure and continuous cooling transformation thermograms of spray formed GCr15 steel," *Materials Science and Engineering A*, vol. 326, no. 1, pp. 20–25, 2002.

[13] O. Modi, N. Desmukh, D. Mondal, A. Jha, A. Yegneswaran, and H. Khaira, "Effect of interlamellar spacing on the mechanical properties of 0.65% c steel," *Materials characterization*, vol. 46, no. 5, pp. 347–352, 2001.

[14] L. Ávila de Oliveira Silva, G. Adinolfi Colpaert Sartori, D. Bondarchuk, I. M. Oliveira Anício Costa, C. Mesplont, and J. B. Vogt, "Effect of Interlamellar Spacing on the Low Cycle Fatigue Behavior of a Fully Pearlitic Steel," *Metallography, Microstructure, and Analysis*, 2021.

[15] W. L. Zhou, K. K. Liu, Y. Li, and H. S. Ho, "Cyclic deformation behavior of gradient structured austenitic stainless steels," *IOP Conference Series: Materials Science and Engineering*, vol. 770, no. 1, pp. 6–12, 2020.

[16] P. Simon, M. Economopoulos, and P. Nilles, "Tempcore, an Economical Process for the Production of High Quality Rebars.," *MPT. Metallurgical plant and technology*, vol. 7, no. 3, pp. 1–6, 1984.

[17] K. Lee, "Image based fe-modelling of electron backscatter diffraction for ultrasonic wave propagation in dissimilar metal welds," 10 2014.

[18] F. Fang, Y. Zhao, P. Liu, L. Zhou, X. j. Hu, X. Zhou, and Z. h. Xie, "Deformation of cementite in cold drawn pearlitic steel wire," *Materials Sciencgastroenterologistae and Engineering A*, vol. 608, pp. 11–15, 2014.

[19] C. Schayes, *Low cycle fatigue of the Fe-3Si steel : damage mechanisms and strain localisation by EBSD*. PhD thesis, Université de Lille, Lille 1, 2016.

[20] J.-B. Vogt, I. M. Costa, A. Addad, and J. Bouquerel, "Fatigue intrusion-extrusion in a fully pearlitic steel," *Materials Letters*, vol. 267, p. 127539, 2020.

[21] X. Zhang, A. Godfrey, N. Hansen, X. Huang, W. Liu, and Q. Liu, "Evolution of cementite morphology in pearlitic steel wire during wet wire drawing," *Materials Characterization*, vol. 61, pp. 65–72, 1 2010.

[22] K. Lambrigh, *Fatigue mechanisms of pearlitic drawn wires*. PhD thesis, Katholieke Universiteit Leuven, Leuven, 2012.

[23] D. Embury, "The formation of pearlite in steels," in *Phase Transformations in Steels*, pp. 276–310, Elsevier, 2012.

[24] G. Langford, "Deformation of pearlite," *Metallurgical Transactions A*, vol. 8, no. 6, pp. 861–875, 1977.

[25] G. Krauss, *Steels: processing, structure, and performance*. Asm International, 2015.

[26] A. Czarski, T. Skowronek, and P. Matusiewicz, "Stability of a lamellar structure - Effect of the true interlamellar spacing on the durability of a pearlite colony," *Archives of Metallurgy and Materials*, vol. 60, no. 4, pp. 2499–2503, 2015.

[27] M. X. Zhang and P. M. Kelly, "The morphology and formation mechanism of pearlite in steels," *Materials Characterization*, vol. 60, no. 6, pp. 545–554, 2009.

[28] W. J. Nam, C. M. Bae, and C. S. Lee, "Effect of carbon content on the hall-petch parameter in cold drawn pearlitic steel wires," *Journal of materials science*, vol. 37, no. 11, pp. 2243–2249, 2002.

[29] A. Walentek, M. Seefeldt, B. Verlinden, E. Aernoudt, and P. Van Houtte, "Electron backscatter diffraction on pearlite structures in steel," *Journal of microscopy*, vol. 224, no. 3, pp. 256–263, 2006.

[30] A. R. Marder and B. L. Bramfitt, "Effect of continuous cooling on the morphology and kinetics of pearlite," *Metallurgical Transactions A*, vol. 6, no. 11, pp. 2009–2014, 1975.

[31] J. Toribio and A. Valiente, "Approximate evaluation of directional toughness in heavily drawn pearlitic steels," *Materials Letters*, vol. 58, no. 27-28, pp. 3514–3517, 2004.

[32] A. Hohenwarter, B. Völker, M. W. Kapp, Y. Li, S. Goto, D. Raabe, and R. Pippan, "Ultra-strong and damage tolerant metallic bulk materials: a lesson from nanostructured pearlitic steel wires," *Scientific reports*, vol. 6, no. 1, pp. 1–10, 2016.

[33] M. I. S. Nishida, A. Yoshie, "Workhardening of hypereutectoid and eutectoid steels during drawing," *ISIJ International*, vol. 38, no. 1 998, pp. 177–186, 1998.

[34] M. Zelin, "Microstructure evolution in pearlitic steels during wire drawing," *Acta Materialia*, vol. 50, no. 17, pp. 4431–4447, 2002.

[35] A. Kumar, G. Agarwal, R. Petrov, S. Goto, J. Sietsma, and M. Herbig, "Microstructural evolution of white and brown etching layers in pearlitic rail steels," *Acta Materialia*, vol. 171, pp. 48–64, 2019.

[36] Z. Hong, X. Zhang, C. Zhang, Z. Wen, X. Jin, and Q. Yan, "Achievement of high strength-ductility combination in railway wheel steel with thin pearlite and spherical cementite via composition and undercooling design," *Materials Research Express*, vol. 6, no. 1, 2019.

[37] H. K. Bhadeshia, "Steels for bearings," *Progress in Materials Science*, vol. 57, no. 2, pp. 268–435, 2012.

[38] X. Luo and G. E. Totten, "High-carbon steel wire: Patenting in lead bath," in *Encyclopedia of Iron, Steel, and Their Alloys*, pp. 1662–1668, CRC Press, 2016.

[39] S. S. Bargujer, N. M. Suri, and R. M. Belokar, "Optimization of lead patenting process for high carbon steel wires," *Proceedings of the National Academy of Sciences, India Section A: Physical Sciences*, vol. 87, no. 2, pp. 267–278, 2017.

[40] S. Tong, Y. E. v. Schirnding, and T. Prapamontol, "Environmental lead exposure: a public health problem of global dimensions," *Bulletin of the world health organization*, vol. 78, pp. 1068–1077, 2000.

[41] E. B. Hawbolt, B. Chau, and J. K. Brimacombe, "Kinetics of Austenite-Ferrite and Austenite-Pearlite Transformations in a 1025 Carbon Steel," vol. 16, no. April, pp. 565–578, 1985.

[42] N. Kennon and N. Kaye, "Isothermal transformation of austenite to pearlite and upper bainite in eutectoid steel," *Metallurgical Transactions A*, vol. 13, no. 6, pp. 975–978, 1982.

[43] M. Masoumi, G. Tressia, D. M. A. Centeno, and H. Goldenstein, "Improving the mechanical properties and wear resistance of a commercial pearlitic rail steel using a two-step heat treatment," *Metallurgical and Materials Transactions A*, vol. 52, no. 11, pp. 4888–4906, 2021.

[44] X. Luo, K. Chen, and G. E. Totten, "Fast primary cooling: alternative to lead baths for high-carbon steel wire patenting," *Materials Performance and Characterization*, vol. 1, no. 1, pp. 1–13, 2012.

[45] K. Chen, Y. Qi, H. Shao, Z. Li, and X. Luo, "Using sodium polyacrylate aqueous solution to replace lead bath for patenting high-strength steel rope wire of automobile industry," *Materials Performance and Characterization*, vol. 8, no. 2, pp. 266–284, 2018.

[46] Y. Yamada and T. Kuwabara, *Materials for springs*. Springer Science & Business Media, 2007.

[47] J. Wistreich, "The fundamentals of wire drawing," *Metallurgical Reviews*, vol. 3, no. 1, pp. 97–142, 1958.

[48] A. Jamoneau, J. H. Schmitt, and D. Solas, "Measurement of Texture Gradient in Heavily Cold-Drawn Pearlitic Wires," *Advanced Engineering Materials*, vol. 1700279, pp. 1–8, 2017.

[49] N. Guo, B. Luan, B. Wang, and Q. Liu, "Microstructure and texture evolution in fully pearlitic steel during wire drawing," *Science China Technological Sciences*, vol. 56, no. 5, pp. 1139–1146, 2013.

[50] F. L. Lian, H. J. Liu, J. J. Sun, X. J. Sun, S. W. Guo, Y. N. Liu, and L. X. Du, "Ultrafine grain effect on pearlitic transformation in hypereutectoid steel," *Journal of Materials Research*, vol. 28, no. 5, pp. 757–765, 2013.

[51] K. Clarke, C. Van Tyne, C. Vigil, and R. Hackenberg, "Induction hardening 5150 steel: effects of initial microstructure and heating rate," *Journal of materials engineering and performance*, vol. 20, no. 2, pp. 161–168, 2011.

[52] T. C. Tszeng and G. Shi, "A global optimization technique to identify overall transformation kinetics using dilatometry data - Applications to austenitization of steels," *Materials Science and Engineering A*, vol. 380, no. 1, pp. 123–136, 2004.

[53] Z. Li, Z. Wen, F. Su, R. Zhang, and Z. Zhou, "Dilatometric research on pearlite-to-austenite transformation of Fe–1C–1.44Cr low-alloy steel," *Journal of Materials Science*, vol. 53, no. 2, pp. 1424–1436, 2018.

[54] J. W. Cahn, "On the kinetics of the pearlite reaction," *JOM*, vol. 9, no. 1, pp. 140–144, 1957.

[55] P. Clemm and J. Fisher, "The influence of grain boundaries on the nucleation of secondary phases," *Acta Metallurgica*, vol. 3, no. 1, pp. 70–73, 1955.

[56] D. Gaude-Fugarolas and H. K. D. H. Bhadeshia, "A model for austenitisation of hypoeutectoid steels," *Journal of Materials Science*, vol. 38, no. 6, pp. 1195–1201, 2003.

[57] S. J. Lee and K. D. Clarke, "A conversional model for austenite formation in hypereutectoid steels," *Metallurgical and Materials Transactions A: Physical Metallurgy and Materials Science*, vol. 41, no. 12, pp. 3027–3031, 2010.

[58] S. J. Lee, K. D. Clarke, and C. J. Van Tyne, "An on-heating dilation conversional model for austenite formation in hypoeutectoid steels," *Metallurgical and Materials Transactions A: Physical Metallurgy and Materials Science*, vol. 41, no. 9, pp. 2224–2235, 2010.

[59] A. Danon, C. Servant, A. Alamo, and J. C. Brachet, "Heterogeneous austenite grain growth in 9Cr martensitic steels: Influence of the heating rate and the austenitization temperature," *Materials Science and Engineering A*, vol. 348, no. 1-2, pp. 122–132, 2003.

[60] B. Pawłowski, "Dilatometric examination of continuously heated austenite formation in hypoeutectoid steels," *Journal of Achievements in Materials and Manufacturing Engineering*, vol. 54, no. 2, pp. 185–193, 2012.

[61] F. L. Oliveira, M. S. Andrade, and A. B. Cota, "Kinetics of austenite formation during continuous heating in a low carbon steel," *Materials Characterization*, vol. 58, no. 3, pp. 256–261, 2007.

[62] J. Orlich, "Beschreibung der austenitisierungsvorgänge bei der schnellerwärmung von stahl in zeit-temperatur-austenitisierung-(zta-) schaubildern," *HTM Journal of Heat Treatment and Materials*, vol. 29, no. 4, pp. 231–236, 1974.

[63] S. Lee, M. T. Lusk, and Y. Lee, "Conversional model of transformation strain to phase fraction in low alloy steels," vol. 55, pp. 875–882, 2007.

[64] B. L. Ferguson, Z. Li, and A. M. Freborg, "Modeling heat treatment of steel parts," *Computational Materials Science*, vol. 34, no. 3, pp. 274–281, 2005.

[65] A. S. Pandit and H. K. Bhadeshia, "Diffusion-controlled growth of pearlite in ternary steels," *Proceedings of the Royal Society A: Mathematical, Physical and Engineering Sciences*, vol. 467, no. 2134, pp. 2948–2961, 2011.

[66] A. S. Pandit and H. K. Bhadeshia, "Mixed diffusion-controlled growth of pearlite in binary steel," *Proceedings of the Royal Society A: Mathematical, Physical and Engineering Sciences*, vol. 467, no. 2126, pp. 508–521, 2011.

[67] M. Hillert, "The role of interfacial energy during solid-state phase transformations," *Jernkontorets Annaler*, vol. 141, pp. 757–789, 1957.

[68] T. Takahashi, D. Ponge, and D. Raabe, "Investigation of orientation gradients in pearlite in hypoeutectoid steel by use of orientation imaging microscopy," *Steel Research International*, vol. 78, no. 1, pp. 38–44, 2007.

[69] B. Bramfitt and A. Marder, "A transmission-electron-microscopy study of the substructure of high-purity pearlite," *Metallography*, vol. 6, no. 6, pp. 483–495, 1973.

[70] Y. L. Tian and R. W. Kraft, "Kinetics of pearlite spheroidizations," *Metallurgical Transactions A*, vol. 18, no. 8, pp. 1359–1369, 1987.

[71] Y. L. Tian and R. W. Kraft, "Mechanisms of Pearlite Spheroidization," *Metallurgical Transactions A*, vol. 18, no. 8, pp. 1403–1414, 1987.

[72] P. Matusiewicz, J. Augustyn-Nadzieja, A. Czarski, and T. Skowronek, "Kinetics of pearlite spheroidization," *Archives of Metallurgy and Materials*, vol. 62, no. 1, pp. 231–234, 2017.

[73] A. Pandit and H. Bhadeshia, "Divorced pearlite in steels," *Proceedings of the Royal Society A: Mathematical, Physical and Engineering Sciences*, vol. 468, no. 2145, pp. 2767–2778, 2012.

[74] J. D. Verhoeven and E. D. Gibson, "The divorced eutectoid transformation in steel," *Metallurgical and Materials Transactions A: Physical Metallurgy and Materials Science*, vol. 29, no. 4, pp. 1181–1189, 1998.

[75] N. V. Luzginova, L. Zhao, and J. Sietsma, "The cementite spheroidization process in high-carbon steels with different chromium contents," *Metallurgical and Materials Transactions A: Physical Metallurgy and Materials Science*, vol. 39 A, pp. 513–521, 3 2008.

[76] C.-l. Zhang, X. Liu, L.-y. Zhou, and Y.-z. Liu, "Influence of pearlite interlamellar spacing on strain hardening behaviour in spring steel 60si2mna," *Procedia Engineering*, vol. 81, pp. 1283–1287, 2014.

[77] F. Kavishe and T. Baker, "Effect of prior austenite grain size and pearlite interlamellar spacing on strength and fracture toughness of a eutectoid rail steel," *Materials science and technology*, vol. 2, no. 8, pp. 816–822, 1986.

[78] L. Zhou, F. Fang, L. Wang, H. Chen, Z. Xie, and J. Jiang, "Torsion delamination and recrystallized cementite of heavy drawing pearlitic wires after low temperature annealing," *Materials Science and Engineering A*, vol. 713, no. December 2017, pp. 52–60, 2018.

[79] F. Wetscher, R. Pippan, S. Sturm, F. Kauffmann, C. Scheu, and G. Dehm, "TEM investigations of the structural evolution in a pearlitic steel deformed by high-pressure torsion," *Metallurgical and Materials Transactions A: Physical Metallurgy and Materials Science*, vol. 37, no. 6, pp. 1963–1968, 2006.

[80] J. Toribio, B. González, and J. C. Matos, "Initiation and propagation of fatigue cracks in cold-drawn pearlitic steel wires," *Theoretical and Applied Fracture Mechanics*, vol. 92, no. April, pp. 410–419, 2017.

[81] C. Schayes, J.-B. Vogt, J. Bouquerel, F. Palleschi, and S. Zaefferer, "Cyclic plasticity mechanism of the m330-35a steel," *International Journal of Fatigue*, vol. 82, pp. 530–539, 2016.

[82] J. Toribio, V. Kharin, F.-J. Ayaso, M. Lorenzo, B. González, J.-C. Matos, and L. Aguado, "Analysis of the bauschinger effect in cold drawn pearlitic steels," *Metals*, vol. 10, no. 1, p. 114, 2020.

[83] J. Polák and J. Man, "Mechanisms of extrusion and intrusion formation in fatigued crystalline materials," *Materials Science and Engineering: A*, vol. 596, pp. 15–24, 2014.

[84] X. Wu, P. Jiang, L. Chen, F. Yuan, and Y. T. Zhu, "Extraordinary strain hardening by gradient structure," *Proceedings of the National Academy of Sciences of the United States of America*, vol. 111, no. 20, pp. 7197–7201, 2014.

[85] W. L. Zhou, K. K. Liu, Y. Li, and H. S. Ho, "Cyclic deformation behavior of gradient structured austenitic stainless steels," *IOP Conference Series: Materials Science and Engineering*, vol. 770, p. 012031, 2020.

[86] C. W. Shao, P. Zhang, Y. K. Zhu, Z. J. Zhang, Y. Z. Tian, and Z. F. Zhang, "Simultaneous improvement of strength and plasticity: Additional work-hardening from gradient microstructure," *Acta Materialia*, vol. 145, pp. 413–428, 2018.

[87] M. Yang, Y. Pan, F. Yuan, Y. Zhu, and X. Wu, "Back stress strengthening and strain hardening in gradient structure," *Materials Research Letters*, vol. 4, no. 3, pp. 145–151, 2016.

[88] K. Lu and J. Lu, "Nanostructured surface layer on metallic materials induced by surface mechanical attrition treatment," *Materials Science & Engineering A: Structural Materials: Properties, Microstructure and Processing*, vol. 375-377, pp. 38–45, July 2004.

[89] Y. Samih, B. Beausir, B. Bolle, and T. Grosdidier, "In-depth quantitative analysis of the microstructures produced by Surface Mechanical Attrition Treatment (SMAT)," *Materials Characterization*, vol. 83, pp. 129–138, 2013.

[90] T. O. Olugbade and J. Lu, "Literature review on the mechanical properties of materials after surface mechanical attrition treatment (SMAT)," *Nano Materials Science*, vol. 2, no. 1, pp. 3–31, 2020.

[91] J. N. Sahu and C. Sasikumar, "A novel method for development of hard nano crystalline surface through SMAT and mechanical alloying," *Materials Today: Proceedings*, vol. 3, no. 6, pp. 1968–1976, 2016.

[92] S. C. Cao, J. Liu, L. Zhu, L. Li, M. Dao, J. Lu, and R. O. Ritchie, "Nature-Inspired Hierarchical Steels," *Scientific Reports*, vol. 8, no. 1, 2018.

[93] W. Zhong, "Fatigue properties of reinforcing steel produced by tempcore process," vol. JOURNAL OF, no. May, pp. 158–165, 1999.

[94] G. Rehm and D. Russwurm, "Assessment of Concrete Reinforcing Bars Made By the Tempcore Process.," *Metall Rep CRM*, no. 51, pp. 3–16, 1977.

[95] Lkic. and B.. Grubi. V. crud Torte& G.E, "Inverse hardness distribution and its influence on mechanical properties," *International conference on Quenching and Control of Distortion*, 1996.

[96] TAinstruments, "Quenching and deformation dilatometer brochure." [Online], Available : https://www.tainstruments.com/dil-805a-quenching-dilatomers/ (visited on 07.12.2021).

[97] ASTM A1033-18, "Standard practice for quantitative measurement and reporting of hypoeutectoid carbon and low-alloy steel phase transformations," standard, ASTM International, West Conshohocken, PA, 2018.

[98] H.-S. Yang and H. K. D. H. Bhadeshia, "Uncertainties in dilatometric determination of martensite start temperature," *Materials Science and Technology*, vol. 23, no. 5, pp. 556–560, 2007.

[99] N. Khodaie, D. G. Ivey, and H. Henein, "Unit cell dilation technique for analyzing dilatometry data in microalloyed steels," *Materials Characterization*, vol. 135, no. November 2017, pp. 84–95, 2018.

[100] J. Z. Zhao, C. Mesplont, and B. C. D. Cooman, "Kinetics of Phase Transformations in Steels: A New Method for Analysing Dilatometric Results," *ISIJ International*, vol. 41, no. 5, pp. 492–497, 2001.

[101] I. Wood, L. Vočadlo, K. Knight, D. P. Dobson, W. Marshall, G. D. Price, and J. Brodholt, "Thermal expansion and crystal structure of cementite, fe3c, between 4 and 600 k determined by time-of-flight neutron powder diffraction," *Journal of Applied Crystallography*, vol. 37, no. 1, pp. 82–90, 2004.

[102] L. Hadjadj, R. Amira, D. Hamana, and A. Mosbah, "Characterization of precipitation and phase transformations in al–zn–mg alloy by the differential dilatometry," *Journal of Alloys and Compounds*, vol. 462, no. 1-2, pp. 279–283, 2008.

[103] O. Renk, R. Enzinger, C. Gammer, D. Scheiber, B. Oberdorfer, M. Tkadletz, A. Stark, W. Sprengel, R. Pippan, J. Eckert, *et al.*, "Stainless steel reveals an anomaly in thermal expansion behavior of severely deformed materials," *Physical Review Materials*, vol. 5, no. 11, p. 113609, 2021.

[104] T. De Cock, C. Capdevila, F. G. Caballero, and C. G. De Andrés, "Interpretation of a dilatometric anomaly previous to the ferrite-to-austenite transformation in a low carbon steel," *Scripta Materialia*, vol. 54, no. 5, pp. 949–954, 2006.

[105] R.-j. Zhao, J.-x. Fu, Y.-y. Zhu, Y.-j. Yang, and Y.-x. Wu, "Dilatometric analysis of irreversible volume change during phase transformation in pure iron," *Journal of Iron and Steel Research International*, vol. 23, no. 8, pp. 828–833, 2016.

[106] N. Khodaie, *A fundamental method to quantify phase change in microalloyed steels by A thesis submitted in partial fulfillment of the requirements for the degree of.* PhD thesis, 2018.

[107] Y. Xu, G. Xu, X. Mao, G. Zhao, and S. Bao, "Method to Evaluate the Kinetics of Bainite Transformation in Low-Temperature Nanobainitic Steel Using Thermal Dilatation Curve Analysis," *Metals*, vol. 7, no. 9, p. 330, 2017.

[108] N. Guo and Q. Liu, "Back-scattered electron imaging combined with EBSD technique for characterization of pearlitic steels," *Journal of Microscopy*, vol. 246, no. 3, pp. 221–228, 2012.

[109] ASTM E1181-02, "Standard Test Methods for Characterizing Duplex Grain Sizes," *ASTM Standards*, 2008.

[110] G. F. Vander Voort and A. Roósz, "Measurement of the interlamellar spacing of pearlite," *Metallography*, vol. 17, no. 1, pp. 1–17, 1984.

[111] S. Zaefferer, N.-N. Elhami, and P. Konijnenberg, "Electron backscatter diffraction (ebsd) techniques for studying phase transformations in steels," in *Phase transformations in steels*, pp. 557–587, Elsevier, 2012.

[112] L. Zhou, F. Fang, X. Zhou, Y. Tu, Z. Xie, and J. Jiang, "Cementite nano-crystallization in cold drawn pearlitic wires instigated by low temperature annealing," *Scripta Materialia*, vol. 120, pp. 5–8, 2016.

[113] F. Fang, Y. Zhao, L. Zhou, X. Hu, Z. Xie, and J. Jiang, "Texture inheritance of cold drawn pearlite steel wires after austenitization," *Materials Science and Engineering A*, vol. 618, pp. 505–510, 2014.

[114] H. Pirgazi, R. H. Petrov, L. Malet, S. Godet, and L. A. Kestens, "Recent developments in orientation contrast microscopy," in *Encyclopedia of Materials: Metals and Alloys*, pp. 662–681, Elsevier, 2021.

[115] C. Hofer, V. Bliznuk, A. Verdiere, R. Petrov, F. Winkelhofer, H. Clemens, and S. Primig, "Correlative microscopy of a carbide-free bainitic steel," *Micron*, vol. 81, pp. 1–7, 2016.

[116] J. G. Wen, "Transmission electron microscopy," in *Practical Materials Characterization*, pp. 189–229, Springer, 2014.

[117] B. Inkson, "Scanning electron microscopy (sem) and transmission electron microscopy (tem) for materials characterization," in *Materials characterization using nondestructive evaluation (NDE) methods*, pp. 17–43, Elsevier, 2016.

[118] K. Fang, J. G. Yang, X. S. Liu, K. J. Song, H. Y. Fang, and H. K. D. H. Bhadeshia, "Regeneration technique for welding nanostructured bainite," *Materials and Design*, vol. 50, pp. 38–43, 2013.

[119] P. Buseck, J. Cowley, and L. Eyring, *High-resolution transmission electron microscopy: and associated techniques*. Oxford University Press, 1989.

[120] P. P. Milella, *Fatigue and corrosion in metals*. Springer Science & Business Media, 2012.

[121] C. Cooper and M. Fine, "Coffin-manson relation for fatigue crack initiation," *TMS (The Metallurgical Society) Paper Selection;(USA)*, vol. 56, no. CONF-840909-, 1984.

[122] S. Janakiram and J. P. Gautam, "Recrystallization texture evolution in HSLA steel," *Lecture Notes in Mechanical Engineering*, vol. PartF2, pp. 135–142, 2018.

[123] A. Chbihi, D. Barbier, L. Germain, A. Hazotte, and M. Gouné, "Interactions between ferrite recrystallization and austenite formation in high-strength steels," *Journal of Materials Science*, vol. 49, no. 10, pp. 3608–3621, 2014.

[124] G. Liu, J. Li, S. Zhang, J. Wang, and Q. Meng, "Dilatometric study on the recrystallization and austenization behavior of cold-rolled steel with different heating rates," *Journal of Alloys and Compounds*, vol. 666, pp. 309–316, 2016.

[125] ASTM E407-07e1, " Standard practice for microetching metals and alloys," standard, ASTM International, West Conshohocken, PA, 2007.

[126] G. F. Vander Voort, "Grain size measurement," in *Practical applications of quantitative metallography*, ASTM International, 1984.

[127] C. García de Andrés, F. G. Caballero, C. Capdevila, and D. San Martín, "Revealing austenite grain boundaries by thermal etching: Advantages and disadvantages," *Materials Characterization*, vol. 49, no. 2, pp. 121–127, 2002.

[128] ASTM E112-12, "Standard Test Methods for Determining Average Grain Size," standard, ASTM International, West Conshohocken, PA, 2012.

[129] S. N. Doi and H. J. Kestenbach, "Determination of the pearlite nodule size in eutectoid steels," *Metallography*, vol. 23, no. 2, pp. 135–146, 1989.

[130] F. G. Caballerol, C. Capdevilal, and C. García De Andrés, "Modeling of the interlamellar spacing of isothermally formed pearlite in a eutectoid steel," *Scripta Materialia*, vol. 42, no. 6, pp. 537–542, 2000.

[131] A. M. Elwazri, P. Wanjara, and S. Yue, "Effect of prior-austenite grain size and transformation temperature on nodule size of microalloyed hypereutectoid steels," *Metallurgical and Materials Transactions A: Physical Metallurgy and Materials Science*, vol. 36, no. 9, pp. 2297–2305, 2005.

[132] N. Ridley, "A review of the data on the interlamellar spacing of pearlite," *Metallurgical and Materials Transactions A*, vol. 15, no. 6, pp. 1019–1036, 1984.

[133] V. L. Buono, B. Gonzalez, T. Lima, and M. Andrade, "Measurement of fine pearlite interlamellar spacing by atomic force microscopy," *Journal of Materials Science*, vol. 32, no. 4, pp. 1005–1008, 1997.

[134] J. Schindelin, I. Arganda-Carreras, E. Frise, V. Kaynig, M. Longair, T. Pietzsch, S. Preibisch, and C. Rueden, "714 saalfeld s, schmid b, tinevez jy, white dj, hartenstein v, eliceiri k, tomancak p, cardona a. 2012. 715 fiji: an open-source platform for biological-image analysis," *Nat Methods*, vol. 9, pp. 676–682.

[135] Minitab, LLC, "Minitab."

[136] Oxford(2020), "Symmetry s2 brochure." [Online], Available : nano.oxinst.com/symmetrys2 (visited on 07.12.2021).

[137] C. García De Andrés, F. G. Caballero, C. Capdevila, and H. K. Bhadeshia, "Modelling of kinetics and dilatometric behavior of non-isothermal pearlite-to-austenite transformation in an eutectoid steel," *Scripta Materialia*, vol. 39, no. 6, pp. 791–796, 1998.

[138] I. G. Wood, L. Vočadlo, K. S. Knight, D. P. Dobson, W. G. Marshall, G. D. Price, and J. Brodholt, "Thermal expansion and crystal structure of cementite, Fe3C, between 4 and 600 K determined by time-of-flight neutron powder diffraction," *Journal of Applied Crystallography*, vol. 37, no. 1, pp. 82–90, 2004.

[139] J. D. Verhoeven and E. D. Gibson, "The Divorced Eutectoid Transformation in Steel," tech. rep., 1998.

[140] C. Capdevila, C. FG, and C. G. De Andrés, "Determination of ms temperature in steels: A bayesian neural network model," *ISIJ international*, vol. 42, no. 8, pp. 894–902, 2002.

[141] H.-S. Yang and H. Bhadeshia, "Uncertainties in dilatometric determination of martensite start temperature," *Materials Science and Technology*, vol. 23, no. 5, pp. 556–560, 2007.

[142] H.-S. Yang and H. Bhadeshia, "Austenite grain size and the martensite-start temperature," *Scripta materialia*, vol. 60, no. 7, pp. 493–495, 2009.

[143] T. Sourmail and C. Garcia-Mateo, "Critical assessment of models for predicting the Ms temperature of steels," *Computational Materials Science*, vol. 34, no. 4, pp. 323–334, 2005.

[144] S. Li, Z. Yang, M. Enomoto, and Z.-G. Yang, "Study of partition to non-partition transition of austenite growth along pearlite lamellae in near-eutectoid fe-c-mn alloy," *Acta Materialia*, vol. 177, pp. 198–208, 2019.

[145] W. Sun, Y. Wu, S. Yang, and C. Hutchinson, "Advanced high strength steel (ahss) development through chemical patterning of austenite," *Scripta Materialia*, vol. 146, pp. 60–63, 2018.

[146] ASTM E 1181, "Test methods for characterizing duplex grain sizes," standard, ASTM International, West Conshohocken, PA, 2005.

[147] D. Chakrabarti, C. Davis, and M. Strangwood, "Characterisation of bimodal grain structures in hsla steels," *Materials characterization*, vol. 58, no. 5, pp. 423–438, 2007.

[148] Y. C. Liu, F. Sommer, and E. J. Mittemeijer, "Abnormal austenite-ferrite transformation behaviour of pure iron," *Philosophical Magazine*, vol. 84, no. 18, pp. 1853–1876, 2004.

[149] Y. Liu, F. Sommer, and E. Mittemeijer, "Abnormal austenite–ferrite transformation behaviour in substitutional fe-based alloys," *Acta materialia*, vol. 51, no. 2, pp. 507–519, 2003.

[150] Y. Liu, F. Sommer, and E. Mittemeijer, "Abnormal austenite–ferrite transformation behaviour of pure iron," *Philosophical magazine*, vol. 84, no. 18, pp. 1853–1876, 2004.

[151] Y. Liu, F. Sommer, and E. Mittemeijer, "Kinetics of the abnormal austenite–ferrite transformation behaviour in substitutional fe-based alloys," *Acta materialia*, vol. 52, no. 9, pp. 2549–2560, 2004.

[152] A. R. Marder and B. L. Bramfitt, "The effect of morphology on the strength of pearlite," *Metallurgical Transactions A*, vol. 7, no. 2, pp. 365–372, 1976.

[153] Y. Liu, F. Sommer, and E. Mittemeijer, "The austenite–ferrite transformation of ultralow-carbon fe–c alloy; transition from diffusion-to interface-controlled growth," *Acta materialia*, vol. 54, no. 12, pp. 3383–3393, 2006.

[154] B. Hutchinson, J. Hagström, O. Karlsson, D. Lindell, M. Tornberg, F. Lindberg, and M. Thuvander, "Microstructures and hardness of as-quenched martensites (0.1–0.5% c)," *Acta Materialia*, vol. 59, no. 14, pp. 5845–5858, 2011.

[155] L. Zhou, F. Fang, L. Wang, H. Chen, Z. Xie, and J. Jiang, "Torsion delamination and recrystallized cementite of heavy drawing pearlitic wires after low temperature annealing," *Materials Science and Engineering A*, vol. 713, no. December 2017, pp. 52–60, 2018.

[156] D. Grygier, M. Rutkowska-Gorczyca, and A. Zak, "The Effectiveness of Recrystallization of Pearlitic Steels in the Regards of the Change the Annealing Time," *International Journal of New Technology and Research*, vol. 2, no. 3, p. 263589, 2016.

[157] C. Borchers, Y. Chen, M. Deutges, S. Goto, and R. Kirchheim, "Carbon-defect interaction during recovery and recrystallization of heavily deformed pearlitic steel wires," *Philosophical Magazine Letters*, vol. 90, no. 8, pp. 581–588, 2010.

[158] Y. J. Li, P. Choi, C. Borchers, S. Westerkamp, S. Goto, D. Raabe, and R. Kirchheim, "Atomic-scale mechanisms of deformation-induced cementite decomposition in pearlite," 2011.

[159] J. Languillaume, G. Kapelski, and B. Baudelet, "Cementite dissolution in heavily cold drawn pearlitic steel wires," *Acta Materialia*, vol. 45, no. 3, pp. 1201–1212, 1997.

[160] Y. L. Tian and R. W. Kraft, "Kinetics of pearlite spheroidizations," *Metallurgical Transactions A*, vol. 18, no. 8, pp. 1359–1369, 1987.

[161] P. Matusiewicz, J. Augustyn-Nadzieja, A. Czarski, and T. Skowronek, "Kinetics of pearlite spheroidization," *Archives of Metallurgy and Materials*, vol. 62, no. 1, pp. 231–234, 2017.

[162] F. Yang, J. Q. Jiang, Y. Wang, C. Ma, F. Fang, K. L. Zhao, and W. Li, "Residual stress in pearlitic steel rods during progressively cold drawing measured by X-ray diffraction," *Materials Letters*, vol. 62, no. 15, pp. 2219–2221, 2008.

[163] F. Liu, F. Sommer, C. Bos, and E. J. Mittemeijer, "Analysis of solid state phase transformation kinetics: Models and recipes," *International Materials Reviews*, vol. 52, pp. 193–212, 7 2007.

[164] J. M. Atienza, J. Ruiz-Hervias, M. L. Martinez-Perez, F. J. Mompean, M. Garcia-Hernandez, and M. Elices, "Residual stresses in cold drawn pearlitic rods," *Scripta Materialia*, vol. 52, no. 12, pp. 1223–1228, 2005.

[165] ASTM E606 / E606M-12, "Standard Test Method for Strain-Controlled Fatigue Testing 1," standard, ASTM International, West Conshohocken, PA, 2012.

[166] J. Dickson, J. Boutin, and L. Handfield, "A comparison of two simple methods for measuring cyclic internal and effective stresses," *Materials Science and Engineering*, vol. 64, no. 1, pp. L7–L11, 1984.

[167] J.-B. Vogt, T. Magnin, and J. Foct, "Effective stresses and microstructure in cyclically deformed 316l austenitic stainless steel: effect of temperature and nitrogen content," *Fatigue & Fracture of Engineering Materials & Structures*, vol. 16, no. 5, pp. 555–564, 1993.

[168] L. Ávila de Oliveira Silva, G. Adinolfi Colpaert Sartori, D. Bondarchuk, I. M. Oliveira Anício Costa, C. Mesplont, and J.-B. Vogt, "Effect of interlamellar spacing on the low cycle fatigue behavior of a fully pearlitic steel," *Metallography, Microstructure, and Analysis*, pp. 1–8, 2021.

[169] R. Milligan, W. Koo, and T. Davidson, "The bauschinger effect in a high-strength steel," *Journal Fluids Engineering originally published in Journal of Basic Engineering*, vol. 88, 1966.

[170] F. Léaux, *Relation entre microstructure et fatigue d'un acier ferritique utilisé dans l'industrie automobile : élaboration d'indicateurs d'endommagement.* PhD thesis, Université de Lille, Lille 1, 2012.

[171] H. Qiu, L. Wang, T. Hanamura, and S. Torizuka, "Prediction of the work-hardening exponent for ultrafine-grained steels," *Materials Science and Engineering: A*, vol. 536, pp. 269–272, 2012.

[172] V. Buono, B. Gonzalez, and M. Andrade, "Kinetics of strain aging in drawn pearlitic steels," *Metallurgical and materials transactions A*, vol. 29, no. 5, pp. 1415–1423, 1998.

[173] B. M. Gonzalez, L. A. Marchi, E. J. da FONSECA, P. J. Modenesi, and V. T. L. Buono, "Measurement of dynamic strain aging in pearlitic steels by tensile test," *ISIJ international*, vol. 43, no. 3, pp. 428–432, 2003.

[174] J. Takahashi, M. Kosaka, K. Kawakami, and T. Tarui, "Change in carbon state by low-temperature aging in heavily drawn pearlitic steel wires," *Acta Materialia*, vol. 60, no. 1, pp. 387–395, 2012.

[175] R. Dippenaar and R. W. K. Honeycombe, "The crystallography and nucleation of pearlite," *Proceedings of the Royal Society of London. A. Mathematical and Physical Sciences*, vol. 333, no. 1595, pp. 455–467, 1973.

[176] H. I. Aaronson, M. Enomoto, and J. K. Lee, *Mechanisms of diffusional phase transformations in metals and alloys*. CRC Press, 2016.

Appendix A

Statistical results

The statics results of the ANOVA tests analyzing the if the effect of the test parameters (time, temperature and heating rates) entail significant effect on the obtained PAGS.

1. Time: The time produces a significant effect on the mean PAGS, meaning that the obtained mean PAGS is different for all the employed times independently of the austenitization temperature with 0.05 level significance.

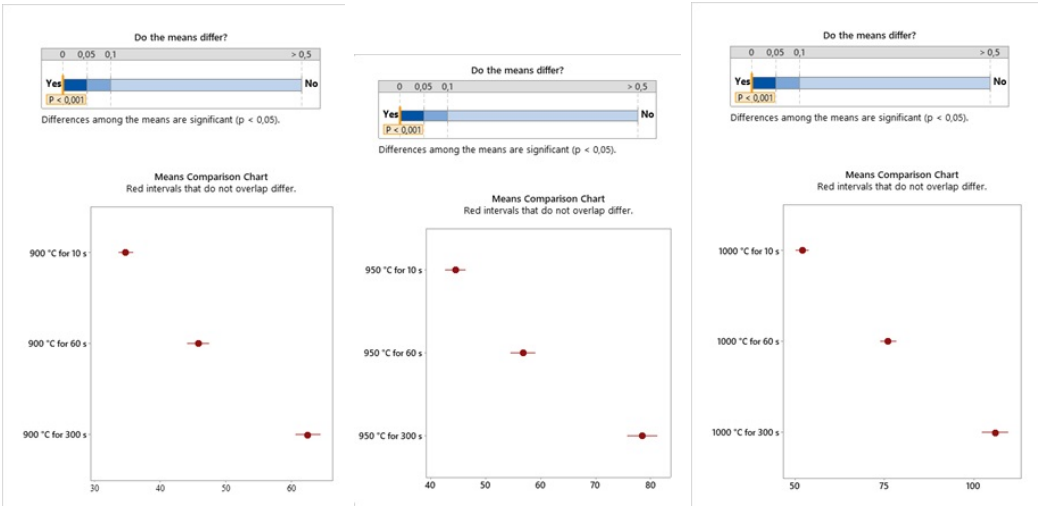

2. Temperature: The temperature produces a significant effect on the mean PAGS, meaning that the obtained mean PAGS is different for all the employed times independently of the austenitization temperature with 0.05 level significance.

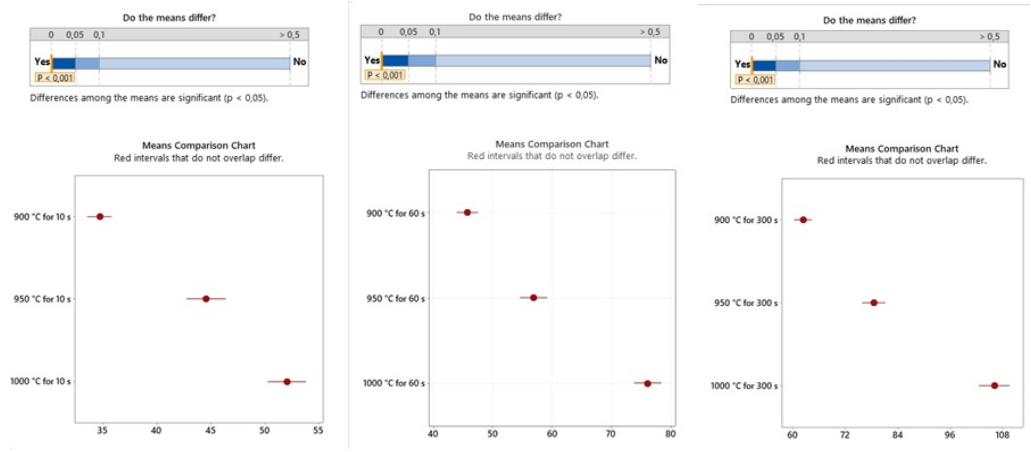

3. Heating rates: The heating rate can produces a significant effect on the mean PAGS, meaning that the obtained mean PAGS can be different for some of the employed heating rates with 0.05 level significance. However, these differences are not physically meaningful and mostly related to the scattering of the measurements, especially important for large PAGS.

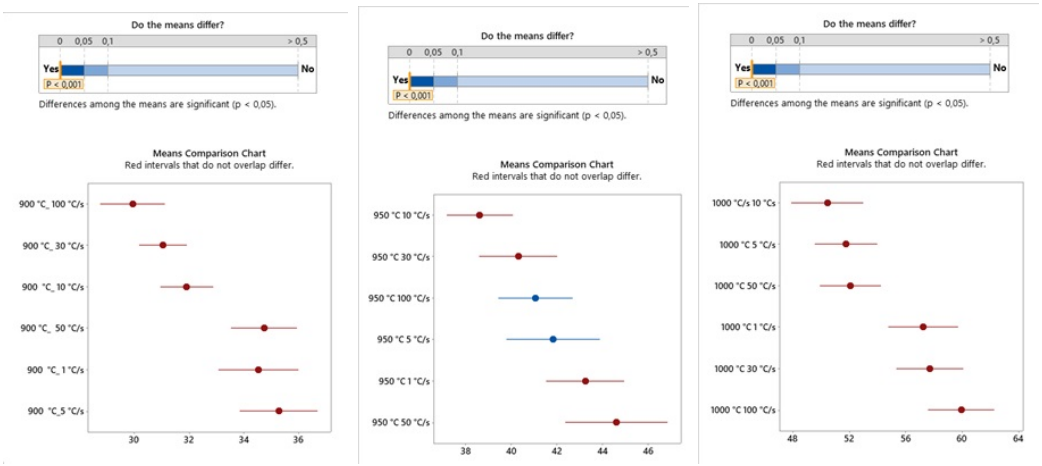

Appendix A

EBSD analysis

Analysis of the memory effect after austenitization of pearlitic steels.

Two wires of 0.87%C were analyzed presenting different accumulated drawing strains ($\epsilon_d = 0.97$ et 1.83). The EBSD analysis was done at the deformed state and then after being austenitized and re-transformed to pearlite.

- EBSD data at the deformed state

  $\epsilon_d = 0.97$

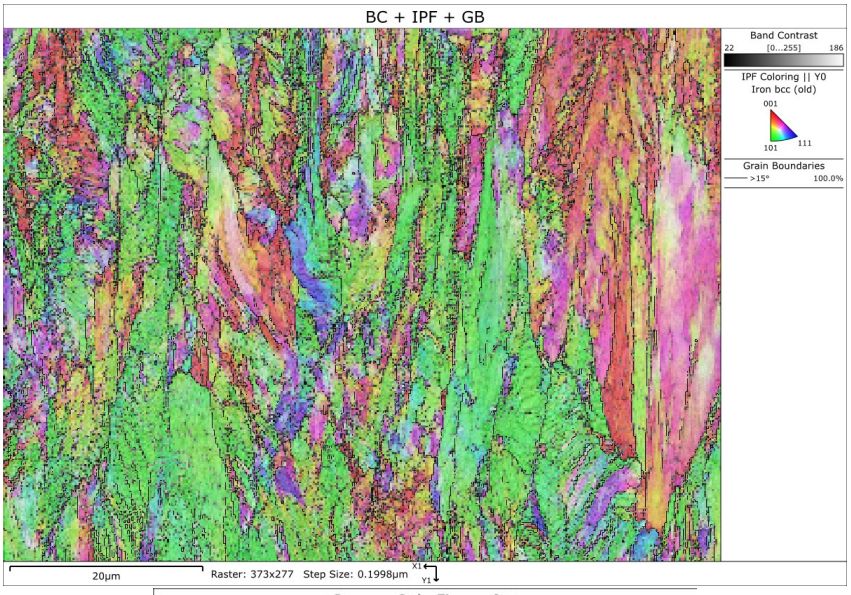

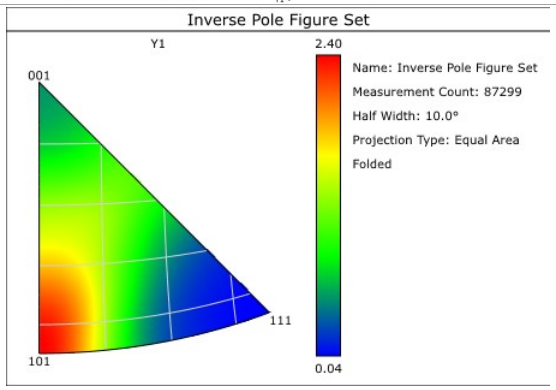

$\epsilon_d = 1.83$

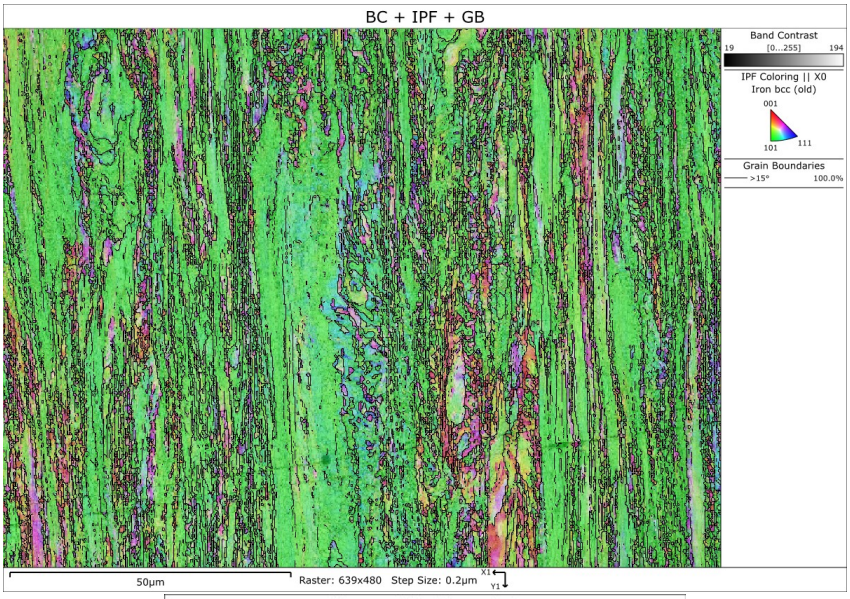

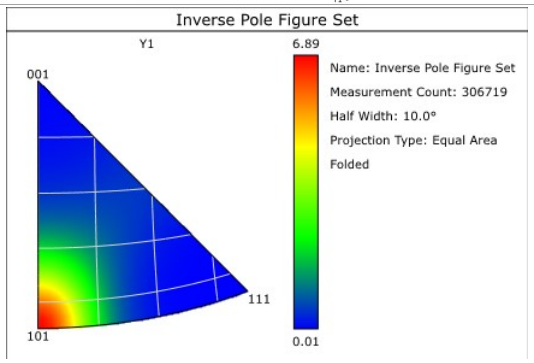

- EBSD data after being austenitized

  Maps from the surface to the core, $\epsilon_d = 0.97$ on the left and on the right $\epsilon_d = 1.83$

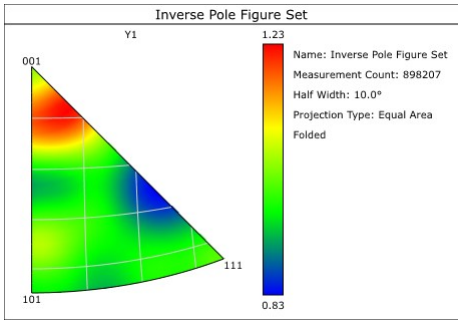

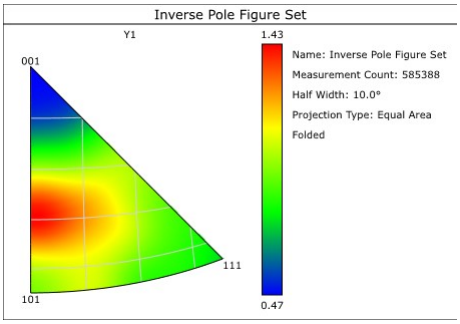

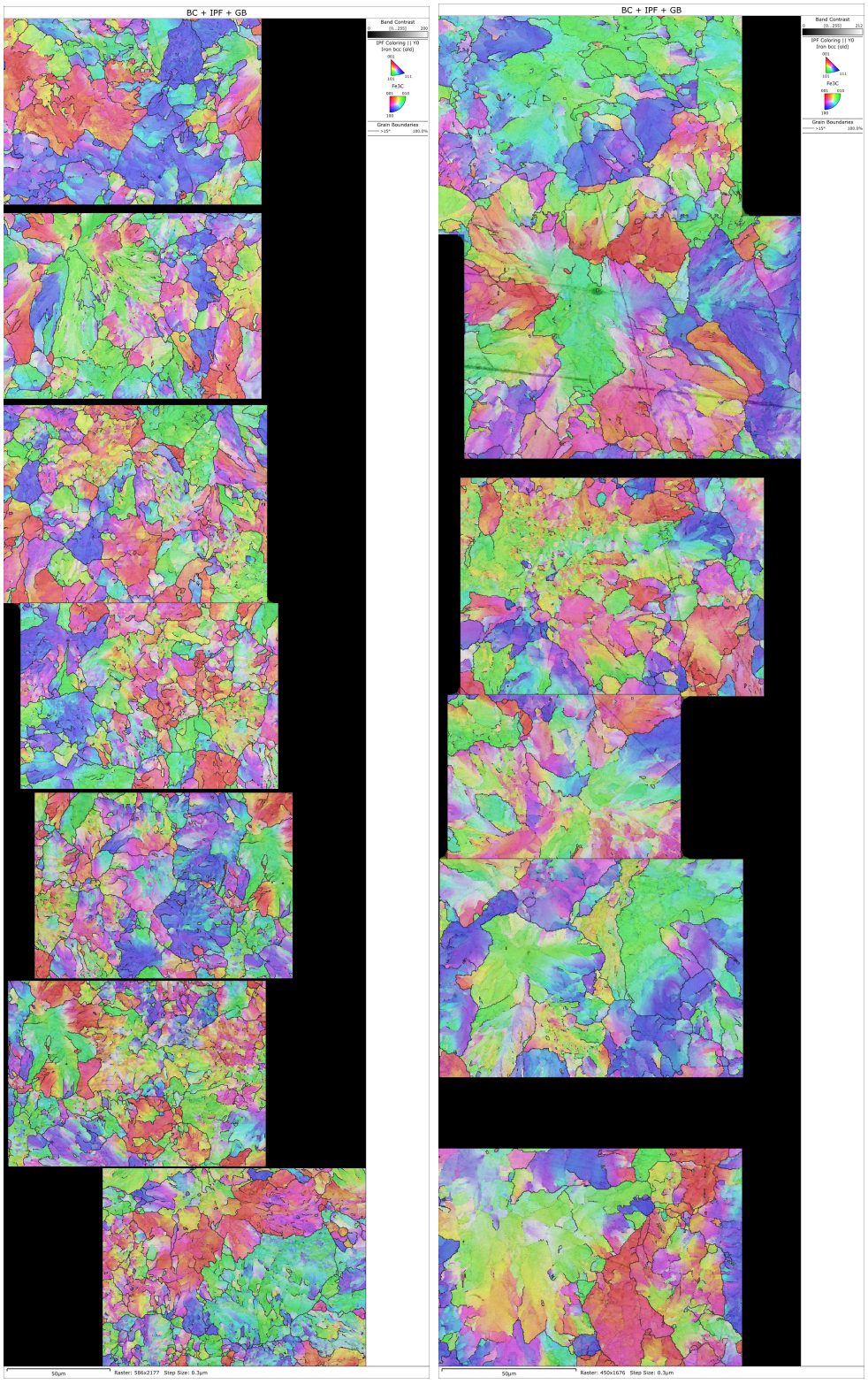
BC + IPF + GB
Band Contrast
IPF Coloring || Y0
Iron bcc (old)
Fe3C
Grain Boundaries
50µm
Raster: 586x2177 Step Size: 0.3µm
BC + IPF + GB
Band Contrast
IPF Coloring || Y0
Iron bcc (old)
Fe3C
Grain Boundaries
50µm
Raster: 450x1676 Step Size: 0.3µm

It is seen a strong texture in which the plans (110) are parallel to the drawing direction. This is the $\alpha - fiber$ texture component, very common in drawn wires, at it is seen to increase the intensity of this texture with the increase of the drawing strain.

After the transformation, this texture disappears. It means that the memory effect was not observed in the analyzed conditions.

GRAPHICAL ABSTRACT

Microstructural gradient production

Heating

Does not affect the gradients

Austenitization

Does not affect the gradients

- Over 1000 °C the austenite is homogeneous
- The heating rates have little effect
- The mechanical history does not influence

Cooling

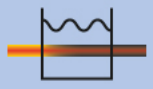

The gradients of fine pearlite at surface + coarse pearlite in the core are feasible

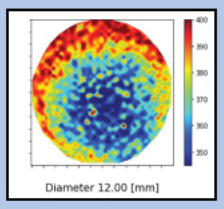

- The interlamellar spacing varies with the transformation temperature
- The pearlite morphology varies with the type of cooling (isotherm or continuous cooling)

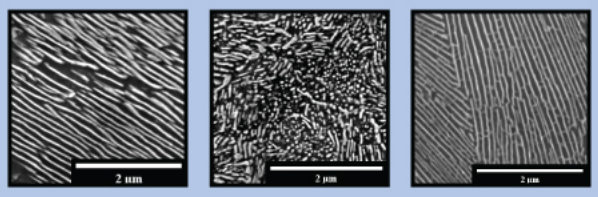

- The kinetics of the transformation varies with the PAGS, carbon content, and temperature of the transformation

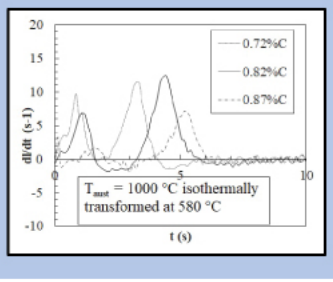

Drawing

No significant gradient

- The gradients created in the wires of diameter 6 mm have kept their proportions after the drawing
- The gradients have improved the fatigue life of drawn wires
- No significant gradient in the 2.25 mm diameter wire

Low cycle fatigue assessement

Monolitic

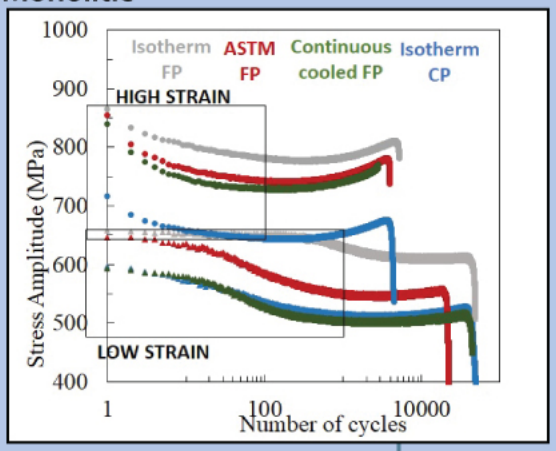

Gradient

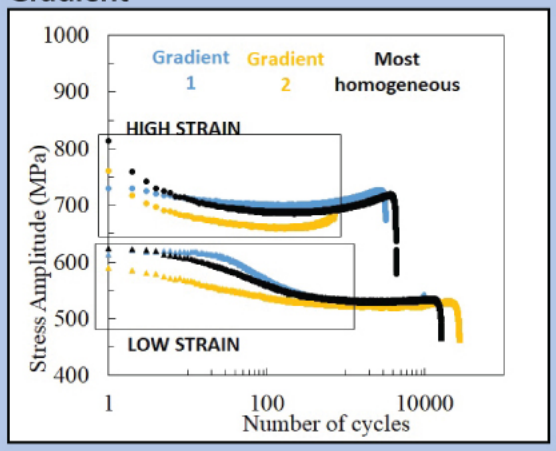

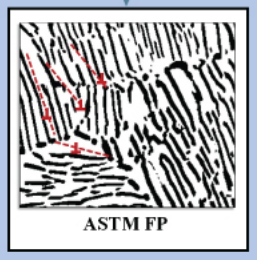

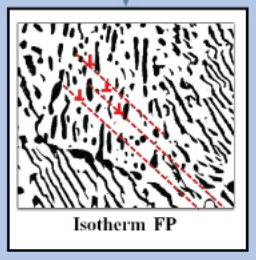

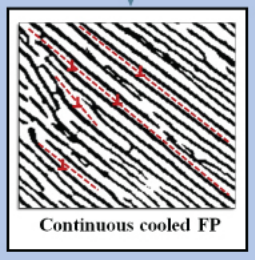

Same interlamellar space and the different morphology entail different stress levels, strain hardening, effective stress and softening.

The different pearlite morphology also presented different mean free path for the dislocations.

The fatigue of pearlitic steels is more affected by the morphology than the gradients.

Investigation de l'effet du gradient microstructural généré pendant le patentage sur les propriétés mécaniques finales des fils

Résumé : Les aciers perlitiques pourraient apparaître comme une microstructure simple, de composition eutectoïde contenant deux phases (cémentite et ferrite) arrangées en lamelles. Cependant, ils présentent une microstructure hiérarchisée, composée de nodules de même cristallographie semblables à des grains. Ces nodules comprennent des colonies formées de lamelles parallèles de ferrite et de cémentite à l'échelle nanométrique. Dès lors, les aciers perlitiques offrent une résistance et une ductilité élevées à un coût raisonnable, en accord avec les applications telles que câbles de pont, ressorts… Bien que les aciers perlitiques soient connus et largement étudiés depuis plus de 150 ans, il pourrait paraître difficile de proposer de nos jours des voies d'amélioration de leurs propriétés mécaniques. Cependant, certaines options n'ont pas encore été envisagées comme le gradient microstructural ou le contrôle des morphologies de la perlite. Le concept de gradient microstructural a été largement exploré pour des microstructures simples d'aciers (ferritique ou austénitique), mais sa transposition vers les aciers perlitiques est plus compliquée. Ce travail de thèse vise à étudier la faisabilité de produire un gradient microstructural dans des aciers perlitiques et de contrôler la morphologie de la perlite. Il repose sur la compréhension des mécanismes métallurgiques impliqués et l'impact sur les propriétés mécaniques, en particulier la fatigue, compte tenu de l'application finale de ce matériau. Le contrôle de la microstructure et du gradient est basé sur la transformation de l'austénite en perlite et, par conséquent, tous les paramètres pouvant influencer cette transformation doivent être étudiés. Cela comprend des paramètres de traitement thermique (vitesse de chauffage, vitesse de refroidissement, mode de refroidissement, température de transformation) et des matériaux (espacement interlamellaire entre ferrite et cémentite initial, état de déformation de la perlite). L'espacement interlamellaire, connu pour contrôler les propriétés mécaniques des aciers perlitiques, varie avec la température de transformation, donnant lieu à une perlite grossière et fine lorsqu'elle est transformée à températures élevée ou basse, respectivement. Nous montrons qu'il est possible de créer un gradient microstructural d'espacement interlamellaire mais ce gradient est limité par le diamètre du fil. A partir d'essais utilisant un dilatomètre, ces gradients ont été obtenus avec succès dans des fils de diamètre 6 et 12 mm. Ces fils à gradient microstructural ont ensuite été tréfilés et les propriétés mécaniques avant et après tréfilage ont été comparées afin de s'assurer que les gradients formés lors du traitement thermique sur des fils de diamètre 6 mm sont toujours présents sur les fils de diamètre final 2,25 mm. La morphologie de la perlite a également été modifiée par la maîtrise des traitements thermiques utilisant un refroidissement continu et isotherme. Des perlites divorcées, connectées et bien alignées de même distance interlamellaire ont été produites. Il s'avère que la morphologie de la perlite dans des échantillons monolithiques a un impact plus important sur la plasticité cyclique que la présence d'un gradient. Les résultats obtenus dans ce doctorat ont donné lieu à discuter de la transformation perlitique lors d'un refroidissement continu et isotherme, des mécanismes contrôlant la morphologie de la perlite (surtout divorcée ou lamellaire), des phénomènes métallurgiques se produisant lors du chauffage (recristallisation, restauration et sphéroïdisation), ainsi que des mécanismes de plasticité de la perlite. Enfin, la possibilité de réaliser des gradients microstructuraux avec les moyens de refroidissement utilisés sur des lignes de tréfilage et de traitements thermiques a aussi été étudiée. L'obtention de gradients par des technologies de refroidissement alternatives autre que le plomb est un réel succès compte tenu des contraintes environnementales. **Mots-clés: Perlite; Transformation de phase; Dilatomètre; Fatigue ; Gradient ; Patentage.**

Investigation of the effect of microstructural gradient generated during patenting of wires on their final mechanical properties

Abstract: Pearlitic steels could appear to be a simple and classic microstructure, with a rather simple eutectoid composition containing two phases (cementite and ferrite) in a lamellar distribution. However, they feature a hierarchical microstructure, which is composed of nodules that present the same crystallography and are grain-equivalent, then the nodules comprise the colonies that contain the parallel ferrite and cementite lamellas at a nanometric scale. As a result, pearlitic steels offer high strength and ductility at a reasonable cost, which fits very well for various structural and reinforcement applications, e.g., steel core, bridge cables, wire ropes, springs…Although pearlitic steels are known and vastly studied for over 150 years, it could appear difficult to still propose manners of improving their mechanical properties. However, some options have not yet been considered such as the microstructural gradient or the control of the pearlite morphologies. The microstructural gradient concept has been widely explored in simple microstructure in steels, such as ferrite or austenite, but it is more complicated to export it in the pearlitic steel. The present Ph.D. aims to investigate the feasibility of producing a microstructural gradient in fully pearlitic steels and of controlling the pearlite morphology. It is sought the understanding of the involved metallurgical mechanisms and the impact on the mechanical properties, especially fatigue, considering the final application of this material. The control of the microstructure and the gradient is based on the transformation of austenite into pearlite and, therefore, all the parameters that could influence this transformation must be studied. It includes heat treatment parameters (heating rates, cooling rates, cooling modes, temperature of transformation…) and materials ones (initial interlamellar spacing, deformation state of pearlite…). The spacing between the ferrite and cementite lamella, known to govern the mechanical properties of pearlitic steels, varies with the transformation temperature, which results in coarse and fine pearlite when transformed at high or low temperatures, respectively. It is found that a microstructural gradient of interlamellar spacing is possible to be formed but is limited by the rod diameter. Using the dilatometer, it was successfully processed in a 6 and 12 mm diameter rod. The gradient-containing wires were then drawn and the mechanical properties before and after drawing are compared to assure that the gradients formed during the heat treatment of the 6 mm diameter wires are still present on the 2.25 mm final diameter wires. The morphology of pearlite has also been modified by control of heat treatments using continuous and isotherm cooling. Divorced, connected and well-aligned perfect pearlites with the same interlamellar distance have been processed. It turns out that the morphology of the monolithic pearlite specimen has a higher impact on cyclic plasticity than the presence of a gradient. The results obtained in this Ph.D. gave rise to discussions on the pearlitic transformation under continuous and isotherm cooling, on the mechanisms controlling the morphology of pearlite (mostly divorced or lamellar), on the phenomena happening during heating, (recrystallization, recovery, and spheroidization), and also on the mechanisms of plasticity of pearlite. Finally, the feasibility of the production of the gradients by real cooling technologies is assessed by transforming the wires in a pilot line. It is of most interest that the gradients are produced by alternative cooling technologies since the lead patenting technique is not the most environmentally friendly, although the most widely used. **Keywords : Pearlite ; Phase transformation ; Dilatometry ; Fatigue ; Gradient ; Patenting;**

Membre du Groupe des Écoles Centrale
Centrale Lille
Cité Scientifique – CS20048 – 59651 Villeneuve d'Ascq Cedex – France
Tél. + 33 (0)3 20 33 53 53 – http://centralelille.fr